Characterisation and Reactivity of Thermal and Photo-Generated Surface Defects and Radical Centres over TiO_2; An EPR Investigation.

Submitted in candidature for the degree of Doctor of Philosophy

By
Anna Lisa Attwood

Department of Chemistry
Cardiff University
September 2004

ProQuest LLC
789 East Eisenhower Parkway
P.O. Box 1346
Ann Arbor, MI 48106-1346

For Mum, Dad, Rhianne, Ross and Ashley, all my love, always.

Abstract

Electron Paramagnetic Resonance Spectroscopy (EPR) has been used to thoroughly characterise the nature of trapped charge carrier pairs (i.e., holes and electrons) generated in different TiO_2 polycrystalline powders (P25 Anatase and two different Rutile materials). The paramagnetic centres were formed by vacuum reduction and UV irradiation of the TiO_2 samples, allowing a comparison of the two methods to be made.

The reactivity of these trapped charge carrier pairs have been examined following the formation of oxygen centred radicals *via* oxygen addition. These generated species can change depending on the pre-treatment conditions and nature of the surface. On thermally reduced Anatase, O_2^- anions are preferentially formed whilst O^- and O_3^- anions are produced on the Rutile forms of TiO_2. Superoxide anions (O_2^-) and trapped holes (O^-) were identified after photo-irradiation of all dehydrated TiO_2 samples. The nature and stability of these oxygen centred radicals have been studied as a function of surface hydration. The ability to generate the radicals and the effects of surface hydration on the stability, and lifetimes have been examined.

Nitric oxide has also been employed as a surface probe to study the surface crystal fields of the different TiO_2 surfaces. The effect of surface hydration and NO have also been studied, revealing the different heterogeneity of sites responsible for NO binding, which was complimentary to the results obtained from the superoxide experiments.

Co-adsorption and subsequent UV irradiation (100K) of acetone and oxygen onto a clean oxidised Anatase surface results in the formation of an unstable peroxy intermediate. The radical decayed irreversibly at temperatures greater than 150K but was regenerated by subsequent low temperature irradiation. Use of isotopically labelled gases (CD_3COCD_3, $^{17}O_2$) enabled the identification of the radical as the $CH_3COCH_2OO^{\bullet}$ species generated by hole transfer to adsorbed acetone.

The photo dynamics of the thermally generated Ti^{3+} and medium polarised conduction electrons in the TiO_2 samples have also been followed as a function of TiO_2 material and temperature. Interestingly, the rate of photoexcitation of surface Ti^{3+} centres follows opposite trends on anatase samples compared to rutile, and this difference has been discussed within the context of the different trapping sites available for electron stabilisation.

Acknowledgements

I would like to thank,

Dr Damien Murphy, for the enthusiasm and encouraging guidance he has shown me throughout my time as a PhD student. Thanks also go to John Edwards of Tioxide Ltd., for the many helpful discussions. I would also like to thank Dr. Chris Rowlands for his assistance throughout my first year of study. Dr. Robert Farley, 'Charlie' for your constant willingness to always help and knowledge of everything.
Financial support was provided by the Engineering and Physical Sciences Research Council (EPSRC) and Huntsman Tioxide LTD., for which I would like to express my gratitude.

Thanks also to,
the many great friends I have made throughout my time as a PhD student and the brilliant times we've all shared together, I know there will be many more to come.

Finally to my family, for the continuous love, support and immense patience you have given me throughout my whole Ph.D.

Chapter Number	Contents	Page Number

Chapter 1 General Properties of Titanium Dioxide

Chapter 2. The Role of EPR in the Characterisation of Oxygen centred Radicals in Photocatalysis

Chapter 3. An Introduction to Solid State Chemistry

Chapter 4. Brief Overview of the Electron Paramagnetic Resonance (EPR) Technique

Chapter 5. Genesis of Paramagnetic Centres in Thermally Reduced TiO_2

Chapter 6. Formation of Oxygen Centred Radicals over Thermal Reduced and Photo-Irradiated TiO_2

Chapter 9. Conclusion

Chapter 1

General Properties of Titanium Dioxide

1.1 Occurrence and Manufacture

Titanium was discovered in 1791 in Cornwall England.[1] It is the ninth most abundant element in the earths crust and is widely distributed around the world. Titanium exhibits typical transition metal properties, forming a range of coordination and addition compounds with non-metals, including halides, chalcogenides, hydrides, sulphides and oxides. Titanium dioxide is the most common form of naturally occurring oxides, existing in the three forms, Anatase, Rutile and Brookite. In comparison to Anatase and Rutile, Brookite rarely occurs and displays no photocatalytic properties or commercial uses and therefore will not be discussed further. Ilemite and mineral rutile are the most important naturally occurring ores. Ilmenite is a black sand or rock with the theoretical chemical formula $FeTiO_3$; the TiO_2 content varies from 45-60% depending on its geological source. Mineral Rutile is naturally occurring titanium dioxide; with the TiO_2 content normally 95%. Both ores may contain considerable amounts of siliceous and iron based impurities, which must be significantly lowered or they may adversely affect the chemical and photochemical properties of the finished product.

Pure titanium dioxide is a colourless, crystalline solid and is stable over the stoichiometric range $TiO_{2.003}$ to $TiO_{1.988}$. $TiO_{<2}$ contains reduced titanium cations in the Ti^{3+} form, causing a colour change from white to dark blue. The Ti^{3+} cations are readily oxidised back to Ti^{4+} by oxygen, water and other oxidising agents. As with other dioxides of the *d block* elements TiO_2 is stable, non-volatile and insoluble in most solvents with its highest solubility in H_2SO_4 and HF. It is amphoteric but contains more acidic properties then basic.

Generally, TiO_2 is prepared primarily *via* two main processes known as the Sulphate Process and the Chloride Process, as discussed below;

The Sulphate Process

The first commercial exploitation of titanium dioxide did not take place until 1913 when the titanium dioxide pigment was manufactured by a fusion process. The sulphate process, developed by Farup and Jebsen, soon replaced this in 1928.[1]

Ilemite is commonly used as the raw material for the sulphate process. The sulphate process can readily produce both Anatase and Rutile forms of the TiO_2. The reactions involved are shown below:

$$FeTiO_3 + 2H_2SO_4 \longrightarrow TiOSO_4 + FeSO_4 + 2H_2O \quad (1.1)$$

$$TiOSO_4 \xrightarrow{OH^-} TiO_2nH_2O + H_2SO_4 \quad (1.2)$$

$$TiO_2nH_2O \xrightarrow{HEAT} TiO_2 + nH_2O \quad (1.3)$$

The finished material typically contains low levels of sulphate-based impurities, which may subsequently modify its chemical and photochemical properties. Crystallisation is initiated by the addition of suitable nuclei, which control the final crystalline form.

The Chloride Process

An alternative method, the Chloride process, is a more recent development, which was commercially introduced in 1958. Its use has expanded rapidly in the USA where it is now the prime method of production. The Chloride process predominately produces the Rutile form of TiO_2. Although it is not impossible to produce Anatase also in the Chloride process, however, the thermodynamics of the route make it more applicable to the production of Rutile pigments. Mineral Rutile is used as the starting material and the reactions involved are shown below in equations 1.4 – 1.5,

$$TiO_{2(impure)} + 2Cl_2 + C \longrightarrow TiCl_4 + CO_2 \quad (1.4)$$

$$TiCl_4 + O_2 \longrightarrow TiO_{2(pure)} + 2Cl_2 \quad (1.5)$$

The Chloride process is more energy efficient and produces less waste than the Sulphate process since chlorine is recycled.[2] Residual chlorine associated with the solid TiO_2 is removed by aqueous hydrolysis or calcined in a kiln to hydrolyse the chlorides and drive off as hydrogen chloride.

Careful control in both the Sulphate and Chloride processes are required in the latter stages to ensure that the finished product is not coloured. Other semi stable oxides of titanium can be produced by reduction of TiO_2 under various conditions, e.g., TiO (yellow), Ti_2O_3 (violet) and Ti_3O_5 (metallic blue). Due to their colouration none of the reduced oxides are of any commercial interest.

1.1.1 Structure of Titanium Dioxide

Of the two most common forms of TiO_2 (i.e., Anatase and Rutile), the Rutile form is generally the more stable form and as a result more abundant. It contains a more closely packed structure than Anatase that gives rise to the difference in properties. In the two crystals, Anatase and Rutile, the Ti atoms are surrounded by six adjacent O atoms positioned at the corners of a distorted octahedron, and each Ti is surrounded by three adjacent Ti atoms. Both TiO_2 structures, Anatase and Rutile, are shown in figure 1.1 below.

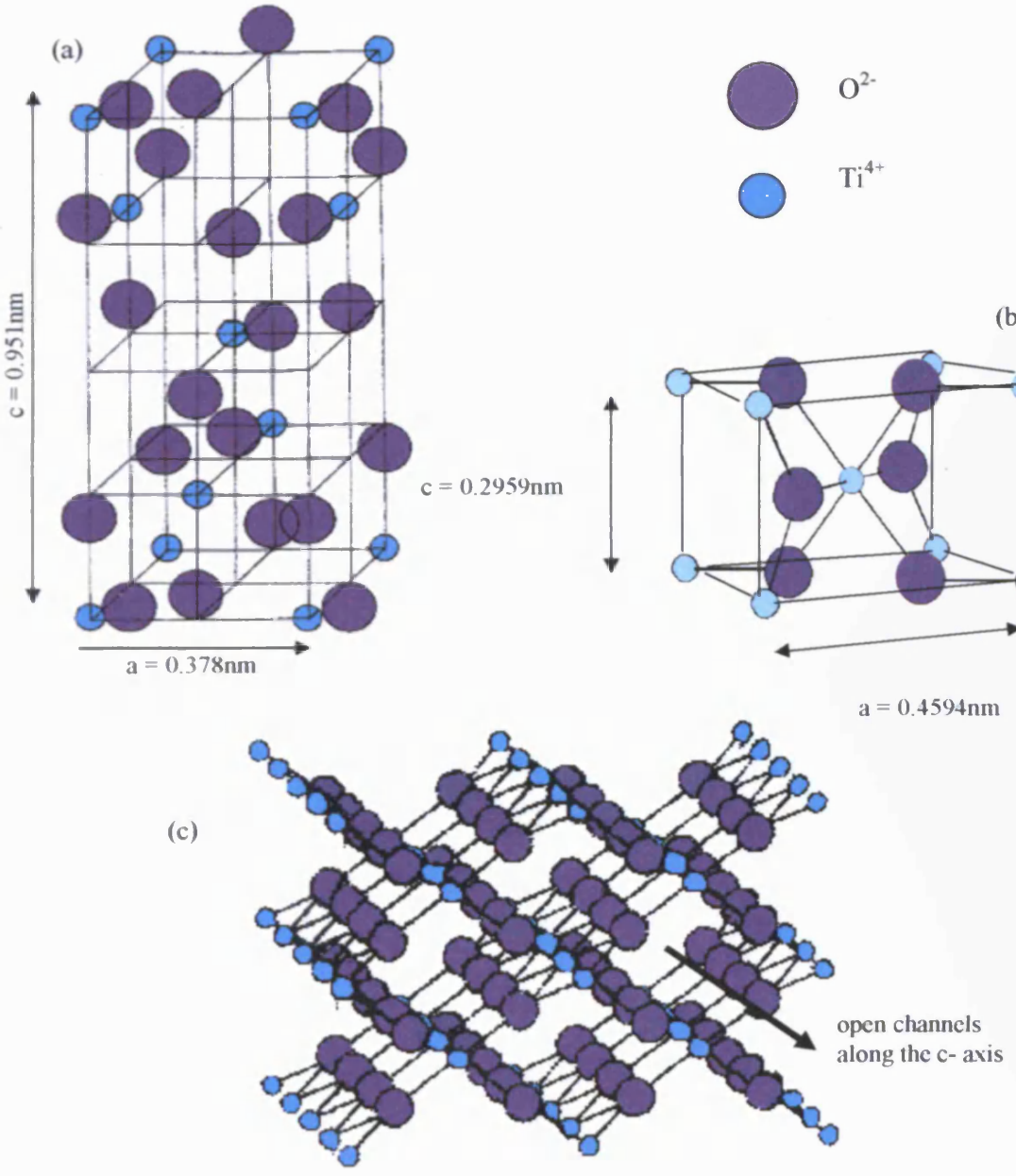

Figure 1.1. Ball and stick models of (a) structure of Anatase TiO_2, (b) unit cell of Rutile and (c) extended crystal structure of Rutile TiO_2

The closer packing in the Rutile structure gives rise to a higher refractive index and greater chemical stability compared to Anatase. While Rutile melts at 1825°C, Anatase has no specific melting point due to its irreversible transformation to Rutile before it reaches its melting point, a process known as rutilisation. Typical temperatures for the rutilisation are in the region 700°C - 1200°C depending on conditions. It is a broad irreversible phase transition (ΔG negative) which is highly sensitive to the presence of impurities, and liberates 8 to 12 kJ mol^{-1}.[3] Both forms of TiO_2 are intrinsic photoactive n-type semiconductors with wide band gaps (*cf.* chapter 3).

Most commercial Titania powder catalysts are a mixture of Rutile and Anatase (e.g., Degussa P25, the most commonly used contains approximately 80-90% Anatase and the rest Rutile). There is growing evidence that Anatase is more active than Rutile for O_2 photo-oxidation but not necessarily more reactive for all photocatalytic processes. Anatase and Rutile show inherent differences in particle size and this might cause some of the observed differences in chemical properties. However, in order to gain a better understanding of TiO_2-based devices, it is clearly important to obtain atomic-scale information on well-characterised Anatase surfaces.[4]

Although the band gap of Anatase and Rutile is only slightly different, Table 1.1, the difference does hold an effect of the photo-efficiencies with Anatase being more efficient than Rutile. This difference in photo-efficiency indicates that they vary as a function of both band gap and crystal structure.

Table 1.1. Selected Physico-Chemical Properties of TiO_2.[5,6]

Property	**Rutile**	**Anatase**
ΔH_f^{θ} / kJ mol^{-1}	-944.70	-933.00
Band Gap / eV	3.23	3.06
Crystal structure	Tetragonal	Tetragonal
Crystal symmetry	$D4_h$	$D4_a$
Melting point / °C	1825	N/A
Refractive index	2.70	2.55
Relative Molecular Mass	79.88	79.88
Specific Gravity / gcm^{-3}	4.23	3.90

1.1.2 Refractive index

TiO_2 has an extremely high refractive index (Table 1), this may be exploited in its use as a pigmentary substance. TiO_2 absorbs almost no incident light in the visible region of the spectrum. The light is transmitted and refracted through the crystal. The refractive index of η_r (Eq.1.6) of a material is defined as the ratio of the speed of light in a vacuum c to its speed in the medium (v),

$$\text{Refractive index, } \eta_r = \frac{c}{v} \qquad (1.6)$$

The refractive index is directly related to the molecular polarizability of the material through which light is propagated. Since photons of high frequency carry more energy than those of lower frequency, they are more effective at distorting the electronic distribution of molecules in their path. Hence, the refractive index of a material increases with increasing frequency of light; a phenomenon known as dispersion. Refractive indices are thus measured at a constant reference frequency. The refractive index of TiO_2 (η_r = 2.7 for Rutile and η_r = 2.55,for Anatase) is typical for most metal oxides, only diamond has a higher refractive index.[7] In comparison, the refractive indices of most common organic compounds lie in the range 1.3 to 1.5.[8]

1.2 Photocatalysis and Heterogeneous Catalysis over TiO_2

1.2.1 Photocatalysis over TiO_2

When light of the correct frequency is shone onto a semiconductor, such as TiO_2, electrons are excited from the valence band to the conduction band. This electron-hole pair may undergo radiation-less recombination in the bulk, or those near the surface may become separated and stabilised under the influence of the space charge layer.

The band gap of TiO_2 is $\approx$ 3.1 eV, specifically 3.23 eV for Rutile and 3.06 eV for Anatase, therefore radiation of < 388 nm provides enough energy to promote an electron from the valence band to the conduction band. An electron-hole pair forms near the surface and migrates under the influence of the space charge layer. This space charge layer encourages the movement of holes to the surface and electrons to

the bulk of the crystal (see figure 1.2). An equilibrium is eventually achieved, where the electrons reach the surface at the same time as the holes (figure 1.3).

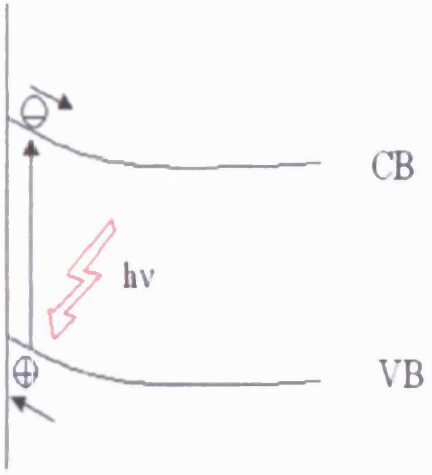

Figure 1.2. Space charge layer.

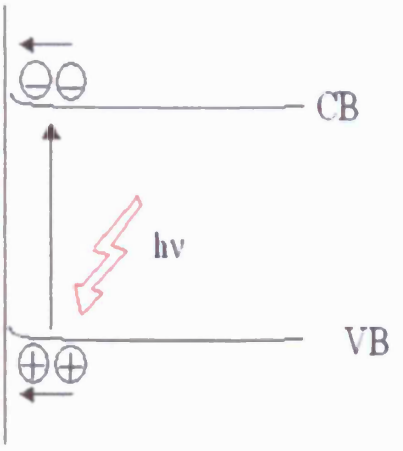

Figure 1.3. Equilibrium point.

At the surface, photo-produced holes and electrons can take part in chemical reactions. For efficient photocatalytic operations to occur, at least two types of adsorbed substrate molecules are required; the substrate to be mineralised, which may be an electron donor (D) or an electron acceptor (A), and some sacrificial species which will accept electrons when the substrate molecule is an electron donor, and donate electrons when the substrate molecule is an electron acceptor.[9]

$$A + e^- \longrightarrow A^- \qquad (1.7)$$

$$D + h^+ \longrightarrow D^+ \qquad (1.8)$$

Oxidation reactions occur when the oxidation potential of the reacting species lies above that of the band gap. For reduction reactions to occur, the reduction potential of the reacting species lies below that of the band edge gap, and so is more positive than the conduction band. These processes are schematically summarised in figure 1.4 on the next page.

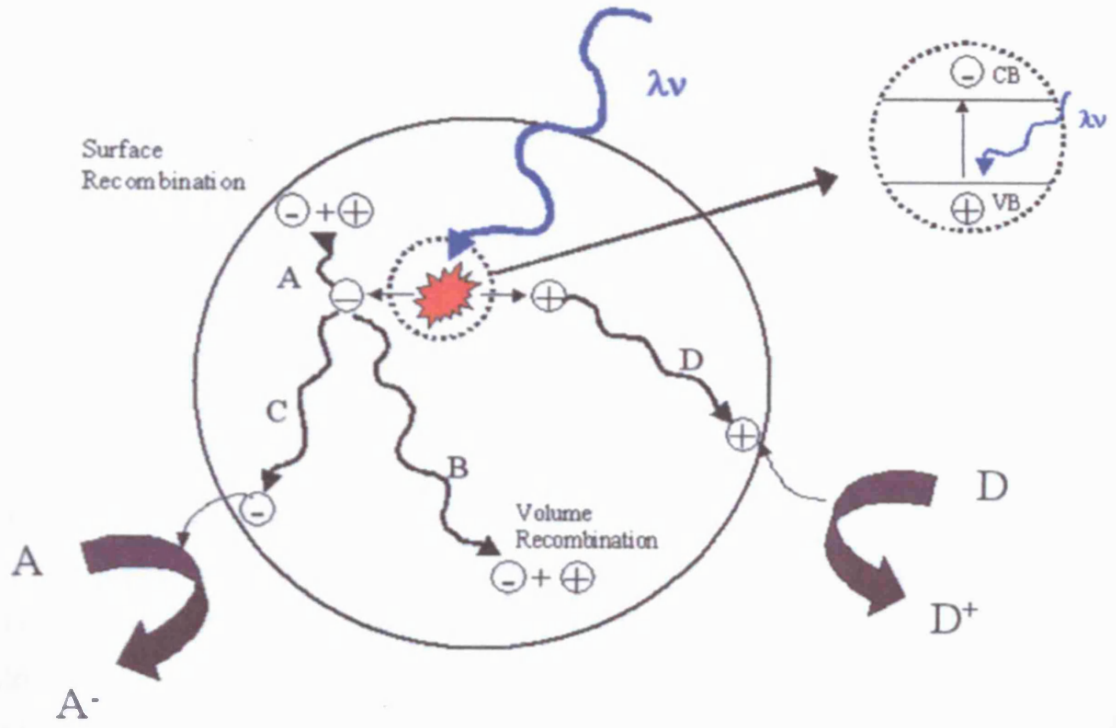

Figure 1.4. Schematic photo excitations of TiO_2 followed by de-excitation events (A-D).[9]

1.2.2 Basic chemical principles of photocatalysis.

The principle of photocatalytic remediation of un-harmful products is to bring about the complete oxidative mineralisation of the pollutant substrate *via* the process.

$$\text{Substrate} + O_2 \xrightarrow[\text{UV Light}]{\text{Semiconductor}} x\,CO_2 + y\,H_2O \qquad (1.9)$$

Thus, eliminating the pollutant or pollutant precursor, by conversion to carbon dioxide and water. These mineralisation products can then be safely disposed. When choosing the type of semiconductor suitable for these purposes several points need to be considered.

- The material must be efficient at absorbing ultra violet (UV) radiation; absorption of visible light does not lead to efficient mineralisation of the substrate.
- The semiconductor must be capable of catalytic operation in both the aqueous and gaseous phases.

- An acceptable working lifetime of the semiconductor is required; therefore resistance to photo-degradation is essential. In general, semiconductors are less prone to photo-degradation then other chalcogenide-based materials.
- Lastly, the material should be cheap to manufacture and biologically inert.

Both TiO_2 polymorphs (Anatase and Rutile) satisfy the majority of these requirements, and generally display high photo-activity and corrosion resistance.

1.2.3 TiO_2 derived Photocatalysis

In order to maximise the surface area of TiO_2 available for photocatalytic electron transfer it is necessary to attempt to minimise the particle size. However, as the semiconductor particle diameter approaches a critical lower limit (*ca.* 10nm), size quantisation effects begin to rise. As the particle diameter approaches the Bohr radius of the first exciton, the electronic energy levels within the particle become discrete and quantisied, i.e., the continuum of band states is lost (*cf.* chapter 3). The result of this quantum confinement is to reduce the wavelength of the first exciton, resulting in a larger 'band gap'.[10] The principal photon absorption of the material is then shifted to higher frequencies ('blue shifted'). A consequence of this is that less of the solar spectrum is made available for absorption, and solar photo-reactor efficiencies may be reduced. The change in surface redox potentials is not necessarily disadvantageous, as it could lead to better redox coupling between semiconductor and substrate.

The use of TiO_2 as a photo-reactor in direct production of energy is therefore difficult. A main problem is the poor relationship between the titanium dioxide absorption spectrum and the solar spectrum in the use of TiO_2 for solar energy conversion. Unmodified TiO_2 absorbs about 3% of the total solar spectrum; this results in a solar energy conversion efficiency of approximately 1%. Altering the band gap properties of TiO_2, e.g., by doping with transition metal ions or implantation with nanoparticles for example, to induce visible light absorption does not necessarily increase the photo-efficiency as this results in lower photo-voltages. Other techniques to improve the photo-efficiency of TiO_2 have proved successful. Metallic Pt or Ag dispersed onto the surface of the TiO_2 particles significantly increases the photo-efficiency for colloidal suspension.

This can be explained by the photoelectrochemical mechanism (*cf.* 1.3.4.), whereby each semiconductor particle behaves as a closed circuit in which the products of charge transfer are spatially separated. The metallic Pt on the TiO_2 surface works effectively at also enhancing the charge separation of the electron hole pair recombination and improving the photocatalytic performance.[11]

1.2.4 Transition Metal Ion Doped TiO_2: Enhancement or Suppression of Photocatalysis

As mentioned above, when titanium dioxide is irradiated with UV light, electrons are excited from the valence band to the conduction band of the TiO_2, leaving holes in the valence band. The efficiency of photocatalysts strongly depends on the lifetime of the electron-hole pairs generated. Recombination of the holes and electrons are an important process in semiconductors therefore, the rate at which they recombine plays a crucial role in the photocatalytic reactions with semiconductor particles, in particular the conversion of solar light energy to fuel.

Doping of TiO_2 powders with low levels of transition metal ions have a major impact upon the photo-generated electron–hole pair recombination rate.[12, 13] Since interfacial electron transfer must compete with electron hole recombination processes, the presence of small amounts of impurity ions ($\approx 0.1\%$) can have a major influence on the photo efficiencies.

Whether or not the photo-efficiency is enhanced or retarded depends upon the type of dopant introduced, as well as the level of doping. For example, at 0.1 to 0.5% dopant concentrations, Fe^{3+} and V^{4+} increase the photo reactivity, whereas Co^{3+} and Al^{3+} cause a significant decrease at the same concentrations.[14] The impurity ions are believed to act either as electron-hole recombination centres (leading to loss of photo activity) or merely as hole traps, thus extending the lifetime of the photo-generated charge pair (leading to an increase in photo reactivity). The purity of TiO_2 samples used in photo catalytic studies is thus critical, since the presence of as little as 0.1% impurity may have a significant effect on experimental observations.

During transition metal ion implantation (V, Cr, Mn, Fe, and Ni) into TiO_2 by high voltage[15] a large shift in the absorption band of the TiO_2 catalysts into the visible region of the electromagnetic spectrum is possible. The ion implantation of Ar, Mg and Ti exhibited no shift in the absorption; therefore the shift was not due to the high-energy implantation but by interaction of the transition metal with the TiO_2.

As mentioned previously, the band gap of TiO_2 is $\approx$ 3.1 eV, therefore wavelengths of < 388nm are required to promote the electrons from the valence band to the conduction band. Energies of this wavelength correspond to the UV part of the spectrum. Since only the UV region of the spectrum can provide the correct amount of energy for promotion, only 3-4% of the solar energy is actually available for any reaction to occur. The metal ion implanted TiO_2 catalysts enable absorption of visible light up to wavelengths of 400 – 600 nm and are able to operate efficiently as photo catalysts, they are therefore termed '*Second Generation* TiO_2.'[16]

In contrast to this Herrmann *et al.*,[17] and Borgarello *et al.*,[18] reported that Cr doping by a chemical method decreased the photoreactivity under both visible and UV illumination. Even though the effects of metal doping on the activity of TiO_2 have been a frequent topic of investigation,[19] it remains difficult to make direct comparisons and unifying conclusions due to the widely varying experimental conditions, sample preparation and determination of photo reactivity.

1.2.5 Catalytic Properties

TiO_2 exhibits both photocatalytic and non-photocatalytic activity.[20] It is important to bear in mind the non-photocatalytic activity of TiO_2 which influences the reaction pathway of photon-initiated processes.

In the extended crystal structure of both Anatase and Rutile, surface hydroxyl groups terminate at the particle surface, which gives rise to titanol moieties Ti_{surf}-OH at the particle surface.[21] The titanol function of TiO_2 may act as a trapping centre for photo-induced electron vacancies (holes/h^+) arising within the bulk of the crystal[21](Eq. 1.10).

$$Ti_{surf}\text{-}OH + h^+ \longrightarrow Ti_{surf}\text{-}OH^{\bullet} \qquad (1.10)$$

Hole transfer to adsorbed substrates may proceed by direct interaction with the TiO_2 surface. Under photocatalytic conditions the photo-generated electrons (e^-) are trapped at cationic sites (Eq. 1.11) associated with the crystalline defects, some of which are catalytically active.

$$Ti^{4+} + e^- \longrightarrow Ti^{3+} \qquad (1.11)$$

Photo-generated electrons can then be transferred to an adsorbed substrate molecule *via* Ti^{3+} states or recombine with a hole either in the bulk of the crystal or at titanol functions.

The titanol groups are responsible for the amphoteric behaviour of TiO_2, and therefore enable it to undergo non-photocatalytic acid or base catalysis (H^+ transfer) in aqueous solution,[22] represented by the equations 1.12 and 1.13.

$$Ti_{surf}\text{-}OH + H+ \rightleftharpoons >Ti\text{-}OH_2^+ \quad (1.12)$$

$$Ti_{surf}\text{-}OH \rightleftharpoons >Ti\text{-}O^- + H^+ \quad (1.13)$$

The presence of both acidic and basic titanol functions arises as a consequence of the intrinsic heterogeneity of TiO_2 surfaces. In general, weak acids and bases do not exhibit strong interactions with unmodified TiO_2 powders. The presence of titanol functions may also alter the photochemical response of small photo-active molecules interacting with the TiO_2 surface.[23] TiO_2 also exhibits thermal heterogeneous catalytic properties at elevated temperatures, and has been proposed as a novel de-NO_x catalyst for automotive applications.[20]

1.2.6 Heterogeneous Photocatalysis; History and Applications

During heterogeneous photocatalysis, photoinduced molecular transformations or reactions take place at the surface of a catalyst. Semiconductor surfaces provide both a fixed environment to influence the chemical reactivity of a wide range of adsorbates and a means to initiate light induced redox reactivity in these weakly associated molecules.

Titanium dioxide was first observed to undergo darkening during photooxidation of citric and tartaric acids from exposure to sunlight in 1921 by Renz.[24] Both TiO_2 and ZnO were among the photoactive metal oxides reported that undergo darkening during photoxidation. This new phenomenon was not appreciated until work by Wilson in 1931[25,26] was undertaken on the electronic theory of semiconductors. During the space race in the 1960's a newfound level of research was undertaken into the electronic structure of the semiconductors. Due to environmental constraints associated with manned space travel, increased research into the development of clean, lightweight energy sources such as solar panels occurred.

Undoubtedly, the biggest scientific interest of TiO_2 arrived in 1972 when Fujishima and Honda[27] provided evidence for the controlled splitting of water with the use of sunlight over a TiO_2 photoanode and Pt electrode. This was the first demonstration for the photo-electrochemical cell used in splitting water as shown in equation 1.14.

$$H_2O + UV \longrightarrow H_2 + \tfrac{1}{2} O_2 \qquad (1.14)$$

This observation prompted extensive work focusing on the production of hydrogen (as a combustible fuel) from water as a means of solar energy conversion. There has been continual growing interest in the use of metal oxide semiconductors and their application as photoactive catalysts. The remediation of industrially contaminated water by photocatalysis has received much attention. The utilization of clean safe and abundant solar energy is now helping in the lead to promising solutions not only for energy issues, due to the exhaustion of natural energy sources, but also for many problems caused by environmental pollution.[28-31]

Organic wastes such as chlorinated hydrocarbons, CFC's, dioxins, pesticides and herbicides pose a threat to both human and animal health. They are known to be present in high concentrations in many aquifers and ground water sources. Some may have a relatively prolonged residence period in the natural environment. Tests were carried out at the Lawrence Livermore National Laboratory, on an outdoor TiO_2/sunlight based photoreactor which succeeded in reducing groundwater levels of tricholoroethylene from ~ 300 to 500 ppb to < 54 ppb.[32] This solar technology has now been patented for the remediation of oil spills at sea, by flotation of TiO_2-coated hollow glass beads within the resulting oil slick[33] thus, minimising the use of environmentally damaging chemical or thermal treatments. Whilst most solar-based water remediation technologies remain at the development stage, a long goal of many environmental scientists is to incorporate semiconductor based photo-reactors directly into industrial effluent management systems.

Gas phase heterogeneous photocatalysis has also assisted in the development of environmental photocatalysis, as first observed by Dibble and Raupp.[34,35] They reported that when TCE is passed over TiO_2, under conditions of UV irradiation, the TCE is ultimately converted to CO_2 and H_2O with a high degree of efficiency. Heterogeneous photocatalytic oxidation of organic compounds in the gas phase using

TiO_2 as a catalyst, appears to be a promising process for remediation of air and groundwater polluted by Volatile Organic Compounds (VOCs).[36]

VOC's are widely used and produced both industrially and domestically and have provided a major threat to the environment.[37] Many VOCs are toxic with some being considered as carcinogenic, mutagenic or teratogenic[38]. A localized problem arising from VOCs is the formation of photochemical smog in large built up areas.[39] The most significant problem related to the emission of VOC's is centred on the production of peroxyacyl nitrate (PAN)[40] in the presence of sunlight, *via* the free radical mechanism shown below:

$$R\text{-}CHO + UV + M \longrightarrow RCO^{\bullet} + H^{\bullet} \quad (1.15)$$

$$RCO^{\bullet} + O_2 \longrightarrow R\text{-}CO_3^{\bullet} \quad (1.16)$$

$$R\text{-}CO_3^{\bullet} + NO_2^{\bullet} \longrightarrow R\text{-}CO_3.NO_2 \quad (1.17)$$

These can ultimately lead to severe respiratory problems in humans as well as damage to crops and have been implicated in the formation of acid rain.[41] During heterogeneous photocatalysis of VOC's, the VOC's are preferentially adsorbed on the surface and oxidized to (primarily) CO_2 and H_2O. Other proposed novel applications reported for TiO_2 based photocatalyst systems include; the removal of organic soilage in interior buildings,[42] removal of waste material from road side lighting,[43] self sterilising surfaces removing bacteria,[44-48] TiO_2 electrodes for killing cancerous cell.[49,50] Reported futuristic applications include the use of TiO_2 photoreactors for life support systems on the moon.[51] Other applications of the photocatalytic properties of TiO_2 are summarised in Table 1.2.

Photocatalytic oxidation of organic compounds in the gas phase using TiO_2 as a catalyst is a promising process for remediation of air and ground water polluted by VOCs. Heterogeneous photocatalysis using TiO_2 have several advantages:

- TiO_2 is relatively inexpensive,
- Shows efficient destruction of toxic contaminants,
- Highly stable chemically,
- Photo-generated holes are highly oxidising and photo-generated electrons are reducing,
- Operates at ambient temperature and pressure, and
- Reaction products are usually CO_2 and H_2O.[36]

Table 1.2. Selected applications of TiO_2 based photocatalysis.

Property	Category	Application
Self-cleaning	Materials for residential and office buildings	Exterior walls kitchen & bathroom components, interior furnishings, plastic surfaces aluminium siding building stone & curtains paper window blinds
	Indoor & outdoor lamps	Translucent lamp shades, coatings on fluorescent lamps and highway tunnel lamp cover glass,
	Materials for roads	Tunnel wall, soundproofed walls traffic signs and reflectors
	Others	Tent material, cloth for hospital garments& uniforms and spray coating for cars
Air - cleaning	Indoor air cleaners	Room air cleaner, photocatalyst-equipped air conditioners and interior air cleaners for factories
	Outdoor air purifiers	Concrete for highways, roadways and footpaths, tunnel walls, sound proof walls and building walls
Water purification	Drinking water	River water, ground water, lakes and water storage tanks
	Others	Fish feeding tanks, drainage water and industrial wastewater
Anti-tumour activity	Cancer therapy	Endoscopic-like instruments
Self - sterilising	Hospital	Tiles to cover the floor and walls of operating rooms, silicone rubber for medical catheters and hospital garments and uniforms
	Other	Public rest rooms, bathrooms and rat breeding rooms

Up to this point the discussion has focused on the photocatalytic properties of TiO_2. However, there is another property of TiO_2, the more recently discovered photo induced hydrophilic effect – superhyrophilicity. Both photocatalytic and hydrophilic processes can occur on the same TiO_2 film but are intrinsically different. Superhydrophilicity was discovered by accident, in Japan[52] in 1995. If a TiO_2 film is prepared with a certain percentage of SiO_2, it acquires superhydrophilic properties after UV illumination. In this case, electrons and holes are still produced, but they react in a different way. The electrons tend to reduce the $Ti^{(IV)}$ cations to the $Ti^{(III)}$ state, and the holes oxidize the O^{2-} anions. In the process, oxygen atoms are ejected, creating oxygen vacancies. Water molecules can then occupy these oxygen vacancies, producing adsorbed OH groups, which tend to make the surface

hydrophilic. The longer the surface is illuminated with UV light, the smaller the contact angle becomes for water; after about 30 minutes under a moderate intensity UV light source, the contact angle approaches zero, meaning that water has a tendency to spread perfectly across the surface.[52-54] TiO_2 coatings can maintain their hydrophilic properties indefinitely as long as they are illuminated. Making use of the idea of cleaning by a stream of water, coated windows can be cleaned by rainfall. There are many new original applications of the superhydrophilicity properties of TiO_2 some of which have been summarised in Table 1.3.

Table 1.3. Applications of superhydrophilicity technology.

Property	Category	Application
Self-cleaning	Roads	Tunnel lighting, tunnel walls traffic signs and sound proofing walls
	Houses	Kitchen & bathroom tiles, exterior tiles, roofs & windows
	Buildings	Aluminium panels, tiles, building stones, crystallized glass & glass films
	Agriculture	Plastic and glass greenhouses
	Electrical & electronic equipment	Computer displays, cover glass for solar cells
	Vehicles	Paint work, exterior windows & headlight covering
	Paint	General-purpose paints & coatings
	Others	Tableware, kitchenware
Anti-fogging	Roads	Road mirrors
	Houses	Bathroom mirrors
	Stores	Refrigerated showcases
	Electrical & electronic equipment	Heat exchangers for air conditioners
	Vehicles	Inside surfaces of mirrors, glass films, rear-view mirrors & windshields
	Paint	General-purpose paints & coating a
	Optical instruments	Optical lenses
	Other	Spray-on antifogging coatings & films
Bio-compatibility	Medical instruments & supplies	Contact lenses & catheters

1.3 General Applications of TiO_2

1.3.1 Commercial Uses

Titanium dioxide is the most widely used white pigment material for coating applications. Figure 1.5 displays the end use breakdown of TiO_2 pigments based on 1992 world consumption data.

Titanium dioxide is an extremely effective white pigment, used in coatings, plastics, printing inks and paper.[55] The most important attribute of TiO_2 is its high refractive index (Table 1.1), which gives it its potential for producing opacity far greater than any other common white powder.[56]

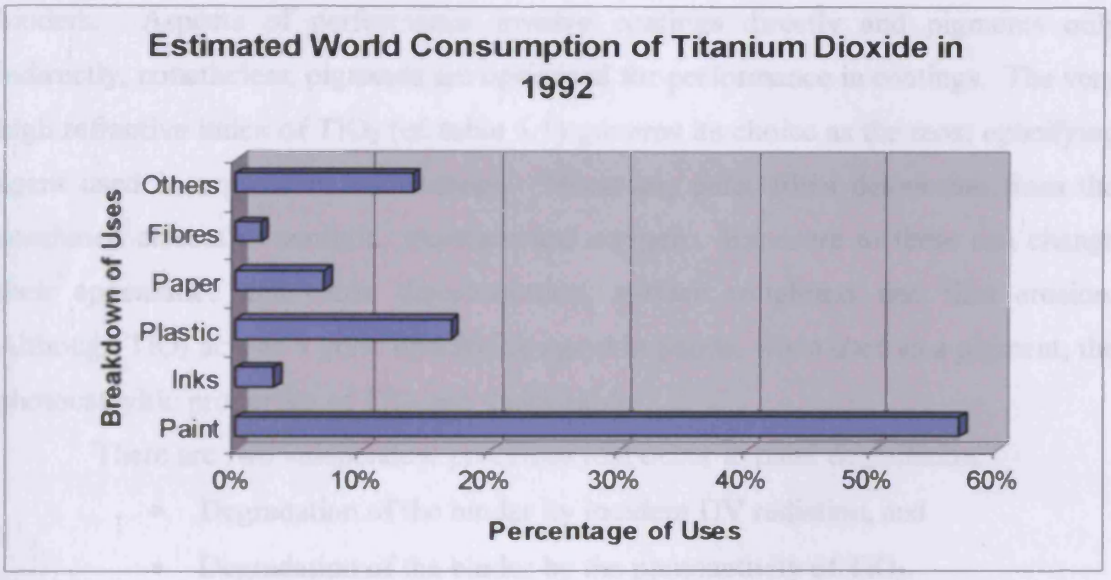

Figure 1.5. Breakdown of Estimated World Consumption of TiO_2 in 1992 (total = 2.9 million tonnes).[57]

Light can either be transmitted or refracted through a crystal, or reflected at the interfaces. Sufficient light is transmitted through a larger crystal of TiO_2 to render it transparent. However, in its finely divided, pigmentary state, there are so many interfaces that light transmitted through one particle will be reflected by others. Consequently, the whiteness of titanium dioxide is a function of particle size during reflectance. The degree of whiteness exhibited by a material may be approximated by calculating its reflectivity (F) using Fresnel's equation 1.18:

$$F = \frac{(\eta_1 - \eta_2)^2}{(\eta_1 + \eta_2)^2} \qquad (1.18)$$

where, η_1 is the refractive index of the pigment, and η_2 is the refractive index of the surrounding medium. The light scattering efficiency of the pigment determines the whiteness and opacity of the coating into which it is incorporated. It varies directly as a function of the difference in refractive index between pigment and the pigment material (Eq.1.18). Provided that the pigment material does not absorb light in the visible region of the spectrum, then the scattered light emerging from a layer of pigmented material will be white.

1.3.2 Photo-degradation of paint

Performance of paint films depends on systems composed of pigments and binders. Aspects of performance involve coatings directly and pigments only indirectly, nonetheless, pigments are optimised for performance in coatings. The very high refractive index of TiO_2 (*cf.* table 1.1) governs its choice as the most opacifying agent used in organic based coatings. However, paint films deteriorate from the combined effects of sunlight, moisture and oxygen. Exposure to these can change their appearance and cause discolouration, surface roughness and film erosion. Although TiO_2 acts as a good opacifying agent in paints, when used as a pigment, the photocatayltic properties of TiO_2 are undesirable.

There are two independent processes that occur in paint degradation:

- Degradation of the binder by incident UV radiation, and
- Degradation of the binder by the photoactivity of TiO_2.

In the former case, the biggest contributor to degradation is UV radiation; causing homolytic bond fission to occur within organic binders, resulting in the release of reactive free radical species within the polymer matrix. This will eventually compromise the structural integrity of the material, and reduce its useful operational lifetime, however, this may be overcome by the use of a durable binder. Incorporation of TiO_2 confers a high degree of degradation resistance to the organic matrix of the polymer coating[58] by providing an alternative medium for UV absorption. However titanium dioxide affects the durability of paint films in two distinct and opposing ways

- As a strong UV absorber, TiO_2 protects the paint film,
- As a UV activated oxidation catalyst, TiO_2 degrades the binder.

As mentioned above, the addition of TiO_2 to the system allows the preferential absorption of the UV radiation over the polymer therefore preventing the breakdown of the coating.

However, the band gap of TiO_2 is ≈ 3.1 eV and lies within the energy levels of the sunlight. Absorption of the UV radiation is therefore able to promote the photocatalytic properties of the TiO_2 forming free radicals, e.g., $OH^{\bullet}$ and $HO_2^{\bullet}$. These free radicals can cause mechanical failure of the binder, giving rise to a phenomenon known as 'chalking'.[28,59-60] This is caused by pigment particles at the surface of the paint slowly eroding the binder. Abrasive contact with the surface of the paint then causes a loose 'chalky' deposit to become detached. In this way, the paint layer slowly crumbles and becomes thinner, leading to an eventual loss of opacity.

Mechanisms of film degradation have been illustrated in figure 1.6 and interpreted by Käempf *et al.*[61] They described the characteristics of weathered paint films in terms of binder/pigment combinations.

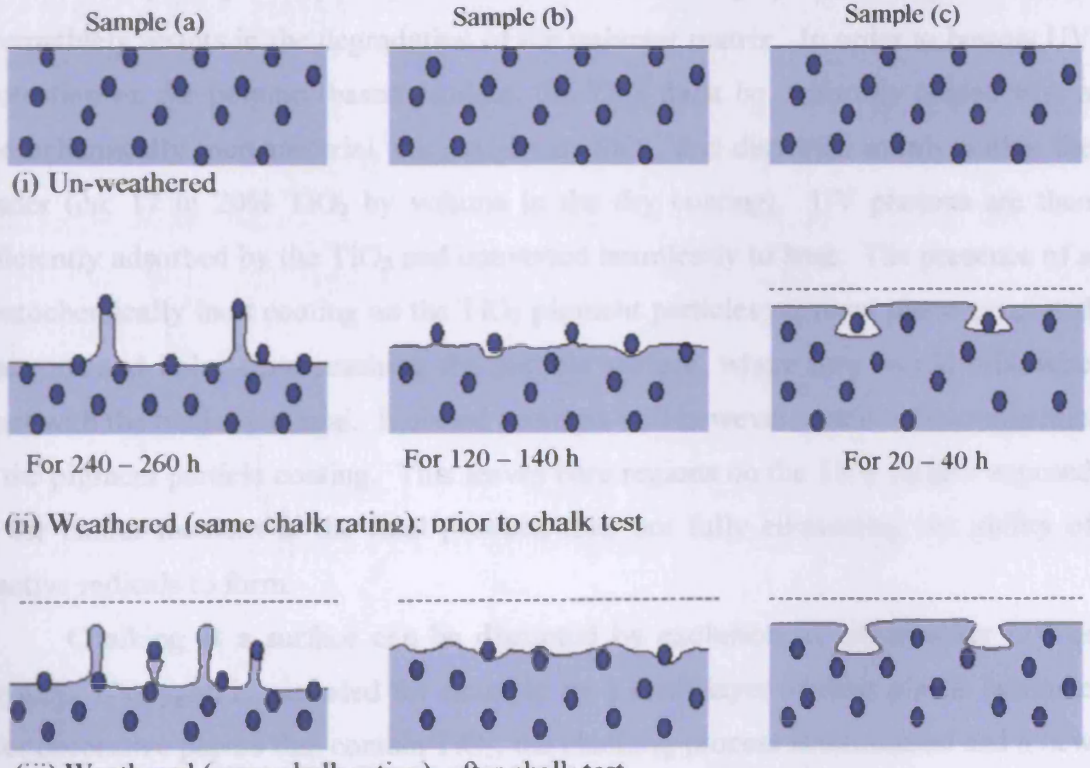

Figure 1.6. Schematic representation of the degradation of a binder pigmented with TiO_2 pigments of different photoactivity.

- Sample (a), the paint film pigmented with treated ZnO stabilised Rutile shows the typical phenomenon of dominating UV degradation, the pigment particles rest on pedestals.
- Sample (b), pigmented with untreated Rutile the degradation of the binder is apparently due not only to UV degradation but also to chalking.
- Sample (c), pigments with untreated Anatase shows characteristics of predominant degradation of the binder at the pigment/binder interface as caused by the chalking process, the pigment particles rest in deep holes in the paint film surface only moderately ablated.

Völz *et al.*,[62] outlined the chemistry of chalking, where UV, water, TiO_2 and oxygen are essential for the TiO_2-catalysed degradation of the organic binder. The overall reaction mechanism is shown in equation 1.19.

$$H_2O + O_2 \xrightarrow[h\nu]{TiO_2} HO^{\bullet} + HO_2^{\bullet} \qquad (1.19)$$

The hydroxyl and peroxyl radicals formed are highly reactive agents, which alternatively results in the degradation of the polymer matrix. In order to bestow UV protection on the polymer-based product, the TiO_2 must be uniformly coated with a photochemically inert material, e.g., Al_2O_3 or SiO_2, and dispersed evenly within the binder (*ca.* 17 to 20% TiO_2 by volume in the dry coating). UV photons are then efficiently adsorbed by the TiO_2 and converted harmlessly to heat. The presence of a photochemically inert coating on the TiO_2 pigment particles prevents photo-generated electrons and holes from reaching the particle surface, where they would otherwise react with the binder material. Finished powders will however, contain discontinuities in the pigment particle coating. This leaves bare regions on the TiO_2 surface exposed to the binder medium in the final product, thus not fully eliminating the ability of reactive radicals to form.

Chalking at a surface can be disrupted by exclusion of either water UV or oxygen. If oxygen is excluded for example by a thick layer of clear plastic laminate over decorative papers that contain TiO_2, the chalking process is terminated and a new phenomenon known as photogreying occurs. This is a result of the direct reduction of the TiO_2 to Ti^{3+} when no oxygen is present in the chalking cycle.

Another form of the photogreying process was once common in older manufactured paint, which used to contain white lead. Chemical interactions used to occur between TiO_2 and white lead. A thunderstorm could cause exteriors painted with mixtures of TiO_2 and white lead to discolour, often quite severely. Eventually, the discolouration would fade. The UV photon of the lightening flash caused the Ti^{4+} to reduce to Ti^{3+}. The Ti^{3+} then reduced Pb^{2+} to metallic lead (Pb^0), which discoloured the paint film. Eventually, the atmospheric oxygen re-oxidized the Pb^0 to Pb^{2+}, bleaching the paint film back to its original colour. The removal of white lead eliminated this problem.[56]

1.3.3 Solar Energy Conversion

Great Britain's total annual electricity consumption is approximately 2.8×10^7 kW.[63] On a clear sunny day in Great Britain the total incident solar energy is approximately 2.4×10^{11} kW. Therefore, if only a minute fraction of incident solar energy could be captured and converted into a usable form, then this would considerably reduce the need to produce energy from other non-renewable sources. A development of new, clean and efficient energy technologies to compensate for future shortages in fossil fuels is necessary. The potential for solar energy utilization is illustrated in photosynthesis, which converts approximately 3% of the total solar energy incident upon the earth; with an efficiency of 25 to 30% of light adsorbed. Amazingly, photosynthetic organisms fix around 1.5×10^{11} tonnes of carbon annually, an amount that is approximately ten times the world's current total annual energy requirements.

Unfortunately TiO_2 systems are not particularly good at converting light into electricity, but are well suited in heterogeneous photocatalysis as demonstrated in section 1.2.6. In many countries, which receive adequate sunlight, titanium dioxide based effluent remediation may be used to significantly lower the costs associated with water treatment.

1.3.4 Photoelectrochemistry

In an *n*-type semiconductor immersed in solution, an electric field forms spontaneously at the semiconductor – electrolyte interface; electron - hole pairs generated in the region of the electric field i.e., the space charge region, are separated

efficiently rather than undergoing recombination. In the *n*-type semiconductor, the photo-generated electron moves into the bulk where it can be transferred through either a wire to a second non-photoactive electrode (Pt) or to a point where an electron acceptor maybe reduced (Figure 1.7).

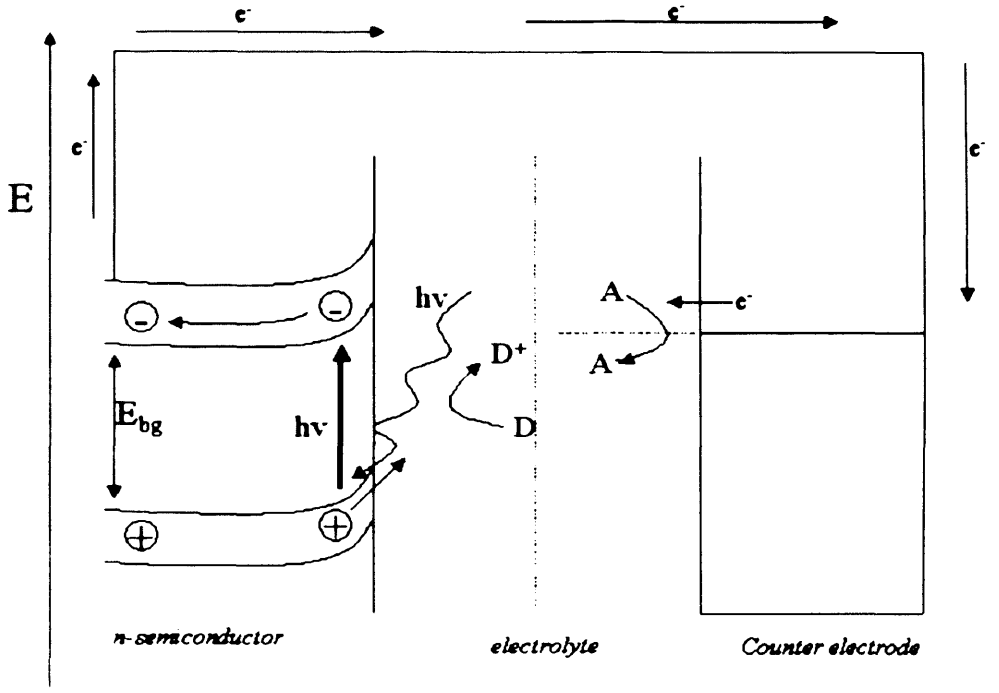

Figure 1.7. Schematic representation of the Photoelectrochemical cell.[64]

The photgenerated hole migrates towards the surface where it can oxidize a suitable electron donor. Thus, sunlight is converted directly into an electrical current, which may be used to drive low power devices, or stored as chemical energy, e.g., *via* the photolysis of water equation 2.20.

$$2H_2O_{(l)} \xrightarrow{\text{PEC Cell}} 2H_{2(g)} + O_{2(g)} \qquad (2.20)$$

The design of the PEC is dictated by whether the light is to be stored as chemical energy or converted directly to electrical energy. Photocatalytic reactors used for decontamination purposes are simply PEC cells modified for the direct conversion of UV to chemical energy. The finely divided semiconductor may be present as a stationary phase over which the reactants flow, or simply held in colloidal suspension.

1.4 Summary

In the opening chapter of this thesis, the general properties and expanding uses of TiO_2 have been discussed. The photoactivity of TiO_2 is one of its technologically most attractive properties. The creation of electron-hole pairs through the irradiation of light, either in TiO_2 itself, or in adsorbed molecules, and the following chemical or electron transfer reactions are at the heart of TiO_2-based photo devices applied in a range of areas. Intense research was initiated by Fujishima and Honda's[27] discovery that water can be photocatalyically split into hydrogen and oxygen.

The development of heterogeneous photocatalysis involving electron-hole pair initiated by band gap excitation of a semiconductor particle has the potential to replace many existing pollutant remediation methods. Photocatalysis, is a widely applicable method for activating adsorbed organic molecules and a promising route to selective synthetic transformations, and as an advanced oxidation process for environmental 'cleanup' an advanced oxidation process has the potential to replace many existing pollutant remediation methods.

Electronic modification of the TiO_2 catalyst by deposition of transition metal particles has a strong effect on the efficiency of electron-hole separation, and the dynamics of interfacial electron transfer can be dramatically influenced. Application of these fundamental principles for the designing photochemical transformation methods is a rich area for technological development.

An understanding of the interfacial photochemistry at the molecular level, particularly the fundamental chemistry of electron and hole transfer to the adsorbed substrate is therefore considered essential to the design of more improved photocatalysts with high quantum yields. Upon band gap irradiation of TiO_2 the photo-generated electrons and holes are ultimately responsible for the photocatalytic redox reactions. While the mechanistic details remain uncertain it is clear that the presence of oxygen and water is crucial in controlling the reaction pathways often *via* the intermediacy of active oxygen species. The aim of this study is to demonstrate that the nature of the paramagnetic oxygen species can change depending on the pre-treatment conditions and nature of the surface, and thereby illustrate the importance of studying these surface radicals under various conditions to fully understand the initial electron-transfer reaction process.

To explore the reaction mechanism of VOC decomposition in heterogeneous photocatalysis, identification of the reaction intermediates by spectroscopic methods

is required under reaction conditions. Considering the role of surface orientation in the photochemical reactivity of TiO_2, it is also necessary to characterize these intermediates directly at the surface, before desorption and subsequent reactivity in the gas phase.

The investigation of these systems will be carried out using Electron Paramagnetic Resonance (EPR). A powerful technique for the characterisation of paramagnetic oxygen species and reaction intermediates stabilised on the TiO_2 surface. One of the advantages of using the EPR technique is to allow the study of low temperature UV stimulated charge transfers. It is possible to measure changes in the concentrations of the paramagnetic defects involved both during and after irradiation by repeatedly sweeping through the resonance lines at regular intervals. This can then lead to a determination of relative rates and their variations with temperature. This technique has been adopted to study the effect of illumination on TiO_2 at various temperatures.

Chapter 2

The Role of EPR in the Characterisation of Oxygen Centred Radicals in Photocatalysis

2.1 Introduction

Oxides have been important catalysts for many years, but it is only recently that attention has been directed towards the various forms of oxygen that may exist on the surface. Early solid-state studies of irradiated salts led to the discovery that paramagnetic oxygen species could be trapped in the salt matrix, and these species were identified and characterised.[1] Later in the field of surface chemistry, kinetic studies on the conductivity of semiconductors during oxygen adsorption indicated that charged oxygen species were formed on the surface.

Reactive oxygen species adsorbed at surfaces are important intermediates in both total and selective catalytic oxidation[1] as well as in various phenomena taking place at the gas-solid and liquid-solid interface. Several kinds of charged dioxygen radicals have been identified on a number of different surfaces by different techniques, including O_2^+, O_2^-, O_2^{2-} and O_2^{3-}.[2] Many of these species can be and have been characterised by EPR spectroscopy (with the exception of O_2^{2-}).

In the particular case of radical intermediates, the EPR technique has provided extensive data on the nature of the surface stabilised oxygen centred radicals. Che and Tench published a thorough review just over 20 years ago, on the characterisation and reactivity of mononuclear[1] and molecular[2] oxygen species on oxide surfaces. They summarised the principle methods of activating oxygen on metal oxides into three main areas;

- Adsorption of gaseous oxygen onto a reduced or slightly reduced oxide surface, such as TiO_2, which is generally reduced by mild thermovacuum conditions,
- Adsorption of gaseous oxygen on UV or γ irradiated stoichiometric oxides such as MgO, containing surface trapped electrons,
- Adsorption of gaseous oxygen onto oxides containing pre-adsorbed reactive molecules (such as H_2, CO, organics, etc). In this case the oxygen radicals are produced as secondary reactions.

In summary, the oxygen radicals produced in these ways, e.g. O^-, O_2^-, O_3^-, have been studied in vast detail and can be regarded as very well characterised.

Electron paramagnetic resonance spectroscopy has been applied to the study of surface chemistry and catalysis since the mid-1960's, in particular the study of paramagnetic species associated with the surface. EPR detects unpaired electron spins; commercial spectrometers are capable of detection levels of at least $10^{-6} - 10^{-9}$ moles of spins. The high sensitivity of the technique allows surface chemists to study low concentrations of active sites or paramagnetic radials successfully. Diamagnetic species are not observed; this can prove to be both a disadvantage and advantage. Although the EPR technique is employed to investigate various aspects of surface chemistry, the technique also combines the use of probe molecules enhancing the informative capability of the technique. The probe molecules are not necessarily paramagnetic; the only requirement is that the species resulting from the interaction of the surface with the probe molecule is paramagnetic.[3a]

The main experimental parameters obtained from EPR measurements are the g tensor of the paramagnetic species and the hyperfine splitting arising from interactions with non-zero spin nuclei or asymmetric crystal fields (giving rise to multiple line spectra). The *g* tensor is a proportionality constant associated with an electron in a given environment and is analogous with the chemical shift (δ) in NMR. Hyperfine couplings provide data relating to the structure of the radical or paramagnetic centre, e.g. the number and type of interacting nuclei, or the vicinal lattice ion distribution. A more detailed account of the EPR technique is presented in chapter 4.

2.1.1 Identification of Oxygen radicals

The O_2^- Ion

The superoxide ion has been widely investigated using EPR, this is because, being paramagnetic, the EPR technique provides a great deal of information on its structure, location, stability, surface mobility and on-side dynamics.[3b] The usual approach is to adopt an ionic model for the superoxide ion at the surface. In this model, an electron is transferred from the surface to the oxygen and an electrostatic interaction between the cation site and the superoxide stabilises the radical. The superoxide radical is characterised by the presence of three electrons in the two $2\pi^*$ antibondinding orbitals as shown in figure 2.1, thus rendering it a paramagnetic species. However, an EPR spectrum is only observed when the degeneration of the

two orbitals is removed by an external perturbation such as an electric field created by the surrounding ions.

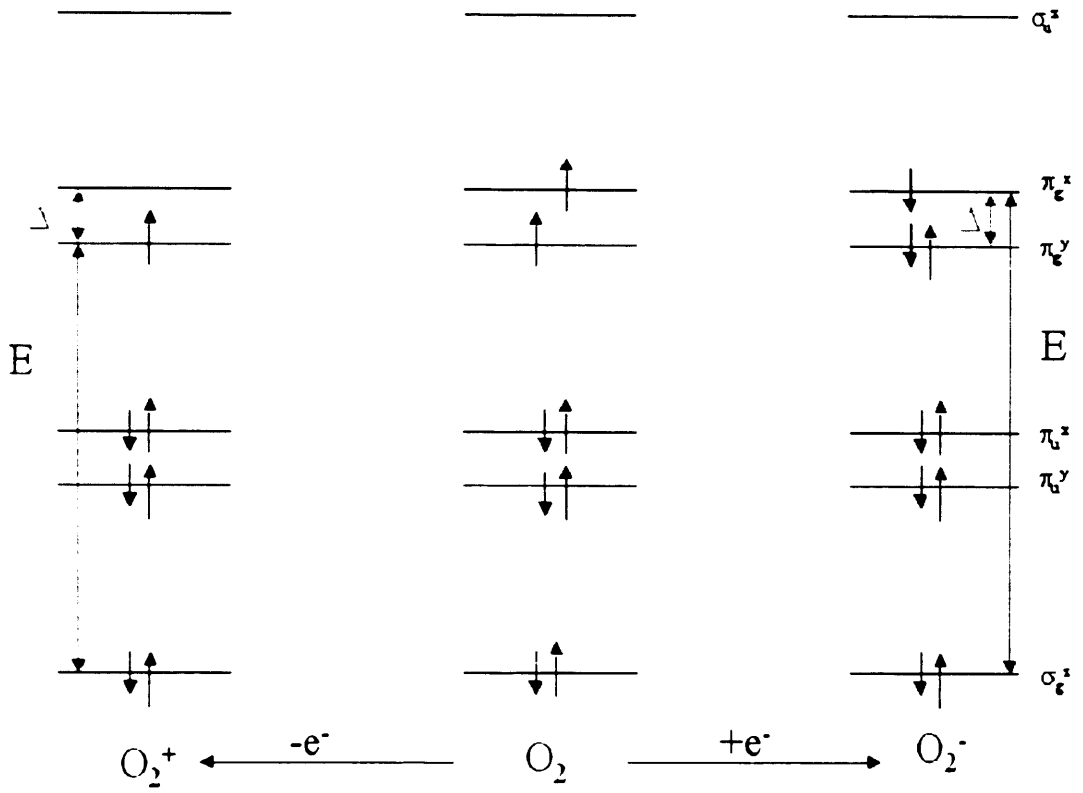

Figure 2.1. The simplified energy level diagram for O_2^+, O_2 and O_2^- in their ground state. When a crystal field is present, the π_g and π_u levels are not degenerate.

The O_2^- Ion

The O_2^- ion has only a single electron in the π_g orbitals, as shown in figure 2.1 above, and is isoelectronic with NO. The presence of the surface will break the degeneracy of the π_g orbitals in the same way as for O_2^-. In this case however, an unoccupied molecular orbital is formed which is slightly higher in energy than the π_g orbital since this must now contain the unpaired electron and the EPR spectrum is observed to have a negative g shift.

The O_2^{2-} Ion

The O_2^{2-} ion is usually referred to as the peroxide ion, which should be distinguished from the covalent peroxy radical ($ROO^\bullet$). It has been previously treated as a dimer O^- species by other authors.[1] This ion is difficult to characterize on the surface, as it is diamagnetic. Studies of metal-dioxygen complexes show that the

peroxide-like complexes have an infrared band ν_{oo} in the range 800-932cm^{-1}.[4] Conductivity and chemical methods of measuring the charge on the oxygen do not distinguish between $2O^-$ and O_2^{2-}. It is therefore not possible to obtain direct evidence on the nature of the oxygen species.

The O_2^{3-} Ion

The O_2^{3-} ion is very short lived, making direct evidence for its existence very difficult. Symons[5] suggested that the O^- species on the surface would be better described as the species O_2^{3-}. However, an experiment[6] with MgO enriched in ^{17}O showed that the interaction of O^- with $^{17}O^{2-}$ ions was not measurable. Taarit *et al.*, [7] reported the species existed on a Pd(I) zeolite with g values of $g_\perp$=2.050 and $g_{||}$=1.99. The g values are inverted from those expected for superoxide (i.e., $g_\perp < g_{||}$), this could be accounted for by rotational averaging. Other authors[8] have suggested that the signal may be due to O_2^{3-} ions with the unpaired electron in a σ^* orbital. This is supported by the suggestion that three Pd(I) ions are lost to form one oxygen species, as expected for O_2^{3-}. At present the argument is open and more evidence is needed to support the existence of O_2^{3-} on surfaces.

The O_3^- Ion

The ozonide ion O_3^- is a 19 electron radical and the only well-established species that contains more than two oxygen nuclei. It is readily formed by the interaction of molecular oxygen with surface O^- radicals. A detailed analysis of this species will be presented in chapter 6.

Mono Oxygen Species (O^- and O^{2-})

Mono-oxygen species on the surface fall into two main types, firstly the O^- ion which is formed either by adsorption or from surface oxide ions of the lattice that have a trapped hole; and secondly the O^{2-} ion of the lattice in low coordination and/or bonded to transition metal ions. O^- ions are not very stable, but have been identified by EPR studies. O^{2-} exists as a bulk lattice species where they are stabilised by Madelung energy. The most commonly used oxidizing agent is gaseous O_2, but it is generally thought that this oxygen must be converted to either O^- or O^{2-} on the surface

and even possibly incorporated into the lattice before it appears in the oxidation products and so follows the general scheme 1.

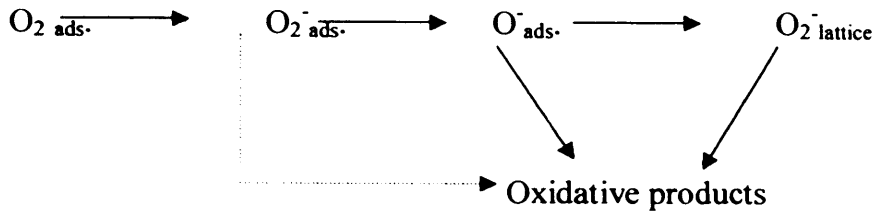

Scheme 1.[1]

Triplet Oxygen

Triplet oxygen is generally accepted as the form in which gaseous oxygen is physisorbed. The formation of singlet oxygen has been suggested on some oxide surfaces. The catalytic ability of the singlet state oxygen is greater than that of the triplet oxygen, as it is electronically excited and therefore more reactive. This leads to different stereochemistry because its two outermost electrons are in the same orbital.

The following sections are designed to bring together the latest research that has been carried out on active oxygen species on the TiO_2 surface, and to attempt to rationalise and identify the most important radical pathways that occur. Furthermore, the role of singlet oxygen, if any, in the photocatalytic activity of titania will be explored.

2.2 Characterisation of Reactive Oxygen Species

Maira *et al.*,[9] used EPR spectroscopy to monitor and characterize changes in the radicals formed by the UV irradiation of oxygen adsorbed on TiO_2 particles of different sizes (from 6nm, 11nm, 16nm). Under irradiation TiO_2 generates holes and electrons. These recombine and dissipate the photon energy as heat, get trapped in metastable surface states or react with electron donors and electron acceptors adsorbed on the semiconductor surface.[10] The radicals formed as a function of particle size are displayed in table 2.1.

The EPR spectra for the P6, P11 and P16 TiO_2 particles showed a progressive weakening of signal A, Ti^{4+}-O^--Ti^{4+}-OH^-, with an increase in signal D, Ti^{4+}-O^{2-}-Ti^{4+}-O^- as particle size increases. This indicated that in the smaller 6nm TiO_2, the holes are trapped by subsurface lattice oxygen forming Ti^{4+}-$[O^-]_{lattice}$-Ti^{4+}-OH^- species. For

TiO_2 particles with a crystal size larger than 10nm, the holes are stabilized on the surface to form Ti^{4+}-$[O^{2-}]_{lattice}$-Ti^{4+}-O^-.

Table 2.1. Identification of radicals formed on various TiO_2 samples after the UV irradiation of oxygen.

Sample	Species	g_1	g_2	g_3	Radical
	A	2.003	2.014	2.022	Ti^{4+}-$[O^-]_{lattice}$-Ti^{4+}-OH^-
P6	B	2.003	2.008	2.034	$O_2H^\bullet$
	C	2.002	2.009	2.026	O_2^-
P11	D	2.003	2.016	2.029	Ti^{4+}-$[O^{2-}]_{lattice}$-Ti^{4+}-O^-
	E	2.002	2.008	2.011	O_3^- (O_2-O^-)

Nakoaka and Nosaka[11] have made similar observations in their study, where they have reported that the location of $[O^-]_{lattice}$ depends on the annealing temperature of the Anatase TiO_2 powder. Their results show that photo-generated holes (h^+) are stabilised at subsurface locations for TiO_2 powders treated at low temperature. High temperature treatment resulted in holes trapped at the surface. These results showed that the EPR technique could be used to understand the performance of photocatalysts.

In order to detect the photocatalytic production of O_2^- and H_2O_2 the luminol chemiluminecense probe (CL) was adopted by Hirakawa *et al.*[12] The basic reaction of luminol chemiluminescence is represented in equations 2.1 and 2.2.

$$O_2^- + L^- + H^+ \rightarrow LO_2H^- \rightarrow AP^* \qquad (2.1)$$

$$HO_2^- + L \rightarrow LO_2H^- \rightarrow AP^* \qquad (2.2)$$

Where L and L^- are luminal radical and two-electron-oxidized luminol, respectively.

The reaction product, LO_2H^-, rapidly decomposes into the excited state of 2-amino phthalate (AP*) causing the emission of light at 425nm. The CL intensity is proportional to the formation of LO_2H^-, so therefore is proportional to the concentration products $[O_2^-][L^-]$ and $[HO_2^-][L]$ (Eqs. 2.1 & 2.2). The following rate equation 2.3 can be derived,

$$d[AP^*]/dt = k_7[O_2^-][L^-] + \phi k_s[HO_2^-][L] \qquad (2.3)$$

where, ϕ is the quantum yield. The fast-decay component ($k_7[O_2^-][L^-]$) intensity decays exponentially at about $1s^{-1}$, which is proportional to the amount of O_2^-, due to the amount of L^- being higher than that of O_2^-. So from this fast decay component the authors could form an estimate of the amount of O_2^- produced.

A pulse radiolysis technique was adopted by Lawless *et al.*,[13] to study the reaction of $^{\bullet}OH$ radicals with small TiO_2 (~13mm) particles in aqueous solutions, in order to prove that the species produced by the reaction of $^{\bullet}OH$ radicals with TiO_2 particles are essentially identical with a trapped hole at the surface. The ability to explore the chemical and physical properties of a charge carrier (in this case a hole), without the fast recombination of charge carriers and without interference from the absorption by the other carrier, is the advantage of this technique over flash photolysis. Oxidation of small TiO_2 particles by pulse radiolysis was found to generate $^{\bullet}OH$ radicals yielding trapped holes on the particle surface, it is these trapped holes that are proposed to undergo photooxidation reactions.

In the study by Park *et al.*, [14] IR spectroscopy in the study of the photo-oxidation of C_2H_2 was used. This was done in order to confirm whether the OH species, as precursors of OH radicals, are produced when water is introduced onto the photocatalyst. The IR spectroscopy results suggested that absorbing water on the surface of TiO_2 does produce OH species as well as OH radicals *via* the OH species under UV irradiation.

Lui *et al.*,[15] used the spin trapping technique to detect radical intermediates in the photooxidation of sulforhodamine B under visible irradiation. The spin-trapping technique can be used to directly observe active radical intermediates. Studies by Noda *et al.*,[16,17] have also used the EPR spin trapping technique to detect active oxygen species in the UV photoexcited TiO_2 aqueous dispersions, in aqueous H_2O_2 solutions and in non-aqueous solvents. Perissinotti *et al.*,[18] used a spin trapping method to detect carbonyl anion radicals formed in the decomposition of formate.

2.3 Heterogeneous catalysis at the liquid-solid interface

The liquid-solid interface is complex as it contains a wide range of variables to be considered. Some of which include; surface composition, surface area,

concentration of photocatalysis, pH of solution, solvent environment, diffusion rates etc. Over the last several years, numerous studies have demonstrated the efficiency of photocatalytic oxidation of organic compounds in aqueous TiO_2 suspensions. As the process yields rapid, non-selective oxidation of a broad range of organic compounds to CO_2 and H_2O its application in the removal of organic contaminants from wastewaters and drinking water has escalated.

The most important reaction in photocatalysis is the oxidation of adsorbed water or hydroxide ions by holes to produce hydroxyl radicals,[19] widely believed to be the most important oxidizing species in TiO_2 photocatalytic systems, (Eqs. 2.5 & 2.6),

$$h^+ + H_2O_{(ads)} \longrightarrow {}^\bullet OH + H^+ \qquad (2.5)$$

$$h^+ + 2OH^-_{(ads)} \longrightarrow {}^\bullet OH + OH^- \qquad (2.6)$$

The detection of the hydroxylation products[20,21] provides supporting evidence of $^\bullet OH$ as an active species, along with the electron paramagnetic resonance EPR detection of $^\bullet OH$ using spin traps to scavenge the $^\bullet OH$, as previously discussed in section 2.2.

When TiO_2 is irradiated, holes in the bulk are formed upon photon adsorption. These holes then migrate to the surface where they can interact with surface water or hydroxyl groups (≡ TiOH) to form $^\bullet OH$ or $\equiv TiO^\bullet$ respectively, or trapped as subsurface holes. The trapped hole may interact with organic molecules through direct electron transfer both through the surfacial –O- or –Ti- species. Through $^\bullet OH$ or $TiO^\bullet$ it reacts *via* a mediated pathway. This distinction is important, as the intermediates formed in the paths may be different. Hence to investigate which pathway is facilitated in the initial process of the photocatalytic reactions, it is necessary to monitor the intermediate radicals formed during the reaction.

Jaeger and Bard[22] authored one of the first reports on the production of $^\bullet OH$ radicals, in the photo-assisted decomposition of water in a TiO_2/Pt photo-electrochemical cell. Using spin traps they reported free radical intermediates during the *in-situ* radiation of TiO_2 and Pt/TiO_2 powders in aqueous solutions. Evidence was provided with the use of spin traps for the formation of hydroxyl ($^\bullet OH$) and hydroperoxy ($^\bullet O_2H$). However, some uncertainty about the results remained due to its indirect method.[23]

Trapped holes have been proposed to directly oxidize adsorbate molecules[24] or react with surface hydroxyl groups or water to produce hydroxyl radicals, which are strong oxidising agents.[25] The trapped hole is usually described as an adsorbed hydroxyl radical whose nature is probably represented by the spin resonance between hydroxyl and lattice oxygen, –O–. However, most evidence favours the $^{\bullet}OH$ radical mechanism of oxidation of organic products. Hole oxidation has been suggested for compounds lacking abstractable hydrogen and for some aromatic compounds as evidenced by reflectance flash photolysis.[26]

Minero *et al.*, [27] were concerned with covering the TiO_2 surface with fluoride ions replacing the hydroxyl groups. The redox process of phenol degradation, would follow direct routes from those in the presence of ≡Ti-OH species; with the reaction proceeding with surface-trapped holes and direct electron transfer. It was concluded that the kinetic pathways for the reaction with subsurface holes and with free $^{\bullet}OH$ in solution predominated. Further, it was shown that the direct electron transfer is at a maximum 10% of the overall reaction rate on fluorinated titania through the free $^{\bullet}OH$ radical pathway. At the end of the study it was found, by kinetic analysis, that three oxidant species are suspected to be present in the photocatalytic system (TiO_2/F), the hole, the surface-trapped hole (≡$TiO^{\bullet}$), and the free $^{\bullet}OH$ radical. It was stated that the photodegradation of phenol proceeds almost entirely through a homogeneous $^{\bullet}OH$ radical reaction. On bare TiO_2, mechanisms involving direct electron transfer and interaction of organics with the bound surfacial hydroxyl radical are responsible for the reaction pathway.

Photogenerated electrons may also play a role in the photocatalytic degradation of chlorinated phenols. Trapped electrons reduce pre-adsorbed acceptors, with subsequent secondary steps. Acceptors need to be preadsorbed at the photocatalyst particle surface to allow the slower chemistry to effectively compete with ultra fast electron/hole recombination at the surface.[28] In a TiO_2 dispersion, the acceptor is the O_2 molecule, producing $^{\bullet}OH_{(ads)}$ radicals, and the superoxide radical anion;

$$\{Ti^{4+}\text{-}O^{\bullet-}\text{-}Ti^{4+}\}\text{-}OH^{-} \longleftrightarrow \{Ti^{4+}\text{-}O^{2-}\text{-}Ti^{4+}\}\text{-}^{\bullet}OH \qquad (2.4)$$

$$O_{2(ads)} + e^{-} \longrightarrow O_2^{\bullet-} \qquad (2.5)$$

On protonation, $O_2^{\bullet-}{}_{(ads)}$ yields the hydroperoxy radical $HO_2^{\bullet}{}_{(ads)}$.

$$O_2^{\bullet-}{}_{(ads)} + H^+ \longrightarrow HO_2^{\bullet}{}_{(ads)} \qquad (2.6)$$

The electron can also be trapped at Ti^{4+} sites to produce surface Ti^{3+},

$$\{Ti^{4+}\text{-}\}_{surface} + e^- \longrightarrow \{Ti^{3+}\text{-}\}_{surface} \qquad (2.7)$$

to impart a blue-violet colouration to the TiO_2 particles in the presence of hole-scavengers.

The major route of mineralization of organic substrates is by hydroxylation. Such products could, in principle, be formed either by homolytic attack by a hydroxyl radical on a π system or by hydration of a singly oxidized intermediate. The competing roles for the photogenerated $^{\bullet}OH$ radicals and for the trapped holes in photocatalysis have been researched in depth.

Lawless *et al.*,[29] used the pulse radiolysis technique in order to study the reaction of $^{\bullet}OH$ radicals with small TiO_2 particles in aqueous solution. They argued that the species produced by the reaction of $^{\bullet}OH$ radicals with TiO_2 particles is essentially identical with a trapped hole at the particle surface. Confirmation of the oxidative abilities of the product was confirmed by the oxidation of SCN^- to give the anion radical $(SCN)_2^{\bullet-}$. A trapped hole was identified at the particle surface as the product of the $^{\bullet}OH$ reaction and the particle surface.

A study of a TiO_2 film irradiated in terephthalic acid solution with UV light[23] tries to determine which of the processes, photogenerated $^{\bullet}OH$ radicals and trapped holes, are in dominance. Over time the fluorescence intensity increased at *ca.* 425nm with increasing illumination time, the spectrum had the identical shape and maximum wavelength of 2-hydroxyterephthalic acid. This implyed that fluorescent products were due to the reaction between $^{\bullet}OH$ and terephthalic acid. In the same study, the role of positive hole oxidation and its importance was also studied. Using the EPR technique and laser flash photolysis it was found that a paramagnetic species is formed after illumination of TiO_2 this could be assigned to surface holes. The identity of the trapped hole is an oxygen anion radical ($O^{\bullet-}$) covalently bound to titanium atoms above or below the surface. Confirmation of this study was provided by other authors Howe and Grätzel[30] and Mićić *et al.*[31]

Howe and Grätzel[30] studied the UV irradiation of hydrated anatase and observed a paramagnetic species. Irradiation at 4.2 K *in-vacuo* produced electrons

trapped in the bulk at Ti^{4+} sites within the bulk and holes trapped at lattice oxide ions immediately below the surface. These species were capable of decaying rapidly in the dark and warming to room temperature. In the presence of O_2 the trapped electrons are removed and the trapped holes are stable to 77 K. Analysis showed that $O^{\bullet-}$ is covalently bound to Ti atoms with non-equivalent crystal field splitting from adjacent atoms.

In the study by Mićić *et al.*,[31] it was also stated that the hole adduct is a subsurface oxygen radical. In aqueous solutions of TiO_2 colloids covered with OH groups, the presence of methanol initiates efficient hole transfer from the oxygen within the lattice to the methanol. In irradiated aqueous solutions of methanol at 1.9K, EPR signals centred around g = 2 and have a line shape characteristic of the $CH_2O(H)$ radical. This observed radical was reported to indicate that transfer of a hole from the oxygen lattice to the methanol molecule occurs. At 1.9 K, only the OH group could be seen and the location of the hole on the OH group could not be seen. In the same solution without methanol, the surface OH groups trap holes as the oxygen anion radical thus, Ti^{4+}-O-Ti^{4+}-$O^{\bullet}$. In the aqueous solution, methanol is directly photo-oxidized by the hole, and products of this reaction (CH_2OH and Ti^{3+}) are different from those in which CH_3OH is chemisorbed on the TiO_2 surface ($^{\bullet}CH_3$, $^{\bullet}CH_2OH$,$^{\bullet}CHO$ and Ti^{3+}).

Further evidence was provided again by Mićić *et al.*,[32] on the paramagnetic species formed on irradiation of aqueous TiO_2 colloids in the presence of methanol. At 1.9K laser irradiation of an aqueous solution of methanol produced an EPR signal characteristic in shape to the $CH_2OH^{\bullet}$ radical. Different radicals are formed when CH_3OH is chemisorbed on TiO_2. The EPR signals show also the formation of the $CH_2OH^{\bullet}$ radical due to the oxidation of chemisorbed methanol on TiO_2, which oxidize further to $CHO^{\bullet}$. In the absence of methanol, holes are trapped by surface hydroxide groups forming Ti^{4+}-O-Ti^{4+}-$O^{\bullet}$.

El-Morsi *et al.*,[33] observed that 1,10-dichlorodecane was shown to be effectively photodegraded in aqueous suspensions of TiO_2. The kinetics of photodegradation followed a Langmuir-Hinshelwood model suggesting that the reaction occurs on the surface of the photocatalyst. The presence of h^{+}_{vb} and $^{\bullet}OH$ radical scavengers including methanol and iodide inhibited the degradation supporting a photooxidation reaction. The lack of transformation of D_2C_{10}, in acetonitrile as

solvent, indicated that the major oxidants were $^{\bullet}OH$ radicals. The presence of tetronitromethane, eliminating the formation of free $^{\bullet}OH$ radicals, was shown to affect the degradation rates significantly. This result, combined with the observed increase in photocatalysis rates, confirmed that the reaction involved adsorbed 1,10-dichlorodecane and surface bound $^{\bullet}OH$ radicals.

Nosaka *et al.*,[34] measured the ratio of carboxymethyl radicals to methyl radicals *in-situ* for the photocatalytic decomposition of acetic acid over platinized TiO_2 powder in deoxygenated aqueous solution at room temperature. The contribution of $^{\bullet}O$ radicals in the oxidation process was discussed. Since carboxymethyl radicals are formed only by indirect oxidation, the radical ratio was used to measure the indirect oxidation *via* $^{\bullet}OH$ radicals. Thus, ratios of the indirect oxidation were estimated for 5 commercial TiO_2 photocatalysts. The ratios were found to be sensitive to the characteristics of the TiO_2 catalysts, the larger the amount of surface OH group, the more likely indirect oxidation *via* $^{\bullet}OH$ radicals occurs. This could be attributed to the difference in the structures of the surface trapped holes elucidated by the EPR measurements of the corresponding TiO_2 powder at 77 K.

In a previous report[35] *in-situ* EPR observation of the photocatalytic oxidation of acetic acid provides information on the ratio of the two pathways. In this reaction system both the methyl ($^{\bullet}CH_3$) and carboxymethyl ($^{\bullet}CH_2COOH$) radicals can be detected. The methyl radicals are formed both from the direct hole oxidation and the indirect oxidation *via* $^{\bullet}OH$ radicals, while the carboxymethyl radicals could be formed only by the indirect oxidation. In the proposed reaction scheme $^{\bullet}CH_3$ radicals are formed *via* two reaction pathways. Firstly, the direct hole oxidation of the adsorbed molecules with the photoinduced holes (h^+) at the valence band, and secondly the indirect oxidation *via* $^{\bullet}OH$ radicals which are formed by the oxidation of water. On the other hand $^{\bullet}CH_2COOH$ radicals are formed only *via* $^{\bullet}OH$ radicals (Eqs. 2.8-2.11),

$$CH_3COOH + h^+ \longrightarrow {}^{\bullet}CH_3 + CO_2 + H^+ \qquad (2.8)$$

$$CH_3COOH + {}^{\bullet}OH \longrightarrow {}^{\bullet}CH_3 + CO_2 + H_2O \qquad (2.9)$$

$$H_2O + h^+ \longrightarrow {}^{\bullet}OH + H^+ \qquad (2.10)$$

$$CH_3COOH + {}^{\bullet}OH \longrightarrow {}^{\bullet}CH_2COOH + H_2O \qquad (2.11)$$

Lui *et al.*,[15] discussed the visible light-induced photocatalytic oxidation of the dye alizarin red (AR) in TiO_2 aqueous dispersions. The active oxygen radicals ($O^{\bullet-}$ or

HOO$^{\bullet}$) and hydroxyl radicals ($^{\bullet}$OH) are generated during visible irradiation of AR/TiO_2 dispersions in the initial photooxidation stage. Adsorption of AR onto TiO_2 is shown through the sulphonate functional group. The main point of attack by the active oxygen radical was the part of the molecule with the largest frontier electron density. This was consistent with the experimental results that phthalic acid was formed as the main photooxidation product.

Investigations[18] have shown that rates of photocatalytic reduction of carbon tetrachloride and trinitritolulene are enhanced when methanol is added as a sacrificial electron donor. The OH and /or hole scavenging by the alcohol not only decreases electron-hole recombination but also generate α-hydroxymethyl radicals, which in conjunction with conduction band electrons reduce CCl_4 and trinitrotoluene directly.

Lui *et al.*,[36] studied the *in-situ* irradiation of aqueous sulforhodamine B (SRB)-TiO_2 air saturated dispersions using the EPR spin traps DMPO and PBN. Hydroxyl radical ($^{\bullet}$OH), hydroperoxyl radical ($HO_2^{\bullet}$) and hydrated electrons (e^-_{aq}) were detected. It has been suggested that oxygen molecules rather than active oxygen radicals are the main oxidizing agent.

$$O_2 + e^-_{aq}\ (\text{or } e^-_{cv}) \longrightarrow O_2^- \qquad (2.12)$$

$$H^+ + O_2^- \longleftrightarrow HO_2^{\bullet} \qquad (2.13)$$

$$HO_2^{\bullet} + HO_2^{\bullet} \longrightarrow O_2 + H_2O_2 \qquad (2.14)$$

$$O_2^- + e^- + 2H^+ \longrightarrow H_2O_2 \qquad (2.15)$$

$$H_2O_2 + e \longrightarrow {}^{\bullet}OH + OH^- \qquad (2.16)$$

The affect of transition metals on the rate of photocatalytic oxidation has been studied by Butler *et al.*[19] Experimental results indicated that Cu(II) , Fe(II) and Mn(II) had a twofold increase in the initial reaction rate. The metals also enhanced the removal rate through a homogeneous reaction pathway rather than through a TiO_2 surface reaction. The pH dependence, the evaluation of kinetic data and the absence of a clear correlation between reaction rate and particular metal hydrolysis species point to a mechanism involving a reactive complex between the discussed metal, the organic substrate, and an oxygen containing species such as H_2O_2 or $O_2^{\bullet-}$.

Schwitzgebel *et al.*,[37] studied the photocatalytic air oxidation of *n*-octane, 3-octanol, 3-octanone or *n*-octanoic acid films on aqueous 0.5M NaCl with buoyant nanocrystalline n-TiO_2-coated glass microbubbles. They observed not only the

inhibition of air oxidation by dissolved Fe^{3+} ions but the products and intermediates proved that not only holes but also electrons participate in the oxidation reaction.

They reported that the molecular oxygen has two roles: it accepts the electron generated in a TiO_2 crystallite and is reduced to a superoxide oxygen ($O_2^{\bullet-}$ or $HO_2^{\bullet}$); and it combines with the organic radical, generated upon the hole or $^{\bullet}OH$ radical reaction with the reactant, to produce an organoperoxy radical ($ROO^{\bullet}$). The superoxide radical combines with the organoperoxy radicals to form an unstable tetraoxide, which decomposes. Early in the reactions CO_2 evolves in the reaction sequence. They stated that as dissolved Fe^{3+} ions compete for the photogenerated electrons, and oxidize the O_2^- to O_2, they reduce the CO_2 yield in the photocatalytic air oxidation of the four electrons. The photocatalytic air oxidation of *n*-octanal is not inhibited by Fe^{3+}; that is, it does not involve the O_2^- radical. It is a hole (or $^{\bullet}OH$ radical) initiated, radical propagated, autoxidation reaction. Not only holes but also electrons have an essential role in the TiO_2-photocatalyzed or oxidation of most organic compounds. Oxidation only by holes or $^{\bullet}OH$ radicals, even when an oxidizing agent other than moleculer oxygen rapidly captured the photogenerated electrons, was much slower than hole initiated molecular oxygen consuming oxidation. The photogenerated electron participated in most, but not all, oxidation processes by reacting with molecular oxygen to form a superoxide radical. This relatively non-reactive radical combined with the organoperoxy radical formed by the hole reaction generated organic radical reacting with molecular oxygen. The product of the combination of the organoperoxy radical and the superoxide radical is an unstable organotetraoxide , which decomposes to products. This pathway does not apply to aldehydes, where the photocatalytic air oxidation is a conventional radical initiated, alkylcarbonyl radical propagated chain reaction that, interestingly, also involves a tetraoxide.

2.4 Heterogeneous Catalysis at the Gas-Solid interface.

Two main focuses of research are involved in the gas-solid interface firstly the identification of the reaction intermediates, including detailed reaction mechanisms, and reaction kinetics. Secondly the optimisation of reaction conditions to enhance the photoreaction rate and yield. Of the two aspects concerning gas-solid interface the

identification of reaction intermediate is more interesting from a fundamental mechanistic viewpoint.

Upon band gap irradiation active intermediate species are believed to be formed on solid catalysts. Several authors have reported the formation of O^{2-}, O^- and O_3^- on illuminated TiO_2 powders at low temperatures as active species for photooxidation reactions.[30, 38,39]

The effects of H_2O and O_2 play an important role in the photocatalytic activity, especially the photochemical degradation of organic compounds, of TiO_2. As shall be discussed in Chapter 3 the adsorption of water onto the TiO_2 surface caused a decrease in the upward band bending, and therefore an increase in the efficiency for the recombination of photogenerated electrons and holes. This is due to the barrier height and width, which is smaller for the return of a surface, trapped electron into the bulk conduction band region. This implies that the reaction rate of degradation decreases with increasing water concentration. Research into the addition of O_2 has shown that this leads to an increase in the upward band bending and therefore suppressed the electron-hole recombination process, leading to more efficient photoactivity.

Nakamura and Sato[23] used the Surface-enhanced IR absorption spectroscopy (SEIRAS) technique in the observation of surface products produced during the photooxidation of gas-phase *n*-decane on TiO_2 films coated with an island Au film. The bands assignable to C=O stretching, O-H stretching and H-O-H bending were observed with good intensity, indicating the formation of ketone(s) and water on the surface. SEIRAS showed that *n*-decane is physisorbed on the surface. Absorptions due to water were first developed. The preferential adsorption at the initial stage of reaction indicates that photooxidation of *n*-decane is initiated by abstraction of hydrogen from *n*-decane. A band at 1720 cm^{-1}, could be assigned to adsorbed ketone(s), the linear-chain hydrocarbons of the ketones exhibit C=O stretching at 1717-1719 cm^{-1} irrespective of their carbon numbers and position of C=O. The dipole-dipole coupling of C=O stretching caused the band to grow with a shift of 1738 cm^{-1}. The $^{16}O_2$ was exchanged for $^{18}O_2$, which resulted in the C=O stretching band shifting in frequency by 19 cm^{-1} to a lower frequency, thus indicating that *n*-decane was oxidised by active oxygen species from O_2.

An issue as to whether gas-phase H_2O enhances photo-oxidation reactions over semiconductor photocatalysts has been questioned. The effects of $H_2O_{(g)}$ on the

adsorption of *n*-decane was examined and the result showed that adsorbed *n*-decane was removed to some extent after the addition of $H_2O_{(g)}$. This may have been caused by the H_2O being more strongly adsorbed on the surface then *n*-decane. For the photooxidation of *n*-decane with a mixture of $H_2O_{(g)}$ and O_2, the increasing rate of C=O stretching band was significantly suppressed in comparison when no $H_2O_{(g)}$ is present. They reported that the oxygen isotopic exchange reaction between $^{18}O_2$ and surface hydroxyl groups (Ti-^{16}OH) over illuminated TiO_2 powders is completely inhibited by the addition of H_2O to the system. This result indicates the inhibition effects of $H_2O_{(g)}$ on the adsorption of O_2. Therefore, decreases in the photooxidation rate in the presence of $H_2O_{(g)}$ would be due to the decrease in the amounts of adsorbed *n*-decane and O_2. Irradiation of *n*-decane in the presence of $H_2O_{(g)}$ alone led to no changes in the SEIRA spectrum. This results that Au/TiO_2 has no ability to promote a photoelectrochemical reaction unlike Pt/TiO_2, on which a photoelectrochemical reaction of *n*-decane with $H_2O_{(g)}$ takes place to produce the C=O stretching band in SEIRAS.[40] The active oxygen formed on Au/TiO_2 remains in the dark. By irradiating in oxygen and adding n-decane in the dark it was observed that the bands decrease with time lapse.

Oxygen would photo-dissociate on TiO_2 surfaces to O^-, which reacts spontaneously with O_2 to form O_3^- (Eq. 2.17). In the presence of O_2, O_3^- was shown to remain in the dark with a lifetime of more than 1 minute and oxidize *n*-decane to at least a ketone. In the absence of O_2, active oxygen species disappear from TiO_2 surfaces, probably due to desorption. The superoxide has been often ruled out due to isotopic exchange reactions. It was also shown that the superoxide ion (O_2^-), if present would be less active for oxidation reactions than O_3^-.

$$O^- + O_2 \longleftrightarrow O_3^- \qquad (2.17)$$

Einiaga[39] studied which active species are responsible for the oxidation of CO. When the Pt/TiO_2 surface was irradiated with UV radiation a paramagnetic species O_3^- was observed. However on just the TiO_2 surface the paramagnetic species O_2^- was observed along with Ti^{3+}. The O_3^- species observed on the Pt/TiO_2 surface possess a weak covalent bond between the π electrons of the oxygen molecule and the free electron in O^-. This type of O_3^- was responsible for CO oxidation irradiated in equation 2.18,

$$O_3^- + CO \rightarrow CO_2 + O_2^- \qquad (2.18)$$

O_3^- was not detected on the TiO_2 sample, and so it can be concluded that the addition of Pt enhances the stability of O_3^-. It was suggested that the hole centre O^- generated from the lattice oxygen (eq. 2.19), reacted with O_2 to form O_3^- as shown in equation 2.20.

$$h^+ + O_2^- \rightarrow O^- \qquad (2.19)$$

$$O^- + O_2 \rightarrow O_3^- \qquad (2.20)$$

There was a detectable signal for the presence of O^-, this could possibly be due to the short relaxation time of the species, but can be seen in the result obtained for CO oxidation. A CO_2^- signal was observed, after irradiation of CO, suggesting the presence of O^-. For that the photochemically formed O^- and O_3^-, the active oxygen species for CO oxidation are stabilised on the Pt/TiO_2 surface.

It has been stated that under aerated conditions, active oxygen species such as superoxide radicals, hydroxyl radicals and hydrogen peroxide are all key species to initiate reactions.[10] To understand this statement Hirakawa[41] used the luminol chemiluminescence (CL) probe method and EPR spectroscopy for TiO_2 produced by HyCOM method (hydrothermal crystallisation in organic media) to research the photocatalytic formations of O_2^- and H_2O_2. The amount of O_2^- produced by photocatalysis decreased with increasing calcinations temperature. This observation indicated a decrease in trap sites and in addition the Ti^{3+} signal at 77K in the EPR spectrum decreased with increasing calcinations temperature. The production of H_2O_2 on HyCOM-TiO_2 was shown to be different in the presence and in the absence of luminol, the production pathways for H_2O_2 being mainly the two-step reduction of O_2. In the absence of luminol, dimerisation of $^{\bullet}OH$ was suggested to be dominant since the amount of H_2O_2 produced was decreased with increased O_2^-. EPR observations also supported the fact that luminol is oxidised preferably by $^{\bullet}OH$ radicals rather than the direct oxidation of a surface hole.

Shang *et al.*,[42] recently investigated the photocatalytic oxidation (PCO) of heptane, illustrating the oxidation mechanism and reaction kinetics. It was found that the PCO of heptane led to the formation of final products CO_2 and H_2O at a conversion of 99.7% *via* the intermediates such as aldehydes and ketones. It was

stated that the reactive oxygen species, O_2^-, O^-, O and $^\bullet OH$ played an important role in the PCO of heptane. The photocatalytic activity of TiO_2 could be sustained indefinitely due to the formation of water as the product, which replenishes the consumed hydroxyl radicals.

Work carried out by Gonzalez-Elipe and Che[43] on the photooxidation of ethylene and oxygen on TiO_2, identified the first direct adsorption of a peroxy radical during the photooxidation. Investigations were followed with both chlorinated and chlorine free samples along with ^{17}O work as regards to the true nature of the radicals involved in the photooxidation of ethylene. All results obtained gave evidence that the mechanism in photooxidation of ethylene could not involve O^-, O_2^- and O_3^- but, in the systems tested, the photo process depended on the formation of $OH^\bullet$ and $Cl^\bullet$ radicals from OH^- and Cl^- surface groups by the capture of a hole while the photogenerated electron is trapped by Ti^{4+} ions.

$$OH^\bullet + C_2H_4 \longrightarrow HO\text{-}CH_2\text{-}CH_2^\bullet \qquad (2.21)$$

$$HO\text{-}CH_2\text{-}CH_2^\bullet + O_2 \longrightarrow HO\text{-}CH_2\text{-}CH_2\text{-}OO^\bullet \qquad (2.22)$$

Tatsuma *et al.*,[44] studied the oxidation of organic compounds on TiO_2 under UV-irradiation. The results obtained showed that aromatic and aliphatic substance was remotely oxidized (see figure 2.2) up to distances of 2.2mm. The active oxygen radicals $^\bullet OH$ were thought to be the causes of organic oxidation. The species diffusing in the gas phase were thought to be either $^\bullet OH$ or H_2O_2 or $^\bullet OH_2$ or both, which directly or indirectly yield $^\bullet OH$ photochemically.

It is still unclear whether $^\bullet OH$ or h^+ are involved as the original active species in conventional photocatalytic oxidation of organic species, however during remote oxidation the hole cannot be involved in the process.

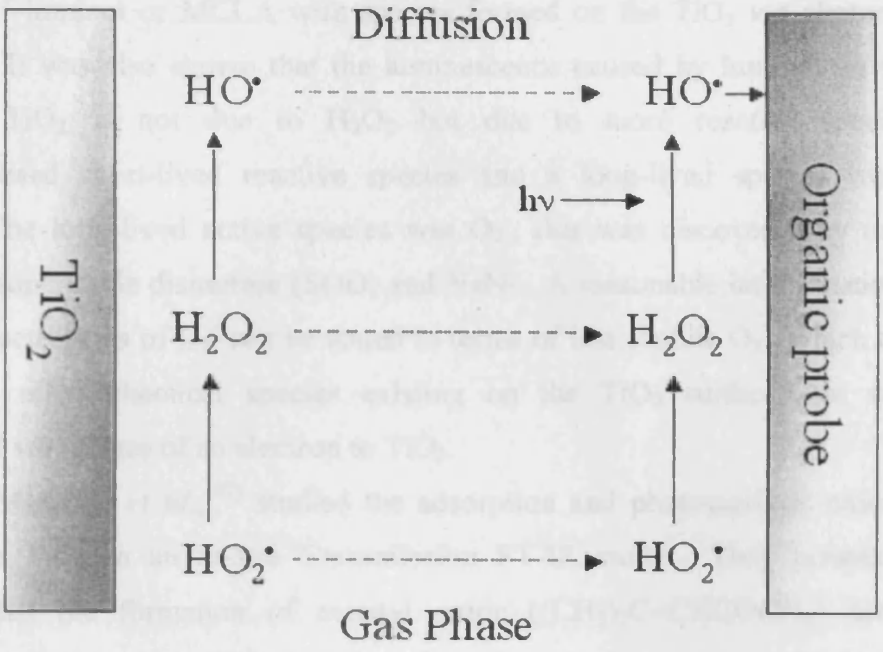

Figure 2.2. Remote oxidation of an organic probe by UV irradition of TiO_2

Ohno *et al.*,[45] studied the epoxidation of 1-Decene by H_2O_2 producing 1,2-epoxydecane on the TiO_2 surface. The Ti-η^2-peroxide generated is considered to be the active species, with one of the oxygen atoms in the peroxo group to be transferred to the oxygen *via* a transition state. The Ti-η^2-peroxides are then regenerated by H_2O_2. Under visible light there are no electron –hole pairs generated in the bulk. Instead it is thought that the reaction occurs *via* surface species, which absorb visible light.

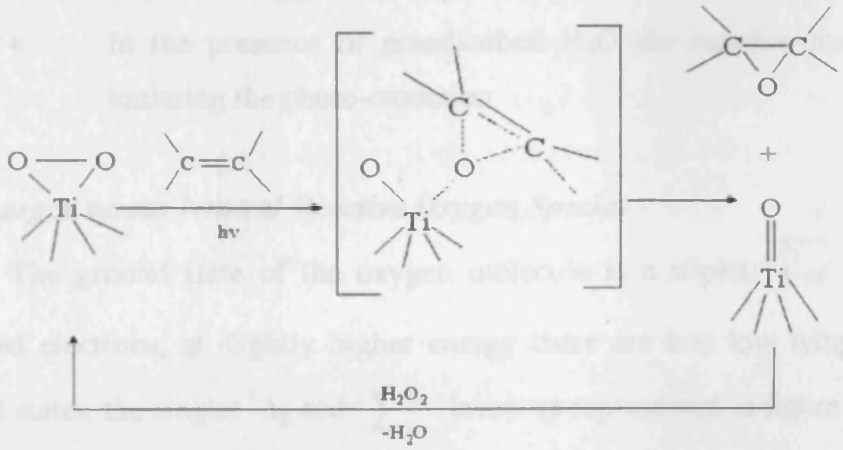

Figure 2.4. Mechanism of the production of 1,2-epoxydecane on TiO_2

Ishibashi[46] studied the formation of active oxygen species on TiO_2 film by use of a chemiluminesence method. The luminescence is caused by chemical

reactions of luminol or MCLA with species formed on the TiO_2 *via* photocatalytic reactions. It was also shown that the luminescence caused by luminol on the pre-irradiated TiO_2 is not due to H_2O_2 but due to more reactive species. An uncharacterised short-lived reactive species and a long-lived species were both formed. The long-lived active species was O_2^-, this was discovered by using the scavenger superoxide dismutase (SOD) and NaN_3. A reasonable interpretation of the decay characteristics of O_2^- can be stated in terms of less mobile O_2^-, which does not react with other chemical species existing on the TiO_2 surface, but which is deactivated *via* release of an electron to TiO_2.

El-Maazawi *et al.*,[47] studied the adsorption and photocatalytic oxidation of acetone on TiO_2 in an *in-situ* Transmission FT-IR study. They presented data showing that the formation of mesityl oxide ($(CH_3)_2C=CHCOCH_3$) during the adsorption of acetone on TiO_2 is a function of acetone coverage and pre-adsorbed water on the TiO_2 sample. The rate of acetone oxidation was found to be higher on the TiO_2 hydrated surface than on the dehydrated TiO_2 surface. Three potential photocatalytic oxidation mechanisms were reported,

- The rate determining step in one mechanism is the formation of the reactive species $O^-_{(ads)}$ from gas phase O_2 in the absence of preadsorbed H_2O,
- In the absence of oxygen the involvement of lattice oxygen occurs, at later reaction times the lattice oxygen is depleted and the role of the molecular oxygen is to replenish these sites,
- In the presence of preadsorbed H_2O the reactive hydroxyl radicals initiating the photo-oxidation.

2.5 Charged versus Neutral Reactive Oxygen Species

The ground state of the oxygen molecule is a triplet ${}^3\sum_g^-$ state with two unpaired electrons, at slightly higher energy there are two low lying electronically excited states, the singlet ${}^1\Delta_g$ and ${}^1\sum_g^+$ levels as represented in figure 2.4 below.

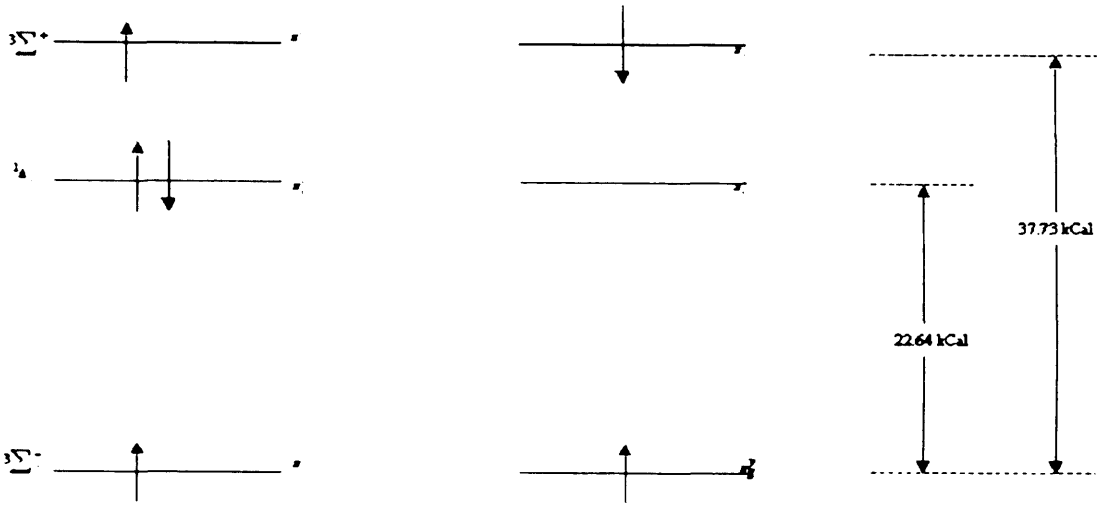

Figure 2.4. π_g orbital occupancy and energies of singlet and triplet dioxygen.

Krylov[48] proposed that singlet oxygen is formed from O_2^- on transition metal oxides and that it is this active form of oxygen that interacts with olefins. Munurea *et al.*,[49] adopted the approach based on the use of chlorinated TiO_2 to produce singlet oxygen on surfaces. A recent investigation[50] into the generation of singlet oxygen in the system of TiO_2 colloid sensitised by hypocrellin B has been reported. TEMPO is a stable nitroxide free radical, which is formed by the reaction of $^1O_2$ and TEMP (an $^1O_2$ probe), with no interference from possible side products.[51] The EPR spectrum shows a triplet due to the TEMPO radical. When sodium azide,[52] commonly used to inhibit singlet oxygen dependant reactions, was introduced to the chelate the EPR signal was found to decrease significantly. This provides further evidence that TEMPO resulted from $^1O_2$ generated in the HB-TiO_2 chelate photosensitization. Few reports have stated that singlet oxygen could be produced by TiO_2 colloid under the irradiation of ultraviolet light due to the large energy gap of the conductor. A proposed pathway of singlet oxygen is the energy transfer between the excited triplet state of the chelate and the ground state oxygen in the B-TiO_2 photosensitization, as shown below in equation 2.23,

$$\text{HB-TiO}_2 \longrightarrow {}^1\text{HB-TiO}_2 \xrightarrow{isc} {}^3\text{HB-TiO}_2 \xrightarrow{O_2} {}^1\text{O}_2 \quad (2.23)$$

Irradiation of TiO_2, but not of coated TiO_2, in ethanol generates singlet oxygen this was demonstrated by Konaka *et al.*[53] Confirmation was obtained by the involvement

of singlet oxygen in the TiO_2-induced photooxidation of uric acid[54] and methyl oleate.[55] The formation of superoxide was also confirmed.

Several possible pathways exist for the generation of singlet oxygen by TiO_2 in ethanol. One possible pathway, although efficiency of the reaction is low, is the dismutation of the superoxide anion to form H_2O_2 and $^1O_2$.[56] The conversion of superoxide to singlet oxygen is energetically unfavourable, no experimental evidence to support this pathway has been observed.[57,58] Trapping of the O_2^- with DMPO causes the EPR signal intensity of 4-oxo TEMPO to increase, thus the generation of $^1O_2$ by O_2^- is unlikely.

A similar pathway to that described above was reported by Suigamato *et al.*[59] The study was concerned with the electrolytic reduction of protons in oxygen containing acteonitrile, generating $^1O_2$ at a platinum-electrode surface that gives orientated molecules with the H-ends of $HOO^\bullet$. A similar mechanism has been proposed at the surface of irradiated TiO_2.

$$TiO_2 + O_2 \xrightarrow{h\nu} O_2^-{}_{(a)} \longrightarrow HOO^\bullet{}_{(a)} \qquad (2.24)$$

$$2HOO^\bullet{}_{(a)} \longrightarrow \begin{array}{l} H{-}O{-}O \\ \quad\quad | \\ H{-}O{-}O \end{array} \longrightarrow H_2O_2 + {}^1O_2$$

Scheme 2

Evidence for the photoproduction of H_2O_2 in aqueous solutions have been provided by several studies.[60-62] A different route for the photogeneration of 4-oxo-TEMPO is the oxidation of 4-oxo-TMP at the semiconductor hole (h^+) of photoexcited TiO_2 followed by the reaction with $^3O_2$ either successively/concertedly. The effect of added DMPO cannot be explained by this mechanism thus this pathway has been eliminated for the generation of singlet oxygen.

The most likely pathway is the generation of $^1O_2$ directly on the surface of TiO_2 is by photosensitization. UV absorption greater than the semiconductor band gap energy of the TiO_2 generates electron-hole pairs. As most of the electron - hole pairs spontaneously recombine liberating energy[63] the singlet oxygen may be formed directly from triplet oxygen in ethanol at the TiO_2 surface. The generation of 4-oxo-TEMPO in the irradiated samples exhibited a lag period, the S shape of the generation

versus time curves suggests the involvement of an induction mechanism for $^1O_2$ formation as shown in figure 2.6 below.

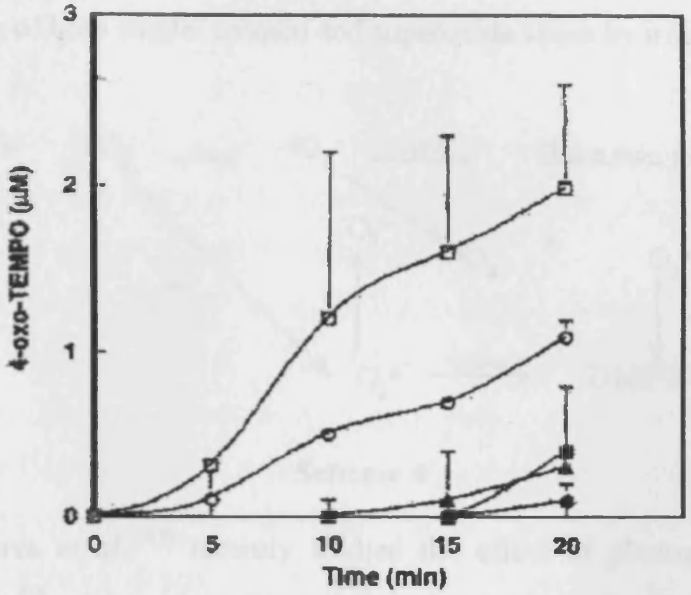

Figure 2.6. Results from the EPR spectra obtained during the irradiation of TiO_2. Signal intensities were obtained with 0.4 (triangles), 1.6 (open circles), and 4mg/mL of TiO_2 (squares). Surface coated TiO_2 (1.6mg/mL) was also used (closed circles). Plotted against concentration of 4-oxo-TEMPO.

Singlet oxygen can also be produced by the reversal of electron transfer (ion-annihilation) between a hole on the TiO_2 surface and the O_2^- ion generated from $^3O_2$ by a photoexcited electron.[61] This mechanism shows that $^1O_2$ and O_2^- can be generated on the TiO_2 surface. This mechanism has also been demonstrated with electrochemically generated 1,2-diphenylisobenzofuran cation radicals.[64] However, this mechanism is thought unlikely as the reverse reaction for the formation of O_2^- *via* a one electron transfer from electron donor, such as amines to $^1O_2$, hardly occurs (scheme 3).[65]

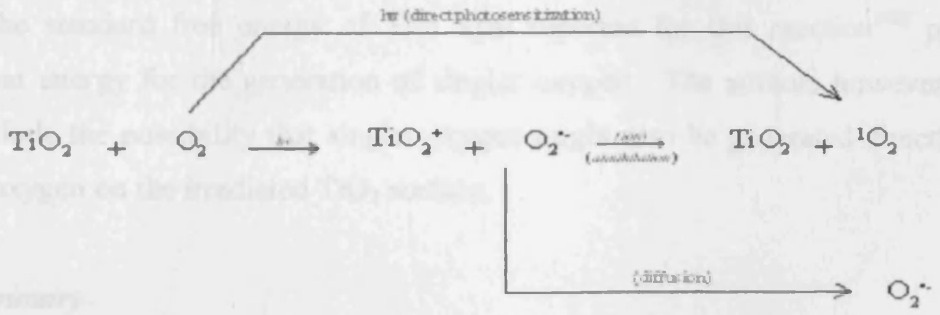

Scheme 3

A singlet oxygen quenching mechanism, which involves electron transfer with O_2^-, has been proposed by Khan[66]. Khan observed that the signal intensity of 4-oxo-

TEMPO substantially increased with increasing concentration of DMPO. The reaction scheme shown in scheme 4 displays the possible mechanism for generation and interaction of both singlet oxygen and superoxide anion by irradiated TiO_2.

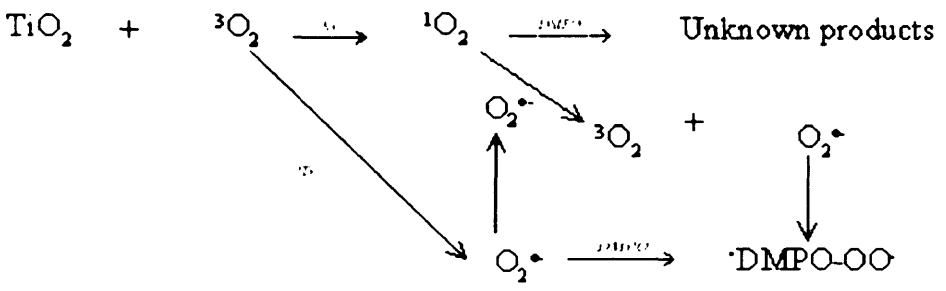

Scheme 4.

Konovalova *et al.*,[67] recently studied the effect of photosensitation of TiO_2 nanoparticles with cartenoids under red light irradiation. It showed that cartenoids facilitate the generation of O_2^- and $^1O_2$ in irradiated TiO_2 colloids. At low cartenoid concentrations ($<3 \times 10^{-5}$ M) the rate of O_2^- production exceeds that obtained in the absence of cartenoid.

EPR experiments with 2,2,6,6-tetramethyl-4-piperidone and spin traps PBN and DMPO showed that both superoxide and singlet oxygen were formed in irradiated TiO_2 suspensions in toluene and CH_2Cl_2. A dismutation of superoxide to singlet oxygen has been proposed *via* the intermediate formation of $HO_2^\bullet$ radicals after identification of the PBN-$HO_2^\bullet$ spin adduct.

$$2O_2^- + 2H^+ \longrightarrow HO_2^\bullet + HO_2^\bullet \longrightarrow [HOO\text{-}OOH] \longrightarrow H_2O_2 + {}^1O_2 \qquad (2.25)$$

The standard free energy of 37.5 kcal reported for this reaction[68] provides sufficient energy for the generation of singlet oxygen. The authors however, could not exclude the possibility that singlet oxygen might also be generated directly from triplet oxygen on the irradiated TiO_2 surface.

2.6 Summary

In the heterogeneous photocatalytic system, the efficiency for chemical transformation depends on the photoactivity of the adsorbate molecule and the catalyst substrates. At the liquid-solid interface the primary active oxygen species

was thought to be the $^{\bullet}OH$ radical formed by the photogenerated holes reacting with either water or hydroxide ions.

Hole oxidation has also been suggested for compounds lacking abstractable hydrogen and for some aromatic compounds. On bare TiO_2 direct electron transfer and interaction of organics with bound surface hydroxyl groups are responsible for the reaction pathway. Photogenerated electrons have also been shown to possibly play a role in the degradation of chlorinated phenols.

Recent studies indicate that at the liquid-solid interface, hydroxyl radicals are the dominant reactive species. The effect of transition metals on the rate of photocatalytic oxidation provided interesting results which indicated that Cu(II), Fe(III) and Mn(II) has a twofold increase in the initial reaction rate.

Research effort into the gas-solid interface has been in the identification of reaction intermediates, reaction mechanisms and reaction kinetics. The research efforts indicate that at the gas-solid interface most of the main reactive oxygen species mentioned play a role in the degradation of organic compounds, depending on the reaction conditions, while the reactant itself plays a role in influencing which reaction pathway the molecule takes.

It has been seen that singlet oxygen is formed from O_2^- on transition metal oxides and singlet oxygen is the species, which interacts with olefins. Research efforts into singlet oxygen seem to be limited when it comes to research efforts of the charged oxygen species, with more work being done on the pathway for generation of singlet oxygen, rather than its reactive properties.

EPR spectroscopy can be widely used to examine paramagnetic species on the surface of TiO_2, particularly with the objective of identifying radicals formed under UV irradiation, which may be important in photocatalytic processes. These paramagnetic species can give valuable information regarding the surface properties of the nanoparticle TiO_2 samples.

1.5 References

1. *Manufacture and general properties of Titanium dioxide pigment,* Titanium pigments, Tioxide UK Ltd, Publications, TiInfo System, February (1992).
2. J. H. Braun, *Journal of Coatings Technology,* **69**, 59, (1997).
3. F. A. Cotton and G. Wilkinson, *Advanced Inorganic Chemistry* 5th Ed., Wiley-Interscience Publication, (New York, Chischester, Brisbane, Toronto, Singapore), 655, **1988**.
4. U. Diebold, *Surf. Sci. Reports*, **48**, 53, (2003).
5. J. Whitehead, *Titanium Compounds (Inorganic)*, Kirk Othmer: Encyclopedia of Chemical Technology, John Wiley, **23,** 131, (1983).
6. J. Barksdale, *Titanium – Its Occurrence, Chemistry and Technology*, 2nd Ed., Roland Press Co, (New York) (1966).
7. Kronos. Inc. (1999)
8. C.A. Jenkins, Ph.D. Thesis, University of Wales, Cardiff, (1998).
9. A. M. Linsebigler, G. Lu, J. T. Yates, Jr., *Chem. Rev.*, **95**, 735, (1995).
10. A. Hagfeldt, M. Gratzel, *Chem. Rev.*, **95**, 49, (1995).
11. A. Furube, T. Asahi, M. Harada, Y. Ichihashi, M. Anpo. *J. Phys. Chem. B,* **102**, 10707, (1999).
12. J. Moser, M. Grätzel, R. Gallay, *Helv. Chim. Acta.*, **70**, 1596, (1987).
13. M. Grätzel, R.F. Howe, *J. Phys. Chem.*, **94**, 2566, (1990).
14. Ibid.
15. H. Yamashita, Y. Ichihashi, S. Kishiguchi, M. Anpo, *J. Synchrotron Rad.*, **6**, 451, (1999).
16. M. Anpo, M. Takeuchi, *J. Catal.*, **216**, 505, (2003).
17. J. M Herrmann, J. Disdier, P. Pichat, *Chem. Phys. Lett.*, **108**, 618, (1984).
18. E. Borgarello, J. Kiwi, M. Grantzel, E. Pelizzetti, M. Visca, *J. Am. Chem. Soc.*, **104**, 2996, (1982).
19. T. Umebayashi, T. Yamaki, H. Itoh, K. Asai, *J. Phys and Chem. of Solids*, **63**, 1909, (2002).
20. H. Idriss, K. S. Kim, M. A. Barteau, *J. Catal.*, **139**, 119, (1993).
21. M. Primet, P. Pichat, M.V. Mathieu, *J. Phys. Chem.*, **9**, 1216, (1971).
22. M. Primet, P. Pichat, M.V. Mathieu, *J. Phys. Chem.*, **9**, 1221, (1971).

23. C. A. Jenkins, D. M. Murphy, C. C. Rowlands, *J. Chem. Soc., Perkin Trans.*, **2**, 2479, (1997).
24. C. Renz, *Helv.Chim. Acta.*, **4**, 961, (1921).
25. A. H. Wilson. *Proc. Roy. Soc. A*, **133**, 458, (1931).
26. A. H. Wilson. *Proc. Roy. Soc. A*, **134**, 277, (1931).
27. A. Fujishima; K. Honda, *Nature*, **37**, 238, (1972).
28. J. G. Balfour, *J.O.C.C.A.*, **12**, 478, (1990).
29. T. Kawai, T. Sakaty, *Chem. Phys. Lett.*, **72**, 87, (1980).
30. M. A. Fox, M. T. Dulay, *Chem. Rev.*, **93**, 341, (1993).
31. M. Anpo, H. Yamashita, *Surface Photochem.*, M. Anpo (Ed.) Wiley, London, (1996).
32. M. Mehos, C. Turchi, J. Pacheco, A. Boegel, T. Merril, R. Stanley, *Pilot Scale study of the Solar Detoxification of VOC-Contminated Groundwater.,'* American Institute of Chemical Engineers, Summer Annual Meeting, Minneapolis, Minn., August 9 (1992), NREL/TP-432-4981
33. A. Heller, J. R. Broch *Materials and Methods for Photocatalysing Oxidation of Organic Compounds on Water*, United states, Patent, 4-997-576, March, (1991).
34. L. A. Dibble, G. B. Raupp, *Catal. Lett.*, **4**, 345, (1990).
35. L. A. Dibble, G. B. Raupp, *Environ. Sci. Technol.*, **26**, 492, (1992).
36. R. M. Alberici, W. F. Jardin, *App. Catal. B: Environ.*, **14**, 55, (1997).
37. K Wolf, A. Yazdani, P. Yates, *J. Air Waste Manage Assoc.*, **41**, 1055, (1991).
38. C. F. Wilkinson, *Environ. Sci. Techno.*, **22**, 1381, (1988).
39. J. Fisherman, *Chemosphere*, **33**, 442, (1991).
40. S. Japer, T. J. Wallington, S. J. Rudy, T. Y. Chang, *Environ. Sci. Technol.*, **25**, 415, (1991).
41. A. D .Cortese, *Environ. Sci. Technol.*, **24**, 442, (1990).
42. A. Fujishima, T. N. Rao, D. A. Tryk, *J. Photochem. Photobiol. C: Photochem. Revs.*, **1**, 1, (2000).
43. H. Honda, A. Isizaki, R. Somu, K. Hashimoto, A. Fujishima, *J. Illum. Eng. Soc.*, 42, Winter, (1998).
44. K. P. Kuhn, *Chemosphere*, **55**, 71, (2003).
45. A. Mills, S. Lehunte, *J. Photochem. Photobiol. A*, **108**, 1, (1998).

46. Y. Kikuchi, K. Sunadam T. Iyoda, K. Hashimoto, A. Fujishima, *J. Photochem. Photobiol: A Chem.*, **106**, 51, (1997).

47. K. Sunada, Y Kikuchi, K. Hashimoto, A. Fujishima, *Environ. Sci. Technol.*, **32** 726, (1998).

48. W. A. Jacoby, P. C. Maness, E. J. Wolfrum, D. M. Blake, J. S. Fennel, *Environ. Sci. Technol.*, **32**, 2560, (1998).

49. A. Fujishima, J. O. Htsuki, T. Yamashita, S. Hayakawa, *J. Photomed. Photobiol.*, **8**, 45, (1986).

50. R. Cai, Y. Kubuto, T. T. Shuin, H. Sakai, K. Hashimoto, A. Fujishima, *Cancer Res.*, **52**, 2346, (1992).

51. K. Tennakone, *J. Photochem. Photobiol. A: Chem.*, **71**, 199, (1993).

52. R. Wang, K. Hashimoto, A. Fujishima, M. Chikuni, E. Kojima, A. Kamura, M. Shimohigoshi, T. Watanabe, *Nature,* **388**, 431, (1997).

53. R. Wang, K. Hashimoto, A. Fujishima, M. Chikuni, E. Kojima, A. Kamura, M. Shimohigoshi, T. Watanabe, *Adv. Mater.*, **10**, 135, (1998).

54. R. Wang, N. Sakai, A. Fujishima, T. Watanabe, K. Hashimoto, *J. Phys. Chem. B,* **103**, 2188, (1999).

55. Vesa P.S. Judin, *Chemistry in Britain,* 503, June, (1993).

56. J. H. Braun, *J. Coatings Tech.*, **69**, May (1997).

57. J. G. Balfour, D. Huchette, 1st Middle East Conference *Technological Developments in Coatings: Their Applications and Uses,* Dubai, (1994), Tioxide UK Ltd. Publication.

58. R. E .Day, T. A. Egerton, *Colloids and Surfaces*, **23**, 137, (1987).

59. M. P. Diebold, *Surface coatings International,* **7**, 294, (1995).

60. W. Hughes *Photogradation of Paint Film Containing Titanium Dioxide Pigments,* Proceedings 10th Fatipec Congress, June, (1970).

61. G. Käempf, W. Papenroth, R. Holm, A. G. Bayer, *Journal of Paint Technology,* **46**, 56, (1974).

62. H. G. Voelz, G. Käempf, H. G. Fitzky, *Farbe und Lack*, **78**, 1037, (1972).

63. S. Boyle, J. Ardill, *The Greenhouse Effect*, N.E.L., 214, London, (1989).

64. A. Mills, S. LeHunte, *J. Photochem. Photobiol. A: Chem.*, **108**, 1, (1997).

2.7 References

1. M. Che, A. J. Tench, *Adv.Catal.*, **31,** 77, (1982).
2. M. Che, A. J. Tench, *Adv. Catal.*,**32**, 1, (1983).

3a. M. Che, E. Giamello in '*Spectroscopic Characterisation of Heterogeneous Catalysis' Part B, Stud. Surf. Sci. Catal.*, (Ed. J. L. G. Fiero), Elsevier Science/Publishers, Amsterdam, **57**, B265, (1987).

3b. M. Anpo, M. Che, B. Fubini, E. Garrone, E. Giamello, M. C. Paganini, *Top. in Catal.*, **8,** 189, (1999).

4. R. D. Jones, D. A. Summerville, F. Basolo, *Chem. Rev.*, **79,** 139, (1979).
5. M. C. R. Symons, *J. Phys. Chem.*, **76**, 3095, (1972).
6. A. J. Tench, J. F. J. Kibblewhite, *Chem. Commun.*, 955, (1973).
7. B. Taarit, J. C. Vedrine, J. F. Dutel, C. Naccache, *J. Magn. Res.*, **31**, 251, (1978).
8. T. G. Castner, W. Kanzig, *J. Phys. Chem. Solids*, **3**, 178 (1957).
9. A. J. Maira, K. L. Yeung, J. Soria, J. M. Coronado, C. Belver, C. Y. Lee, V. Augugliaro, *App. Catal. B*, **29**, 327, (2001).
10. M. R. Hoffmann, S. T. Martin, W. Choi, D. W. Bahnemaan, *Chem. Rev.*, **95**, 65, (1995).
11. Y. Nakaoka, Y. Nosaka, *J. Photochem. Photobiol. A: Chem.*, **110**, 299, (1997).
12. T. Hirakawa, Y. Nakaoka, J. Nishino, Y. Nosaka, *J. Phys. Chem. B*, **103**, 4399 (1999).
13. D. Lawless, N. Sepone, D. Meisel, *J. Phys. Chem.*, **95**, 5166, (1991).
14. D. Park, J. Zhang, K. Ikene, H. Yamashita, M. Anpo, *J. Catal.*, **185**, 114, (1999).
15. G. Lui, X. Li, J. Zhao, S. Harikoshi, H. Hidaka, *J. Mol. Catal. A*, **153**, 221, (2000).
16. H. Noda, K. Oikawa, H. Kanada, *Bull. Chem. Soc. Jpn.*, **65**, 2505, (1992).
17. H. Noda, K. H. Nishiguichi, H. Kamada, *Bull. Chem. Soc. Jpn.*, **66**, 3542, (1993).
18. L. L. Perissinotti, M. A. Brusa, M. A. Grela, *Langmuir*, **17**, 8422, (2001).
19. E. C. Butler, A. P. Davies, *J. Photochem. Photobiol. A*, **70**, 273, (1993).
20. M. Fujihira, Y. Satoh, T. Osa, *Nature*, **293**, 206, (1981).
21. C. J. Richard, *J. Photochem. Photobiol. A*, **72,** 179, (1993).

22. C. D. Jaeger, A. J. Bard, *J. Phys. Chem.*, **83**, 3146, (1979).

23. R. Nakamura, S. Sato, *J. Phys. Chem. B*, **106**, 5893, (2002).

24. K. Ishibashi, A. Fujishima, T. Watanabe, K. Hashimoto, *J. Photochem. Photobiol. A*, **134**, 139, (2000).

25. R. W. Matthews, *J. Catal.*, **111**, 264, (1988).

26. D. Banhnemann, D. A. Heinglein, J. Lillie, L. Spanhel, *J. Phys. Chem.*, **88**, 709, (1984).

27. C. Minero, G. Mariella, D. Maurino, D. Vione, E. Pelizzetti, *Langmuir*, **16**, 8964, (2000).

28. N. Serpone, I. Texier, A. V. Emiline, P. Pichat, H. Hidaka, J. Zhao, *J. Photochem. Photobiol. A*, **136**, 145, (2000).

29. D. Lawless, N. Serpone, D. Meisel, *J. Phys. Chem.*, **95**, 5166, (1991).

30. R. F. Howe, M. Gratzel, *J. Phys. Chem.*, **91**, 3906, (1987).

31. O. L. Mićić, Y. Zhang, K. R. Cromack, A. D. Trifunoc, M. C. Thurnauer, *J. Phys. Chem.*, **97**, 7277, (1993).

32. O. I. Mićić, Y. Zhang, K. R. Cromack, A. D. Trifunac, M. C. Thurnauer, *J. Phys. Chem.*, **97**, 13284, (1993).

33. T. M. El-Morsi, W. R. Budakowski, A. S. Abd-el-aziz, K. J. Friesen, *Environ. Sci. Technol.*, **34**, 1018, (2000).

34. Y. Nosaka, M. Kishimoto, J. Nishino, *J. Phys. Chem. B*, **102,** 10279, (1998).

35. Y. Nosaka, K. Koenuma, K. Ushida, A. Kira, *Langmuir*, **12**, 736, (1996).

36. G. Lui, J. Zhao, H. Hidaka, *J. Photochem. Photobiol. A: Chem.*, **133**, 83, (2000).

37. J. Schwitzgebel, J. G. Ekerdt, H. Gerischer, A. Heller, *J. Phys. Chem.*, **99**, 5633, (1995).

38. A. L. Attwood, D. M. Murphy, J. L. Edwards, T. A. Egerton, R. W. Harrison, *Res. Chem. Intermed.*, **29**, 449, (2003).

39. H. Eniaga, A. Ogata, S. Futamura, T. Ibusuki, *Chem. Phys. Lett.*, **338**, 303, (2001).

40. R. Nakamura, S. Sato, *Langmuir*, in press.

41. T. Hirakawa, H. Kominami, B. Ohtani, Y. Nosaka, *J. Phys. Chem. B*, **105**, 6993, (2001).

42. J. Shang, Y. Du, X. Zih, *Chemosphere*, **46**, 93, (2002).

43. A. R. Gonzalez-Elipe, M. Che *Journal de chimie physique*,**79**, 355, (1982).

44. T. Tatsuma, S. Tachibana, A. Fujishima, *J. Phys. Chem. B*, **105**, 6987, (2001).
45. T. Ohno, Y. Masaki, S. Hirayama, M. Matsumura, *J. Catal.*, **204**, 163, (2001).
46. K. Ishibashi, Y. Nosaka, K. Hashimoto, A. Fujishima, *J. Phys. Chem. B*, **102**, 2117, (1998).
47. M. El-Maazawi, A. N. Finken, A. B. Nair, V. H. Grassian, *J. Catal.*, **191**,138, (2000).
48. O. V. Krylov, *Kinet. Catal.*, **14**, 24, (1973).
49. G. Munuera, A. Navio, V. Rives-Arnau, *J. Chem. Soc. Faraday Trans. I*, **77**, 2747, (1981).
50. S. Xu, J. Shen; M. Zhang, T. Shen, *J. Photochem. Photobiol. B. Biol.*, **67**, 64, (2002).
51. Y. Lion, M. Dilmelle, V. D. Van, *Nature*, **263**, 442, (1976).
52. R. D. Hall, C. F. Chignell, *J. Photochem. Photobiol.*, **48**, 459, (1987).
53. R. D. Konaka, E. Kasahara, W. C. Dunlap, Y. Yamamoto, K. C. Chien, M. Inoue, *Free Rad. Biol. Med.*, **27**, 294, (1999).
54. N. C. Dunlap, Y. Yamamoto, M. Inoue, M. Kashiba-Iwatsuki, M. Yamaguchi, K. Tomita, *Int. J. Cosmetic Sci.*, **20**, 1, (1998).
55. Y. Yamamotot, W. C. Dunlap, N. Imai, R. Moshima, M. Inoue, Y. Hasegawa, T. Miyishi, *Proceedings of the 20th Congress of the International Federation of Societies of Cosmetic Chemists*, Cannes, **1**, 153, (1998).
56. E. J. Corey, M. M. Mehrota, A. U. Khan, *Biochem. Biophys. Res. Comm.*, **145**, 842, (1987).
57. R. Ponpho, I. Rosenthal, *J. Phys. Chem.*, **77**, 1722, (1973).
58. R. Nilsson, D. R. Kearns, *J. Phys. Chem.*, **78**, 1681, (1974).
59. H. Suigimoto, D. T. Sawyer, J. J. Kanofsky, *J. Am. Chem. Soc.*, **110**, 8707, (1988).
60. J. R. Harbour, J. Tromp, M. L. Hair, *Com. J. Chem.*, **63**, 204, (1985).
61. S. P. Pappas, R. M. Fischer, *J. Paint Tech.*, **46**, 65, (1974).
62. M. V. Rao, K. Rajeshwar, V. R. P. Vemeter, J. Dubow, *J. Phys. Chem.*, **84**, 1987, (1980).
63. N. Serpone, D. Lawless, R. Khairutdinov, *J. Phys. Chem.*, **99**, 16655, (1995).
64. E. A. Mayeda, A. J. Bard, *J. Am. Chem. Soc.*, **95**, 6223, (1973).
65. I. Saito, T. Matsumura, K. Inoue, *J. Am. Chem. Soc.*, **105**, 3200, (1983).
66. A. U. Khan, *J. Am. Chem. Soc.*, **99**, 370, (1977).

67. T. A. Konovalova, J. Lawrence, L. D. Kispert, *J. Photochem. Photobiol. A: Chem.*, **162**, 1, (2004).

68. W. M. Latimer (Ed.), *Oxidation Potentials*, *2nd ed.*, Prentice-Hall, New York, (1952).

Chapter 3

An Introduction to Solid State Chemistry

3.1 An Introduction to Solid State Chemistry

Most of the chemical elements and their compounds are solids at room temperature. The study of solids and the factors that determine their structure and properties are therefore important areas of research for chemists. The electronic theory of valency provides the basis of our modern understanding of chemistry. This makes the study of the electronic structure of solids particularly important. Many of the characteristic properties of solids depend directly upon the behaviour of the electrons within them, for example, electrical conductivity, the optical, magnetic and surface properties of solids. At the turn of the 20th century the classical electron theory was developed. Paul Drude[1,2] postulated that free electrons in metals 'drift' in a response to an external field and interact with certain lattice atoms. This was the first microscopic description of electrons in solids.

Solid-state chemistry is a subject that is relevant to modern technology. It is concerned with the synthesis, structure, properties and applications of solid materials.[3] This encompasses inorganic and metallic solids. Organic solids, which exhibit physical properties such as electrical conductivity, can also be included. Of particular relevance in the field of solid-state chemistry is the study of metals, semiconductors and insulators; this shall be considered in more detail shortly. An understanding of the variety and complexity of structure types is central to an appreciation of solid-state chemistry. This includes not only the description and classification of crystal structures, with a working knowledge of space groups but also an evaluation of the factors that influence and control crystal structures.

An important structural aspect is the defect structure of solids. All solids contain defects of some kind and often these have a great influence on properties such as electrical conductivity, mechanical strength and chemical activity. Several methods are available to synthesize solids some of which are unique to solid-state chemistry. Methods include solid-state reaction, vapour phase transport, precipitation and electrochemical methods. There are a variety of physical techniques and methods used to analyse and study solids, unlike the techniques used to study liquids and

solutions. There is less emphasis on spectroscopic methods and more on various diffraction (e.g. X-ray diffraction), and microscopic techniques.

As mentioned previously metals, semiconductors and insulators are of particular importance in the solid-state chemistry studies, the main difference between metals, semiconductors and insulators is the magnitude of their conductivities, σ. Metals have the ability to conduct electricity very easily, with typical values of σ in the range $\sigma \sim 10^4$ to 10^6 $ohm^{-1}cm^{-1}$, insulators $\sigma \lesssim 10^{-15}$ $ohm^{-1}cm^{-1}$ and semiconductors lie in between, $\sigma \sim 10^{-5}$ to 10^3 $ohm^{-1}cm^{-1}$.

The reason for this large difference in conductivities originates from the mechanism of conduction in metals and semiconductors/insulators; the conductivity of most semiconductors/insulators increases with increasing temperature, on the other hand metals show a slight decrease in conductivity on increasing temperature. The conductivity, σ, is given by the equation,[3]

$$\sigma = n e \mu \qquad (3.1)$$

where, n is the number, e the charge and μ the mobility of the charge carriers. In the case of metals, as the temperature is raised the electrons gain energy causing collisions, which in turn results in an increase in lattice vibrations. This leads to a greater displacement of the ions from their lattice sites, thus hindering the movement of electrons through the ionic material and, therefore, reducing their mobility as shown in figure 3.1. In solids, conduction can only occur if electrons are promoted to the conduction band, as only then will there be a partially full band.

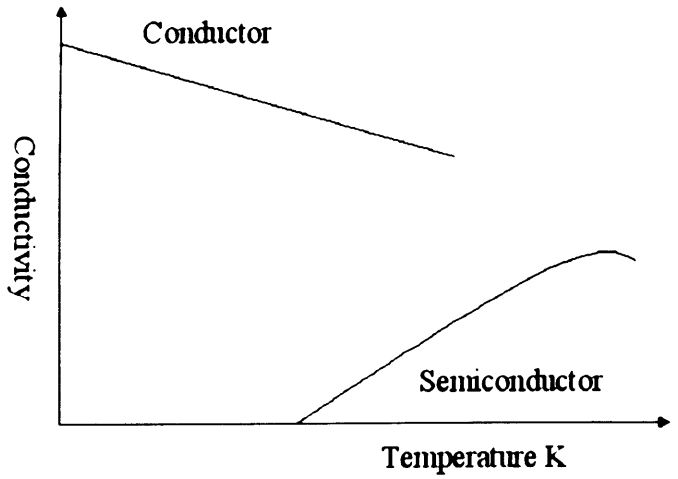

Figure 3.1. Conductivity of semiconductors and conductors as a function of temperature.[5]

As the temperature rises the number of electrons promoted increases and so the current increases as demonstrated in figure 3.1. At any one temperature more electrons will be promoted for a solid with a small band gap than for one with a large band gap, so that the solid with the smaller band gap will be a better conductor.[4]

3.2. Band Theory – Electronic structure of solids

Metallic structure and bonding are characterised by delocalised valence electrons (these are responsible for the high electrical conductivity of metals[6]). This opposes that of ionic and covalent bonding in which the valence electrons are localized on particular atoms or ions and are not able to move through the structure. The electronic structure of metals, semiconductors and other solids can be described in terms of the band or zone theory. Within this theory the differences between metals, semiconductors and insulators depend on,[7]

- The band theory structure of each,
- Whether the valence bands are full or partially full,
- The magnitude of any energy gap between full and empty bands.

The band theory of solids is well supported by X-ray spectroscopic data and by two independent theoretical approaches, the *chemical approach* and *physical approach.*

3.2.1 The 'Chemical Approach'

The chemical approach to band theory is to extend molecular orbital theory, which is usually applied to small finite sized molecules, toward infinite three-dimensional structures.[3] In a diatomic molecule, an atomic orbital from atom one overlaps with an atomic orbital on atom two resulting in the formation of two molecular orbitals, as shown in figure 3.2, which are delocalised over both atoms. One of the molecular orbitals is 'bonding' and has lower energy than that of the atomic orbitals the other is 'antibonding' and is of higher energy than the atomic orbitals.

In polyatomic molecules, a greater variety of molecular orbitals can be formed.[6] The molecular orbital theory emphasizes the delocalised nature of the electron distribution, so that molecular orbitals are generally extended over all the atoms. The total number of molecular orbitals formed (which may be bonding,

antibonding or non-bonding) is the same as the number of valence orbitals used to make them. As the molecules become larger their molecular orbitals become progressively more abundant and more closely spaced in energy, and the molecular orbitals formed will not be arranged uniformly over all energies.

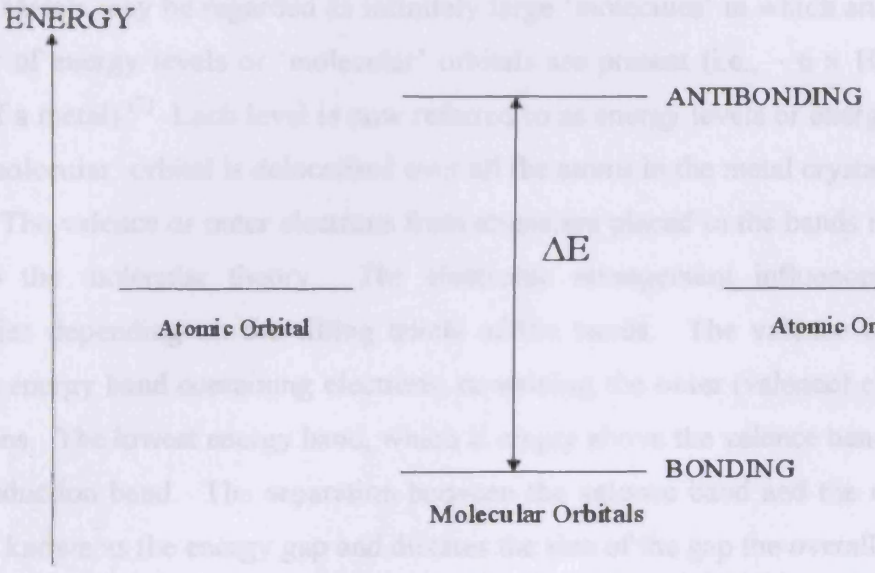

Figure 3.2. Schematic representation for the formation of bonding and antibonding combinations of 2s-orbitals.[3,5]

In some energy regions there are no orbitals, which corresponds to a gap between the bands. Within allowed bands more orbitals can be concentrated together at some energies more than others, as illustrated in figure 3.3.

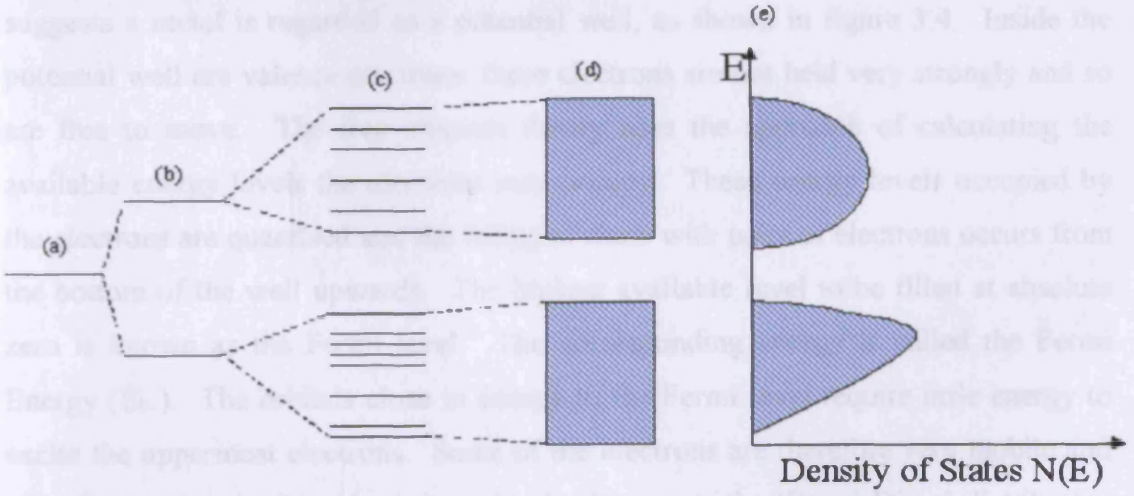

Figure 3.3. Orbital energies of (a) atom, (b) small molecule, (c) large molecule (d) solid and (e) density of states corresponding to (d).[6]

The density of states (N(E)) is defined as: -

- N(E)δE is the number of allowed energy levels per unit volume of the solid, in the energy range E to E+δE.
- N(E) is zero in the forbidden band gaps.

Metals may be regarded as infinitely large 'molecules' in which an enormous number of energy levels or 'molecular' orbitals are present (i.e., ~ 6 x 10^{23} for one mole of a metal).[7] Each level is now referred to as energy levels or energy states as each 'molecular' orbital is delocalised over all the atoms in the metal crystal.

The valence or outer electrons from atoms are placed in the bands in a similar way to the molecular theory. The electronic arrangement influences different properties depending on the filling levels of the bands. The valence band is the highest energy band containing electrons; containing the outer (valence) electrons of the atoms. The lowest energy band, which is empty above the valence band, is called the conduction band. The separation between the valence band and the conduction band is known as the energy gap and dictates the size of the gap the overall electronic properties of the metal.

3.2.2 The 'Physical Approach'

The physical approach to band theory is to consider the energy and wavelength of electrons in a solid.[3] The free electron theory of Sommerfeld[2,8] suggests a metal is regarded as a potential well, as shown in figure 3.4. Inside the potential well are valence electrons; these electrons are not held very strongly and so are free to move. The free electron theory uses the approach of calculating the available energy levels the electrons may occupy. These energy levels occupied by the electrons are quantised and the filling of them with pairs of electrons occurs from the bottom of the well upwards. The highest available level to be filled at absolute zero is known as the Fermi level. The corresponding energy is called the Fermi Energy (E_F). The orbitals close in energy to the Fermi level require little energy to excite the uppermost electrons. Some of the electrons are therefore very mobile and give rise to electrical conductivity. At absolute zero, the 'Fermi Dirac' distribution corresponds to a sharp cut off between completely filled levels below the energy E_F and completely empty levels above it.

At temperatures above 0 K some electrons just below the Fermi level can be excited to levels just above the Fermi level by thermal motion of the atoms. The number however, is small compared to the number of electrons in the band. To date most theories involve an approximation that is, electrons occupy all levels below the Fermi level.

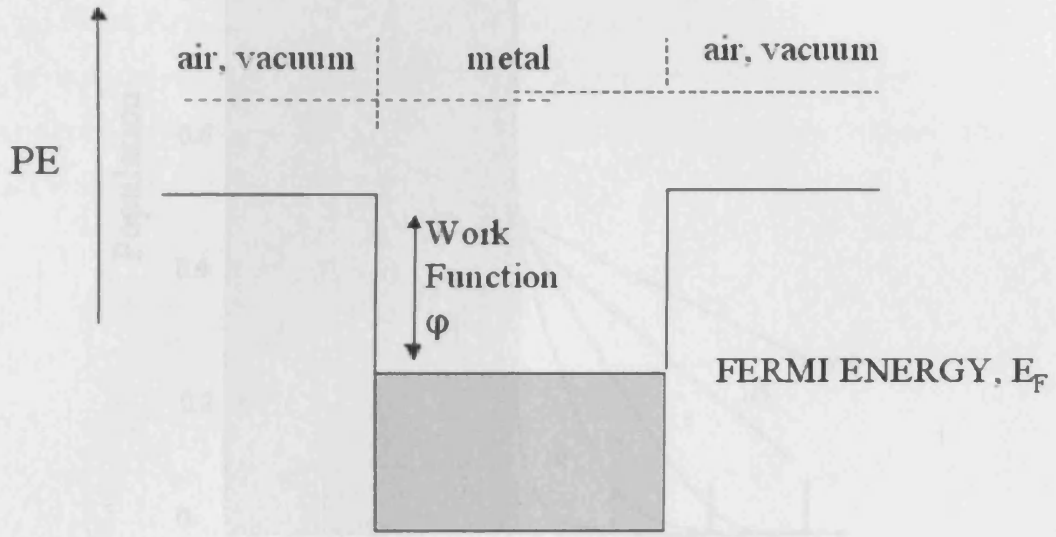

Figure 3.4. Schematic representation of electrons in a potential well, as discussed in the free electron theory.

The population P, of the orbitals is given by the 'Fermi-Dirac' distribution, a version of the Boltzman distribution[5,9] that takes into account the effect of the Pauli principle.

$$P = \frac{1}{e^{(E-\mu)/kT} + 1} \qquad (3.2)$$

where, μ is the chemical potential which is the energy of the level for which P= ½, E is the energy and kT the Boltzman distribution. The shape of the Fermi Dirac distribution is shown in figure 3.5. For energies well above μ, the 1 in the denominator can be neglected and then

$$P \approx e^{-(E-\mu)/kT} \qquad (3.3)$$

The population now resembles a Boltzmann distribution, decaying exponentially with increasing energy. The higher the temperature the longer the exponential tail.

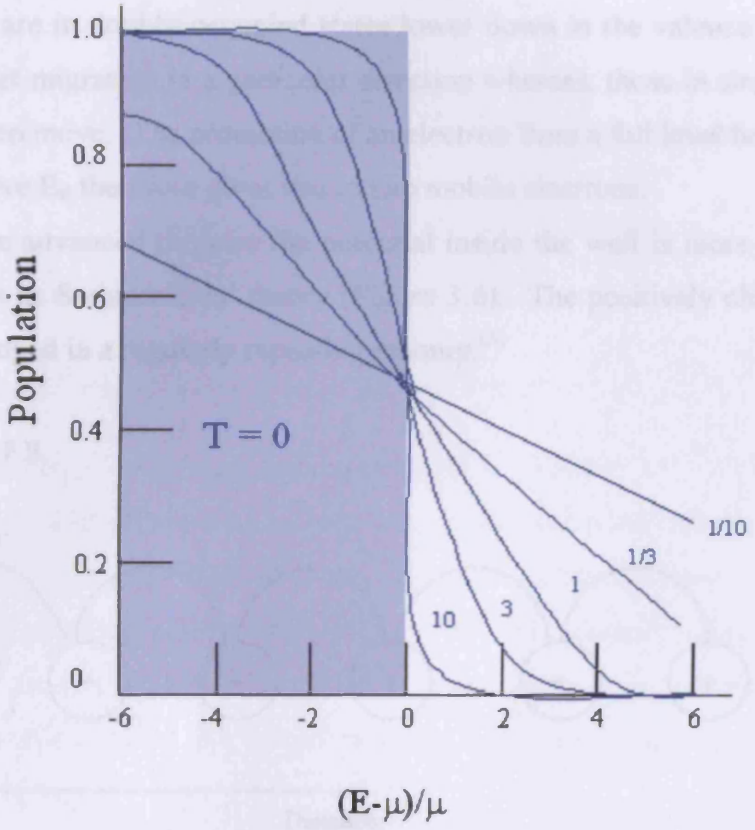

Figure 3.5 The Fermi-Dirac distribution, which gives the population of the levels at temperature T. The high-energy tail decays exponentially towards zero. The curves are labelled with the value μ/kT. The tinted region shows the occupation of levels at T= 0.[9]

The normal reference point for energy within a solid is the Fermi level. Outside the solid, however, the natural zero of energy is the vacuum level, Ev, which is the energy of an electron at rest, and far away from any electrical charge. The relation between the two energies is given by the work function (see figure 3.4) and is defined as:

$$\varphi = E_V - E_F \qquad (3.4)$$

The work function, φ, is the energy required to remove the uppermost valence electrons from the potential well, and is analogous to the ionisation potential of an isolated atom.

The work function of a metal is, therefore, the minimum energy required to remove an electron from the solid into the vacuum. The high electrical conductivity of metals is due to the drift of electrons that are in half-occupied states close to E_F. Electrons that are in doubly occupied states lower down in the valence band cannot undergo any net migration in a particular direction whereas, those in singly occupied levels are free to move. The promotion of an electron from a full level below E_F to an empty one above E_F therefore gives rise to two mobile electrons.

In more advanced theories the potential inside the well is more periodic and not as constant as Sommerfelds' theory (Figure 3.6). The positively charged atomic nuclei are arranged in a regularly repeating manner.[3]

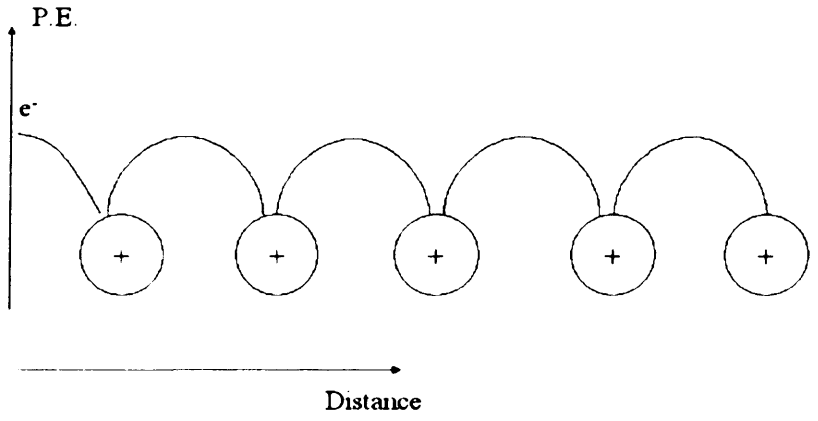

Figure 3.6. Potential energy of electrons as a function of distance through a solid.

The potential energy of the electrons passes through a minimum at the positions of the nuclei, due to coulombic attraction, and passes through a midway point between adjacent nuclei. With the solution of the Schrödinger equation for a periodic potential function an uninterrupted continuum of energy levels does not occur but, only certain bands or ranges of energies are permitted for the electrons. Subsequently, the density of states diagrams shows discontinuities (figure 3.7).

Similar conclusions about the existence of energy bands in solids are obtained either from both the molecular orbital and periodic potentional approaches. From both theories, a similar model exists with bands of levels for the valence electrons. In some materials, overlap of different bands occurs. In others, a forbidden gap exists between energy bands.

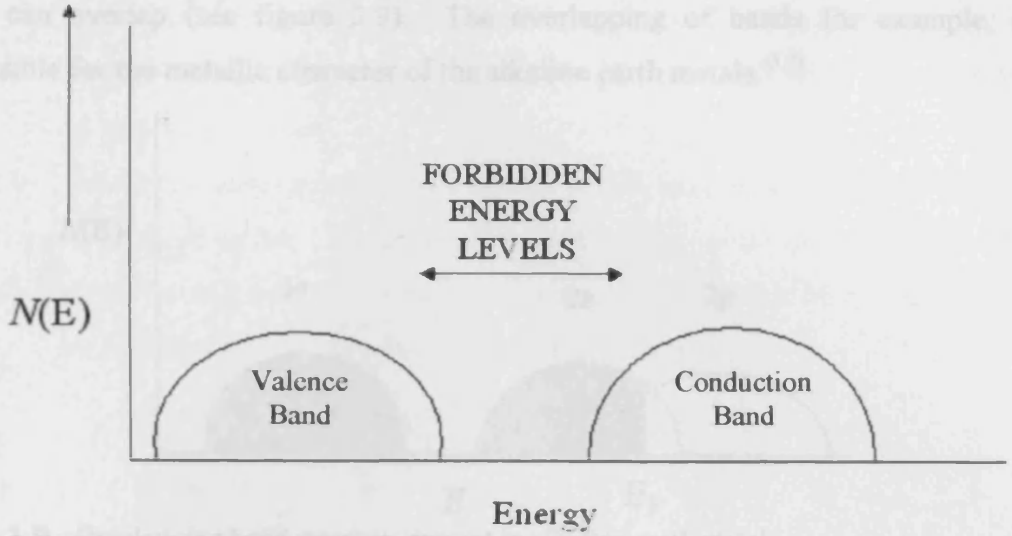

Figure 3.7. Density of states based on band theory.

3.2.3 Band structure of metals, insulators and semiconductors

Metals are characterised by a band structure in which the valence band is only partially full.[7,10] For conduction to occur, the electrons have to have enough energy to move to a vacancy in another energy level. For this reason conduction does not occur in filled bands as the electrons have nowhere to move to. Some levels lying just below the Fermi level are vacant whereas some above the Fermi Level are occupied (Figure 3.8).

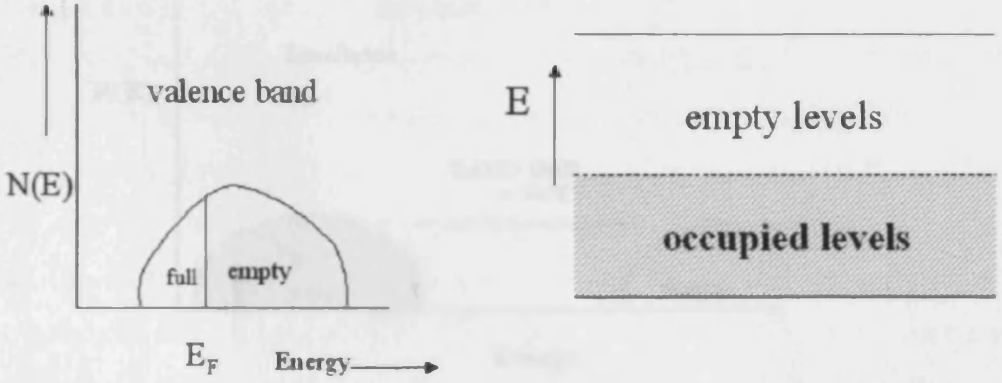

Figure 3.8. Density of states for a metal. The highest occupied band, the valence band, is only partly full. The shading shows the occupied levels schematically.

The electrons in singly occupied states close to the Fermi Level are able to move thus causing the high conductivity in metals.[5] This means very little energy is required to move an electron to a new level. Movement of an electron also results in a vacancy, or hole, in the level it has just moved from. In some metals the energy

bands can overlap (see figure 3.9). The overlapping of bands for example, is responsible for the metallic character of the alkaline earth metals.[3,7]

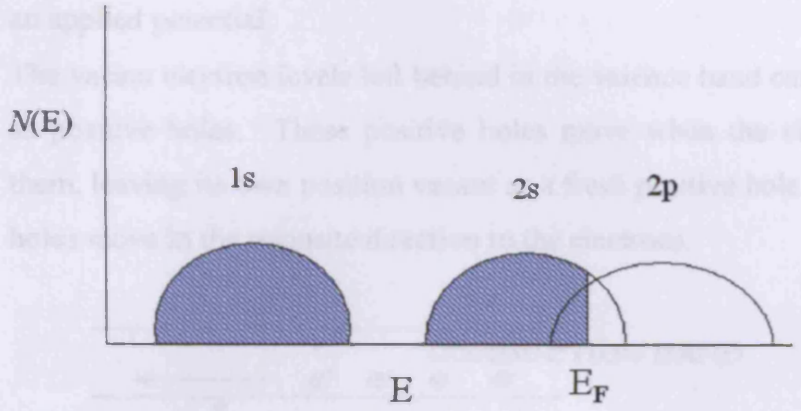

Figure 3.9. Overlapping band structure present in alkaline earth metals.

The valence bands of insulators are full and the conduction band empty. The two are separated by a large, forbidden gap from the next energy band, which is empty (see figure 3.10). The band gap of Diamond for example is ~ 6eV, thus making it an excellent insulator. Very few electrons from the valence band have sufficient thermal energy to be promoted into the empty band above, therefore the conductivity is negligibly small.

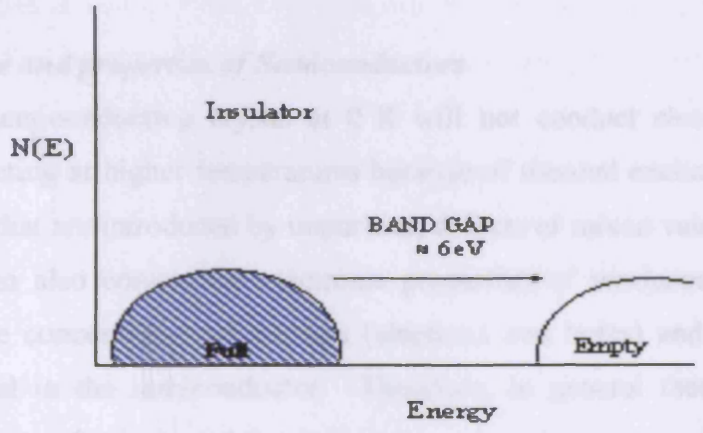

Figure 3.10. Band structure of an insulator i.e., diamond.

Although semiconductors have a band structure similar to that of insulators, the band gap is not as large, usually in the range 0.5 to 3.0eV. This smaller band gap as shown in figure 3.11 below, therefore allows some electrons with sufficient energy to be promoted into the empty band. As a result of this two types of conduction mechanisms exist in semiconductors;

- Any electrons that are promoted into the conduction band are regarded as negative carriers moving towards a positive electrode when placed under an applied potential.
- The vacant electron levels left behind in the valence band can be regarded as positive holes. These positive holes move when the electron enters them, leaving its own position vacant as a fresh positive hole. Effectively, holes move in the opposite direction to the electrons.

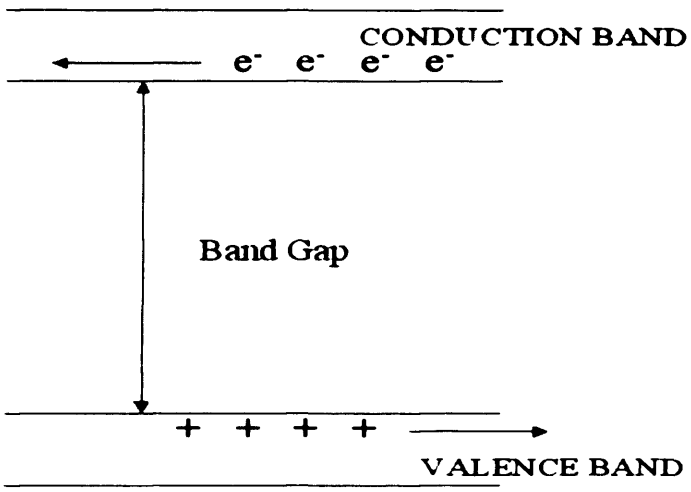

Figure 3.11. Positive and negative charge carriers present in semiconductors.

3.3 Nature and properties of Semiconductors

A semiconducting crystal at 0 K will not conduct electricity. It becomes semiconducting at higher temperatures because of thermal excitations over the small band gaps that are introduced by impurities, defects or mixed valence.[11] Doping the material can also control the electronic properties of semiconductors.[2,3] Doping controls the concentration of carriers (electrons and holes) and the position of the Fermi Level in the semiconductor. Therefore, in general there are two types of semiconductors, Intrinsic and Extrinsic.

3.3.1. Intrinsic and Extrinsic Semiconductors

A semiconductor in its pure state, where holes and electrons are created solely by thermal excitation across the energy gap is called an *intrinsic* semiconductor. The Fermi level is essentially halfway between the valence and conduction bands. Although at 0 K no conduction occurs, as shown in figure 3.12a. By increasing the

temperature a finite number of electrons can now reach the conduction band this is illustrated in figure 3.12b. The concentration of electrons and holes must always be identical as thermal excitation of an electron creates a corresponding hole. The number of electrons (n), which may be in the conduction band, can be controlled in two ways either by the magnitude of the band gap present in the material or by the temperature.[3,7]

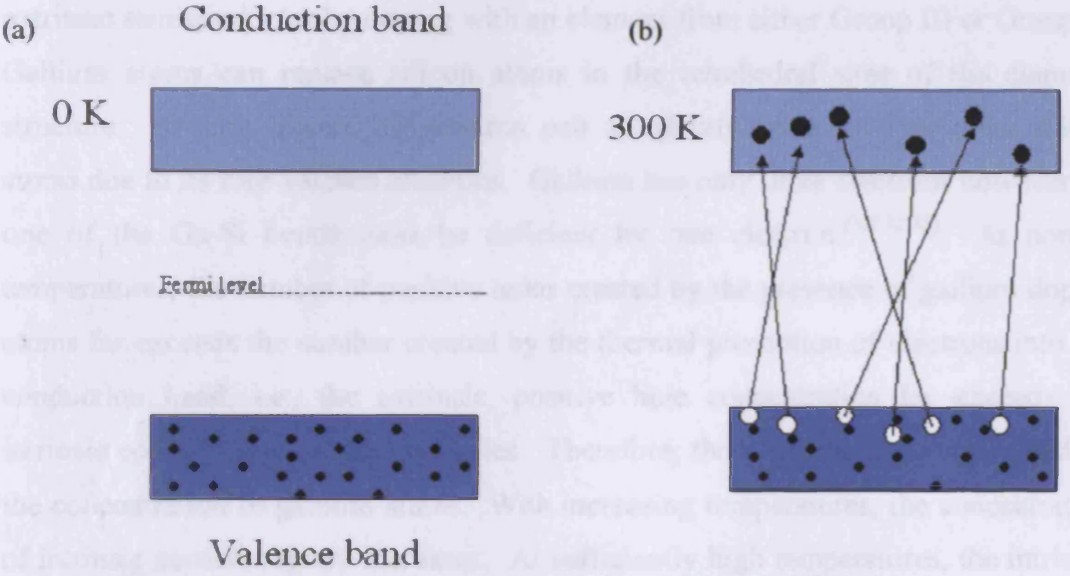

Figure 3.12. An Intrinsic semiconductor at (a) 0 K and (b) 300K.[12]

Elements and compounds which are not semiconducting in the pure state can be made semiconducting by doping, these types of semiconductors are known as *extrinsic semiconductors*. Doping involves removing a very small amount of the lattice element and replacing with another element that contains either fewer or more electrons per atom. The doping element must have energy levels similar to those of the host. Two forms of extrinsic semiconductors may be formed in this way.

3.3.2 p-type and n-type semiconductors

If a foreign atom, which contains fewer electrons than the host semiconductor is implanted into the host semiconductor, the bonds formed between the two atoms will, therefore, be electron deficient. Using band theory it is found that discrete levels or atomic orbitals are formed just above the top of the valence band as illustrated in figure 3.13a. This level is known as the acceptor level as it is capable of accepting an electron. The Fermi Level is shifted to a point halfway between the acceptor levels and the valence band. The gap between the acceptor levels and the top of the valence band is ~ 0.1eV. Therefore, electrons from the valence band may have sufficient

thermal energy to be promoted readily to the acceptor levels. It is not possible for electrons in the acceptor levels to contribute to conduction. The positive holes that are left behind in the valence band are able to move, however, a positive hole can only move when an electron moves into it leaving its original site vacant as a fresh positive hole, the doped semiconductor is known as a *p-type semiconductor*.[3-7,9,11-13]

Silicon, which is an intrinsic semiconductor, can be converted into an extrinsic semiconductor by doping with an element from either Group III or Group V. Gallium atoms can replace silicon atoms in the tetrahedral sites of the diamond structure. In pure silicon, the electron pair covalently bonds to four other silicon atoms due to its four valence electrons. Gallium has only three electrons however, so one of the Ga-Si bonds must be deficient by one electron.[3,7,12,13] At normal temperatures, the number of positive holes created by the presence of gallium dopant atoms far exceeds the number created by the thermal promotion of electrons into the conduction band, i.e., the extrinsic, positive hole concentration far exceeds the intrinsic concentration of positive holes. Therefore, the conductivity is controlled by the concentration of gallium atoms. With increasing temperatures, the concentration of intrinsic carriers rapidly increases. At sufficiently high temperatures, the intrinsic carrier concentration may exceed the extrinsic value, in which a change over to intrinsic behaviour would be observed.

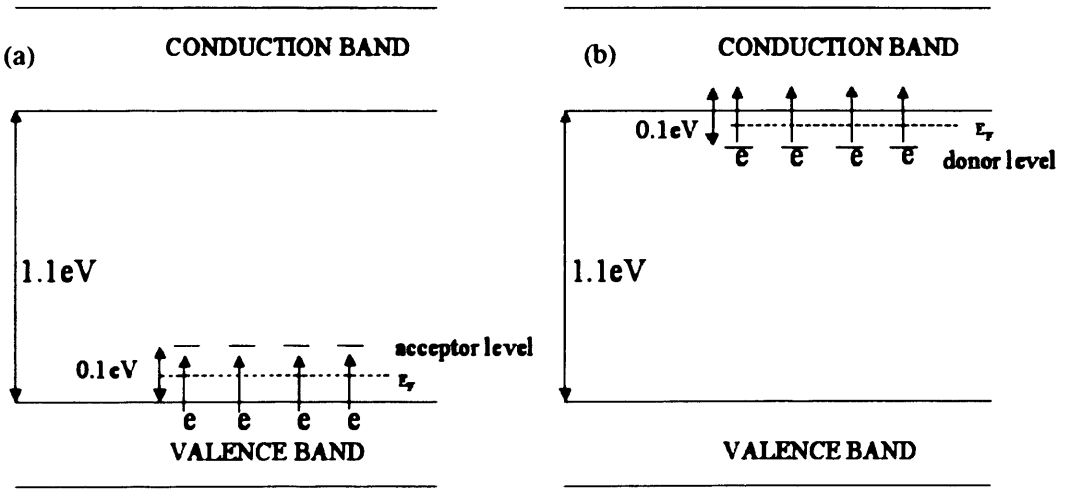

Figure 3.13 Representation of the two types of semiconductors. (a) a p-type semiconductor (b) an n-type semiconductor.[3,7]

In the second case a dopant with extra electrons may be added to the host semiconductor. The extra electron occupies a discrete level that lies 0.1eV below the

bottom of the conduction band. Again the Fermi Level is adjusted this time to lie between the donor levels and the conduction band (figure 3.13b). These levels can act as donor levels as the electrons have sufficient thermal energy allowing them to be elevated up into the conduction band where they are free to move. Such a material is known as an *n-type semiconductor.*[3-7,9,11-13] Silicon can also be converted to an n-type semiconductor, when a phosphorus atom is substituted for a silicon atom; four out of its five electrons are used up in pairing with electrons of the neighbouring silicon atoms. The other electron is weakly attracted to the phosphorus as it has more positive charge than silicon, but otherwise it is free to float around and carry electric current. The more phosphorus-atom impurities present, the more conduction electrons, which results in a higher electrical conductivity of the silicon.[9,4,12]

3.3.3. Differences between Intrinsic and Extrinsic Semiconductors

Extrinsic semiconductors have higher conductivities than similar intrinsic ones at normal temperatures. Controlling the concentration of doping can accurately control the extrinsic semiconductors conductivity. Materials with desired values of conductivity may, therefore, be designed. With intrinsic semiconductors, the conductivity is very dependant on temperature, stray impurities and band gap size.

The thermal excitation of electrons is governed by the Fermi-Dirac distribution function.[9] At low temperatures the E_F represents the boundary between filled and empty levels and so in a non-metallic solid must therefore lie in the gap between the valence and conduction bands. In a pure solid the density of states in the valence and conduction bands are assumed to be equal; the Fermi level is therefore placed midway in the energy gap.

$$E_F = (E_V - E_C)/2 \qquad (3.5)$$

An n-type semiconductor has more electrons in the conduction band than holes in the valence band, the extra electrons or in the case of the p-type semiconductor extra holes cause a shift of the Fermi level away from its ideal mid gap position as shown in figure 3.14.

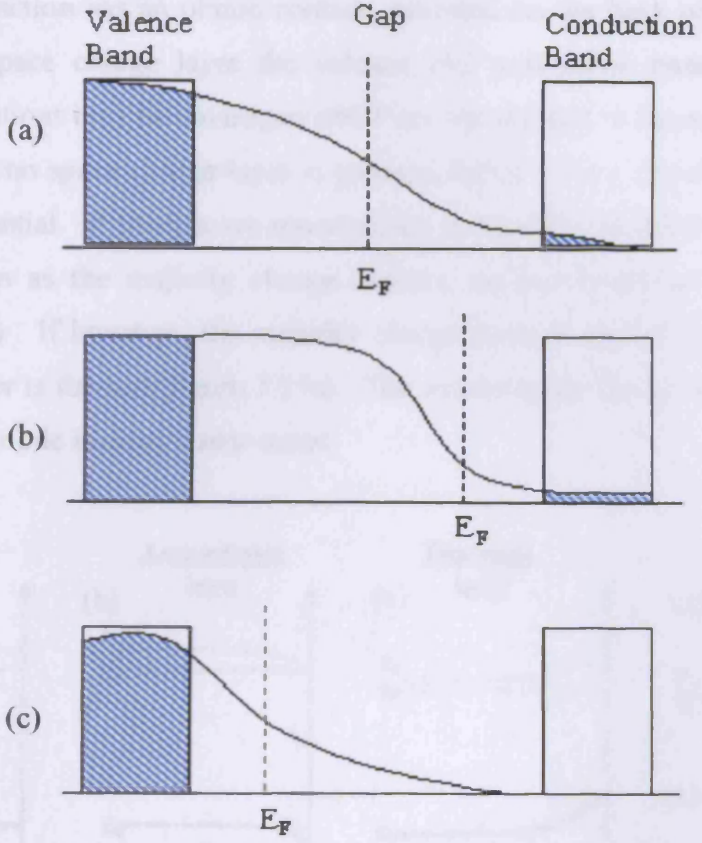

Figure 3.14. Fermi-Dirac distribution in different types of semiconductors: a) pure solid, b) n-type and c) p-type semiconductors. (Shading represents occupied levels).[6]

3.3.3 Band bending at semiconductor surfaces

Contact between a semiconductor and another phase generally involves a redistribution of electric charges and the formation of a double layer.[14] The position of the Fermi level is usually controlled by the energy levels introduced by doping in the bulk of a semiconductor. The position of the Fermi level may not be the same at the surface compared to the bulk due to energies of the surface states linked with defects or adsorbates.[6] The Fermi level however, is the same throughout a solid in equilibrium. It is therefore the band energies themselves that are different at the surface. The transfer of mobile charge carriers between semiconductors and the contact phase at the surface interface produces a space charge layer.

The transfer of mobile charge carriers between the semiconductor and electrolyte leads to the generation of a space charge layer.[14] The charge transfer can take place directly across the semiconductor solution surface when the electro-active species is present in the electrolyte. In the absence of a suitable redox couple in solution, the semiconductor can be polarized by applying an external bias voltage

across the function *via* an ohmic contact, mounted on the back of the electrode.[15] Within the space charge layer the valence and conduction bands are bent, four different situations may be envisaged which are represented in figures 3.15a-d.[14-16]

When no space charge layer is present (figure 3.15a), the electrons are at the flat band potential. If charges are accumulated at the semiconductor side, which have the same sign as the majority charge carriers, an accumulation layer is obtained (figure 3.15b). If however, the majority charge carriers deplete into the solution, a depletion layer is formed (figure 3.15c). The excess space charge within this layer is given by immobile ionised donor states.

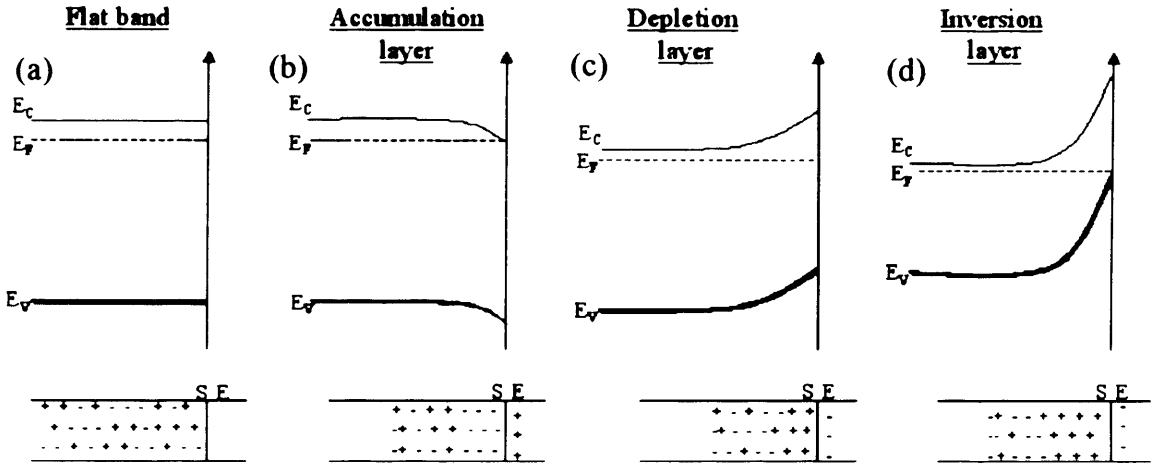

Figure 3.15. Space charge layer formation at the n-type semiconductor interface. (a) Flat band situation, (b) accumulation layer, (c) depletion layer and (d) inversion layer.[14-16]

The depletion of majority carriers can go so far that the concentration at the surface decreases below the intrinsic level. If the electronic equilibrium is maintained, the concentration of holes in this region of the space charge layer exceeds that of the electrons. The Fermi level is then closer to the valence band than the conduction band and the semiconductor is p-type at the surface and n-type in the bulk, i.e., inversion layer (figure3.15d).[14-16]

For p-type materials, analogous considerations apply, whereby the holes are the mobile charge carriers. This leads to the negatively charged acceptor states forming the excess space charge within the space charge layer, and the bands bend down.[15]

3.4 Applications of Semiconductors.

3.4.1 p-n junctions

The fundamental components of solid-state devices such as transistors, silicon chips, photocells, etc., are provided by the use of semiconductors in devices. A simple example is that of the *p-n junction.*[3,4,6,7,10] Diffusing a doped semiconductor of one type into a semiconductor layer of another type forms a p-n junction.

If the bands are level, the junction cannot be in equilibrium as the Fermi levels on the two sides are not equal as illustrated in figure 3.16 below. In the absence of an externally applied potential difference a small number of electrons are capable of moving from left to right across the junction however, the band structure then rapidly adjusts itself so that E_F becomes the same on either side.

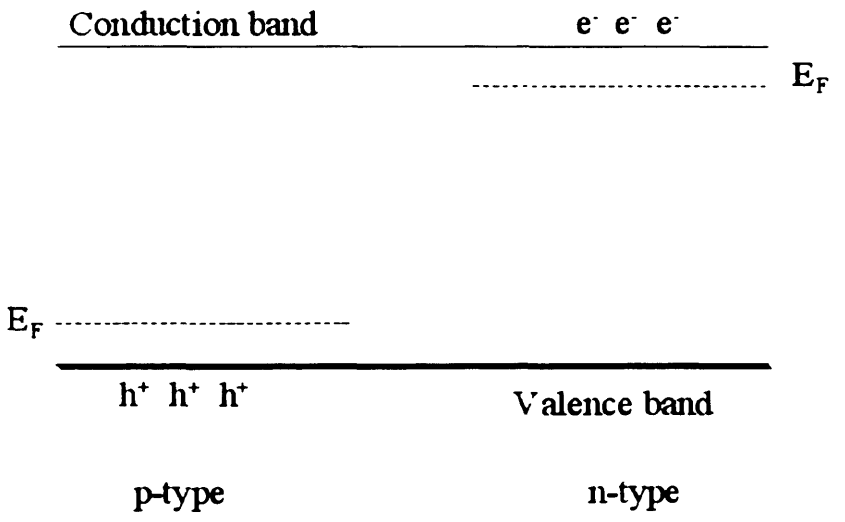

Figure 3.16. *p-n* junction level bands are not in equilibrium because of different Fermi levels in *p* and *n* sides.[3,6]

An alternative explanation is that a space charge layer rapidly develops at the junction as electrons flow across it. The space charge then acts as a barrier to further electron flow by creating a depletion region, this then inhibits any further electron transfer. The electrons, which have migrated from the *n* to the *p* region during the formation of the depletion layer, have now reached equilibrium (figure 3.17).[12] However, if an external potential difference is applied, the situation changes and the p-type end becomes positive while the n-type becomes negative. A continuous current is able to flow through the circuit; electrons enter the crystal from the right electrode. They flow through the conduction band of the *n-type* region, drop into the valence band of the p-type region at the *p-n* junction and then flow finally through the valence band *via* the positive holes, to leave at the left hand electrode. A continuous

current cannot flow in the opposite direction, as, under normal circumstance, with a relatively low applied voltage, electrons cannot surmount the barrier necessary in order to pass from left to right across the junction.

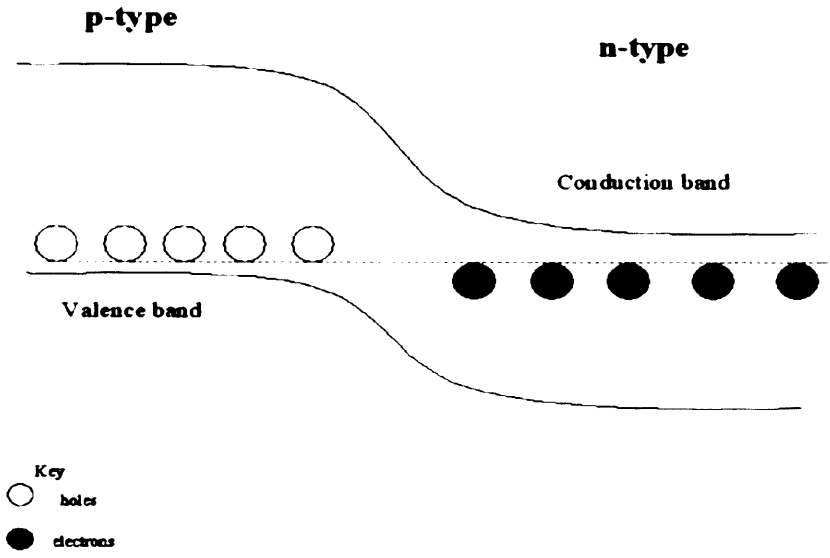

Figure 3.17. p-n junction in equilibrium, with Fermi level constant throughout.[6]

The p-n junction can therefore be characterised as a rectifier,[6] that is the current may only pass in one direction. It may be used to convert a.c.(alternating current) into d.c. (direct current) electricity. Rectification of a p-n junction occurs when a passing current moves more easily in one direction than the other. The depletion of carriers from the junction regions effectively forms an insulating barrier between the two sides. If a positive potential is applied to the n-type side, more carriers are removed which in turn causes the barrier to become wider this situation is known as a reverse bias[6,12] and is shown in figure 3.18a.

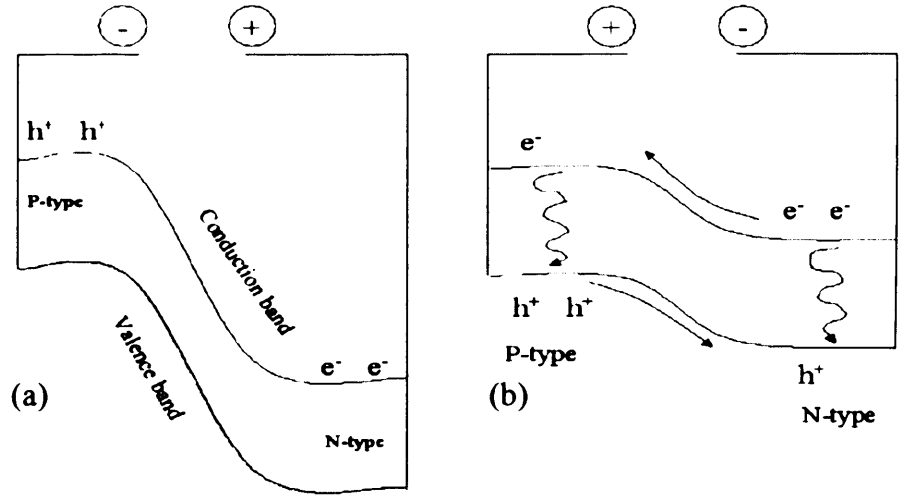

Figure 3.18. Rectification of p-n junction under (a) reverse bias, and (b) forward bias mode.[6]

When a negative potential is applied to the n-type side the energy barrier for the electron and holes at the junction decreases, the carriers may now flow through the junction this is known as a forward bias[6,12] and is represented schematically in figure 3.18b. Electrons passing into the p-type semiconductor recombine with holes, and the same occurs with holes reaching the p-type side.

The recombination of electrons and holes can occur under two mechanisms, the first being non-radiative in which the energy of recombination passes into lattice vibrations and so appears as heat. The second is radiative whereby a photon is emitted, with the corresponding energy to the band gap of the semiconductor. In some semiconductors made of doped silicon, the recombinations are non radiative. Whilst in other semiconductors a fair proportion of radiative recombination occurs. This type of recombination can also occur at impurity sites. Radiative recombination occurring in p-n junctions can act as light emitting diodes (LEDs), as they are capable of emitting light when current is passed under forward bias conditions.[6,9] Some light emitting semiconductor junctions can also act as lasers where recombination of electrons and holes are stimulated by incoming photons.

The photovoltaic effect[4,6] is the reverse of light emission; these are used in simple solar cells. Photons with energy greater than the band gap of a semiconductor can be absorbed to produce holes and electrons. These usually recombine but when light is adsorbed in a p-n junction, the slope of the bands causes the electrons and holes to move in opposite directions resulting in separation as shown in figure 3.19. Electrons pass to the n-type, and holes to the p-type, preventing recombination. The carriers can be collected by metal electrodes at either end and used to do work in an electrical circuit (figure 3.19).

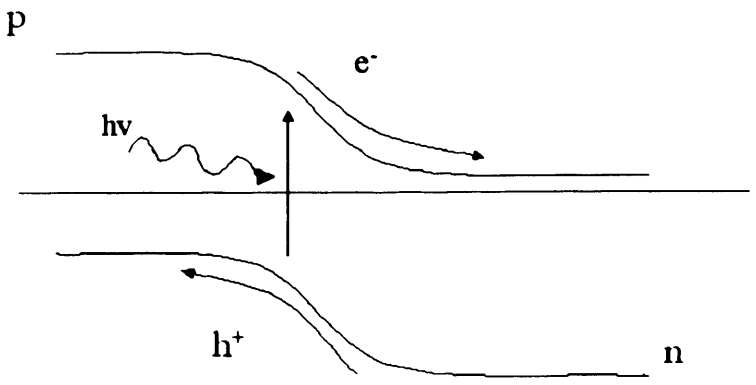

Figure 3.19. Photovoltaic effect. Electrons and holes produced by absorption of light in the junction and separation by band bending.[6]

When the band bending in the junction corresponds to the normal equilibrium value there is no potential, as the effective energy of electrons and holes reaching each electrode is the same. To do electrical work a potential must be generated, which reduces the band bending in the junction. Some current will flow as long as the potential developed by the cell does not eliminate the bending necessary to separate the carriers. As the equilibrium band bending is determined by the difference of the Fermi levels of the n and p type it is this difference that controls the maximum voltage from a single junction. For a reasonable proportion of photons to be adsorbed the band gap of the semiconductor must be obviously low enough. Most solar cells are made of silicon, which has a band of 1.1 eV, but compound semiconductors can also be used i.e., cadimium selenide with band gap of 1.8 eV.

More complex arrangements are the pnp or npn junction.[3] These can act as a current or voltage amplifier. Controlled valency semiconductors find applications as thermistors, thermally sensitive resistors. In these use is made of the large temperature dependence of the conductivity. Some semiconductors conductivity increases gently with irradiation of light these are photoconductive.[3,4]

3.4.2 Schottky Barrier

In many semiconductor applications, it is the interface between the semiconductor and other medium that is important.[6,14,17] Figure 3.20 shows a semiconductor-metal interface, where the Fermi level has been *pinned* in the middle of the gap, for example by interface states resulting from a chemical reaction between the two solids. This is known as a Schottky barrier; the depletion layer gives rise to rectifying properties similar to those in a p-n junction. Band bending can also be increased by a reverse bias, when the n-type semiconductor is made positive, as shown in figure 3.20.

Only under a forward bias can easy conduction occur, this reduces the energy barrier needed for electrons to flow from the semiconductor to the metal. Schottky diodes are often used, for high-frequency applications, as they possess a faster response than ones with p-n junctions.

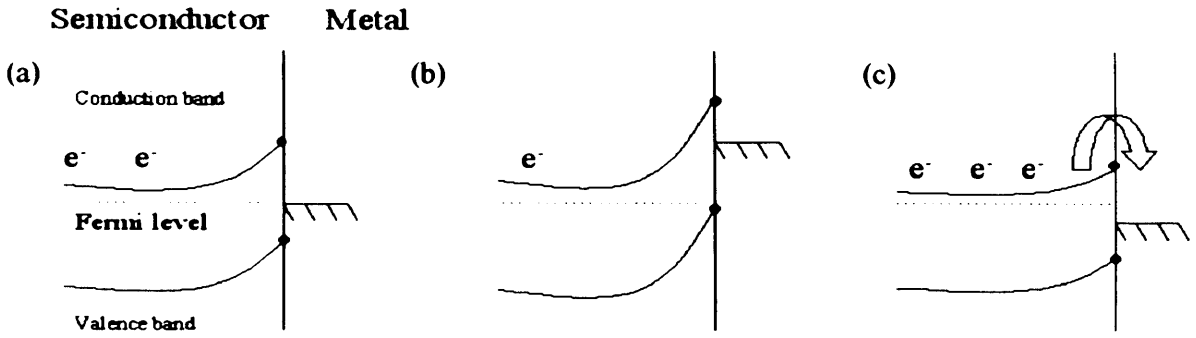

Figure 3.20. Schottky barrier formed by metal semiconductor interface. (a) equilibrium, (b) reverse bias- no current flows, (c) forward bias decreases barrier to prevent current flow.[6]

3.4.3 MOSFET

One of the most important switching devices in integrated circuits is the MOSFET: the metal-oxide-semiconductor-based field-effect transistor,[6] shown in Figure 3.21. An n-type material separates two regions of p-type silicon, which form the source and the drain. Current between the source and drain is normally blocked, since one of the p-n junctions must be under reverse bias. However, when a negative potential is applied to the insulated metal gate, the bands at the surface are bent upwards. In the case of Silicon, which possesses a band gap of 1.1eV, a bending of 1eV is sufficient enough to push the valence band edge up close to the Fermi level, so as to produce a surface inversion layer with some p-type carriers. This allows current to flow between the p-type regions, and therefore switches on the MOSFET. Only a small surface charge is required to produce a significant band bending, and it is possible to couple a field effect transistor to various chemical reactions that involve a charge separation.

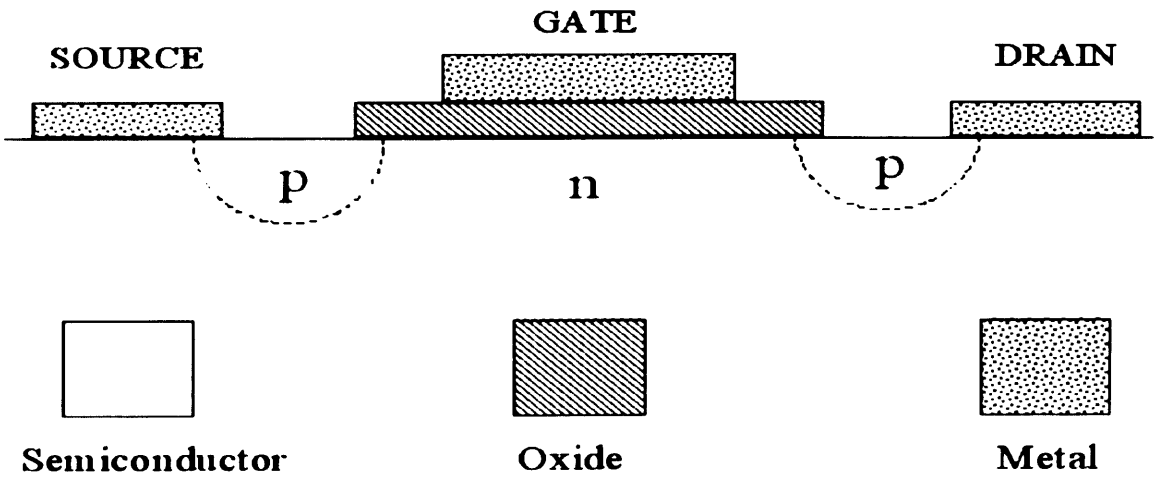

Figure 3.21. Schematic representation of a MOSFET circuit.[6]

3.4.4 Photoelectrochemistry

When considering the electrochemical interface between a semiconducting electrode and an electrolyte solution it is often found that the position of the semiconductor band edges at the interface are fixed as in the Schotty barrier. The surface Fermi level and band bending can be altered by varying the potential of the semiconductor with respect to the reference electrode. The potential where there is no band bending is known as the flat-band potential. This is important as it provides energies of the semiconductor valence and conduction bands relative to the redox processes in solution.

Band bending at the semiconductor electrolyte interface is important in photo-electrochemistry.[6,18] Section 3.4.1 described the action of a simple solar cell, where electrons are generated by adsorption of light are separated by the band bending in the p-n junctions. The same effect is produced by the band-bending present at the surface and is shown in figure 3.22. In an n-type semiconductor, electrons migrate to the bulk and holes migrate to the surface where they produce electrochemical reactions, therefore, acting as the photoanode. A p-type semiconductor acts correspondingly as a photocathode with electrons coming to the surface. As shown in figure 3.22 two semiconductor electrodes from the same cell it is possible to use a metal such as platinum as a counter electrode. When opposite redox processes take place at the two electrodes there is no net chemical reaction but a potential can be generated as in the photovoltaic device.

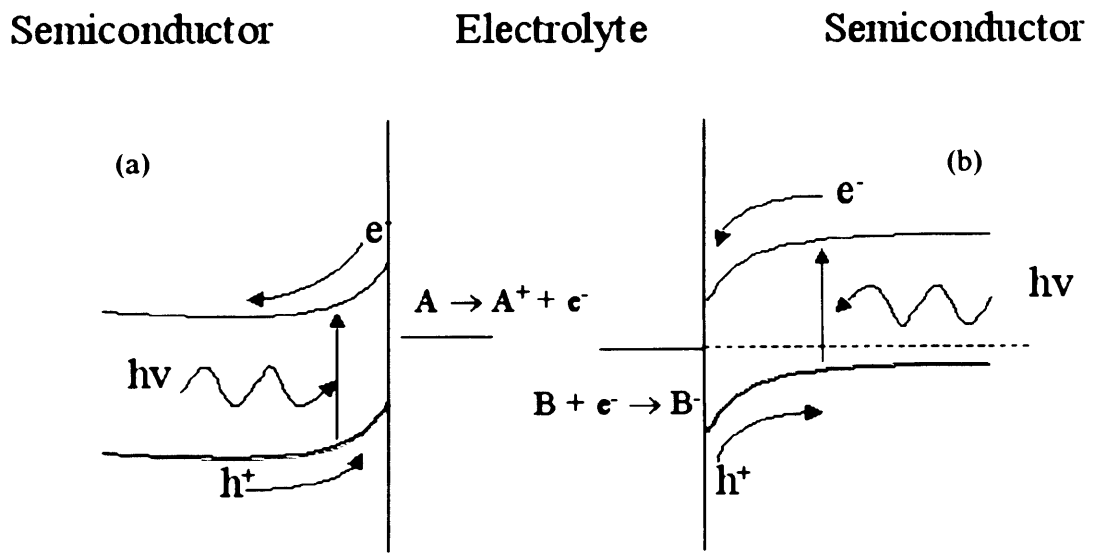

Figure 3.22. Semiconductor photoelectrodes (a) An n-type photoanode, (b) A p-type photocathode. Electrons and holes produced by light absorption separated by the surface band bending.[6]

3.5 Band Structure of Inorganic solids (TiO_2)

Most inorganic materials are more complex structurally than metals and semiconducting elements. Many inorganic solids can also be treated profitably using band theory, whether or not they are regarded as electrical conductors. Band theory can provide an additional insight into the structures, bonding and properties of inorganic solids which complements those results obtained with ionic/covalent models. Inorganic materials have also received less theoretical attention of the type involving band structure calculations. Consequently, their band structures are often known only by approximation.[3]

Due to their high lattice energies, simple oxides can contain defects, however, creation of these defects requires more energy than that for halides. On the other hand, transition elements can have high concentrations of defects under equilibrium conditions. The defects are often associated with deviations from perfect stoichiometry and formed because of the relative ease of reduction or oxidation of the metal ion. Due to the high dielectric constants the electrons or holes are not firmly bound to the defects. Thus, the carriers can be thermally excited into the conduction or valence bands producing semiconducting properties.[6]

n-type behaviour in an oxide is a result of slight reduction, which leaves extra electrons in the solid. This is found in compounds such as ZnO, SnO_2 and TiO_2. Electrons are mobile in the conduction band at higher temperatures but in the ground state the electrons are trapped by the lattice defect. Reduction can be accompanied by formation of interstitial metal atoms, or by oxygen vacancies. An interstitial cation in the lattice will give a positive potential that has the ability to trap an electron in a bound orbital just below the conduction band edge. The unbalanced positive charge at an oxide vacancy also forms a trap.

In understanding the structures of metal oxides, the ionic model is a good starting point.[19,20] The oxygen *2p* acts as the valence band and a conduction band from the metal orbitals. The lowest metal orbitals are normally *d*, rather than *s* as in the pre-transition elements. The *d*-orbitals of the transition metal ions have five-fold degeneracy in the free ions. These different directional properties of the five orbitals produce different bonding interactions with nearby atoms. This is known as crystal-field or ligand-field splitting and is important in all transition metal oxides.

The most common coordination geometry for transition metal ions in oxides is octahedral. The orbitals on the transition metal fall into two groups according to their

symmetry properties. The doubly degenerate e_g orbitals have lobes of maximum density pointing towards the ligand and three t_{2g} orbitals pointing away (see figure 3.23).

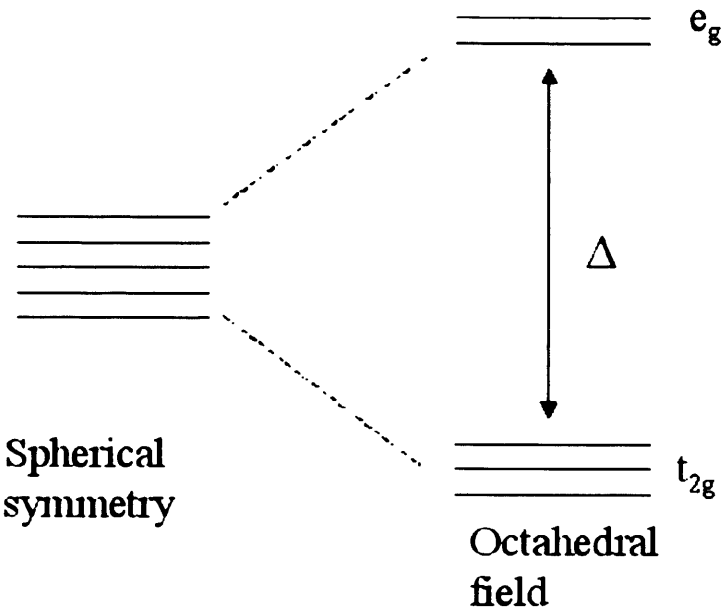

Figure 3.23. The d orbitals of a transition metal ion in an octahedral site resulting orbitals with crystal field splitting.[20]

The extremely wide range of electronic behaviour of transition metal oxides creates difficulties, not just of understanding and interpretation but also of classification. d^0 insulators are stoichiometric oxides, not only are they good insulators, but they show other properties expected of insulators: they have no optical absorptions at photon energies less than the band gap, and are diamagnetic with no unpaired electrons.[19]

The d^0 configuration is associated with the Ti^{4+} of TiO_2 and so has no electrons in the *d* band.[6] This compound has a filled valence band of predominately O 2p character and a gap between this and the conduction band as shown in figure 3.24. The observed gap of ~3.1 eV is fairly small and does suggest an appreciable covalent mixing between the atomic orbitals and metal orbitals. Thus the metal *'d'* conduction band acts as an antibonding combination. The description in terms of oxygen and a metal is useful, as it denotes the principal atomic orbital constituents of each level. Stoichiometric d^0 oxides are therefore good insulators and have no excitations at energies less than the band gap.

Many of the transition metal oxides are relatively easily reduced to form semiconductors. Many d^0 insulators are susceptible to loss of oxygen, which gives

rise to semiconducting properties. Semiconducting properties are in principle a feature of all the 'insulating' oxides but in most cases the band gaps are large enough the intrinsic semiconduction is hard to observe. In practical terms semiconduction is characteristic of defective or non-stoichiometric oxides. These include reduced do compounds such as TiO_{2-x}, non-stoichiometric samples of magnetic insulators such as $Ni_{1-x}O$, as well as oxides with deliberate or inadvertent doping by another element, as in $Li_xMn_{1-x}O$. The relationship between semiconduction and defect structure and chemistry is complex. A qualitative description shows how an electron introduced by chemical reduction can be held in a defect level with an energy slightly below the empty conduction band: thus the formation of an n-type semiconductor (figure 3.24).[19]

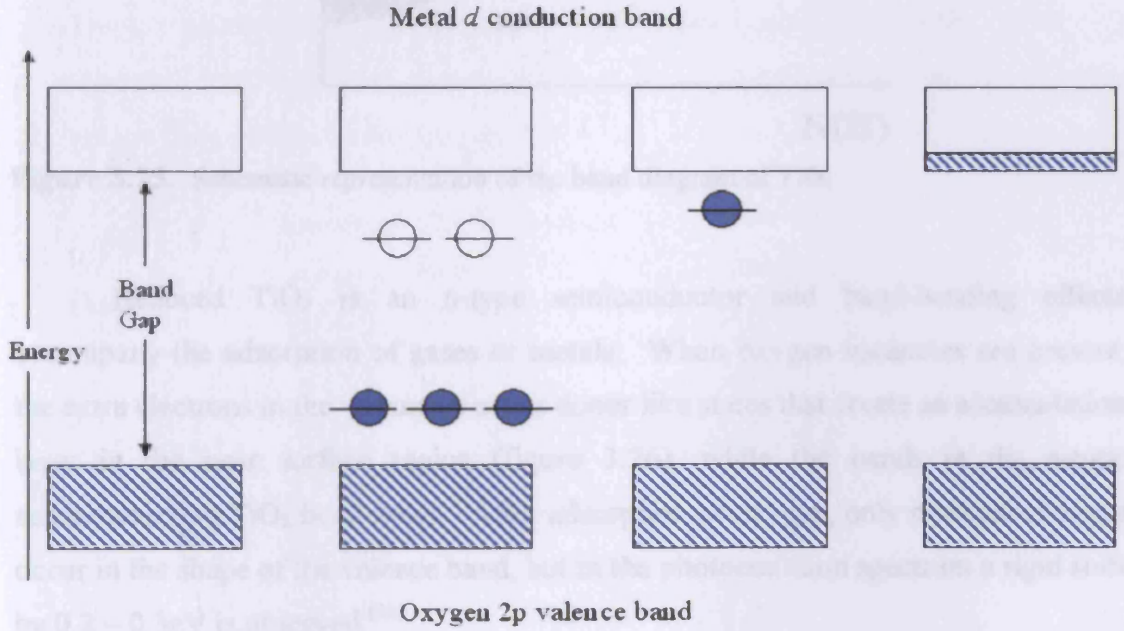

Figure 3.24. Qualitative electron energy-level diagrams for transition metal oxides. (a) bands of a d^0 compound, with a gap between the *'oxygen 2p'* valence band and the empty metal d^n conduction band; (b) the localized d levels appropriate to a transition metal impurity, and to a magnetic insulator; (c) a donor level associated with semiconduction in a non-stoichiometric oxide and; (d) the partially filled conduction band of a metallic oxide.[19]

n-doped TiO_2 is a semiconductor and finds use in liquid junction photovoltaic cells. The band diagram of TiO_2, illustrated in figure 3.25, shows that the O 2p band is full and the 3d (t_{2g}) band empty. The 3d energy levels are delocalised with the lower forming the conduction band. Whereas TiO_2 is an insulator, the compound Ti_2O_3 has one electron in the d band and therefore is metallic in character, at least at

higher temperatures. The electronic nature of a transition-metal compound can be understood in terms of the d electron configuration of the metal atom.[4]

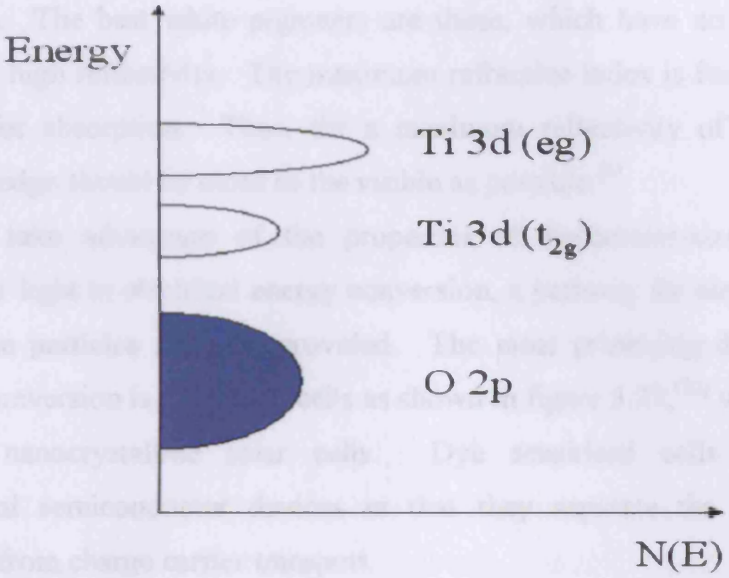

Figure 3.25. Schematic representation of the band diagram of TiO_2

Reduced TiO_2 is an n-type semiconductor and band-bending effects accompany the adsorption of gases or metals. When oxygen vacancies are present, the extra electrons in the vacancies act as donor like states that create an accumulation layer in the near surface region (figure 3.26), while the bands in the n-type semiconducting TiO_2 bend down. After adsorption of oxygen, only minimal changes occur in the shape of the valence band, but in the photoemission spectrum a rigid shift by 0.2 – 0.3eV is observed.[21]

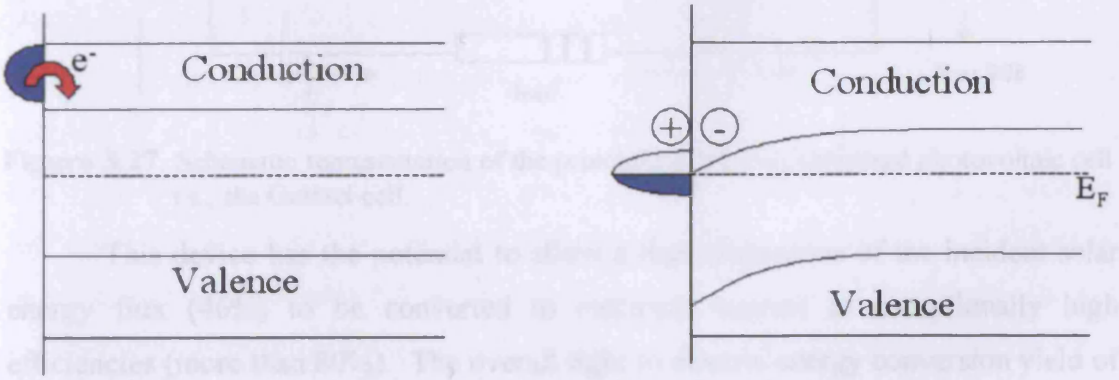

Figure 3.26 Schematic diagram of the band bending effect due to donor like surface defect sites. An accumulation layer is created in the near surface region.[21]

When the band gap is greater than 3 eV, no absorption occurs in the visible, and a good quality crystal will be transparent. Light is scattered however, at crystal flaws and at the crystallite surfaces in a powdered sample, and this leads to a white appearance. The best white pigments are those, which have no absorption in the visible, but high reflectivity. The maximum refractive index is found just below the threshold for absorption. Thus, for a maximum reflectivity of visible light, the absorption edge should be close to the visible as possible.[6]

To take advantage of the properties of nanometer-sized semiconductor particles for light to electrical energy conversion, a pathway for electrical conduction between the particles must be provided. The most promising device for light to electrical conversion is the Grätel cells as shown in figure 3.27,[22] which contains dye sensitised nanocrystalline solar cells. Dye sensitised cells differ from the conventional semiconductor devices in that they separate the function of light adsorption from charge carrier transport.

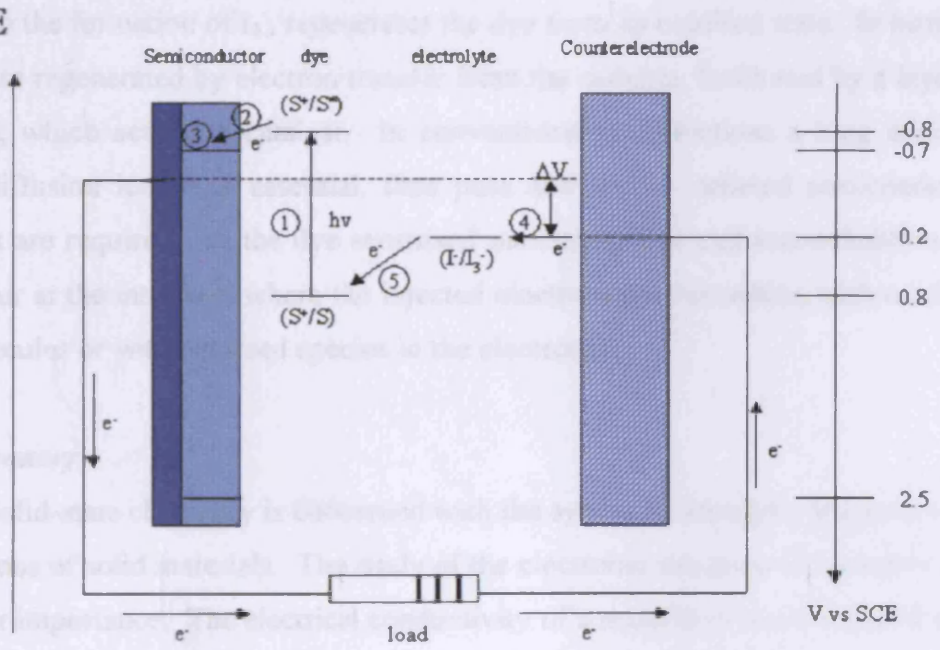

Figure 3.27. Schematic representation of the principle of the dye sensitised photovoltaic cell i.e., the Grätzel cell.

This device has the potential to allow a high proportion of the incident solar energy flux (46%) to be converted to electrical current at exceptionally high efficiencies (more than 80%). The overall light to electric energy conversion yield of 7.1 – 7.9% in simulated solar light and 12% in diffuse daylight cells have been optimised to achieve power conversion efficiencies exceeding 10%.[23] All of which

indicate clearly that dye-sensitised cells had the potential to compete with conventional inorganic thin film photovoltaic cells[24] and thus allowing them to be competitors in the continuing international effort to develop low cost terrestrial photovoltaic cells based on thin film technology.

There are several aspects of the dye sensitised nanocrystalline solar cells that make it novel. The cells are constructed using a high surface area film of nanocrystalline TiO_2 coated onto a conducting glass.[25] The film is sensitised using a ruthenium complex that is adsorbed onto the TiO_2. The role of the ruthenium complex is to absorb the incident sunlight and exploit the light energy to induce a vectorial electron transfer reaction. The photoexcited dye electrons are transferred from the HOMO to the LUMO band of the dye, the latter lying just above the conduction band of the TiO_2, and then into the TiO_2. The non-aqueous electrolyte contains the I_3^-/I^- couple, and the sandwich cell is completed by sealing on a second glass plate coated with a thin layer of platinum. Electron transfer from the I^- ions, leading to the formation of I_3^-, regenerates the dye from its oxidised state. In turn, the I_3^- ions are regenerated by electron transfer from the cathode, facilitated by a layer of platinum, which acts as a catalyst. In conventional p-n junctions a long minority carrier diffusion length is essential, thus pure and well – ordered semiconductor materials are required. In the dye sensitised nanocrystalline call recombination can only occur at the interface, where the injected electrons can recombine with oxidized dye molecules or with oxidized species in the electrolyte.

3.6 Summary

Solid-state chemistry is concerned with the synthesis, structure, properties and applications of solid materials. The study of the electronic structure of the solids is of particular importance. The electrical conductivity of a material is characterised by the number of free charge carriers (i.e., electrons) available to allow passage of an electric current. As demonstrated the electronic structure of metals, semiconductors and other solids can be described in terms of the band or zone theory. Conduction electrons are delocalised in the valence shell, therefore, in a conductor there is a high number of free electrons. An insulator is characterised by having close to zero free conduction electrons. Semiconductors are classified as materials with charge carrier numbers intermediate between conductors and insulators, as they allow limited passage of an electric current. Semiconductors can be classified into two groups i.e.,

intrinsic and extrinsic. While intrinsic semiconductors are pure forms of semiconductors and their conductivity controlled by the magnitude of the band gap and the temperature, extrinsic forms of semiconductor are materials whose conductivity are controlled by the addition of dopants. Two types of extrinsic semiconductors may be formed (i.e., *n* and *p* doped) and the nature of the dopant material controls the formation of these semiconductors. Solid-state devices such as transistors, silicon chips, photocells, etc., use semiconductors in their devices. A basic component of these solid-state devices is the use of extrinsic semiconductors in the form of *p-n junctions*, detailed applications of these devices have been discussed above.

The focus of this thesis is on metal oxides, which are either insulators or semiconductor. The ability of the metal oxide M_xO_y to be electrically conducting depends on several factors including the identity of M, and the type of crystal system. Different allotropes of the same oxide may vary largely in their electrical properties, in general the more electropositive the metal ion, the lower the conductivity of the solid. TiO_2 with the d^0 configuration may be classed as a *borderline* insulator but can be readily reduced or doped to become an n-type semiconductor as discussed earlier.

3.7 References

1. P. Drude, *Ann. Physik*, **1**, 566, (1900).
2. John P. McKelvey *Solid State and Semiconductor Physics*, (Ed.Robert E. Krieger) Publishing Company, (1966)
3. A.R.West, *Solid Chemistry and its Applications*, Wiley, (1994).
4. Lesley Smart & Elaine Moore, *Solid State Chemistry. An Introduction*, Second Edition, Chapman and Hall, (1996).
5. Sandra Dunn, *Reactions and Characterisation of Solids*, RS.C., 2000.
6. P. A. Cox, *The Electronic Structure and Chemistry of Solids*, Oxford Science Publications, (1987).
7. Anthony R. West, *Basic Solid State*, Second Edition, Wiley, (1999).
8. A. Sommerfield, *Z. Physik*, **47**, 1, (1928).
9. Peter Atkins & Julio de Paula, *Physical Chemistry*, Seventh Edition, Oxford, (2002).
10. Charles Kittel, *Introduction to Solid State Physics*, Sixth Edition, John Wiley & Sons Inc., (1986).
11. Elaine M. McCash, *Surface Chemistry*, Oxford, (2001).
12. http://www.hyperphysics.phy-astr.gsu.edu
13. http://www.chem.boun.edu.tr
14. A. L. Linsebigler, G. Lu, J. T. Yates Jr., *Chem. Rev.*, 95, 735, (1995).
15. Michael Grätzel, *Heterogeneous Photochemical Electron Transfer*, CRC Press, Inc. Boca Raton, Florida.
16. A. Hagfeldt, M. Grätzel, *Chem. Rev.*, **95**, 49, (1995).
17. Kurt W Kolasinbci, *Surface Science – Foundations of Catalysis and Nanoscience*, Wiley, 2002.
18. A. Mills, S. LeHunte, *J. Photochem. Photobiol. A: Chem.*, **108**, 1, (1997).
19. P. A. Cox, *Transition Metal Oxides, an Introduction to the Electronic Structure and Properties*, Internal Series of Monographs of Chemistry 27, (1995).
20. V. E. Henrich & P. A. Cox *The Surface Science of Metal Oxides*, Cambridge, University Press, (1994).
21. U. Diebold, *Surf. Sci. Reports*, **48**, 53, (2003).
22. B. O'Regan, M. Gratzel, *Nature*, **353**, 737, (1991).

23. M. K. Nazeeruddin, A. Kay, I. Rodicio, R. Humphrybaker, E. Muller, P. Liska, N. Vlachopoulos, M. Gratzel, *J. Am. Chem. Soc.*, **115**, 6382, (1993).
24. L. M. Peter, N. W. Duffy, R. L. Wang, K. G. U. Wijayantha, *J. Electroanalytical Chem.*, **524**, 127, (2002).
25. N. W. Duffy, L. M. Peter, R. M. G. Rajapakse, K. G. U. Wijayantha, *Electroechem. Comm.*, **2**, 658, (2000).

Chapter 4

Brief Overview of the Electron Paramagnetic Resonance (EPR) Technique

4.1 Introduction

Electron Paramagnetic Resonance (EPR) is a powerful tool for investigating paramagnetic entities in the fields of chemistry, physics and biology. The limitation of the technique is that all diamagnetic systems are excluded from EPR investigations. This limitation however, can also be an advantage as, for example, reactive paramagnetic intermediates present in complex media or paramagnetic centres belonging to a complex chemical system (e.g. a paramagnetic ion in a protein) can be studied without any spectroscopic interference.

The first EPR spectrum in Kazan (USSR) in 1945 after the Second World War had catalysed the development of microwave techniques to be employed for radar, by E. Zavoinski,[1] whilst studying $CrCl_3$ in 1945. The technique was mostly developed however at Oxford from both a theoretical, (by Pryce and Abragam), and an experimental, (by Bleany), point of view with its foundations being in the earlier magnetic susceptibility work of Van Vleck.[2]

Much of the fundamental physics and spin relaxation theory behind EPR is essentially the same as that for Nuclear Magnetic Resonance (NMR) and thus the EPR technique shall be briefly outlined in this section, with an introduction to the basic principles of EPR with emphasis on solid state EPR (powder EPR). For a more detailed account of the physics behind EPR see Giamello and Che.[1] For an overview of the principles of single crystal, solution and powder-type EPR, see the numerous and excellent textbooks[3,4] in the subject area of EPR including Atherton,[5] or Weil, Wertz and Bolton.[6]

4.1.1 Basic Principles of the Technique

The properties of the electron

A free electron has a spin angular momentum (**S**), if the component of spin is restricted to one specified direction, the z direction, then the spin angular momentum component can only assume one of two possible values $\pm$ ½. As a consequence the

electron, with virtue of its spin, also processes a magnetic moment μ_s, which is co-linear and anti-parallel to the spin itself[7] and is represented by:

$$\mu_s = -g_e\mu_B\mathbf{S} \qquad (4.1)$$

where, g_e = free electron g value with g_e = 2.0023, μ_B = Bohr magneton (μ_B = em/4πmc where e = electron charge, m = electron mass, c = speed of light) = 9.27 x 10^{-24} J T^{-1} and **S** is the spin angular momentum.

The negative sign arises because of the negative charge on the electron, which results in the magnetic dipole being in opposite direction to the angular momentum vector. For a single unpaired electron two possible spins (Ms = ± ½) produce two magnetic moments of opposing polarity. These two spins are degenerate when in the absence of an applied external magnetic field (and there is no net bulk magnetisation in a paramagnetic substance). The interaction energy, E, of the electron magnetic moment with an externally applied magnetic field is given by:

$$E = -\mu_s\mathbf{B} \qquad (4.2)$$

where, E = the energy, and B = the applied field (or magnetic flux density, in units of Tesla(T) or Gauss(G)). In quantum mechanics, the μ vector is replaced by the corresponding operator, leading to the following Hamiltonian (energy operator):

$$\hat{H} = g_e\mu_B\mathbf{B}.\hat{\mathbf{S}} \qquad (4.3)$$

Assuming that B is applied along the z direction ($B_x = B_y = 0$, $B=B_z$):

$$\hat{H} = g_e\mu_B\mathbf{B}.\hat{\mathbf{S}}_z \qquad (4.4)$$

The Hamiltonian in equation 4.4 is referred to as a 'spin Hamiltonian', as it deals only with spin contribution to the energy of the system, for practical reasons it is written as:

$$E = \pm \tfrac{1}{2}\, g_e\mu_B\mathbf{B} \qquad (4.5)$$

For a single unpaired electron Ms = ± ½ this gives rise to two energy levels known as the Zeeman levels, with the difference between them known as the Zeeman splitting. Upon application of an applied magnetic field the degeneracy of the Zeeman level is removed as illustrated in figure 4.1. The lower energy state occurs when the electron magnetic field is parallel with the applied magnetic field (Ms = - ½,

β). The higher energy state occurs when μ_s is anti-parallel to the magnetic field (Ms = + ½, α). Transitions between the two Zeeman levels can be induced by the absorption of a photon of energy *hv* equal to the difference between the two levels. The energy difference between the two states, known as the Zeeman splitting, is given by:

$$\Delta E = g_e \mu_B B = hv \qquad (4.6)$$

where *h* = Planck's constant and *v* = frequency of electromagnetic radiation.

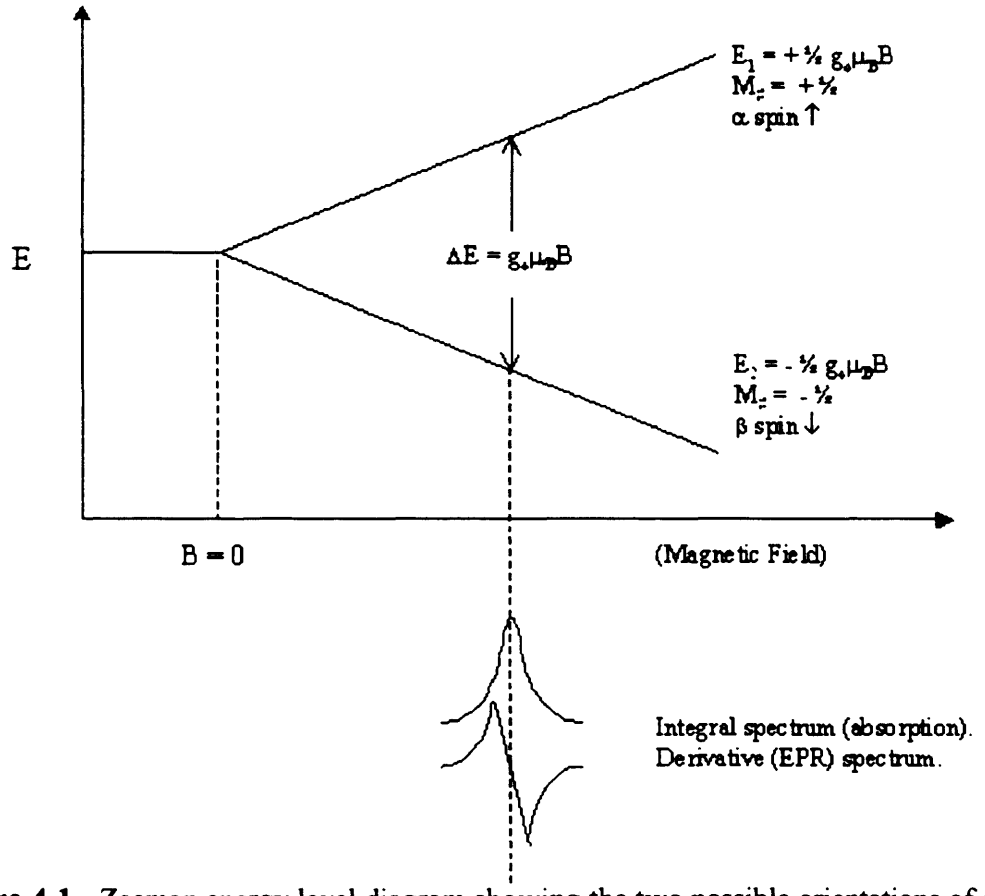

Figure 4.1. Zeeman energy level diagram showing the two possible orientations of spin in an applied magnetic field.[6]

When electromagnetic radiation of energy ΔE is applied to the system resonance occurs to satisfy the above condition for a given magnetic field.[6] In X-band EPR, the frequency is approximately in the GHz region at 0.35 T, and usually operative in a static frequency, swept field mode.

Under the influence of an external applied field, and at thermal equilibrium, the spin population is split between the two energy levels according to the Maxwell – Boltzman distribution law:

$$n_1/n_2 = e^{-\Delta E / kt} \qquad (4.7)$$

where, k = Boltzmann constant (1.381×10^{-23} J K^{-1}), T = the absolute temperature (K), n_1, n_2 = spin population characterised by the M_S values of + ½ and – ½ respectively.

Relaxation Processes

The resonance signal is represented by the energy absorption necessary to promote electrons from lower to upper energy levels (or vice versa). The overall net absorption results from the fact that there are more spins in the lower levels than in the upper. The two-population energy levels, n_1 and n_2, tend to equalise at large microwave powers since application of electromagnetic radiation effectively raises the temperature of the system. This in turn leads to the loss of the absorption and electrons have to dissipate the quantum of energy (*hν*) efficiently in order to return to the lower level. The dissipation process from the excited electron to the ground state is known as relaxation.

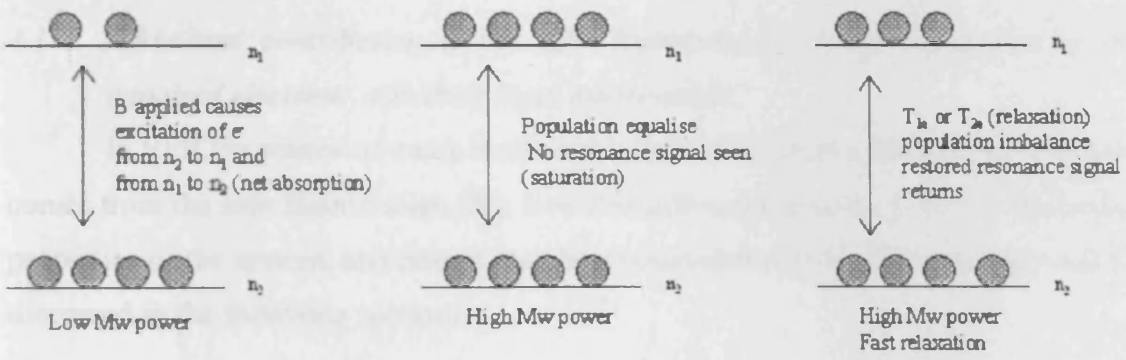

Figure 4.2. The effect of energy absorption and relaxation rate on the population of the energy levels.[7]

To maintain a population excess, electrons in the upper level must be able to return to their low energy state. Therefore they must be able to transfer their excess spin energy either to other species or to the surrounding lattice as thermal energy. The time taken for the spin system to lose $1/e$ of its excess energy is called the relaxation time. There are two types of dissipation mechanisms;

- **"Spin – Lattice" relaxation (T_{1e})**: This process is due to the magnetic energy being dissipated within the lattice as phonons i.e. as vibration, rotational or translational energy. Spin-lattice relaxation is characterised by an exponential decay of energy as a function of time (T_{1e}). The exponential time constant is sensitive to: *(a)* Temperature. A decrease in temperature decreases the

population of phonons and leads to a longer relaxation time and correspondingly narrower lines. *(b)* Presence of nearby excited states. Where these are close ($\approx 100cm^{-1}$) to the ground state the relaxation time will be short and the line width very large.

- **"Spin – Spin" relaxation (T_{2e})**: The excess energy is exchanged between the spins without transfer of energy to the lattice, which is characterised by a time constant (T_{2e}), it possesses a complex relationship with temperature. This mode of relaxation is important when the concentration of the paramagnetic species is high (spins are close together). If the relaxation time is too fast then the electrons will only remain in the upper state for a very short period of time and give rise to a broadening of the spectral line width as a consequence of Heinsenberg's uncertainty principle.

T_{1e} is sometimes referred to as the longitudinal relaxation time and T_{2e} the transverse relaxation time.

4.1.2. Additional contribution to the spin Hamiltonian; Basic interactions of the unpaired electrons with their local environment.

In EPR the source of much structural information from a paramagnetic system comes from the spin Hamiltonian ($\hat{H}$); how this information arises from the molecular properties of the system, and how it may be extracted from the EPR spectrum will be discussed in the following sections.

The g Tensor: Significance and Origin

The energy levels of an electron subjected only to the force of an applied magnetic field were given by the solutions of the simple spin Hamiltonian, eq. 4.4. However, electrons in atoms and molecules are subject to a variety of magnetic interactions, which can shift and split the simple Zeeman levels and thus the effects are reflected in the EPR spectrum. This means that equations 4.4 and 4.6 do not always hold for an unpaired electron belonging to a real chemical system due to the effect of orbital angular momentum, $g \neq g_e$ (free spin value). Orbital angular momentum is non-zero in the case of orbitals exhibiting p, d and f character. The spin therefore is no longer quantified or aligned along the direction of the external magnetic field, and the g value cannot be expressed by a scalar quantity, but by a

tensor value. The orbital angular momentum **L** is associated with a magnetic momentum given by

$$\mu_L = \mu_B \mathbf{L} \qquad (4.8)$$

Considering a system with a doublet (Ms = ± ½) non-degenerate electronic ground state and nuclei with zero nuclear magnetic moment ($\mu_n = 0$) for simplicity, for such a system the interaction with the external magnetic field can be expressed in terms of a perturbation of the general Hamiltonian by:

$$\hat{H} = g_e \mu_B \mathbf{B}\hat{\mathbf{S}} + \mu_B \mathbf{B}\mathbf{L} + \lambda \mathbf{L}\hat{\mathbf{S}} \qquad (4.9)$$

Where, $g_e \mu_B \mathbf{B}\hat{\mathbf{S}}$ = Electron Zeeman term, $\mu_B \mathbf{B}\mathbf{L}$ = Orbital Zeeman term (usually quenched to zero), $\lambda \mathbf{L}\hat{\mathbf{S}}$ = Spin Orbit Coupling and λ = spin orbit coupling constant which mixes ground state wave function with excited states.

Spin orbit coupling is the magnetic interaction which links **L** and **S**, the extent of interaction depends on the nature of the chemical system and the symmetry. If $|\lambda|$ is small, then $g \cong g_e$ (close to free spin $g_e \pm 0.003$) e.g., an organic radical. If $|\lambda|$ is large, then $g \neq g_e$ (large shift from free spin $g_e \pm 5$) e.g., a transition metal ion.

There are two possible ways to measure a g value; either with a reference sample (e.g. DPPH) using the equation;

$$g = g_{ref} B_{ref} / \mathbf{B} \qquad (4.10)$$

or, by using an absolute method, by carefully measured ν and B values directly using an NMR gaussmeter and a frequency meter with the equation

$$h\nu = g \mu_B \mathbf{B} \qquad (4.11)$$

4.1.3 The Hyperfine Interaction, A: Significance and Origin

The hyperfine interaction (A) comes from the interaction between the magnetic moment of the electron with the magnetic moment of a nearby nucleus (B_{local}) therefore equation 4.6 may be modified as shown:

$$h\nu = g_e \mu_B \mathbf{B} + E_{(hyperfine)} \qquad (4.12)$$

The nuclear spin quantum number (**I**) has an associated magnetic moment (μ_N) written as:

$$\mu_n = g_n \mu_N \mathbf{I} \qquad (4.13)$$

where, g_n = nuclear g factor (proton value), μ_N = nuclear magneton value (μ_N is smaller than μ_B by a factor of 1838, i.e. the ratio of the mass of a proton to that of an electron).

The contribution from the magnetic field and the orbital, as well as the contribution from the magnetic field of the nucleus are considered in the complete spin Hamiltonian as shown:

$$\hat{H} = g_e \mu_B \mathbf{B}\, \hat{\mathbf{S}} - g_n \mu_n \hat{\mathbf{I}} + \hat{\mathbf{I}}\, \mathbf{A}\, \hat{\mathbf{S}} \qquad (4.14)$$

Where, $\hat{\mathbf{I}}$ = nuclear spin, **A** = hyperfine term, $\hat{\mathbf{S}}$ electron spin

The interaction between the unpaired electron and a spin active nucleus gives origin to further splitting of the lines in the spectra, (see figure 4.3) which gives the EPR spectrum hyperfine structure. The selection rule for the transitions are $\Delta M_S = \pm 1$, $\Delta M_I = 0$. Two types of electron spin-nuclear spin interactions occur, an isotropic interaction (E_A) and an anisotropic interaction (E_B), which will be discussed in the next section.

$$\Delta E_A = E_1 - E_4 \quad \text{and} \quad \Delta E_B = E_2 - E_3 \qquad (4.15)$$

For a solid state paramagnetic species where the unpaired electron is localised upon a magnetic nucleus, each of the principal g tensor components will be split into 2nI +1 lines, where I is the spin quantum number of the nucleus involved. For each g tensor component, the set of lines (determined by $2nI + 1$) will be spaced by a splitting constant, which corresponds to the appropriate component of the anisotropic coupling, where g_1 is split by A_1, g_2 split by A_2 etc. In powder samples, the EPR spectra often have large linewidths. Consequently some hyperfine detail is sometimes not clearly resolved, and the precise splitting constant remains uncertain.[8]

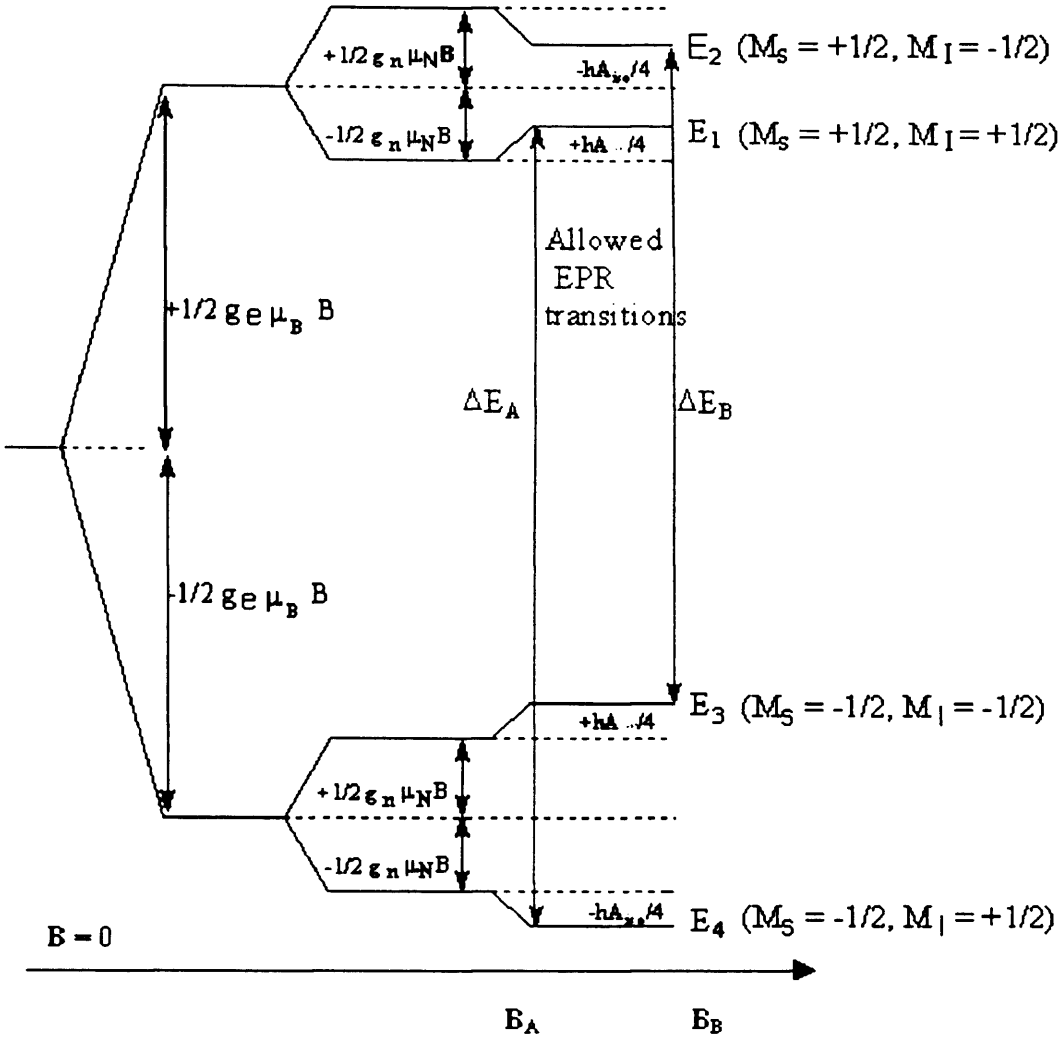

Figure 4.3. Energy level diagram for the interaction of a proton (I= ½) with an unpaired electron (S= ½), in an applied magnetic field.

Isotropic Interaction (a_{iso})

S type orbitals or orbitals with partial s character (such as hybrid orbitals constructed from s-type orbitals) are exclusively the focus of isotropic interaction, and arises from the fact that these orbitals have a probability distribution that includes the nucleus, i.e. there is electron density at the nucleus itself; this is known as the Fermi Contact interaction expected for a 100% s-valence electron. Using the experimentally determined value (a_{iso}) it is possible to calculate the percentage s character to an orbital. Isotropic interactions can be large interactions (electron and nucleus can get close together).[9]

Anisotropic (dipolar) interaction (B)

Anisotropic hyperfine couplings are due to through space dipolar interactions between the nucleus and electron magnetic moments where the unpaired electron is in

non-spherically symmetrical orbitals (p, d, f orbitals). As the orbitals are not spherically symmetric and contain a node (where there is zero electron density at the nucleus), the interaction between them will be small and dependant on the direction of the orbital with respect to the applied magnetic field as well as their separation. B_o is the theoretical anisotropic coupling constant, and as for an isotropic contact, may be used to define the characteristics of the system. Anisotropic interactions have a classic dipolar coupling interaction:

$$E = \mu_s\mu_n/r^3 - 3(\mu_s r)(\mu_n r)r^5 \qquad (4.16)$$

where r is the vector relating the electron and nuclear moments and r is the distance between the two dipoles.

Hybridisation, spin density and bond angles

In a real system, isotropic and anisotropic interactions mix due to hybrid orbitals, and therefore the hyperfine interaction contains contributions from both the isotropic and anisotropic component. It is necessary to analyse the spectrum to obtain values for both a_{iso} and B. The A tensor may be split into an anisotropic and isotropic part as follows:

$$a_{iso} = \frac{(A_\perp + A_\perp + A_\parallel)}{3} \qquad (4.17)$$

And

$$B = a_{iso} - A_\perp \qquad (4.18)$$

The s and p character of the orbital hosting the unpaired electron is written are given by the following relations:

$$C_s^2 = a_{iso} / A_o \qquad (4.19)$$
$$C_p^2 = B / B_o \qquad (4.20)$$

where a_o and B_o are the theoretical hyperfine coupling constants (assuming pure s and p orbitals for the elements under consideration). The extent of hybridisation is given by:

$$\lambda^2 = c_p^2/c_s^2 \qquad (4.21)$$

λ^2 can be used to measure dihedral angles (ϕ) in triatomic molecules.

All triatomic radicals have orthorhombic symmetry and the dihedral angle can be discovered by:

$$\phi = 2\cos^{-1}(\lambda^2+2)^{-½} \qquad (4.22)$$

For tetra-atomic radicals, the dihedral angle is given by:

$$\phi = \cos^{-1}[1.5/(2\lambda^2+2)-½]^{(7)} \qquad (4.23)$$

4.2 Symmetry of real systems

The EPR technique can be applied to materials in a range of various phases and physical states. The very major fraction of the EPR spectra recorded in the solid state does not come from single crystals but polycrystalline materials or powders whose spectra are usually called 'powder' spectra.[1] Polycrystalline materials are composed of numerous small crystallites randomly orientated in space. As many chemical systems of interest are polycrystalline or cannot be prepared easily as single crystals the practical interest in powder spectra in EPR is very high. The resultant powder EPR spectrum is the 'envelope' of spectra corresponding to all possible orientations of the paramagnetic species with respect to the magnetic field. The profile of the powder spectrum depends on the symmetry of the system under study. Several parameters, determine the profile of the powder spectrum, including its symmetry of the *g* tensor, the actual values of its components, and the line shape and the line width of resonance. There are three possible symmetries: Isotropic, Axial and Orthorhombic for a system comprising solely of Zeeman interactions[7] (in the case of orthorhombic, other symmetries are possible for systems with hyperfine interactions e.g., monoclinic).

4.2.1 Isotropic (High symmetry case)

In this case the *g* tensor is characterised by a single symmetrical line (where, $g_{zz} = g_{yy} = g_{xx}$) and arises from systems with perfect cubic symmetry such as octahedral (O_h) and tetrahedral (T_d). This is most commonly seen in low-viscosity solutions, where the g value (termed g_{iso}) is the result of the averaging of the three components, it is however rare in solids see figure 4.4.

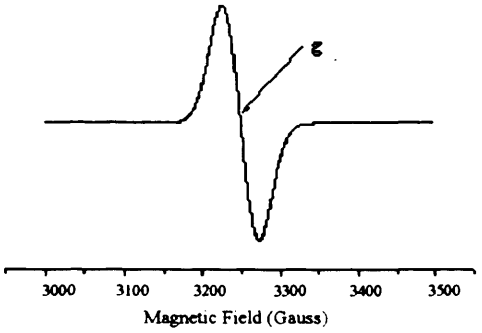

Figure 4.4. Simulated isotropic EPR spectrum

4.2.2. Axial symmetry

When two of the principle g values (x and y) are equal the molecule displays axial *g* values. The unique value is usually designated as $g_{\|}$ (i.e., g_{zz}) '*g parallel*', whilst the other value is $g_{\perp}$ (i.e., $g_{yy} = g_{xx}$), '*g perpendicular*'. In the particular case of axial symmetry of the system, if z is the unique symmetry axis of the species and θ the angle between z and the magnetic field, the x and y directions are equivalent, the angle ϕ becomes meaningless. Systems with uniaxial symmetry such as square pyramidal (C_{4v}) and square planar (D_{4h}) have g tensors in which the x and y values are the same i.e., $g_{zz} \neq g_{yy} = g_{xx}$.

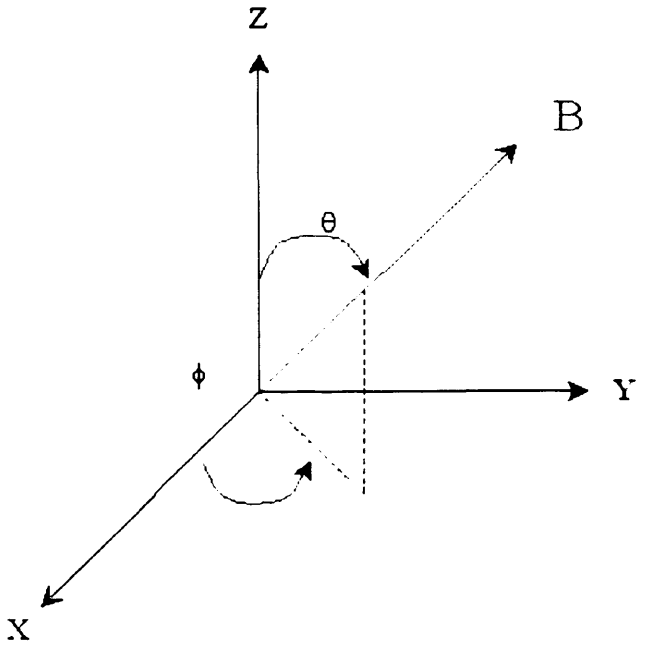

Figure 4.5. Symmetry axis of axial symmetry, where $g_{\perp} = g_x$ and g_y and $g_{\|} = g_z$.[5]

The resonant field may be calculated using the equation:

$$B_{res} = h\nu / \mu_B(g_\perp^2 \sin^2\theta + g_\parallel^2 \cos^2\theta)^{-\frac{1}{2}} \qquad (4.24)$$

$g_\parallel = g_{zz}$ and $g_\perp = g_{yy} = g_{xx}$ are g values measured when the axis of the paramagnetic species is respectively parallel and perpendicular to the applied magnetic field. In an actual EPR spectrum, we only see $g_\perp$ and $g_\parallel$, not $g_\perp^2$ and $g_\parallel^2$. As the powder spectrum is the '*envelope*' of the individual spectra arising from every possible orientation in the whole range of θ and ϕ, provided the crystallites are randomly distributed, simple considerations show that the absorption intensity, which is proportional to the number of the micro crystals at resonance for a given θ value, is a maximum when $\theta = \pi / 2(B_\perp)$ and minimum for $\theta = 0$ $(B_\parallel)$. This allows the extraction of the g values that correspond to the turning points of the spectrum.

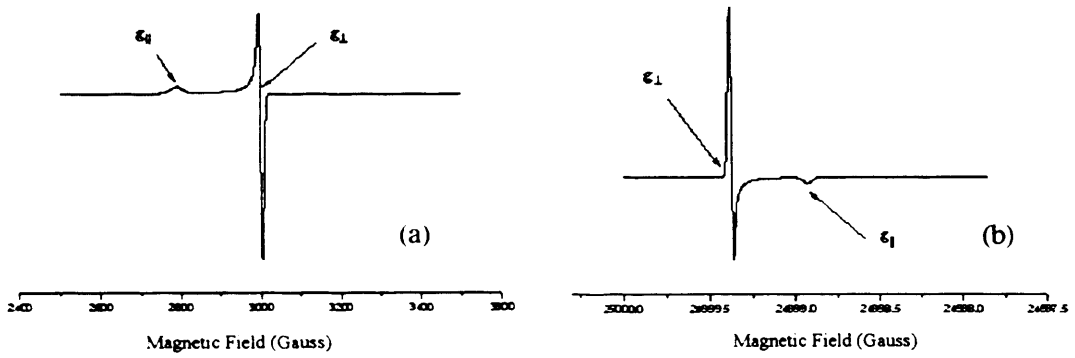

Figure 4.6. Simulated axial EPR spectra where (a) $g_\parallel > g_\perp$ and (b) $g_\perp > g_\parallel$.

4.2.3 Orthorhombic symmetry

Three distinct principal components are expected in the case of a system with orthorhombic symmetry ($g_{zz} \neq g_{yy} \neq g_{xx}$), and arise from systems with point symmetries including angular distorted planar MA_2B_2 (C_{2h}) and XMA_2B_2 square pyramid (C_{2v}). It should be noted that the terms g_{zz}, g_{yy} and g_{xx} should only be used when the orientation of the principal axes with respect to the molecular axes are known. Otherwise, g_1, g_2 and g_3 (A_1, A_2, A_3) are assigned arbitrarily and used when this is not the case.

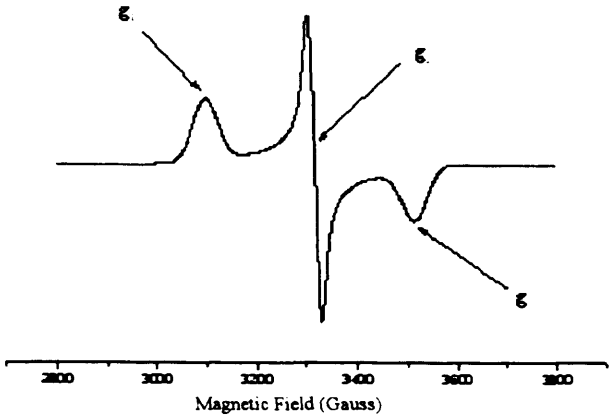

Figure 4.7. Orthorhombic EPR spectrum (no hyperfine interaction).

The relatively simple powder spectra shown in Figure 4.6 and Figure 4.7, become much more complex in the presence of hyperfine interactions. The whole shape of the hyperfine powder spectrum depends on various factors:

- The nuclear spin (I) of the magnetic nucleus (nuclei) interacting with the unpaired electron.
- The isotopic abundance of the magnetic nucleus (nuclei).
- The symmetry of the hyperfine tensor and the values of the various elements of the tensor itself.

4.3 Real Powder EPR Spectra

Interpreting the powder line spectra can prove difficult with various effects that can further complicate the resultant spectra. These effects can include:

- The presence of species that have different (or slightly different) parameters.
- The presence of various nuclei with different nuclear spins.
- The broadening of the lines due to dipolar spin-spin interactions or to motional phenomena that causes loss of resolution.
- Second order effects and/or nuclear quadrupolar effects influencing the regular spacing of hyperfine lines.

4.3.1 Characterisation of Surfaces by Probe Molecules and EPR.

As discussed in chapter 2, a probe molecule is a species whose properties are monitored by EPR when they are in the adsorbed state, providing useful information about the surface. Either the probe molecule itself maybe monitored or the surface

site and the changes of its properties upon adsorption can be monitored. Thus the probe molecule does not have to be paramagnetic itself but the resulting species from the interaction of the probe and the surface must be.[1] The probe molecules employed fall into two different categories:

- Crystal field insensitive – the radical's ground state is non-degenerate and the energy levels are well separated and insensitive to the influence of local crystal fields. Therefore the *g* tensor acts as a fingerprint for the radical. Examples of this type are SO_2^- and CO_2^-.
- Crystal field sensitive – the ground state is usually degenerate so that the surface crystal field removes the degeneracy, splitting the two energy levels proportionally to the intensity of the crystal field. The *g* values are therefore drastically modified. Examples of this type are O_2^- and CO^-

4.3.2 The g Tensor and Transition Metal Ions (TMI's)

A great deal of information may be obtained about the co-ordination features of the transition metal ions/complexes with the EPR parameters. The nature of the central ion, type of bonding with the ligands, co-ordination and symmetry of the surroundings, relaxation mechanism and the type of the motion of the paramagnetic species can also be inferred from the EPR spectra. In particular the g tensor values are characteristic of a given metal complex in a given surrounding (i.e., crystal field symmetry and strength, type of bonding with ligands etc). The crystal field splittings for a d^1 ion (i.e., Ti^{3+}) will be discussed in chapter 5.

4.4 Experimental

4.4.1 Apparatus Vacuum Line

The construction of the line used for the thermal activation of titanium dioxides is shown in figure 4.8. The line is constructed from 12mm bore Pyrex glass tubing. Greased taps were used in order to isolate various parts of the line. Apiezon type T hydrocarbon grease was used to seal all taps and non-fused glass joints. The glass taps were able to maintain pressures of less than 10^{-6} Torr. The line was connected to a two stage Edwards diffusion pump via a liquid N_2 cold trap. Pressure measurements were made with an Edwards active pirani/penning gauge controller.

A thermostatically controlled electric furnace fitted with a chrome-nickel thermocouple, which could maintain stable temperatures between 323 and 1073K, heated samples. Powder samples were heated in the bulb section of the EPR cell, then transferred to the capillary section (4mm bore) for exposure to reagent vapours and gases at 77K. The capillary section of the EPR cell was constructed from quartz to enable in situ UV irradiation. The organic vapour reservoir was used as a mixing chamber for co-adsorption of vapours and gases.

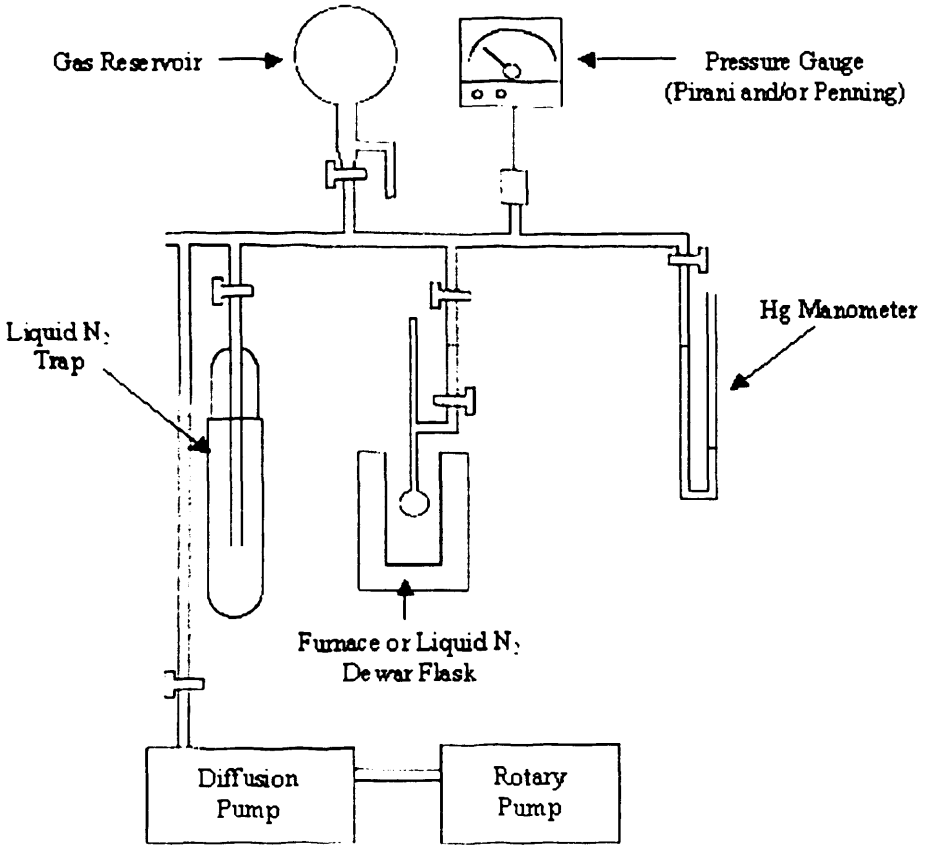

Figure 4.8. Schematic view of the vacuum line assembly used for activating samples.

Ultra Violet Lamp

An *Oriel Instruments UV lamp* (model N° 66021) was used for all irradiations. The construction of the lamp is shown in Figure 4.19. The power output from the lamp could be varied between 50 and 1000W. The Hg/Xe arc lamps used have abroad band spectral output from 250 nm to > 2500nm; the UV output below 280nm accounts for only 4 to 5% of the total lamp output. In all experiments, a water filter was used in order to absorb infrared frequencies and prevent sample heating by the UV beam.

EPR spectrometers

All EPR spectra were recorded either on a Varian E109 spectrometer or a Bruker ESP300e spectrometer, all operating in the X-band frequencies (*ca.* 9.5GHZ), and employing 100 KHz field modulation. The Varian E109 was linked to a *Stellar* data acquisition system, allowing peak area measurements to be made by double integration of the first derivative spectrum. As sample tuning often requires modification of the microwave frequency employed, g value measurements were made by reference to the known standard diphenyl picryl hydrazyl (DPPH), g = 2.0036.

The Bruker ESP300e spectrometer had an ER 4102 ST cavity and variable temperature studies (100-300K) were conducted using a Bruker B-VT2000 gaussmeter, calibrated for sample position using the pereylene radical cation g = 2.002569 ± 0.000006.[9,10] The microwave frequency is held constant during the course of the EPR measurement and the magnetic field is swept. EPR spectra are thus measured in microwave absorption mode. Magnetic field modulation is employed in order to enhance the signal output and to obtain acceptable signal: noise ratio. EPR computer simulations were performed using the SIM14S program (QCPE 265).

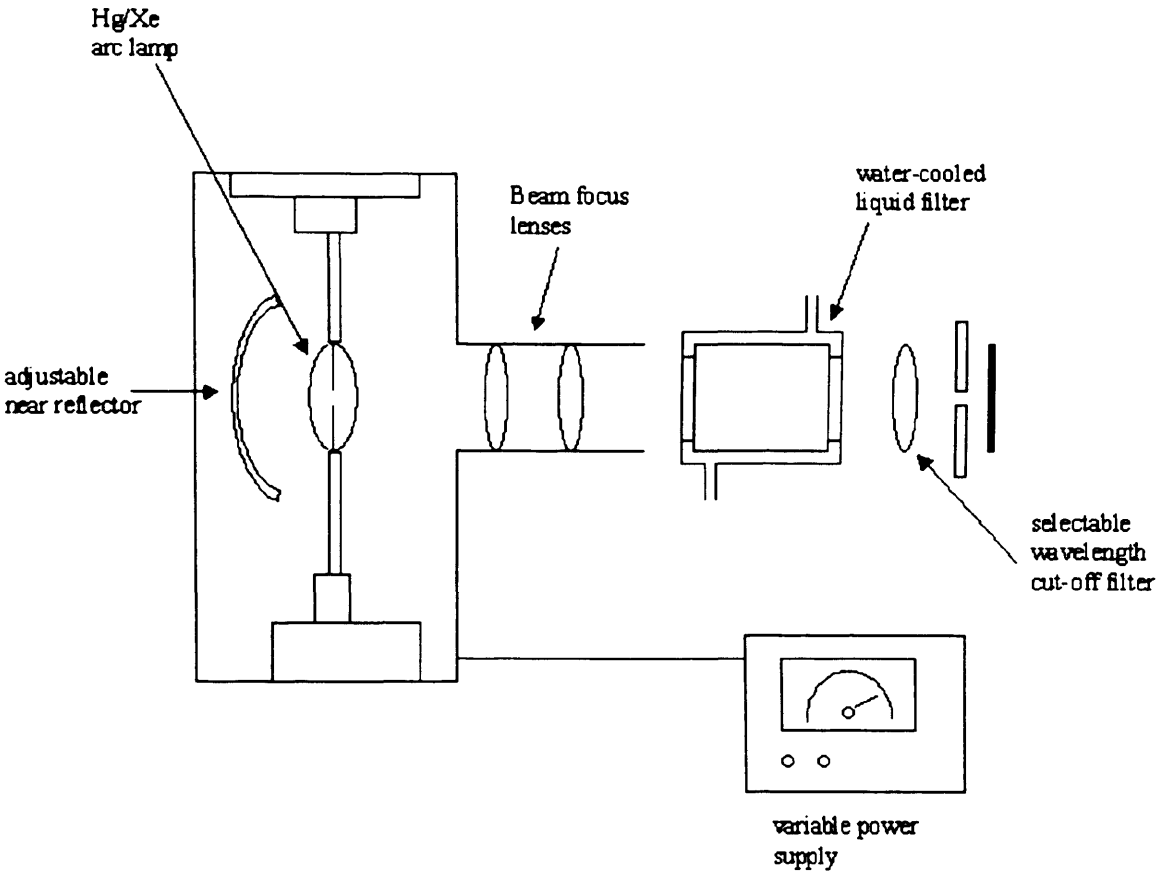

Figure 4.9. Construction of UV light source.

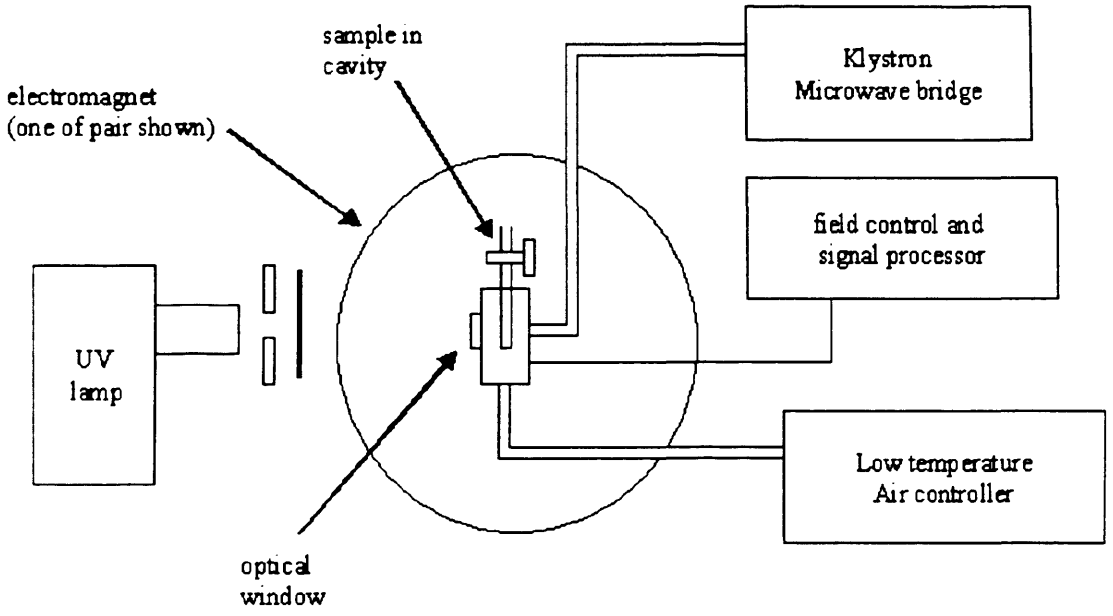

Figure 4.10. Construction of light source positioning with respect to the EPR cavity.

4.5 Materials

Liquids

All reagents were of analytical grade and supplied by *Aldrich Chemicals Ltd* (unless individually stated). Further purification was not therefore employed except for the deoxygenation of liquids, performed when required by freeze-pump-thaw. Triply distilled water was used in hydration experiments, and was also subjected to repeated freeze-pump-thaw steps prior to use.

Gases

All gases were supplied by *BOC Limited* (unless stated) and were of an extremely high purity (individually stated). The gases were added to the sample *via* the vacuum line at room temperature (unless specifically stated otherwise). The volume of gas added to the sample was measured using a mercury manometer attached to the line. The volume of each gas applied will be specified individually. *Icon Services Inc.* (New Jersey) supplied the ^{17} O-labelled dioxygen gas (63% enrichment) and was used without further purification.

Solids

Three TiO_2 samples were studied during the course of this thesis. The P25 Anatase sample was supplied by *Degussa* and has surface area *ca.* 49 m^2g^{-1}. A Rutile sample synthesised by hydrolysis of an aqueous solution (about 5 M) of $TiCl_4$[12] with a surface area *ca.* 135m^2g^{-1} this sample hereafter labelled Rutile A. The final Rutile TiO_2 sample hereafter labelled Rutile B was supplied by the Solaveil business of ICI, Uniqema when owned by Tioxide with a surface area *ca.* 97m^2g^{-1}.

4.6 Methods

Freeze-Pump-Thaw for purification of liquids

A small quantity of liquid (e.g., de-ionised water) is added to an empty quartz EPR cell. The sample is then purified and the cell evacuated using FPT, which involves:

- The liquid sample is frozen using liquid nitrogen
- Cell is opened to the vacuum line (taking care the liquid remains frozen) until a high vacuum returns.

- *After closing the cell to the vacuum*, the sample is *carefully* thawed, allowing impurities in the liquid to bubble to the surface.

This procedure is then repeated (three/four times) until the liquid is deoxygenated and pure. The purified liquid is then added to the sample by *closing the vacuum line to the pump* and opening both cells to the line. The liquid vapour is then free to interact with the sample.

Evacuation

A sample is placed in the bulb section of a quartz EPR cell attached to a high vacuum stopcock which is designed for connection to a vacuum line. The cell is gently opened to the vacuum line with the *diffusion pump closed.* After a standard rotary pump vacuum has been achieved (~$1x10^3$ Torr), the diffusion pump is opened. The length of time a sample is exposed varies from sample to sample.

Reduction / Oxidation

The sample is reduced in the bulb portion of the EPR cell, under dynamic vacuum on a vacuum line. The sample was initially left at 393K overnight under vacuum to remove any physisorbed water from the surface. The samples are then heated over a period of 5 hours to a temperature of 823 K (unless otherwise stated) and left annealing for 1 hour.

Oxidation of a sample would involve a repeat of this method with the addition of oxygen (50 Torr, *via* the vacuum line) to the cell, still at 823K. The sample is then closed to the vacuum (still under O_2), and left for an hour at 823K before cooling to room temperature and evacuating, leaving a fully oxidised white sample free from contaminants or surface hydroxyls. At no time was the sample open to the air, ensuring that the surface remains clean.

Low temperature UV irradiation

Following preparation of the TiO_2 samples, the samples were transferred to the EPR cavity for irradiation and EPR measurements at the required temperature. Irradiation of samples at low temperature were preformed *in situ* in the EPR cavity *via* an optical transmission window (figure 4.10). Illumination of the EPR cavity did not result in a temperature increase of the sample.

4.7 References

1. M. Che, E. Giamello, in '*Spectroscopic Characterisation of Heterogeneous Catalysts' Part B, Stud. Surf. Sci. Catal.*, (Ed. J. L. G. Fierro), Elsevier Science Publishers, Amsterdam, 57, B265, (1987).
2. H. Van Vleck, *Phys. Rev.*, **33**, 467, (1923).
3. W. Gordy, *Theory and Applications of Electron Spin Resonance*. Wiley, (1980).
4. J. R. Pilbrow, *Transition Ion Electron Paramagnetic Resonance*, (Ed. J. R. Pilbrow), Laredon Press, Oxford, (1990).
5. N. M. Atherton, *ESR, theory and Applications*, John Wiley and Sons, (1973)
6. J. A. Weil, J. R. Bolton, J. E. Hertz, *Electron Paramagnetic Resonance: Elementary theory and Practical applications*, John Wiley and Sons, (1994).
7. K. A. Antcliff, Ph.D. Thesis, University of Wales, Cardiff, (2002).
8. F. E Mabbs and D. Collison, *EPR of d Transition Metal Compounds, Studies in Inorganic Chemistry* **16**, Elsevier, (1992).
9. A. Abragam and B. Bleaney, *Electron Paramagnetic Resonance of Transition Ions*, Oxford, Clarendon Press, (1970).
10. B. G. Segal, M. Kaplan, G. K. Fraenkel, *J. Phys. Phys.*, **43**, 4191, (1965).
11. T. A. Egerton, E. Harris, E. J. Lawson, B. Mile, C. C. Rowlands, *Phys. Chem. Chem. Phys.*, **2**, 3275, (2000).

Chapter 5

Genesis of Paramagnetic Centres in Thermally Reduced TiO_2

5.1 Introduction

There is a growing awareness that in order to understand heterogeneous photocatalysis at the molecular scale, one needs to explore and understand surface morphological states at the molecular level. This is a challenging task for any experimentalist, but particularly so for the photocatalytic investigator dealing with heterogeneous polycrystalline materials including pigments. A polycrystalline material, composed of numerous small crystallites randomly orientated in space and exposing various crystal faces, does not present an ideal platform on which to pursue and test the modern theories of surface electron-hole pair utilisation (i.e., how electrons and holes are transferred across the interface). However it must be argued that these are precisely the systems that must be studied in order to explain the basic processes occurring in real heterogeneous systems.

For example, Lowekamp *et al.*,[1, 2] recently demonstrated that the anisotropic reactivity of both thin films and bulk samples of TiO_2, were related to differences in the efficiency of electron-hole pair *utilisation* rather than electron – hole pair *creation*. In other words, the photoactivity of the semiconductor depends on the exposed surface planes rather than the bulk orientation or structure. This result has far reaching consequences and important implications on the photoactivities of various treated TiO_2 materials, because it is known that the pre-treatment conditions of the oxide can influence the final surface properties of the oxide, which may in turn be manifested in the photoactivity. It should be remembered that the surface properties and surface states of a polycrystalline oxide, can be varied and will suffer significant degrees of perturbation and change depending on the physical and or chemical pre-treatment conditions. In turn the defectivity and extent of exposed surface planes will vary, so ultimately the photochemical reactivity may change.

In order to explore and study the reactivity of these surface trapped charge carrier pairs (i.e., holes and electrons), one must first thoroughly characterise the nature of the trapped states themselves. In this thesis, the experimental approach that has been adopted is to first generate the trapped charge carrier states under 'dark' non-equilibrium conditions. For example, by (i) thermally reducing the material under vacuum, and (ii) by thermal reduction under a reducing atmosphere (e.g. H_2 or CO).

In this case Ti^{3+} reduced centres are easily generated, while the trapped hole states which are less stable are often not simultaneously seen. The trapping of the electron centres generated under these thermal conditions can then be compared to the states produced under radiative conditions.

The second method of experimental generation for the trapped charge carriers on the TiO_2 surface is the UV irradiation of the sample. Ti^{3+} centres together with the paramagnetic trapped hole species (O^-), can be formed under UV irradiation. Both species are simultaneously formed on the surface following UV irradiation at low temperature. The varying methods of generation for the trapped charge centres i.e., both thermally and photo-initiated, allows one to investigate the different processes of electron-hole pair generation and utilisation under vacuum reductive condition (in general creating a defective surface) along with those generated under the radiative conditions.

In this chapter therefore, evidence will be provided which demonstrates the formation of trapped charge carrier states produced both thermally and under photo-irradiated conditions. This allows the nature of the paramagnetic species formed in these initial stages of surface trapping to be identified. In later chapters (6 and 7) the subsequent reactivity of these surface trapped charge carrier states, with different adsorbates, will be presented and discussed.

5.2 Experimental

A detailed account of the experimental methods used in the handling of the powders, manipulation of the samples on the vacuum line and operation of spectrometers and UV lamp were thoroughly described in chapter 4. In this section, only the specific experimental conditions used in the preparation and study of paramagnetic centres in TiO_2 will be summarised.

5.2.1 Thermal activation of polycrystalline TiO_2 under vacuum

Throughout the work described in this chapter the titanium dioxide, P25 Anatase (*Degussa*) with a surface area of *ca.* 49 m^2g^{-1} was used, along with a Rutile sample hereafter labelled Rutile A, with a surface area of *ca.* 135 m^2g^{-1} this material was synthesised by hydrolysis of an aqueous solution of $TiCl_4$ [3] A second Rutile sample, hereafter labelled Rutile B, sample with a surface area of *ca.* 97 m^2g^{-1} supplied by Huntsman Tioxide was also used in this work. The polycrystalline TiO_2

powders (*ca.* 5mg) were initially evacuated to a residual pressure of 10^{-4} Torr at 298K in EPR quartz cells. The samples were then heated to 393K under vacuum overnight in order to remove any physisorbed water from the surface.

The samples were then slowly heated under vacuum to a final temperature of 823 K (over a 5 hour period), and held at this temperature for approximately 1 hour. Under these conditions the TiO_2 surface is reduced, as lattice O^{2-} anions are removed, producing a non-stoichiometric surface containing an excess of Ti^{3+} cations. The sample is blue in colour due to the excess number of Ti^{3+} centres.[4]

5.2.2 Thermal activation of polycrystalline TiO_2 under H_2

In this method of pre-treatment only Anatase (P25) was studied. As stated above, the TiO_2 sample was prepared by evacuation to 10^{-4} Torr at 298 K in an EPR quartz cell and heated at 393K to remove any physisorbed water. Hydrogen gas (50 Torr) (ex. *Argo*) was admitted to the sample at 298 K and the sample heated under the H_2 atmosphere to a range of temperatures between 673 and 873 K in 50 K steps. The sample temperature was maintained at each temperature for 1 hour.

5.2.3 UV irradiation of polycrystalline TiO_2

The polycrystalline TiO_2 sample Rutile A, was subsequently slowly heated (over a 5 hour period) to a temperature of 823 K, and held at this temperature for approximately 1 hour. Oxygen (50 Torr) was added to the sample at 823 K and the samples cooled to room temperature under the excess oxygen atmosphere. This produced a clean dehydrated surface free from contaminants or surface hydroxyls. Exposure of TiO_2 to O_2 at high temperatures (823 K) leads to the formation of diamagnetic surface O^{2-} lattice anions, as the surface is effectively re-oxidised at this high temperature. Oxygen (10 Torr) was then admitted to the sample at 298 K, and UV irradiated for 30 minutes at 77 K. A 1000W *Oriel Instruments* UV lamp, incorporating Hg/Xe arc lamp (250nm to >2500nm) fitted with a water filter to adsorb infrared frequencies was used. The UV output below 280 nm accounts for only 4-5% of the total lamp output.

5.2.4 Measurement of EPR spectra

The EPR spectra were recorded on a Bruker ESP 300e series spectrometer, incorporating an EPR 4102 ST rectangular cavity. Variable temperature studies were

conducted using a Bruker B-VT2000 temperature controller. All spectra were recorded at X band frequencies (≈ 9GHz) employing 100 kHz field modulation, and 10 mW.

5.3 Results

5.3.1 Characterisation of Thermally Activated TiO_2

Each of the three samples (i.e., the P25 Anatase material and the two Rutile materials, Rutile A and Rutile B) were slowly heated under vacuum to a final temperature of 823 K and held at this temperature for 1 hour, producing a blue coloured powder in each case indicative of Ti^{3+} formation. The samples were then cooled to 100K and the resultant series of EPR spectra are shown in figure 5.1.

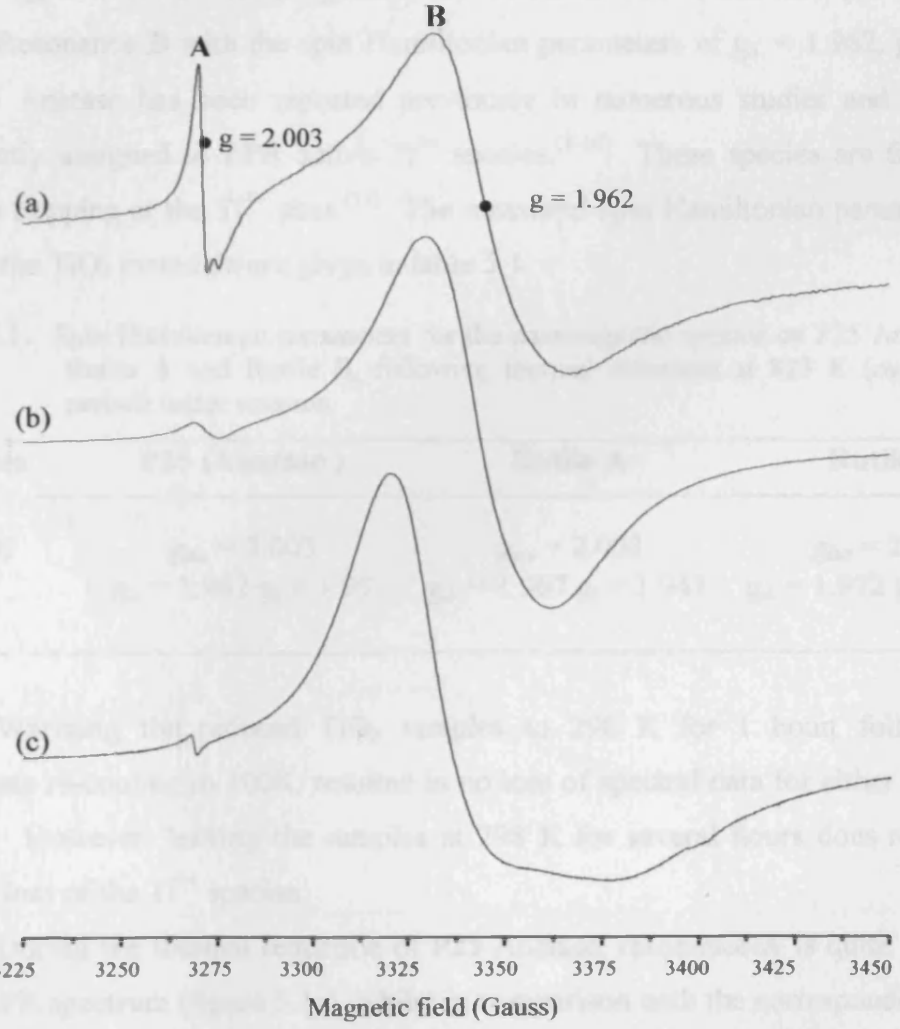

Figure 5.1. X- band EPR spectra recorded at 100K of (a) P25 Anatase, (b) Rutile A and (c) Rutile B after thermal reduction at 823 K under vacuum.

The low temperature series of EPR spectra reveal the presence of two distinct signals labelled **A** and **B** in each spectrum. The two signals are not related to each other as the relative intensities of the two vary arbitrarily from sample to sample and furthermore a previous analysis of the signals[5] has revealed a significantly different saturation profile for each one. In addition, the sharp resonance at g = 2.0030 was previously measured accurately using an NMR gaussmeter calibrated to the perylene radical cation in concentrated H_2SO_4, and this was therefore used as an internal marker for the g values in all of the following spectra. Resonance **A**, as previously mentioned, is responsible for the sharp feature at g = 2.0030, and this signal has been assigned to medium polarised conduction electrons.[6,7] These electrons are characterised by the sharp, isotropic EPR signal with a g value close to that of a free electron (g_e = 2.0023). This assignment will be discussed in detail later (*cf.* 5.4.1).

Resonance **B** with the spin Hamiltonian parameters of $g_\perp$ = 1.962, $g_\parallel$ = 1.95, for P25 Anatase has been reported previously in numerous studies and has been confidently assigned to EPR active Ti^{3+} species.[8-10] These species are formed by electron trapping at the Ti^{4+} sites.[11] The measured spin Hamiltonian parameters for each of the TiO_2 materials are given in table 5.1.

Table 5.1. Spin Hamiltonian parameters for the paramagnetic species on P25 Anatase and Rutile A and Rutile B, following thermal reduction at 823 K (over a hour period) under vacuum.

Species	P25 (Anatase)	Rutile A	Rutile B
(A) LCE	g_{iso} = 2.003	g_{iso} = 2.003	g_{iso} = 2.003
(B) Ti^{3+}	$g_\perp$ = 1.962 $g_\parallel$ = 1.95	$g_\perp$ = 1.967 $g_\parallel$ = 1.941	$g_\perp$ = 1.972 $g_\parallel$ = 1.939

Warming the reduced TiO_2 samples to 298 K for 1 hour, followed by immediate re-cooling to 100K, resulted in no loss of spectral data for either signal (**A** and **B**). However, leaving the samples at 298 K for several hours does result in a gradual loss of the Ti^{3+} species.

During the thermal reduction of P25 Anatase, resonance **A** is quite dominant in the EPR spectrum (figure 5.1a), whilst in comparison with the corresponding signal Rutile A and Rutile B (figure 5.1b and 5.1c respectively) is much less and it is found that the Ti^{3+} resonance dominates both of these systems. It should be noted however, that the reported spectra in figure 5.1 are not normalised in any way to sample weight

or surface area. The resulting spectra are therefore compared qualitatively and not quantitatively. Nevertheless, the relative intensity ratios of signal **A** to **B** in each sample are clear in this figure.

Following the thermal reduction of the TiO_2 materials, variable temperature EPR studies were preformed for each sample, and the resulting series of spectra are displayed in figures 5.2, 5.3 and 5.4 (for P25 Anatase, Rutile A and Rutile B respectively).

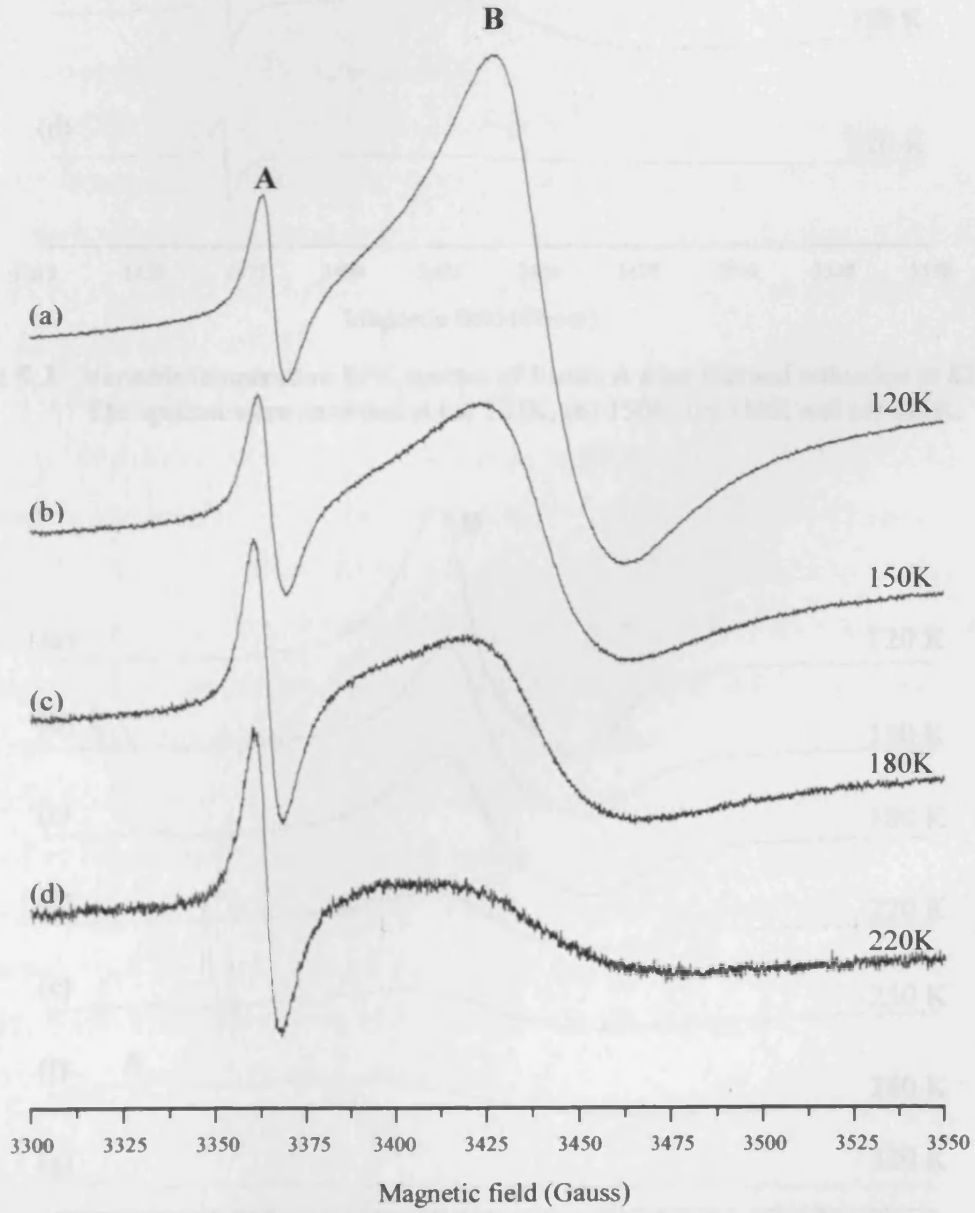

Figure 5.2. Variable temperature EPR spectra of P25 Anatase after thermal reduction at 823K. The spectra were recorded at (a) 120K, (b) 150K, (c) 180K and (d) 220K.

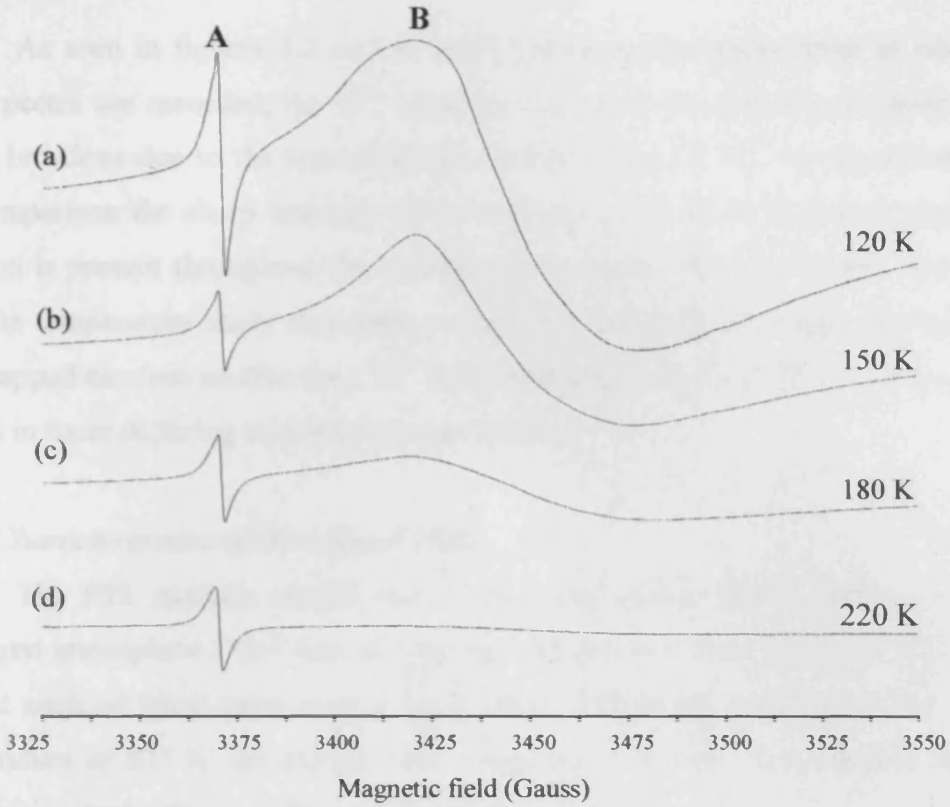

Figure 5.3. Variable temperature EPR spectra of Rutile A after thermal reduction at 823K. The spectra were recorded at (a) 120K, (b) 150K, (c) 180K and (d) 220K.

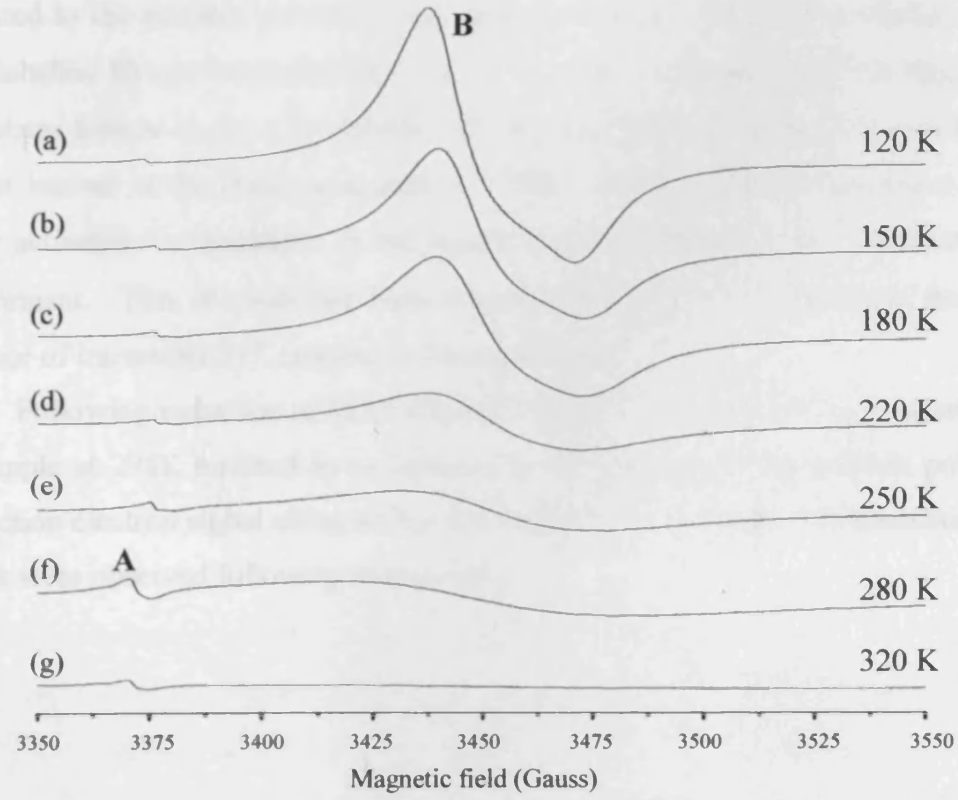

Figure 5.4. Variable temperature EPR spectra of Rutile B after thermal reduction at 823K. The spectra were recorded at (a) 120K, (b) 150K, (c) 180K, (d) 220K, (e) 250 K, (f) 280K and (g) 320K.

As seen in figures 5.2 to 5.4, upon increasing the temperature at which the EPR spectra are recorded, the Ti^{3+} signals in all cases dramatically diminish as the signal broadens due to the fast relaxation characteristics of Ti^{3+} (as discussed later). By comparison the sharp intensity of the resonance due to the localised conduction electron is present throughout the variable temperature study of all three cases. The variable temperature study therefore, reveals the very different environments of the two-trapped electron centres (i.e., Ti^{3+} and localised conduction band electron), which results in these differing saturation characteristics.

5.3.2 Characterisation of H_2 reduced TiO_2

The P25 Anatase sample (*ca.* 5 mg) was slowly heated under a constant hydrogen atmosphere (50 Torr), at varying temperatures from 673 K to 823 K, and held at each of these temperatures for 1 hour. Following reduction at the highest temperature of 823 K, the sample was evacuated at 298 K. The resultant series of EPR spectra (recorded at 100K) are shown in figure 5.5.

Three signals labelled **A**, **B** and **B′** can be identified in the spectra. As previously mentioned above, the resonance labelled **A** at g = 2.0030 has been attributed to the medium polarised conduction electrons, whilst the resonance at g ≈ 1.97 (labelled **B**) can be attributed to the Ti^{3+} cation. In addition to these signals, an extra sharp feature at g = 1.99 (labelled **B′**) can also be seen. This additional feature is most intense at the lower temperature (673K), and becomes less dominant at the higher activation temperature, as the signal at g ≈ 1.99 due to Ti^{3+} becomes more predominant. This **B′** peak has been reported previously[12,13] and arises from the presence of interstitial Ti^{3+} centres, as discussed later.

Following reduction at 823K (figure 5.5e) in the presence of H_2, evacuation of the sample at 298K resulted in an increase in the intensity of the medium polarised conduction electron signal along with a decrease in the Ti^{3+} signal. No interstitial Ti^{3+} centres were observed following evacuation.

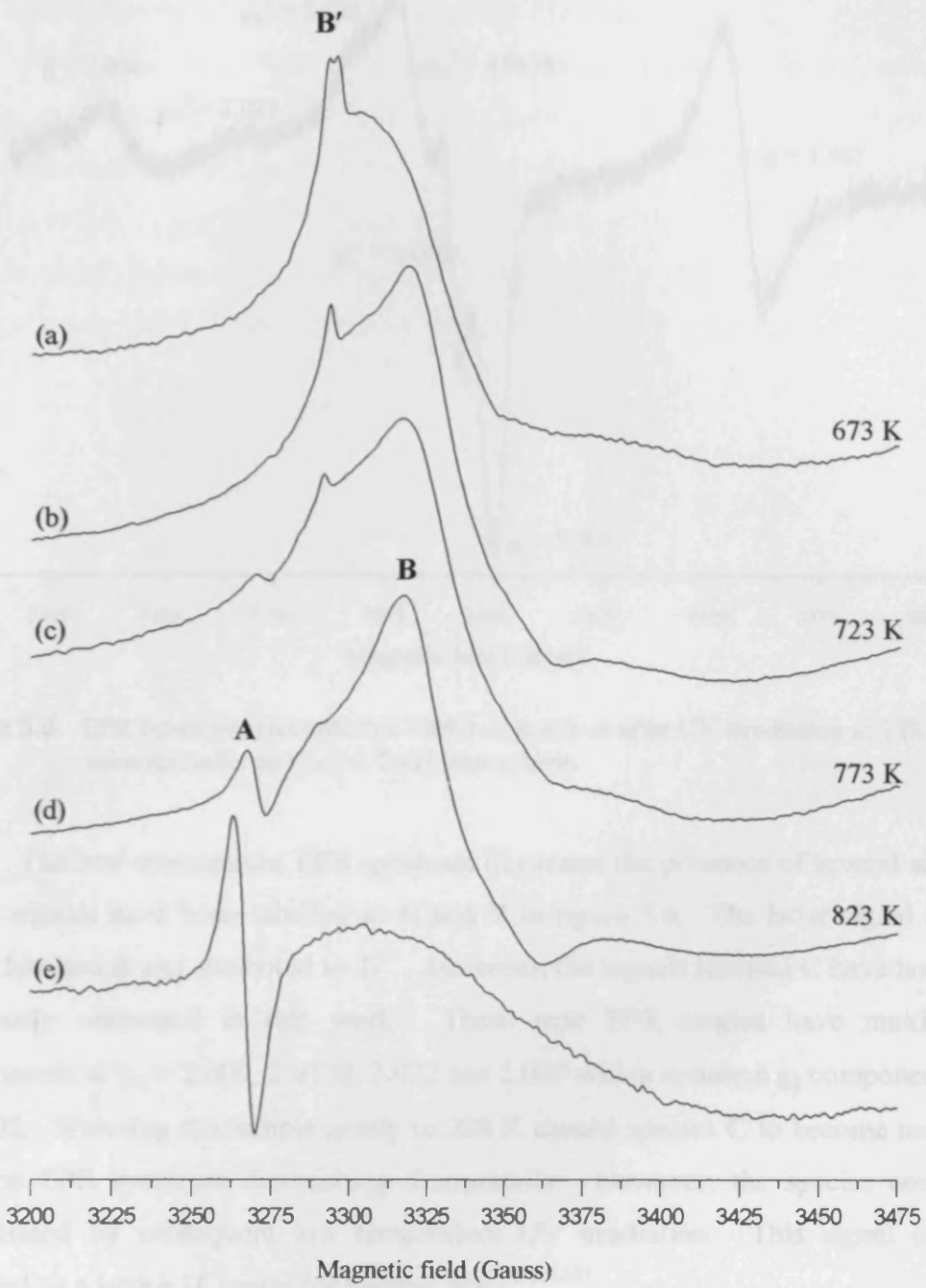

Figure 5.5. EPR spectra of P25 Anatase recorded at 100K after thermal reduction under H_2 (50 Torr) at increasing temperatures (a) 673K, (b) 723K, (c) 773K, (d) 823K and (e) after evacuation of the excess H_2 gas at 298 K.

5.3.3 Characterisation of UV irradiated polycrystalline TiO_2

Following the preparation of the activated TiO_2 sample (Rutile A), the clean dehydrated sample was UV irradiated under an oxygen atmosphere (10 Torr) for a period of 30 minutes at 100K. The resultant EPR spectrum recorded at 100K is shown in figure 5.6.

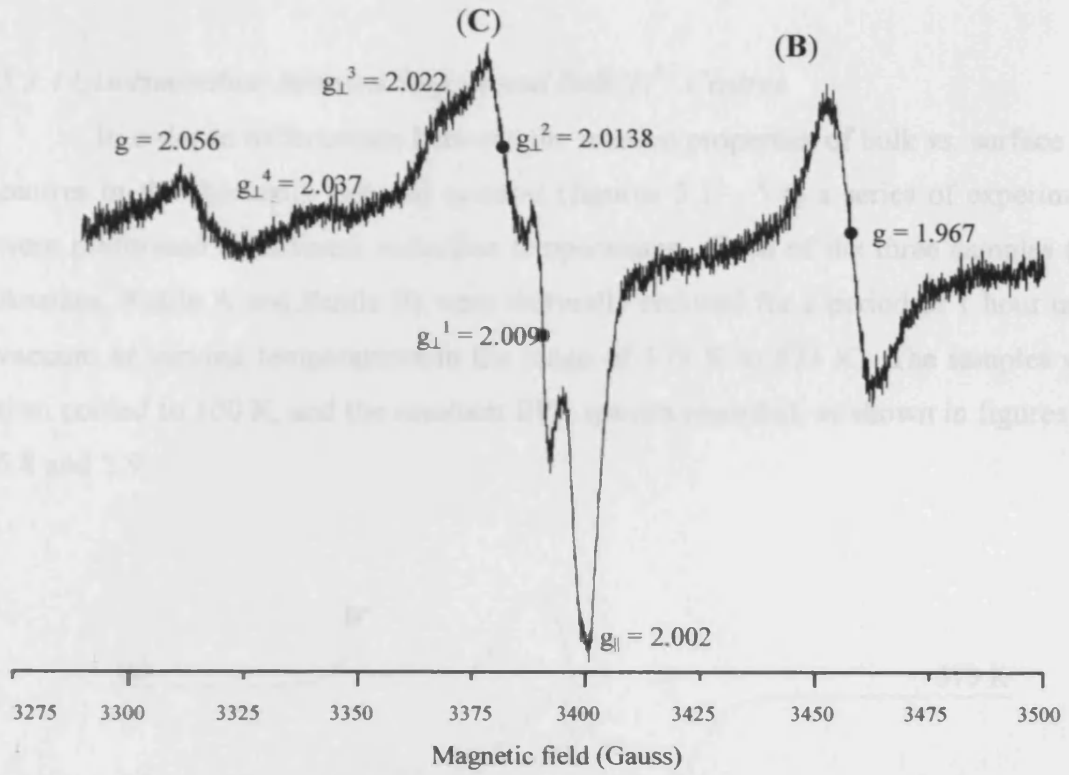

Figure 5.6. EPR Spectrum (recorded at 100K) of Rutile A after UV irradiation at 77K for 30 minutes under an O_2 (10 Torr) atmosphere.

The low temperature EPR spectrum illustrates the presence of several signals. These signals have been labelled as **C** and **B** in figure 5.6. The latter signal at g = 1.967 labelled **B** and attributed to Ti^{3+}. However, the signals labelled **C** have not been previously witnessed in this work. These new EPR singles have multiple g components at $g_\perp$ = 2.009, 2.0138, 2.022 and 2.037 with a common $g_\parallel$ component at g = 2.002. Warming the sample gently to 298 K caused species **C** to become unstable and the EPR spectrum diminishing dramatically. However, the species could be regenerated by subsequent low temperature UV irradiation. This signal can be assigned to a lattice O^- centre (or trapped hole).[9,14-18]

Characterisation of the low field signal at g = 2.056 is slightly more difficult, the largest g values observed for O^- in P25 is $g_\perp$ = 2.026 whilst, studies by Jenkins and Murphy[18] reported a multiple of $g_\perp$ components with the largest at g = 2.043 on a Rutile sample. In order for the g values to become larger significant levels of cationic impurities need to be present in the bulk of the material, causing an increase in the splitting of the π orbitals of the O^- radical (which in turn influence the g values). This could be a possible cause for the high g value observed here as the exact purity of the Rutile A sample is unknown. Another possibility is the presence of physisorbed oxygen on the surface. This site will therefore not be discussed further.

5.3.4 Discrimination between Surface and Bulk Ti^{3+} Centres

In order to differentiate between the relative properties of bulk *vs.* surface Ti^{3+} centres in the thermally reduced systems (figures 5.1 – 5.4) a series of experiments were preformed at different reduction temperatures. Each of the three samples (i.e., Anatase, Rutile A and Rutile B) were thermally reduced for a period of 1 hour under vacuum at varying temperatures in the range of 573 K to 873 K. The samples were then cooled to 100 K, and the resultant EPR spectra recorded, as shown in figures 5.7, 5.8 and 5.9.

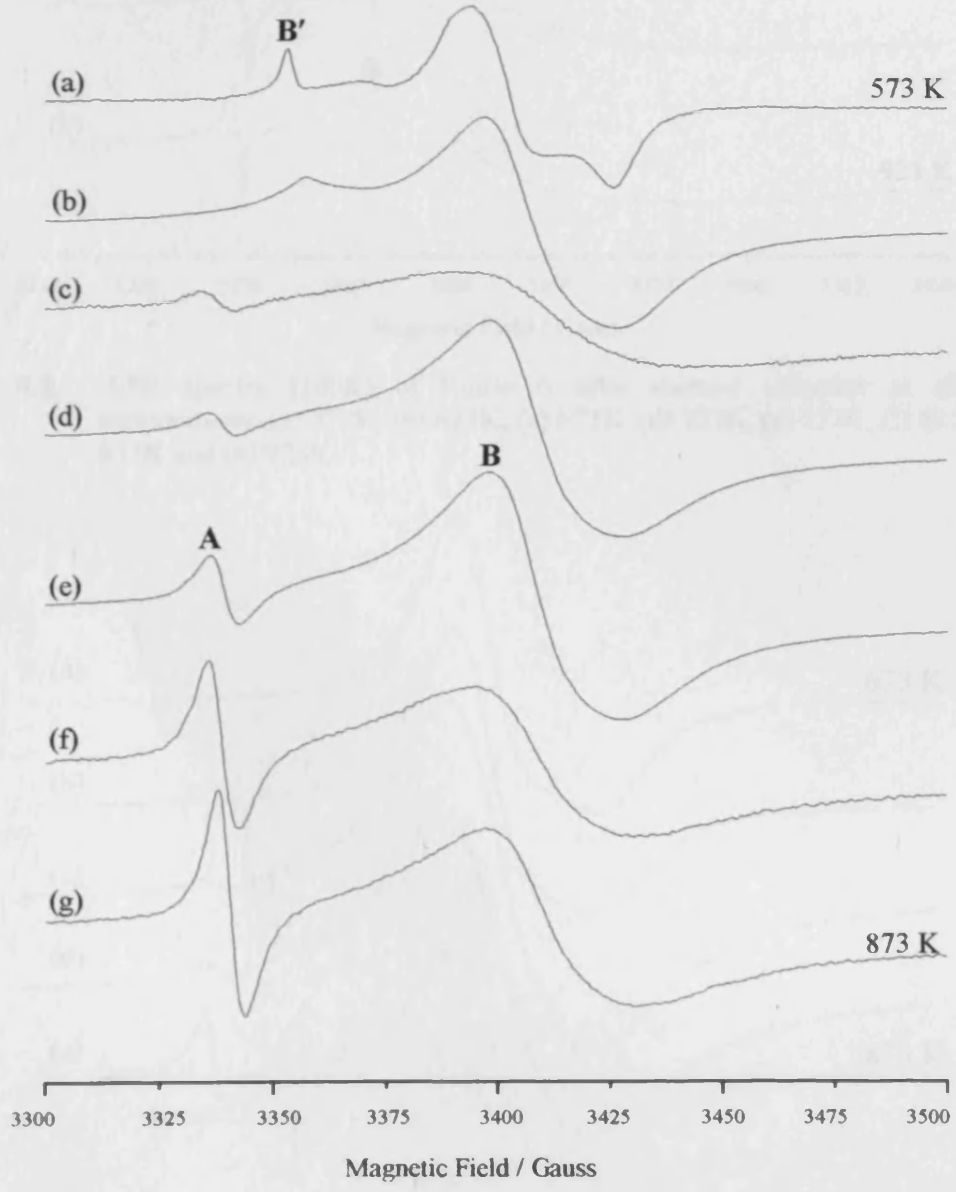

Figure 5.7. EPR spectra (100K) of P25 Anatase after thermal reduction at different temperatures: (a) 573 K, (b) 623 K, (c) 673 K, (d) 723 K, (e) 773 K, (f) 823 K and (g) 873 K.

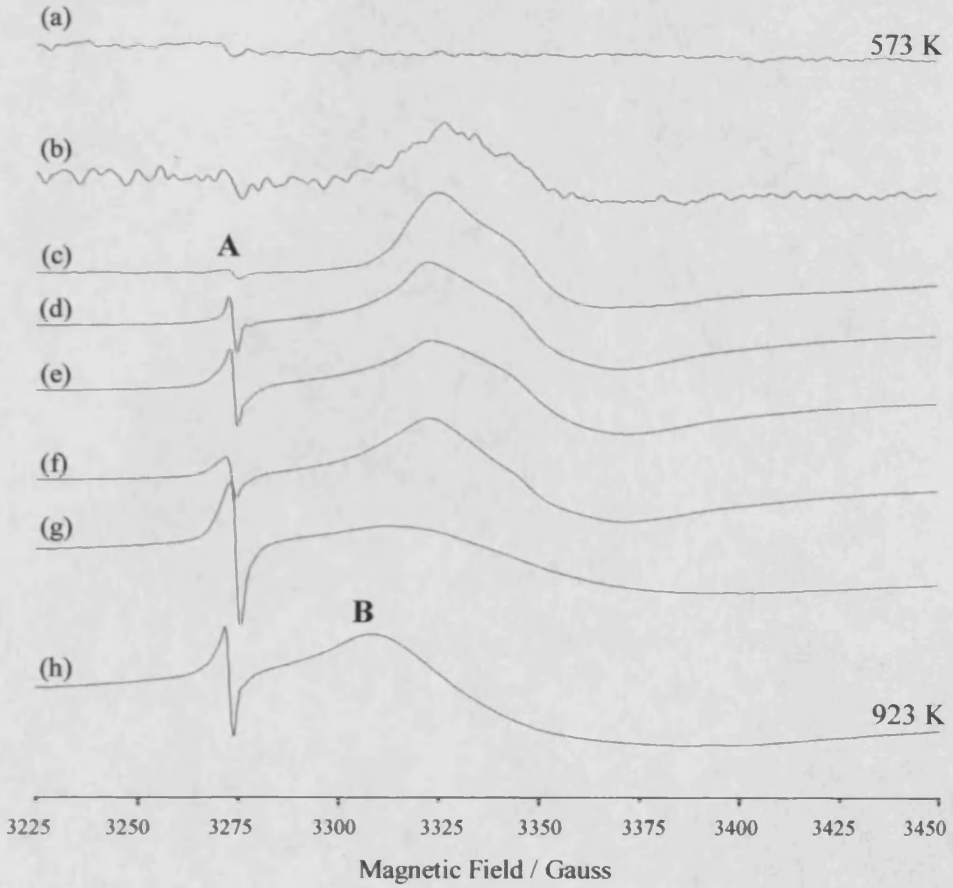

Figure 5.8. EPR spectra (100K) of Rutile A after thermal reduction at different temperatures: (a) 573K, (b) 623K, (c) 673K, (d) 723K, (e) 773K, (f) 823K, (g) 873K and (h) 923K.

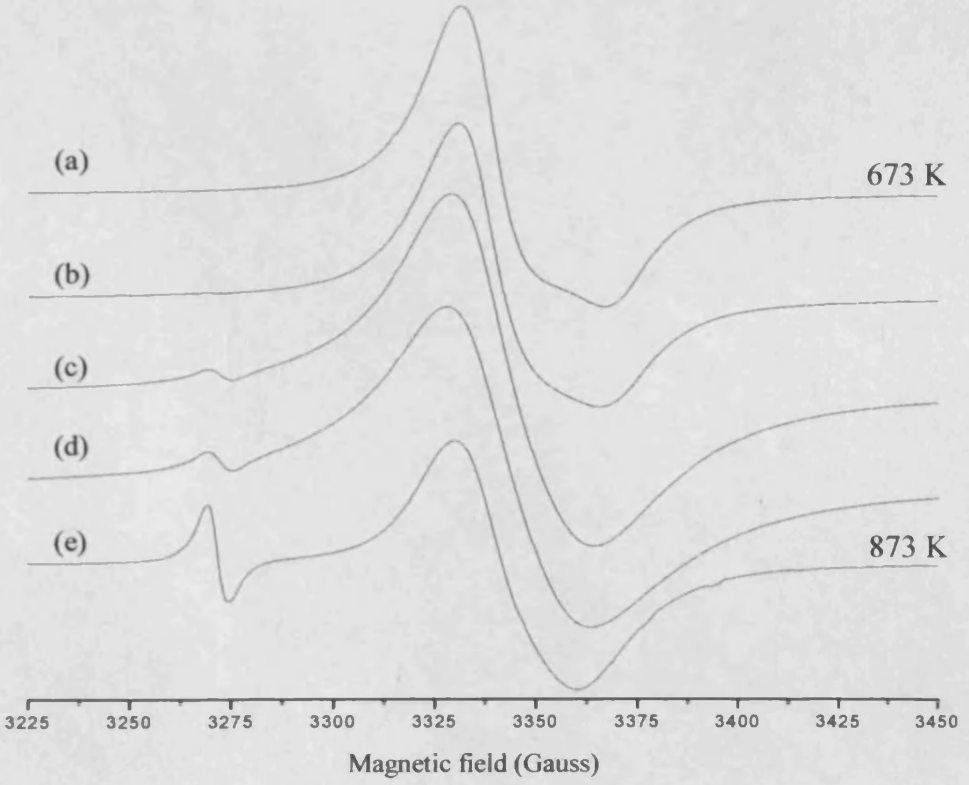

Figure 5.9. EPR spectra (100 K) of Rutile B after thermal reduction at different temperatures: (a) 673 K, (b) 723 K, (c) 773 K, (d) 823 K and (e) 873 K.

As illustrated in figures 5.7 to 5.9 upon increasing the reduction temperature, the intensity of signal **A** due to the medium polarised conduction electrons at g = 2.0030 increases. Simultaneously, the Ti^{3+} signals **B** also broadens as the temperature of reduction increases. As a result accurate integrations of the spectra are difficult due to extensive spin-spin interactions occurring at the higher Ti^{3+} concentrations. At temperatures greater than 873 K extensive bulk reduction occurs, as the proportion of Ti^{3+} centres formed in the oxide bulk increases as a fraction of the total Ti^{3+} centres.[18]

A further signal labelled **B'** in figure 5.7 at g = 1.99 has been attributed to traces of interstitial Ti^{3+} centres. This signal was only observed on the P25 Anatase sample during thermal reduction at 573 K (figure 5.7a), since no evidence of this signal was observed in figures 5.8 and 5.9, Rutile A and Rutile B respectively.

5.4 Discussion

As previously mentioned, in order to explore and study the reactivity of surface trapped charge carrier pairs (i.e., holes and electrons), the nature of the trapped states themselves must first be characterised. The trapped charge carriers can be produced using various conditions, i.e., thermal reduction, reduction under a H_2 atmosphere and UV irradiation of the TiO_2 sample, and their EPR features will be discussed in the following sections.

5.4.1 Nature of Signal A: Medium Polarised Conduction Electrons

During thermal reduction of the TiO_2 samples, two paramagnetic species labelled **A** and **B** are observed in the EPR spectrum (figure 5.1). The resonance at g = 2.0030, arising from a medium polarised conduction electron, was observed under thermal reduction for all materials. This signal has been reported previously by many authors[6] and has been associated with polarised conduction band electrons. Previous reports into the nature of this signal have suggested that it could be due to O^- species.[11] However, research by Tench *et al.*,[7] showed that the signal at g = 2.0030 was unaffected when treated with oxygen enriched with the ^{17}O isotope, therefore, proving that the assignment of the signal to a surface or even subsurface O^- was incorrect. As at 77 K, rapid exchange of lattice oxygens are unlikely, therefore the signal cannot be attributed to the O^-. Further evidence was provided by Serwicka *et*

al.,[6] who concluded that the signal at g = 2.0030 could not be due to O^- centres. Experiments clearly showed that the signal was not connected to any adsorbed oxygen species, since it appeared also with acceptor molecules not containing O_2, e.g., SF_6 and H_2S[6].

Tench *et al.*,[7] attributed the formation of these centres to medium polarisation by adsorbates leading to conduction electrons becoming localised in the sub-surface regions of the TiO_2 lattice. The appearance of a peak at g = 2.0030 in the reduced spectra prior to adsorbate exposure was also reported by Serwicka *et al.*,[6] who noted that the feature exhibits different EPR relaxation characteristics following exposure to adsorbates with medium to high electron affinity.

Since the g value of species **A** is close to g_e, it is unlikely to be associated with any transition metal ion species. As previously discussed in section 5.3.1. the two signals **A** and **B** are not related to each other since the relative intensities of the two vary arbitrarily from sample to sample. The isotropic EPR signal **A** is indicative of an unpaired electron located in a spherically symmetrical environment, and is consistent with suggestions of localised conduction band electrons. It has been suggested that this species may be due to electrons trapped at defect structures in the bulk[6] (such as an anion vacancy, labelled AV, in equation 5.1. below), although this has not yet been proven.

$$AV + e^-_{cb} \longrightarrow AV^- \qquad (5.1)$$

There appears to be little consensus in the TiO_2 literature into the nature and spatial distribution of this polarised electron centre, and a correct model for the behaviour observed in the EPR signal with surface adsorbates (i.e., signal increases) may be analogous to similar effects observed for porous silicon.[19]

Nevertheless, this polarised electron does not react chemically with surface adsorbates forming radicals and within the scope and aims of this work, will not be discussed further.

5.4.2 Nature of Signal B: Ti^{3+} cations

The thermal annealing of TiO_2 under vacuum and resulting deviation from the stoichiometric polycrystalline surface was first reported by Gray *et al.*,[20] in 1959. Research several years later attributed these earlier results to conduction electrons trapped at defect centres forming EPR active Ti^{3+} species.[8]

During the thermal reduction treatment of TiO_2 under a vacuum the surface undergoes loss of lattice oxygen, thus generating four electrons per O_2 molecule *via* the process shown in equation 5.2. These four electrons are trapped at the Ti^{4+} sites as Ti^{3+} (equation 5.3), which are EPR active.

$$2\,O^{2-}_{(latt)} \longrightarrow O_{2\,(g)} + 4\,e^-_{(cb)} \qquad (5.2)$$

$$4\,Ti^{4+} + 4\,e^- \longrightarrow 4\,Ti^{3+} \qquad (5.3)$$

Resonance **B** (figure 5.1) has been reported numerous times in the literature[9,10,18] and therefore has been confidently assigned to the Ti^{3+} centres formed by electron trapping at the Ti^{4+} site

$$Ti^{4+}_{(surf/bulk)} + e_{cb} \longrightarrow Ti^{3+}_{(surf/bulk)} \qquad (5.4)$$

Both Ti^{3+} centres (surface or bulk) associated with resonance **B** display axial symmetry with g (surf) ≈ g (bulk), so that resonance **B** may be considered a composite signal. For a d^1 ion (such as Ti^{3+}) in a tetragonally distorted octahedral field, the g tensor components are known to fit the first order expressions:[21]

$$g_{\parallel} = g_e - 8\lambda/\Delta \qquad (5.5(a))$$
$$g_{\perp} = g_e - 2\lambda/\delta \qquad (5.5(b))$$

where λ = the spin orbit coupling constant for Ti^{3+} (154 cm^{-1})
4δ = the energy separation between ^2E_g doublet and the $^2B_{2g}$ ground state (due to tetragonal distortion)
Δ = the energy separation between the $^2B_{2g}$ and $^2B_{1g}$ states

The crystal field splittings for a d^1 ion are shown in Figure 5.10. The Ti^{3+} ion experiences a tetragonal splitting both at the surface and in the bulk. The surface $g_{\perp}$ component is then approximately equal to the bulk $g_{\perp}$ component, and the EPR spectra of the two centres remain unresolved. However, in colloidal systems surface Ti^{3+} centres experience a relative shift in δ due to the presence of adsorbates occupying the sixth coordination sites at the surface, e.g., H_2O or OH^-. The $g_{\perp}$ component of the surface Ti^{3+} centres is then variant according to the identity of the sixth coordination species, and has been resolved from that of bulk Ti^{3+} centres by Howe and Grätzel[9] for colloidal Anatase TiO_2.

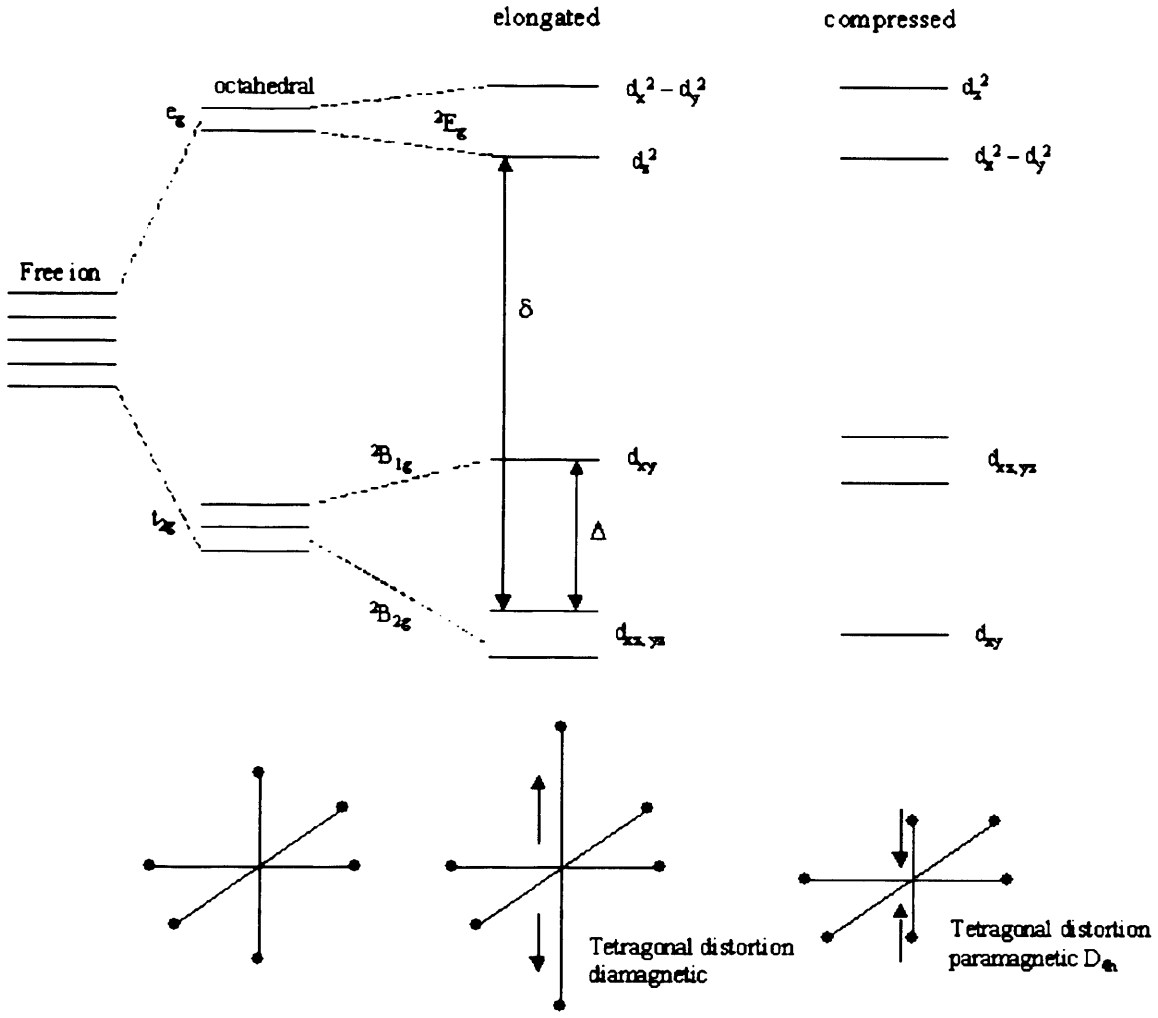

Figure 5.10. Crystal field splittings of the orbitals in a d^1 transition metal ion.

The large linewidths associated with the Ti^{3+} resonance are typical for Ti^{3+} centres in polycrystalline TiO_2. It has been attributed to an envelope of Ti^{3+} absorptions arising from sites having a distribution of slightly different local geometries and individual g values.[9] Precise simulation of the observed line shape is thus difficult to achieve owing to the large number of species involved i.e., resonance **B** representing an envelope of multiple EPR absorptions.

The variable temperature study of the reduced TiO_2 samples displayed a loss in intensity of the Ti^{3+} signal **B** for all TiO_2 samples studied as illustrated in figures 5.2 to 5.4. This loss of the Ti^{3+} signal at temperatures close to room temperature has been associated with the rapid relaxation time of the spin – orbit coupling and the signal appears to broaden. In contrast to this, signal **A** remained constant throughout the variable temperature study for all TiO_2 materials, thus providing further evidence that the two signals (localised conduction electron and Ti^{3+}) are unrelated.[8]

5. 4. 3 Discrimination Between Surface and Bulk Ti^{3+} Centres in TiO_2

In order to gain a fuller understanding of the formation of Ti^{3+} and localised conduction electrons, the response of Anatase and Rutile TiO_2 samples to reduction *in vacuo* at various temperatures was measured. This study, therefore, allowed the optimum temperature of reduction for solid-gas interface studies to be determined along with an understanding of the surface to bulk Ti^{3+} ratio acquired at various reduction temperatures. Therefore, the optimum concentration of surface Ti^{3+} centres (with a minimum concentration of interfering bulk species) for reaction with adsorbates can be obtained.

Generally, as illustrated in figures 5.7, 5.8 and 5.9, the increase in reduction temperature causes an increases in the signal due to the medium polarised conduction electrons at g = 2.0030 (signal **A**). Simultaneously as the temperature is increased the Ti^{3+} signal broadens considerably due to extensive spin - spin interactions occurring at the higher Ti^{3+} concentrations from extensive TiO_2 reduction. At temperatures higher than 873 K extensive bulk reduction occurs as the proportion of Ti^{3+} centres formed in the oxide bulk increases as a fraction of the total Ti^{3+} signal at $g \approx 1.962$. Along with the increase in the total Ti^{3+} signal, an increase in the blue colour intensity also occurred which is an indication of the extent of TiO_2 reduction.

When the temperature of reduction exceeds 823K, only extensive bulk reduction of the TiO_2 powder occurs, since the surface region is fully reduced. Thus, reduction above this temperature simply produces a large bulk Ti^{3+} resonance at $g \approx 1.962$, which will obscure the EPR signals of any surface radical. The ratio of surface to bulk Ti^{3+} production therefore, begins to decrease rapidly i.e., as the temperature is increased, the surface concentration of Ti^{3+} decreases. This was demonstrated in a study by Jenkins and Murphy,[18] who compared the signal intensities of the Ti^{3+} centres before and after various reduction temperatures.

In the reported study the TiO_2 sample was reduced under vacuum for 1 hour in the temperature range 723 – 923 K. The thermally reduced sample was then exposed to O_2 (10 Torr) at 300 K for 10s. The excess gaseous O_2 was then evacuated at this temperature. This results in the re-oxidation of the surface Ti^{3+} centres to Ti^{4+} *via* electron transfer to the adsorbed O_2 (forming the well known adsorbed superoxide anion, *cf.* chapter 6) so that only a bulk Ti^{3+} remnant EPR signal remained. The sample was then heated to 500 K under vacuum, a temperature sufficiently high enough to destroy adsorbed O_2^- but too low to generate new Ti^{3+} centres. The signal

intensities of the Ti^{3+} centres before and after thermal reduction could then be compared. The results obtained from this investigation are presented in figure 5.11.

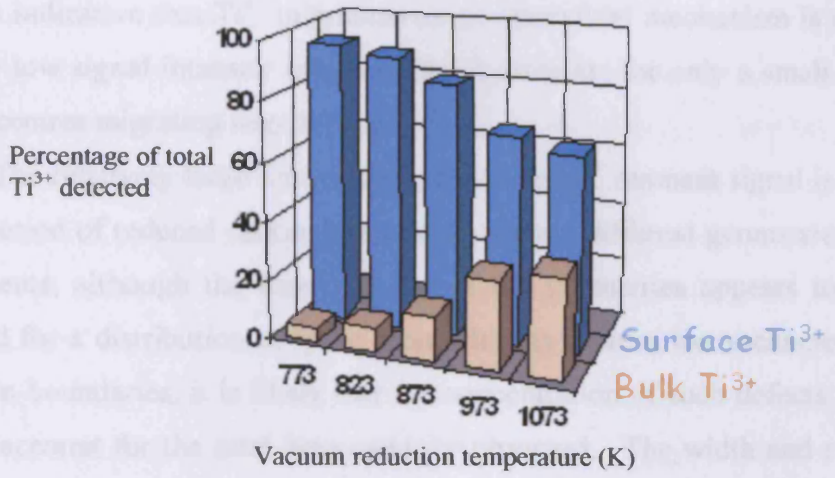

Figure 5.11. Variation of the surface:bulk Ti^{3+} composition in TiO_2 as a function of vacuum reduction temperature.

Similar results to those shown above in figure 5.11, were also obtained when the analogous experimental technique was preformed on the three TiO_2 samples here. At temperatures higher than 873 K extensive bulk reduction occurs as the proportion of Ti^{3+} centres formed in the bulk increases as a fraction of total Ti^{3+} signal at $g \approx 1.962$. Further EPR studies on polycrystalline TiO_2 powders[22] reduced at temperatures 723 - 923 K under vacuum have also confirmed, that the surface to bulk Ti^{3+} ratio decreases as the reduction temperature increase. Following reduction at T > 1000K (not shown here) the broad Ti^{3+} remnant at $g \approx 1.962$, most likely arises from Ti^{3+} ions in lattice sites in the bulk and sub surface regions.[13]

The findings that higher reduction temperatures produce an increase in bulk reduction of the TiO_2 has also been supported by results obtained from Henderson,[23] who studied the re-oxidation of TiO_2 surfaces by a diffusion mechanism involving Ti^{3+} mass transfer between the surface and the bulk of the oxide. However, Henderson suggested that the majority of bulk reduction occurs *via* a defect transport mechanism involving diffusion of interstitial Ti^{3+} cations above 700K. Results obtained here and by Jenkins and Murphy[18] are partially in agreement with this (as the levels of interstitial Ti^{3+} cations[9] at $g = 1.99$ were observed), although most of the bulk Ti^{3+} are clearly not located at interstitial sites as observed in figures 5.7 to 5.9. This could possibly be due to the method of preparation of the TiO_2 samples used.

As mentioned earlier, the weak shoulder at g = 1.99 (resonance **B'** in figure 5.7(a)) arises from the presence of interstitial Ti^{3+}[12,13] and can be generated both thermally (under reduction and H_2 atmosphere) and radiatively. The presence of this signal is indicative that Ti^{3+} migration *via* an interstitial mechanism is occurring, but the very low signal intensity indicates that it accounts for only a small proportion of all Ti^{3+} centres migrating into the bulk.

The relatively large linewidths of the bulk Ti^{3+} remnant signal is suggestive of a distribution of reduced cation sites having slightly different geometries and g tensor components; although the heterogeneity of the geometries appears to be less than expected for a distribution of 'pure' point defects such as ion vacancies, lattice slips and grain boundaries, it is likely that the concentration of such defects is sufficiently high to account for the total heterogeneity observed. The width and relatively high intensity of the remnant Ti^{3+} signal at $g \approx 1.962$, may be explained by taking into account the contribution from Ti^{3+} centres in sub surface-sites where there is crystalline disorder and crystal field perturbation due to the proximity of the particle surface.

The formation of reduced Ti^{3+} centres is associated with the presence of a crystalline defect structure - which are most abundant at the particle surface - high surface area materials tend to produce more intense EPR signals following thermal reduction, as reflected in figure 5.1. Lower coordination states of Ti^{2+} and Ti^{+} can be produced under severe reducing / sputtering conditions.[24,25] The reduced surface also contains a higher number of intrinsic defects, such as oxygen vacancies, which result in stronger attachment of oxygen - containing molecules and enhanced rates of dissociative chemisorption.

The electrons stabilised at the Ti^{4+} sites as Ti^{3+} can be very reactive and are readily transferred to adsorbates at the surface oxidising them as shown in the equation 5.6 below,

$$Ti^{3+} + Ads \longrightarrow Ti^{4+} + Ads^{-} \qquad (5.6)$$

5.4.4 Formation of trapped charge carriers following H_2 treatment

A second experimental approach under dark non-equilibrium conditions can also generate the trapped charge carriers i.e., the thermal reduction under a H_2 atmosphere.[26,27] The variable temperature study shown in figure 5.5, revealed the

presence of several signals labelled **A**, **B** and **B′**. These signals have been identified as, due to medium polarised conduction electrons (signal **A**) and to surface and sub-surface Ti^{3+}centres (signal **B**), while resonance **B′** due to presence of interstitial Ti^{3+}.

Hydrogen acts as a strong reducing agent, and as seen in figure 5.5, upon increasing the temperature under a H_2 atmosphere the TiO_2 (surface or bulk) undergoes extensive reduction. At the lower temperature of reduction only traces of interstitial Ti^{3+} centres (**B′**) are observed. However, upon increasing the reduction temperature an increase in signal **A** due to medium polarised conduction electron and signal **B** due to the Ti^{3+} centres. As previously discussed, increasing the temperature causes the Ti^{3+} signal to broaden due to the increase in bulk Ti^{3+}, thus obscuring the EPR signals of any other species. Upon evacuation of the excess hydrogen from the reduced surface at 298 K, the resulting EPR spectrum (figure 5.5e) still displays the two paramagnetic species **A** and **B**, although at a lower intensity.

Prior to any thermal annealing of the TiO_2 under the H_2 atmosphere there was no evidence of any production of Ti^{3+} following addition of the hydrogen at 298 K. The first traces of any surface reduction of the TiO_2 sample was witnessed following annealing to 673 K as observed in figure 5.5 (a). The results presented here have also been supported in a recent study by Liu *et al.*,[28] They reported that for thermal treatment in a constant hydrogen pressure the optimum temperature was in the range of 773 – 873°C for effective reduction, this is in agreement with the results in figure 5.5. Also they reported a signal at g = 1.955 which they assigned to the Ti^{3+} cation, however, no differentiation between the surface and bulk formed Ti^{3+} species were made. Following the thermal pre-treatment under the excess H_2 atmosphere Lui *et al.*,[28] reported a significant improvement in the photocatalytic degradation of both sulfosalicylic acid (SSA) and phenol using the H_2-treated TiO_2. Similar results were reported by Okamoto *et al.*,[29] who adopted H_2 reduction as a simple pre-treatment of TiO_2 in the photocatalytic degradation of phenol.

Several other authors have also studied the treatment of TiO_2 with hydrogen under varying conditions. Thermal hydrogen treatment of TiO_2 was reported to be capable of prolonging the lifetime of the holes by reducing the number of bulk recombination centres.[30] However, in this work no traces of trapped holes were observed before or after evacuation of the excess H_2. The use of H_2 treatment is a common method used to improve the surface and photoelectrochemical properties of TiO_2.[31-33] Heller *et al.*,[34] reported the enhanced photocatalytic activity of the TiO_2

catalyst by a thermal reduction treatment using hydrogen gas at 550°C. They also proposed that the reduction of the TiO_2 particles raised the Fermi Level and increased the height of the barrier that repels electrons from the particles because of more Ti^{3+} available in the TiO_2 particles.

5.4.5 Nature of signal C: Trapped hole (O^-)

The above discussion has concentrated on the thermal methods used to generate trapped electrons on the TiO_2 surface and in the bulk. However, UV irradiation of the sample also has the ability to generate holes in the TiO_2 material.

As shown in figure 5.6, following UV irradiation of an activated TiO_2 sample, two signals labelled **B** and **C** were formed. The former resonance at g = 1.967 has been attributed to the Ti^{3+} cation, i.e., the trapping of an electron. The second signal with multiple g components at $g_\perp$ = 2.009, 2.0138, 2.022 and 2.037 and a common $g_\parallel$ component at g = 2.002 were not previously observed during the thermal reduction of TiO_2. However, this signal has been previously reported during the UV irradiation of a TiO_2 sample and has been attributed to that of a trapped hole (O^-).[9,14-18]

Following UV irradiation, both trapped charge carriers (i.e., Ti^{3+} and O^-) were simultaneously formed and stabilised at low temperature on the TiO_2 surface; this was previously not observed during thermal reduction of the TiO_2 materials where only trapped electrons were observed. However, by comparison the species generated under UV conditions produced no evidence of a localised conduction electron compared to that obtained during thermal conditions. This result is not surprising when considered within the context of how the trapped electron centres are generated. For thermally reduced TiO_2, the electrons trapped at the Ti^{4+} centres from the lattice O^{2-} anions, released when gas phase O_2 is generated in this non-stoichiometric system. However, in the radiative case, the charge separated pairs form (Ti^{4+}-O^{2-} $\longrightarrow$ Ti^{3+}-O^-) so that no itinerant or excess electrons escape into the conduction bands to form polarised conduction electrons.

These active oxygen species appear to have axial symmetry formed here and are characterised by the spin Hamiltonian parameters $g_\perp^1$ = 2.009, $g_\perp^2$ = 2.0138, $g_\perp^3$ = 2.002 and $g_\perp^4$ = 2.037 and $g_\parallel$ = 2.002. For the case of O^- with axial symmetry (figure 5.12), the p_x and p_y orbitals are symmetrically - and energetically – degenerate, and a single crystal field splitting results. For the O^- species, the simplified g tensor

components in octahedral symmetry were derived by Che and Tench[17] and are given by the first order relations;

$$g_{zz} = g_e \qquad (5.7a)$$
$$g_{xx} = g_e + 2\lambda/\Delta E_1 \qquad (5.7b)$$
$$g_{yy} = g_e + 2\lambda/\Delta E_2 \qquad (5.7c)$$

where, λ = spin coupling constant of the interacting cation and ΔE_1 and $E\Delta_2$ are the energy differences between p_z - p_x and $p_y - p_x$, respectively.

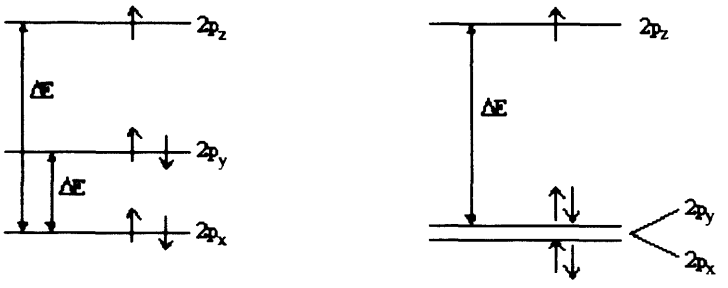

Orthorhombic symmetry $x \neq y \neq z$ Axial symmetry $x = y \neq z$

Figure 5.12. Electronic structure of the O^- species in (a) orthorhombic and (b) axial crystal field.

In a pure axial system $\Delta E_1 = \Delta E_2$, so that a two g system is observed with the following components;

$$g_{\parallel} = g_{zz} = g_e \qquad (5.8a)$$
$$g_{\perp} = g_{xx} = g_{yy} \qquad (5.8b)$$

This simplified treatment, with $\lambda > 0$, leads to one value close to g_e and two values exceeding g_e. In reality $g_{\parallel}$ is rarely observed to be exactly 2.0023 due to some degree of spin – orbit coupling between the spin system and cations of the crystal lattice. The value of the $g_{\parallel}$ component depends upon the energy splitting Δ, which is governed by the local cationic charge.[5] The hole centres and light induced surface Ti^{3+} ions are stable only in the low temperature regime, and are annihilated at 300K due to recombination. The two species can, however, be regenerated by low temperature irradiation of the sample.

The bulk material of TiO_2 has a band gap of 3.23 eV with the valence band edge of + 2.6 eV (vs NHE), and the conduction band edge of – 0.6eV (vs NHE).[14] Irradiation of TiO_2 with light of energy higher than the bad gap (λ<380nm) therefore, leads to generation of electron-hole pairs. These charge carriers can be trapped at several centres; the electrons in Ti^{4+} ions (at the bulk or the surface)[10] whilst holes at bulk or surface anions as shown in equation 5.9

$$TiO_2 \xrightarrow{h\nu} (e^- + h^+)TiO_2 \qquad (5.9)$$

The positive holes can be trapped by lattice oxide ions equation 5.9, and at surface hydroxyl groups forming hydroxyl species as demonstrated in equations 5.10 and 5.11.[35]

$$Ti^{4+} - O^{2-} + h^+ \longrightarrow Ti^{4+} - O^- \qquad (5.10)$$

$$OH^- + h^+ \longrightarrow OH^\bullet \qquad (5.11)$$

Studies by Nakaoka and Nosaka,[36] also reported the simultaneous generation of a trapped hole and trapped electron on a TiO_2 surface. The trapped hole was assigned to a photoproduced hole trapped at the lattice oxygen atoms located in the subsurface layer of the TiO_2. The assignment of this species was in agreement with Howe and Gratzel[10] who suggested the radical has a structure of $Ti^{4+}O^-Ti^{4+}OH^-$, and a set of g values with $g_1 = 2.002$, $g_2 = 2.012$ and $g_3 = 2.016$. However, the results presented here (figure 5.6) are concerned with the stabilisation of the species on an activated dehydrated form of the TiO_2 material, since no layer of hydroxyl groups were present.

Micic *et al.*,[14,15] reported that the holes produced by band gap irradiation of a TiO_2 colloid move from the oxygen lattice to the surface and are trapped directly on oxygen atoms bound to the Ti^{IV} atoms. The results obtained with TiO_2 colloids prepared with oxygen – 17 enriched water support the identification of trapped holes as an oxygen surface anion radical covalently bound to titanium atoms, $Ti^{4+}O^{2-}Ti^{4+}O^-$. The results obtained here are consistent with the conclusions of Howe and Gratzel[10] that the hole adduct is a subsurface oxygen anion radical.

The generation of trapped holes and electrons by UV irradiation were also attempted on the dehydrated forms of P25 Anatase and Rutile B. However, following UV irradiation of the materials only a signal due to a trapped hole was stabilised on the surface and no photogenerated Ti^{3+} was observed. During the UV irradiation of the lower surface area materials, the excess oxygen acts as a very efficient electron scavenger inhibiting the formation of Ti^{3+}, forming O_2^- which is only observed following removal of the excess oxygen from the cell. Details of this mechanism will be discussed later in chapter 6.

5.5 Conclusions

In order to obtain a full understanding of the surface interactions between TiO_2 oxides and a variety of adsorbates, an understanding of the surface morphological states at the molecular level is required. Thus, knowledge of the conditions leading to the formation of the generated trapped charge carrier pairs (i.e., holes and electrons) is extremely important in the understanding of surface interactions. Analysis of the carefully controlled pre-treatment conditions, which lead to the formation of Ti^{3+} ions, and trapped holes in TiO_2 have been summarised in this table 5.3. As evidenced in this chapter, and summarised in table 5.3, the trapped charge centres can be generated in a number of ways i.e., both thermally and photo-initiated, allowing comparison of the methods used and the species formed.

During the thermal activation of TiO_2 the EPR spectra indicated the formation of two trapped electron centres (i.e., localised conduction electrons and reduced Ti^{3+} sites). By comparison, no experimental evidence of a trapped hole was witnessed following thermal reduction[5] as expected. The relative intensities of the Ti^{3+} formation varied form sample to sample, as the higher surface area materials tend to produce a more intense EPR signal following thermal reduction.

Table 5.3. Summary of the pre-treatment conditions and their effects on the activation of the TiO_2 samples.

Activation procedure	**Effect on TiO_2**
Heat at > 873 K *in vacuo*	Extensive surface reduction (defect formation) Extensive sub-surface reduction
Heat at 823K *in vacuo*	Extensive surface reduction Moderate sub surface reduction
Heat at 723 to 773K *in vacuo*	Moderate surface reduction Low sub-surface reduction
1. Heat at 723 to 823 K *in vacuo* 2. Anneal in O_2 (10 Torr) at 723 to 823K	1. Moderate surface reduction 2. Surface re-oxidation, vacancy restoration
Heat at 823K in H_2 atmosphere	Extensive surface reduction Moderate sub-surface reduction

Knowledge of the surface:bulk ratio of Ti^{3+} formation during various reduction temperatures provides an understanding of the most favourable temperature to use in order to create the optimum concentration of surface Ti^{3+} cations with a minimum interference from the bulk Ti^{3+} species. As demonstrated here and previously reported[18] increasing the temperature of reduction increases the formation of bulk Ti^{3+} and therefore decreases the ratio of surface to bulk Ti^{3+} formation.

Under a reductive atmosphere of hydrogen, the TiO_2 sample undergoes reduction when heated to temperatures over 600K. No formation of electrons trapped at Ti^{4+} sites as Ti^{3+} cations and localised conduction electrons are observed without any form of thermal treatment.

By comparison to the 'dark' experiments previously discussed, trapped charge carriers can also be generated by UV irradiation of an activated TiO_2 sample at low temperature. In this case however both the Ti^{3+} centres and trapped hole O^- species can be formed under UV irradiation. Both UV generated species were observed simultaneously on the surface at low temperature.

The lifetime of the generated surface trapped charge carrier pairs (i.e., electrons and holes) was notably different for those produced under 'dark' conditions and those under UV irradiation. During thermal reduction the Ti^{3+} and localised conduction electrons formed are stable at room temperature, and a loss in Ti^{3+} intensity occurs only after several hours. However, the UV generated trapped hole (O^-) and Ti^{3+} where both reported to be unstable following gentle warming to 300 K.

During both methods of thermal treatment no trapped holes were observed, only Ti^{3+} cations and localised conduction electrons were observed in the EPR data collected. However, under UV conditions trapped electrons and trapped holes are produced but no signal due to localised conduction electrons are observed.

As demonstrated in this chapter the formation of trapped charge carrier states can be produced both thermally and under photo-irradiated conditions. The formation of the charge carriers required or produced depends on the pre-treatment conditions used. In addition to this the role of varying surface morphologies (i.e., P25 Anatase, Rutile A and Rutile B) and surface areas of the TiO_2 samples have also demonstrated the differences that can occur during the generation and formation of these trapped charge carriers. Therefore, in order to obtain a full understanding of the surface interactions between TiO_2 and adsorbates the type of TiO_2 material used must be considered along with the pre-treatment conditions.

5.6 References

1. J. B. Lowekamp, G. S. Rohrer, P. A. Morris, J. D. Bolt, W. E. Farneth, *J. Phys. Chem. B*, **102**, 7323, (1998).
2. P. A. Morris Hotsenpiller, J. D. Bolt, W. E. Farneth, J. B. Lowekamp, G. S. Rohrer, *J. Phys. Chem. B*, **102**, 3216, (1998).
3. T. A. Egerton, E. Harris, E. J. Lawson, B. Mile, C. C. Rowlands, *Phys. Chem. Chem. Phys.*, **2**, 3275, (2000).
4. P. Claus, A. Brückner, C. Mohr, H. Hofmeisteer, *J. Am. Chem. Soc.*, **122**, 11430, (2000).
5. C. A. Jenkins, PhD Thesis, University of Wales, Cardiff (1998).
6. E. Serwicka, M. W. Schlierkamp, R. N. Schindler, *Z. Naturforsch.*, **36a**, 226, (1981).
7. C. Naccache, P. Meriaudeau, M. Che, A. J. Tench, *Trans. Faraday Soc.*, **67**, 506, (1971).
8. R. D. Iyengar, M. Codell, J. Kara, J. Turkevitch, *J. Am. Chem. Soc.*, **88**, 5055, (1966).
9. R. F. Howe, M. Gratzel, *J. Phys. Chem.*, **89**, 4495, (1985).
10. R. F. Howe, M. Gratzel, *J. Phys. Chem.*, **91**, 3906, (1987).
11. R. D. Iyengar, M. Codell, *Adv. Colloid Interface. Sci.*, **3**, 365, (1972).
12. M. Che, C. Naccache, B. Imelik, M. Prettre, *C. R. Acad. Sci. Ser. C.*, **264**, 1901, (1967).
13. J. Kiwi, J. T. Suss, S. Szopiro, *Chem. Phys. Lett.*, **106**, 135, (1984).
14. O. I. Micic, Y. Zhang, K. R. Cromack, A. D. Trifunac, M. C. Thurnauer, *J. Phys. Chem.*, **97**, 7277, (1993).
15. O. I. Micic, Y. Zhang, K. R. Cromack, A. D. Trifunac, M. C. Thurnauer, *J. Phys. Chem.*, **97**, 13284, (1993).
16. D. Zwingwl, *Solid State Commun.*, 20, 397, (1976).
17. M. Che, A. J. Tench, *J. Adv. Catal.*, 31, 77, (1982).
18. C. A. Jenkins, D. M. Murphy, *J. Phys. Chem. B*, **103**, 1019, (1999).
19. M. Chiesa, G. Amato, L. Boarino, E. Garrone, F. Geobaldo, E. Giamello, *Angew. Chem. Int. Ed.*, **42**, 5032, (2003).
20. T. G. Gray, C. C. McCain, N. G. Masse, *J. Phys. Chem.*, **63**, 472, (1959).
21. Z. Sojka, *Catal. Rev. Sci. Eng.*, **37**, 461, (1995).
22. B. Regan, M. Gratzel, *Nature*, **353**, 737, (1991).

23. M. A. Henderson, *Surf. Sci.*, **343**, L1156, (1995).
24. Gopel W. Anderson, *Surf. Sci.*, **139**, 333, (1984).
25. H. Idriss, K. S. Kim, M. A. Barteau, *Surf. Sci.*, **113**, 262, (1992).
26. M. S. Lazarus, T. K. Sham, *Chem. Phys. Lett.*, **92**, 670, (1982).
27. Q. Zhong, J. M. Vohs, D.A. Bonnell, *J. Am. Ceram. Soc.*, **76**, 1137, (1993).
28. H. Liu, H. T. Ma, X. Z. Li, W. Z. Li, M Wu, X. H. Bao, *Chemosphere*, **50**, 39, (2003).
29. K. Okamoto, Y. Yamamoto, H. Tanaka, M. Tanaka, A. Itaya, *Bull. Chem. Soc. Jpn.*, **58**, 2015, (1985).
30. L. A. Harris, R. Schumacher, *J. Electrochem. Soc.: Solid State Sci Techno.*, **127**, 1186, (1980).
31. Y. X. Chen, Z. B. Wei, Y. X. Chen, H. H. Li, Z. P. Hong, H. Q. Liu, Y. L. Dong, C. U. Yu, W. Z. Li, *J. Mol. Catal.*, **21**, 275, (1983).
32. D. Qin, W. Chang, Y. Chen, M. Gong, *J. Catal.*, **142**, 2, 719, (1993).
33. J. E. Rekoske, M. A. Barteau, *J. Phys. Chem. B*, **101**, 7, 1113, (1997).
34. A. Heller, Y. Degani, D. W. Johnson Jr., P. K. Gallagher, *J. Phys. Chem.*, **91**, 23, 5987, (1987).
35. A. L. Attwood, D. M. Murphy, J. L. Edwards, T.A. Egerton, and R. W. Harrison. *Res. Chem. Intermed.*, **29**, 449, (2003).
36. Y. Nakaoka, Y. Nosaka. *J. Photochem. Photobiol. A: Chem.*, **110**, 299, (1997)

Chapter 6

Formation of Oxygen Centred Radicals over Thermal Reduced and Photo-Irradiated TiO_2

6.1 Introduction

Photocatalytic reactions involving semiconductor metal oxides have a wide range of applications as discussed earlier (*cf.* chapter 1). The successful application of these materials relies on the photocatalytic reactions that occur at the oxide surface. An understanding of the interfacial photochemistry at the molecular level, particularly the fundamental chemistry of electron and hole transfer to the adsorbed substrate, is therefore considered central to the design of more improved photocatalysts with high quantum yields.

Several types of oxygen species have been characterised and proposed as reaction intermediates in photocatalytic processes; some of these include mononuclear oxygen anion (O^-), superoxide (O_2^-), ozonide (O_3^-), hydroxy ($HO^\bullet$), hydroperoxy ($HO_2^\bullet$), alkylperoxy ($ROO^\bullet$), or other precusor states such as hydrogen peroxide (H_2O_2) or singlet oxygen ($^1O_2$).[1-14] These radicals are formed by interfacial charge transfer at the gas-solid interface, and provided the lifetime of the radicals are sufficiently long, many can be unambiguously detected by EPR. For example, superoxide anions are easily formed by interfacial electron transfer from trapped electron sites to adsorbed dioxygen ($Ti^{3+}_{surf} + O_2 \longrightarrow Ti^{4+} \ldots O_2^-$), and it has been reported that the anions can react with protons on the hydrated surface producing hydroperoxy radicals ($O_2^- + H^+ \longrightarrow HO_2^\bullet$). Both radicals produce very characteristic spin Hamiltonian EPR parameters. On the other hand the positive holes can be trapped by lattice oxide ions ($Ti^{4+} + O^{2-} + h^+ \longrightarrow Ti^{4+} - O^-$) and at surface hydroxyl groups forming hydroxy radicals ($OH^- + h^+ \longrightarrow OH^\bullet$). The formation of ozonide radicals by reaction of molecular oxygen with a trapped hole has also been reported ($Ti^{4+} - O^- + O_2 \longrightarrow Ti^{4+} \ldots O_3^-$).[9] Other competing surface reactions may also occur, leading to a decrease in surface radical concentration, such as the recombination of surface hydroxy radicals producing additional radical species ($2OH^\bullet \longrightarrow H_2O_2$, and $H_2O_2 + OH^\bullet \longrightarrow O_2H^\bullet + H_2O$), or continued capture of photogenerated electrons producing diamagnetic species ($O_2^- + e \longrightarrow O_2^{2-}$) not visible by EPR.

The complexity of the interfacial reactions, coupled with the variabilities in the abundance, nature and lifetime of the radicals as a function of surface treatment or morphology, suggests that the nature of the active oxygen species may change during the reaction conditions. While EPR provides clear evidence for the existence of the stable surface oxygen radicals, it may not readily detect transient unstable species, which may be more reactive and participate more extensively in the photocatalytic process, at the expense of the long-lived EPR visible species. In this chapter it will be demonstrated that the nature of the surface paramagnetic oxygen species can change depending on the pre-treatment conditions and nature of the surface, and thereby illustrate the importance of studying these surface radicals under various conditions to fully understand the initial electron-transfer reaction process.

Therefore, in this chapter a number of different methods have been employed in order to study the generation of the surface oxygen radicals. These methods include,

- (A) Radical formation (O_2^-) over a thermally reduced TiO_2,
- (B) Radical formation (O_2^-) over UV irradiated TiO_2,
- (C) Radical formation (O_2^-) over a UV irradiated sample of TiO_2 that has been hydrated.

As discussed later in the chapter, the superoxide anion is an excellent probe of surface heterogeneity and therefore for comparison purposes, a number of experiments have also been carried out using NO as a complimentary probe of the surface.

6.2 Experimental

A detailed treatment of the experimental methods used in the handling of the powders, manipulation of the samples on the vacuum line and operation of spectrometers was thoroughly described in chapter 4. In this section, the specific experimental conditions used in the preparation and study of the oxygen centred radicals will be outlined.

6.2.1 Thermal activation of polycrystalline TiO_2 under vacuum.

Throughout the work described in this chapter the titanium dioxide, P25 Anatase (*Degussa*) with a surface area of *ca.* 49 m^2g^{-1} was used, along with a Rutile sample hereafter labelled Rutile A with a surface area of *ca.* 135 m^2g^{-1} this material

was synthesised by hydrolysis of an aqueous solution (about 5 M) of $TiCl_4$ [15] A second Rutile sample, hereafter labelled Rutile B sample with a surface area of *ca.* 97 m^2g^{-1} supplied by Huntsman Tioxide was also used in this work. Each TiO_2 sample (*ca.* 5mg) was initially evacuated to a residual pressure of 10^{-4} Torr at 298 K in an EPR quartz cell. The polycrystalline TiO_2 powders were initially evacuated to a residual pressure of 10^{-4} Torr at 298K. The samples were then heated to 393K under vacuum overnight in order to remove any physisorbed water from the surface.

The samples were then slowly heated under vacuum to a final temperature of 823 K (over a 5 hour period), and held at this temperature for approximately 1 hour. Under these conditions the TiO_2 surface is reduced, as the lattice O^{2-} anions are removed, producing a non-stoichiometric surface containing an excess of Ti^{3+} cations. The reduced powder (is blue in colour due to the excess number of Ti^{3+} centres[5]) was then cooled to 298 K and exposed to oxygen (10 Torr) at this temperature for 5 minutes. The excess oxygen was subsequently evacuated at room temperature before any EPR measurements were taken. The high purity O_2 gas was supplied by *BOC Ltd.* ^{17}O-labelled dioxygen gas (63% enrichment) was supplied by *Icon Services Inc.* (New Jersey) and used without further purification.

6.2.2 UV irradiation of polycrystalline TiO_2

Following initial evacuation of the polycrystalline powders (*ca.* 5mg) to a residual pressure of 10^{-4} Torr at 298 K in an EPR quartz cell, the samples were then heated to 393 K under vacuum overnight in order to remove any physisorbed water from the surface. The polycrystalline TiO_2 samples were then subsequently slowly heated (over a 5 hour period) to a temperature of 823 K, and held at this temperature for approximately 1 hour. Oxygen (50 Torr) was added to the sample at 823 K and the samples cooled to room temperature under the excess oxygen atmosphere. This produced a clean dehydrated surface free from contaminants or surface hydroxyls. Exposure of a thermally reduced TiO_2 surface to O_2 at 298 K leads to the formation of paramagnetic surface oxygen radicals (i.e., O^-, O_2^- or O_3^- as discussed later). However, exposure of TiO_2 to O_2 at high temperatures (823 K) leads to the formation of diamagnetic surface O^{2-} lattice anions, as the surface is effectively re-oxidized at this high temperature. At no time during this treatment were the samples exposed to air, thus ensuring that the surface remained clean.

Prior to UV irradiation of the dehydrated samples oxygen (10 Torr) was added to the samples at room temperature before irradiation at 77 K for approximately 30 minutes. Following UV irradiation the excess oxygen gas was evacuated. A 1000 W *Oriel Instruments* UV lamp, incorporating a Hg/Xe arc lamp (250 nm to 2500 nm), was used for all irradiations in the presence of a water filter. The UV output below 280 nm accounts for only 4 – 5% of the total lamp output.

6.2.3 UV irradiation of hydrated polycrystalline TiO_2

As stated above, the previous method of preparation was used in order to produce clean dehydrated TiO_2 surfaces. However, the samples were subsequently exposed to water in two different ways in order to study the effects of surface hydration on the nature of the photogenerated oxygen radicals. The two forms of surface hydration are referred to as (i) *fully hydrated* and (ii) *partially hydrated.*

Following activation of the polycrystalline TiO_2 surfaces (as described above), the vapours of triply distilled water (10 Torr) were added to the samples under vacuum at 673 K for 1 hour. The water was purified by repeated freeze-pump-thaw cycles before use. The samples were subsequently evacuated at 298 K for 30 minutes to remove the excess physisorbed water molecules. The samples hereafter will be referred to as a *fully-hydrated* surface. Before UV irradiation of the hydrated surfaces oxygen (10 Torr) was added at 298 K.

In order to produce a partially–hydrated surface, a mixture of oxygen and water vapour (10:1 ratio; 10 Torr pressure) were co-adsorbed at 298 K on the clean dehydrated TiO_2 surfaces. The samples hereafter will be referred to as a *partially-hydrated* surface. The partially-hydrated samples were then UV irradiated at low temperature under the excess mixture for 30 minutes

6.2.4 Addition of NO probe gas

Throughout this section of study only the P25 Anatase and Rutile B samples were examined. Prior to any NO adsorption clean dehydrated TiO_2 surfaces free from contaminants and surface hydroxyls were prepared (*cf.* section 6.2.2). The NO gas (5, 20 and 40 Torr) was then added at 298 K to the TiO_2 samples. The NO (ex. *Argo*) gas was purified by repeated freeze-pump thaw cycles before use, to remove any oxygen.

6.2.5 Measurement of EPR spectroscopy

The EPR spectra were recorded on a Bruker ESP 300E series spectrometer incorporating an EPR 4102 ST rectangular cavity. All spectra were recorded at X-band frequencies, 100 kHz field modulation and 10 mW microwave power. The g values were obtained using a Bruker ER035M NMR gaussmeter calibrated using the perylene radical cation in concentrated H_2SO_4 (g = 2.002569). EPR computer simulations were performed using the SIM14S program (QCPE 265).

6.3 Results A: Radical Formation on Thermally Reduced TiO_2

6.3.1 Thermal reduction of P25 Anatase TiO_2.

When the TiO_2 sample was heated under vacuum to 823 K and held at this temperature for 1 hour a blue coloured powder was produced, indicative of the Ti^{3+} cation formation (*cf.* chapter 5). Addition of oxygen gas (10 Torr) at 298 K to the reduced material caused the powder to be bleached almost immediately. The resulting EPR spectrum was recorded at low temperature (100 K) and is shown in figure 6.1.

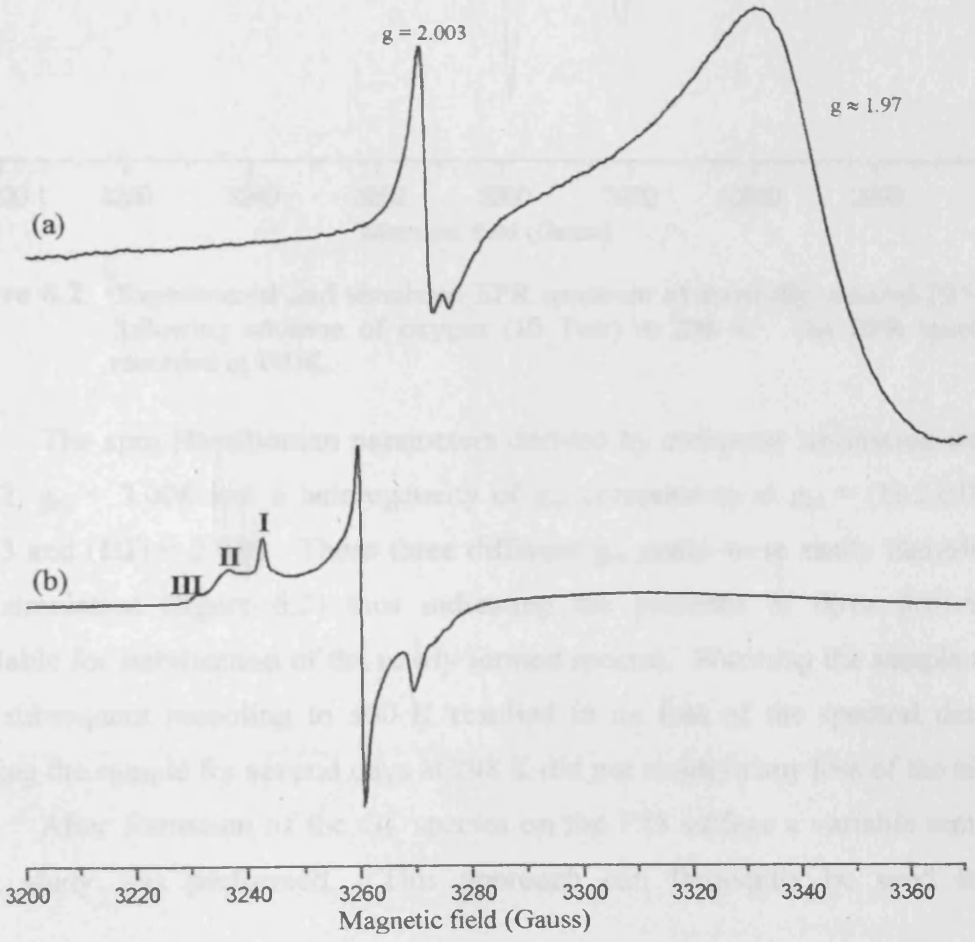

Figure 6.1. X-band EPR spectra (100K) of P25 Anatase after (a) thermally reduced at 823 K for 1 hour and (b) addition of oxygen at 298 K.

The signal due to the Ti^{3+} centres has virtually disappeared and is replaced by the easily recognisable signal due to O_2^- (figure 6.1b). The latter signal is particularly well resolved in the g_{zz} region, and the distribution of sites responsible for this profile (discussed later) were further highlighted by computer simulation (see figure 6.2).

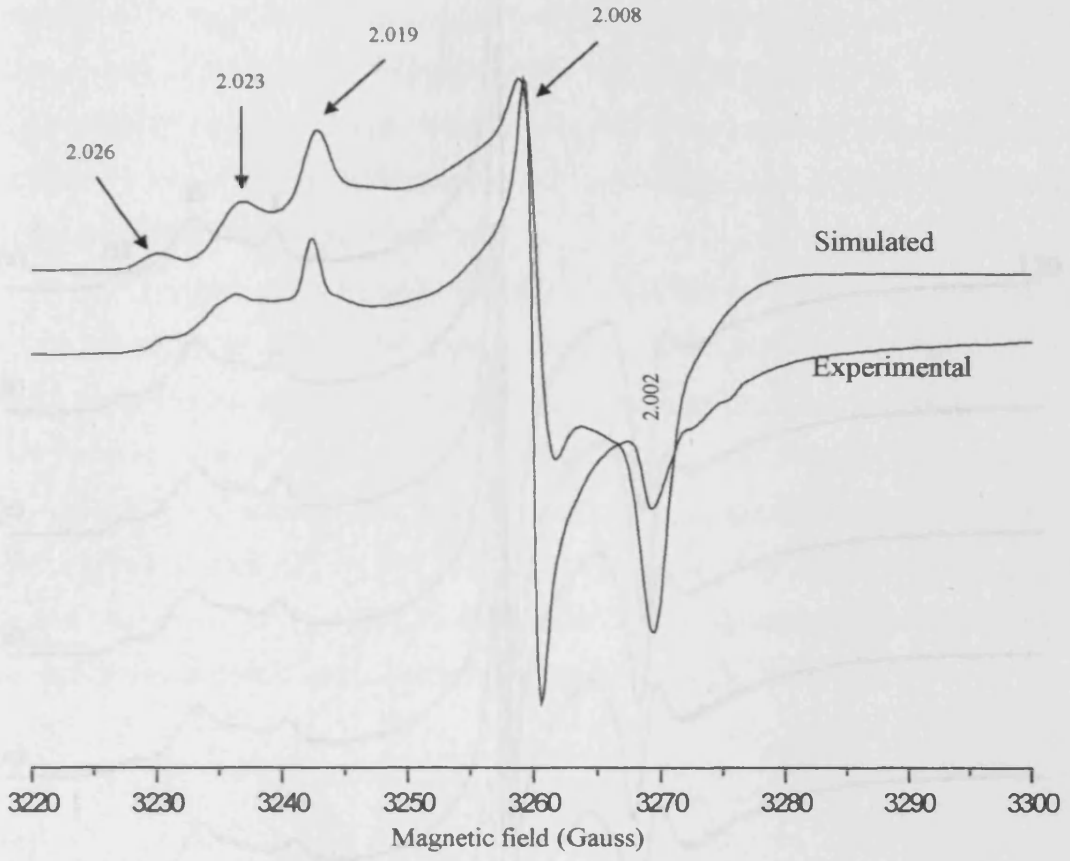

Figure 6.2. Experimental and simulated EPR spectrum of thermally reduced P25 Anatase, following addition of oxygen (10 Torr) at 298 K. The EPR spectrum was recorded at 100K.

The spin Hamiltonian parameters derived by computer simulation were g_{xx} = 2.002, g_{yy} = 2.008 and a heterogeneity of g_{zz} components at g_{zz} = (**I**) 2.019, (**II**) = 2.023 and (**III**) = 2.026. These three different g_{zz} peaks were easily identified from the simulation (figure 6.2) thus indicating the presence of three different sites available for stabilisation of the newly formed species. Warming the sample to 298 K and subsequent recooling to 100 K resulted in no loss of the spectral data. Also leaving the sample for several days at 298 K did not result in any loss of the signal.

After formation of the O_2^- species on the P25 surface a variable temperature EPR study was performed. This approach can frequently be used to obtain

information on the local mobility and rotational dynamics of the adsorbed species on the surface.[16,17] The resulting series of spectra are shown in figure 6.3.

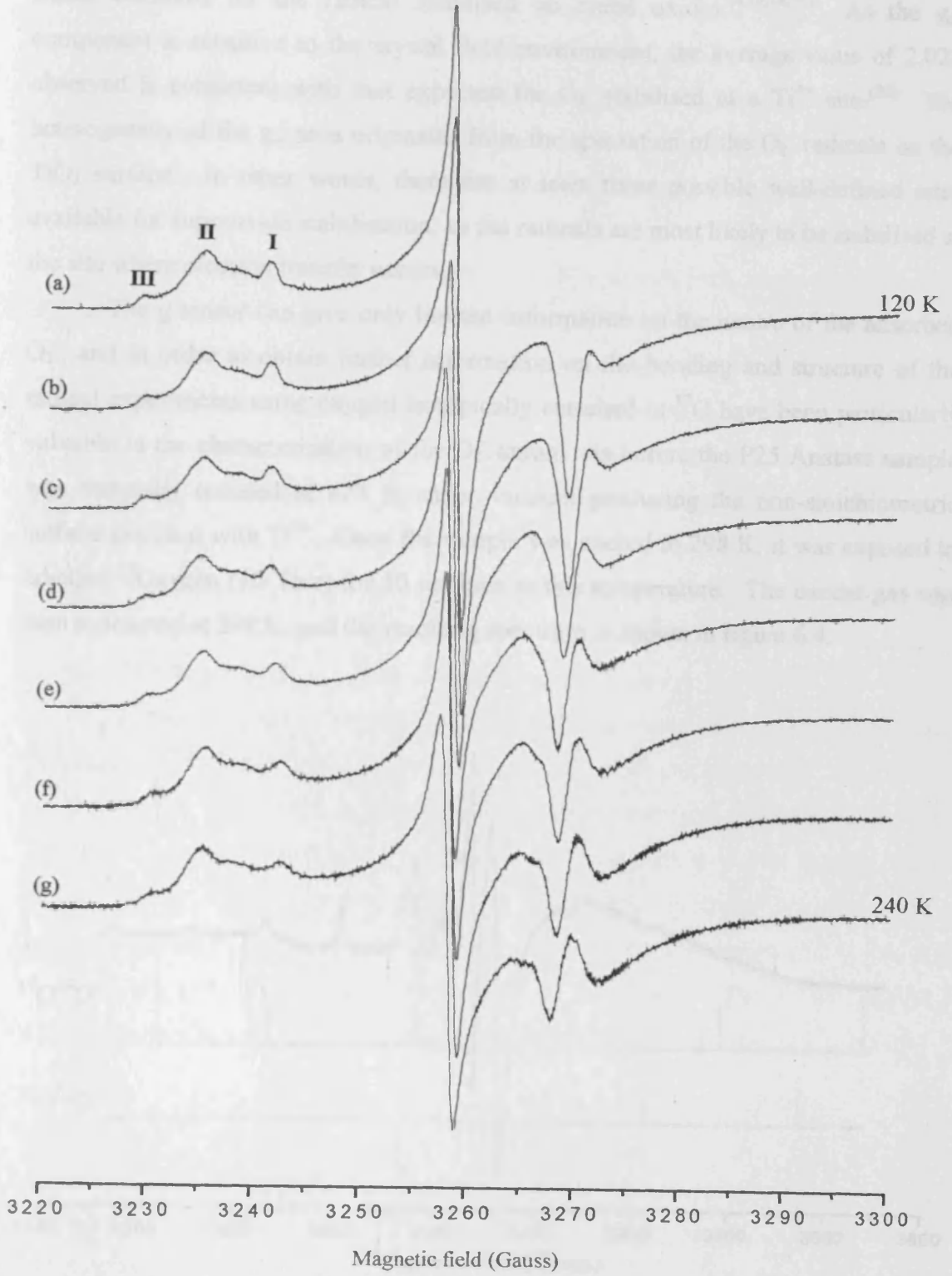

Figure 6.3. X band EPR spectra of P25 Anatase following thermal reduction at 823 K and addition of oxygen (10 Torr) at 298 K. The resulting spectra were recorded at (a) 120 K, (b) 140 K, (c) 160 K, (d) 180 K, (e) 200 K, (f) 220 K, and (g) 240 K.

As seen in figure 6.3 upon increasing the temperature at which the spectrum was recorded, the intensity of the signal was found to decrease slightly. The signal in figures 6.1 to 6.3 can easily be assigned to the O_2^- anion based on the characteristic g tensor elements for the radical stabilised on metal oxides.[8,16,18,19] As the g_{zz} component is sensitive to the crystal field environment, the average value of 2.022 observed is consistent with that expected for O_2^- stabilised at a Ti^{4+} site.[20] The heterogeneity of the g_{zz} area originates from the speciation of the O_2^- radicals on the TiO_2 surface. In other words, there are at least three possible well-defined sites available for superoxide stabilisation; as the radicals are most likely to be stabilised at the site where electron transfer occurs.

The g tensor can give only limited information on the nature of the adsorbed O_2^-, and in order to obtain further information on the bonding and structure of the radical experiments using oxygen isotopically enriched in ^{17}O have been particularly valuable in the characterisation of the O_2^- anion. As before the P25 Anatase sample was thermally reduced at 823 K under vacuum producing the non-stoichiometric surface enriched with Ti^{3+}. Once the sample was cooled to 298 K, it was exposed to labelled ^{17}Oxygen (10 Torr) for 10 minutes at this temperature. The excess gas was then evacuated at 298 K, and the resulting spectrum is shown in figure 6.4.

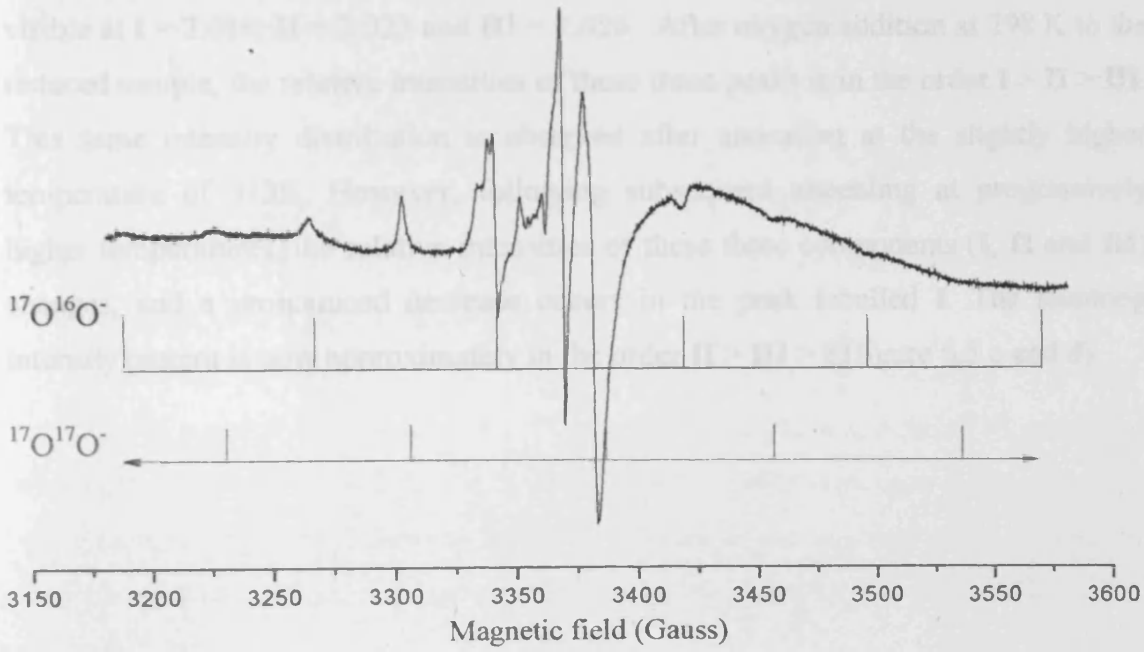

Figure 6.4. Experimental EPR spectrum, of P25 Anatase after thermal reduction at 823 K, followed by the addition of ^{17}O-labelled oxygen of 63% isotopic enrichment (10 Torr). The EPR spectrum was recorded at 10 K.

The nucleus of ^{17}O has a spin of I = 5/2[21] and for exactly equivalent oxygen nuclei then ($^{17}O^{16}O^-$) and ($^{16}O^{17}O^-$) will produce a sextet hyperfine pattern with a coupling of 77 G. The presence of these two-labelled species ($^{17}O^{16}O^-$ and $^{16}O^{17}O^-$) indicates that the predominant species must be a diatomic form of oxygen in which both nuclei are equivalent. The $^{17}O_2^-$ results show that the unpaired spin density is similar in both oxygen nuclei and the electron must be regarded as distributed over the entire molecular ion. The observed hyperfine pattern is identical to that expected for the 'side-on' bonded ionic superoxide species, which will be discussed in greater detail later.

In the case of ($^{17}O^{17}O^-$) an 11-line hyperfine pattern with a significantly lower intensity, due to the lower probability of having $^{17}O^{17}O^-$ radicals, will be observed. The intensity of the outer lines in this 11-line pattern were too small to be observed, but nevertheless the inner lines could be clearly identified as seen in figure 6.4.

In order to obtain additional information about the TiO_2 surface stabilised O_2^- anion, the response of the radical to gentle annealing was investigated. This study provides information concerning the stability and diffusional characteristics of the radical. Following the formation of superoxide on the surface as before, the sample was heated to temperatures of 313, 333 and 353 K for periods of 15 minutes and the resultant EPR spectra (figure 6.5 b-d respectively) recorded at 100 K.

As shown earlier in figures 6.1 and 6.2, three distinctive g_{zz} components are visible at **I** = 2.019, **II** = 2.023 and **III** = 2.026. After oxygen addition at 298 K to the reduced sample, the relative intensities of these three peaks is in the order **I** > **II** > **III**. This same intensity distribution is observed after annealing at the slightly higher temperature of 313K. However, following subsequent annealing at progressively higher temperatures, the relative intensities of these three components (**I**, **II** and **III**) changes, and a pronounced decrease occurs in the peak labelled **I**. The resulting intensity pattern is now approximately in the order **II** > **III** > **I** (figure 6.5 c and d).

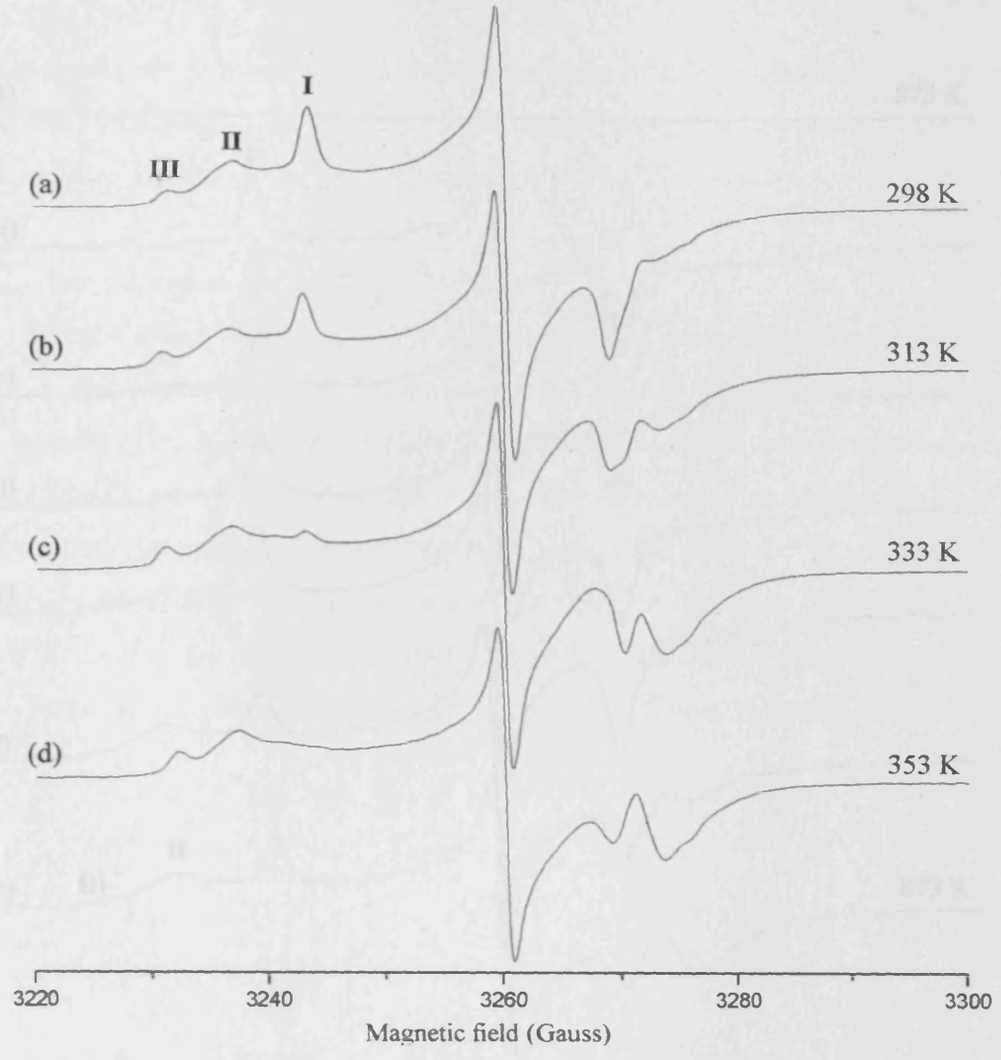

Figure 6.5. EPR spectra (100K) of O_2^- on a thermally reduced P25 Anatase sample after annealing at (a) 298 K, (b) 313 K, (c) 333 K and (d) 353 K.

It should be mentioned that the resonance at $g_{xx} = 2.002$ in figures 6.1, 6.2 and 6.5 is due to the existence of the localised conduction electron. The presence of the additional O_2^- charge on the surface causes the signal to change and the resonance to suffer some distortion, as discussed in chapter 5.

In order to determine the optimum temperature of reduction at which formation of superoxide is favoured, a P25 Anatase sample was reduced at increased temperatures 573 K to 873 K in 50 K intervals. Following each new reduction temperature, oxygen (10 Torr) was added to the sample for a period of 10 minutes at room temperature before evacuation. The resulting spectra recorded at 100 K are shown in figure 6.6.

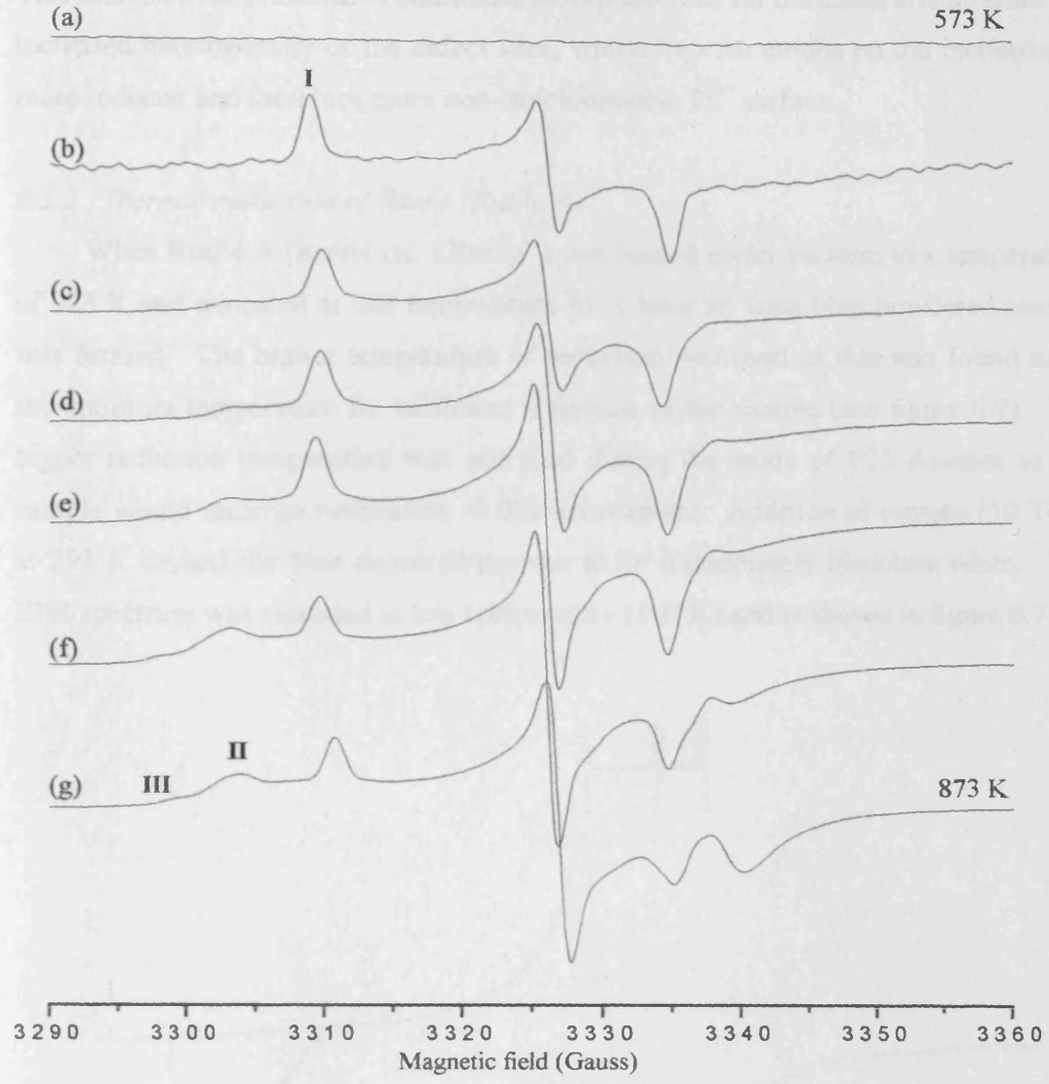

Figure 6.6. X band EPR spectra (100 K) of P25 Anatase, following thermal reduction at increasing temperatures; (a) 573 K, (b) 623 K, (c) 673 K, (d) 723 K, (e) 773 K, (f) 823 K (g) 873 K and addition of oxygen (10 Torr) at 298 K.

As shown in figure 6.6, at the lowest temperature of reduction 573 K no evidence of superoxide stabilisation on the surface was observed. Thermal reduction of the sample at this temperature resulted in the generation of bulk interstitial Ti^{3+} at g = 1.99 (*cf.* chapter 5 figure 5.7) but with no available surface Ti^{3+} for reduction of O_2.

Following reduction at 623 K, an orthorhombic signal with the g components g_{xx} = 2.002, g_{yy} = 2.008, g_{zz} = 2.018 is observed. The single g_{zz} component indicates the presence of a single adsorption site for the O_2^- anion on the TiO_2 surface at this temperature. However, as the temperature of reduction increases so does the complexity of the g_{zz} region; with the new features at g_{zz} = 2.023 and 2.026 emerging.

This indicates the presence of additional adsorption sites for the anion arising from the increased heterogeneity of the defect sites, which trap the anions on the increasingly more reduced and therefore more non-stoichiometric Ti^{3+} surface.

6.3.2. Thermal reduction of Rutile (Rutile A)

When Rutile A (Rutile *ca.* $130m^2g^{-1}$) was heated under vacuum to a temperature of 923 K and annealed at this temperature for 1 hour an aqua blue powdered sample was formed. The higher temperature of reduction was used as this was found to be the optimum temperature for sufficient reduction of the sample (see figure 6.9). The higher reduction temperature was not used during the study of P25 Anatase as the sample would undergo rutilisation at this temperature. Addition of oxygen (10 Torr) at 298 K caused the blue coloured powder to be immediately bleached white. The EPR spectrum was recorded at low temperature (100 K) and is shown in figure 6.7.

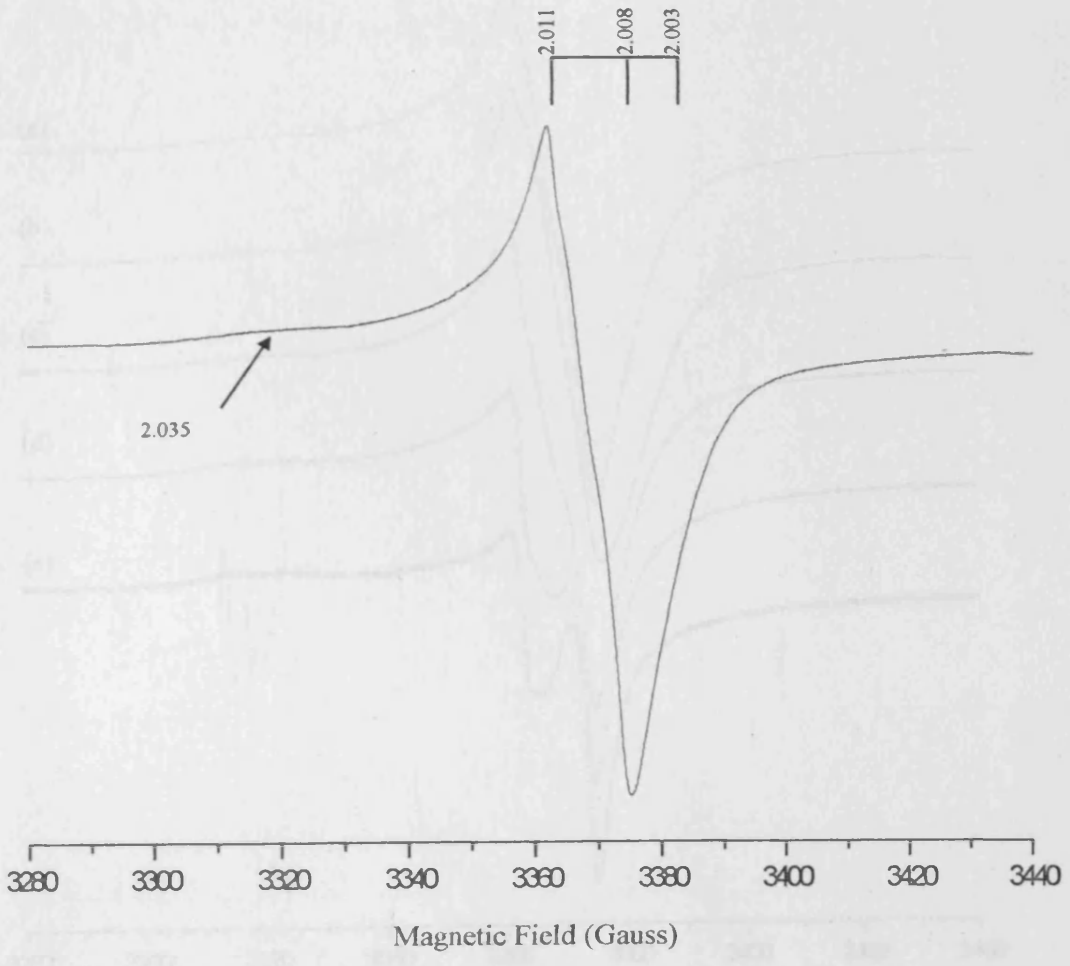

Figure 6.7. X band EPR spectra (100 K) of Rutile A, addition of oxygen (10 Torr) at 298 K after thermal reduction at 923 K.

As shown in figure 6.7, the resultant EPR spectrum displayed a signal with the spin Hamiltonian parameters g_{xx} = 2.003, g_{yy} 2.008 and g_{zz} = 2.011. The new EPR spectrum was virtually absent of any O_2^- formation. However, traces of a second signal with a g value of 2.035 have also been observed. This signal has been identified as a hydroperoxy radical ($HO_2^{\bullet}$) on the surface. The g_{zz} component of such species on TiO_2 is always *ca.* 2.034, and often used to identify the species.[16,20,22,23] A possible explanation for the existence of this radical is the incomplete removal of surface hydroxyls following thermal reduction of the sample. To prevent the formation of the $HO_2^{\bullet}$ complete removal of the surface hydroxyls are needed by thermal reduction at >923 K. To obtain further information about the identification of the former signal a variable temperature study was carried out as shown in figure 6.8.

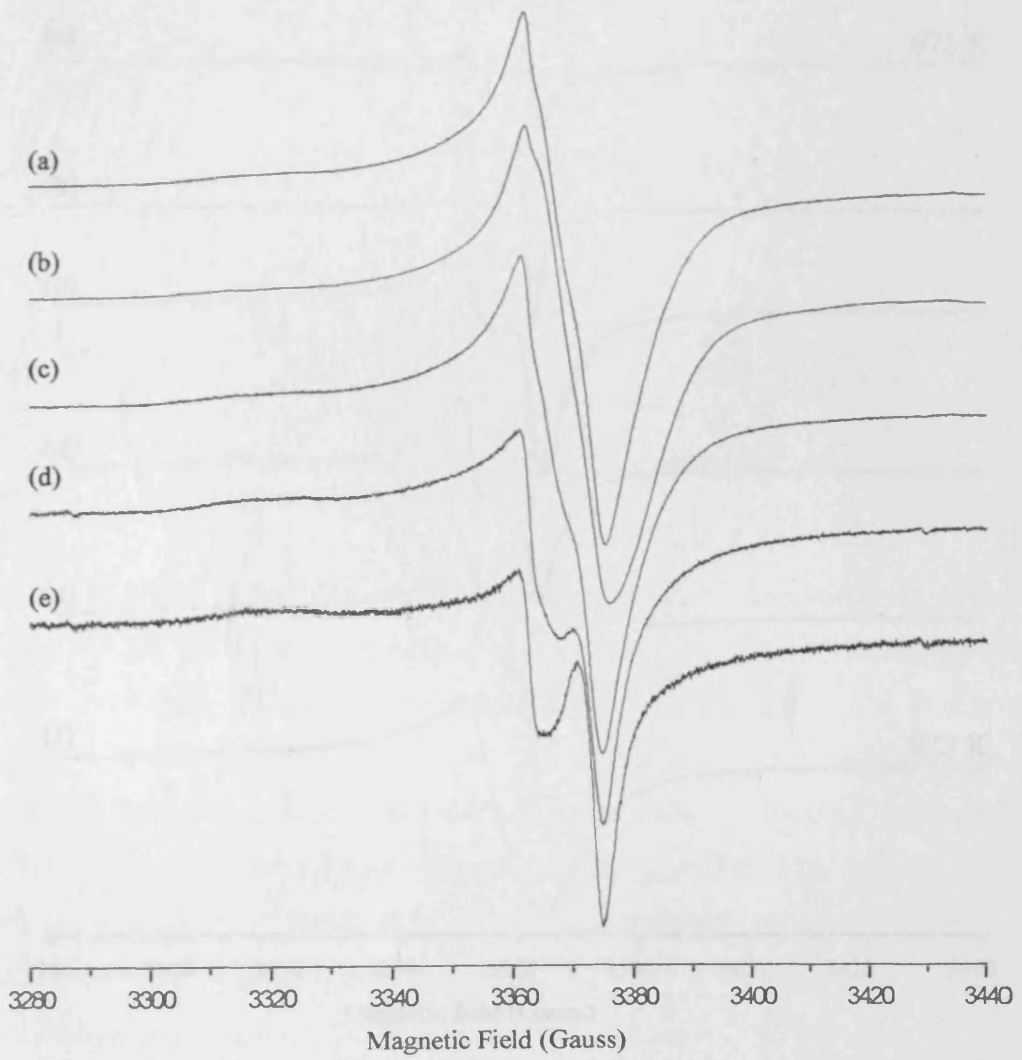

Figure 6.8. EPR spectra Rutile A after thermal reduction at 923 K and addition of oxygen (10 Torr) at 298 K. The EPR spectra were recorded at (a) 35 K, (b) 80 K, (c) 130 K, (d) 210 K and (e) 280 K.

As shown in figure 6.8 increasing the temperature from 35 to 280 K causes the resultant signal to alter due to the signal averaging out as the temperature approaches room temperature. The spin Hamiltonian parameters for the newly formed oxygen centred radical on the Rutile A surface can be easily assigned to the adsorbed ozonide O_3^- radical. Confirmation from the variable temperature study (figure 6.8) indicates the dynamic rotational characteristics of the anion at elevated temperatures which is a typical feature of the O_3^- anion.[9,16,20]

In order to determine the optimum temperature of TiO_2 reduction for maximum ozonide formation on the Rutile A material, the sample was thermally reduced at increasing temperatures from 673 K to 923 K in 50 K steps for periods of 1 hour. Oxygen (10 Torr) was then added to the sample at 298 K for 15 minutes. The resulting spectra were recorded at 100K and are shown in figure 6.9. It appears that the optimum temperature for O_3^- formation occurs at >923 K.

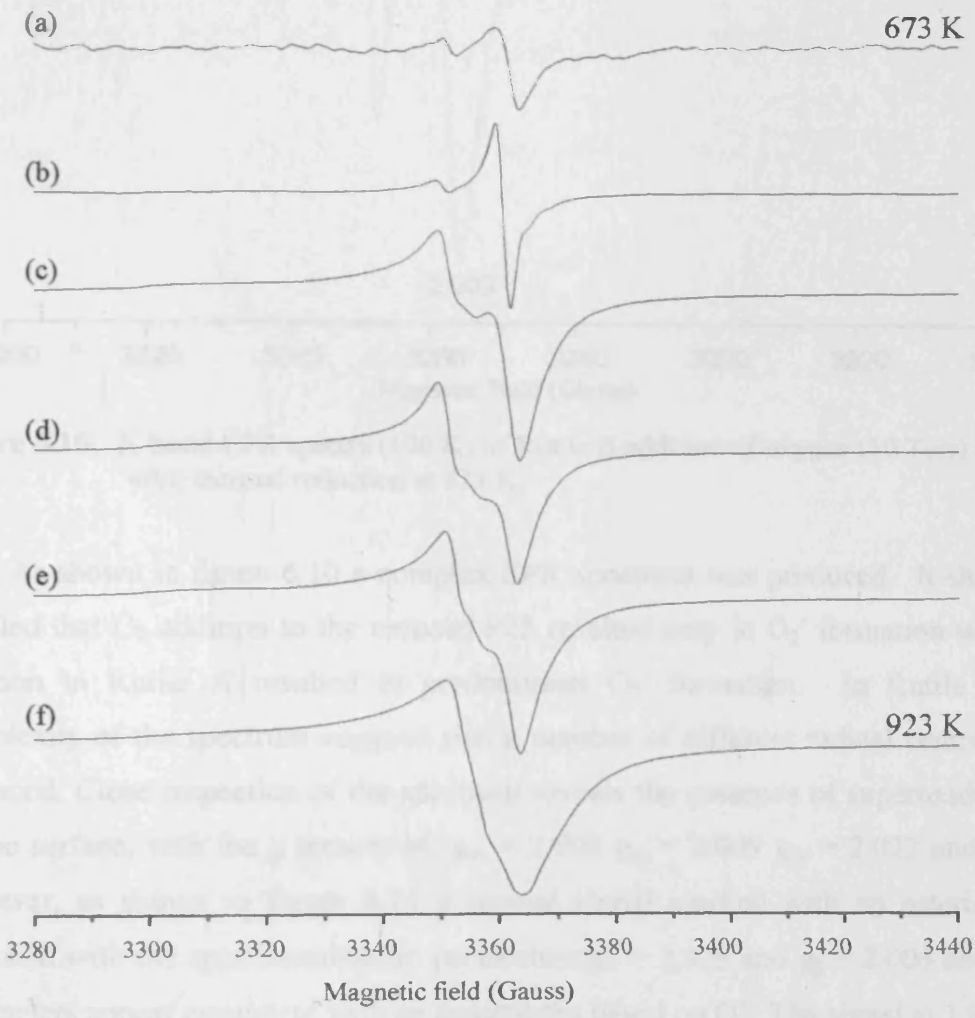

Figure 6.9. EPR spectra (100 K) of Rutile A following thermal reduction at increasing temperatures and subsequent O_2 addition at 298 K. The reduction temperatures were; (a) 673 K, (b) 723 K, (c) 773 K, (d) 823 K, (e) 873 K (f) 923 K.

6.3.3 Thermal reduction of Rutile (Rutile B)

When Rutile B (Rutile *ca.* $97m^2g^{-1}$) was heated under vacuum to a temperature of 823 K and held at this temperature for 1 hour a dark blue coloured powder was produced. Addition of oxygen (10 Torr) at 298 K to the reduced non-stoichiometric surface caused a lightening in colouration of the powder. The EPR spectrum of the reduced sample after addition of oxygen is shown in figure 6.10.

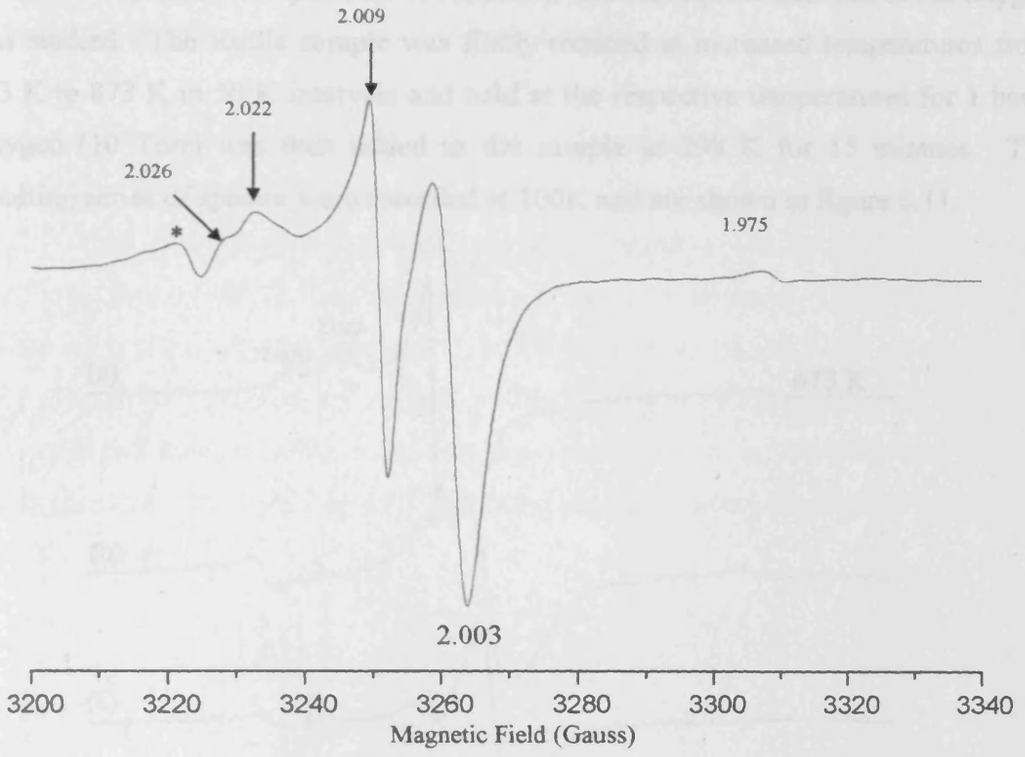

Figure 6.10. X band EPR spectra (100 K) of Rutile B addition of oxygen (10 Torr) at 298 K after thermal reduction at 823 K.

As shown in figure 6.10 a complex EPR spectrum was produced. It should be recalled that O_2 addition to the reduced P25 resulted only in O_2^- formation while O_2 addition to Rutile A resulted in predominant O_3^- formation. In Rutile B, the complexity of the spectrum suggests that a number of different radical centres were produced. Close inspection of the spectrum reveals the presence of superoxide anion on the surface, with the g tensors of, $g_{xx} = 2.003$ $g_{yy} = 2.009$ $g_{zz} = 2.022$ and 2.026. However, as shown in figure 6.11 a second signal marked with an asterisk * is produced with the spin Hamiltonian parameters $g_{\perp} = 2.029$ and $g_{\parallel} = 2.003$ and these parameters appear consistent with an assignment based on O^-. The signal at 1.975 has been attributed to Ti^{3+} centres in the bulk of the sample.

Furthermore, comparison of the integrated signal intensity in figure 6.10 compared to the signal of the reduced powder containing Ti^{3+} only, suggests that the new radicals are far less intense compared to the initial Ti^{3+} signal by approximately 60 %. This suggests that the majority of the reduced oxygen species following electron transfer from the Rutile surface producing diamagnetic centres.

In order to study the formation of the two radicals on the reduced Rutile B surface the optimum temperature of reduction and subsequent addition of the oxygen was studied. The Rutile sample was firstly reduced at increased temperatures from 673 K to 873 K in 50 K intervals and held at the respective temperatures for 1 hour. Oxygen (10 Torr) was then added to the sample at 298 K for 15 minutes. The resulting series of spectra were recorded at 100K and are shown in figure 6.11.

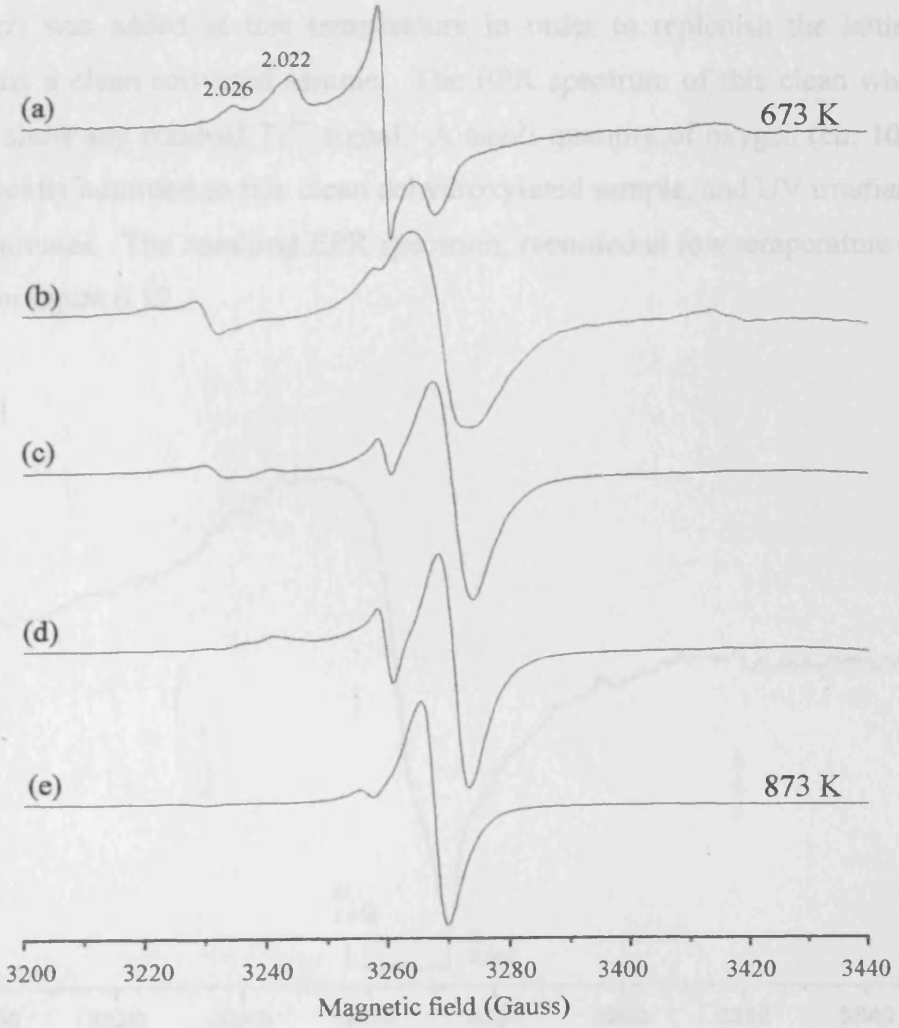

Figure 6.11. EPR spectra (100 K) of Rutile B following thermal reduction at increased temperatures (a) 673 K, (b) 723 K, (c) 773 K, (d) 823 K (e) 873 K after addition of oxygen (10 Torr) at 298 K.

Following thermal reduction to 673 K an orthorhombic signal with the spin Hamiltonian parameters g_{xx} = 2.003, g_{yy} = 2.009 and a heterogeneity of g_{zz} sites at 2.022 and 2.026 has been formed. The g tensors are characteristic of O_2^- formation, and the heterogeneity of the g_{zz} region displays two sites for O_2^- formation (figure 6.11a). However, increasing the temperature of reduction increases the complexity of the EPR spectra. The simultaneous stabilisation of both radicals (O_2^- and O^-) on the surface is observed at the higher temperature of reduction. Following thermal reduction at 873 K no traces of the O_2^- radical is seen.

Results B: Radical Formation Radiatively on Dehydrated TiO_2

6.3.4 UV irradiation of dehydrated P25 Anatase TiO_2.

When P25 Anatase (*ca.* 5mg) was heated under a vacuum to 823 K, oxygen (50 Torr) was added at this temperature in order to replenish the lattice oxygen, producing a clean activated sample. The EPR spectrum of this clean white powder did not show any residual Ti^{3+} signal. A small quantity of oxygen (*ca.* 10 Torr) was subsequently admitted to this clean dehydroxylated sample, and UV irradiated at 77 K for 30 minutes. The resulting EPR spectrum, recorded at low temperature (100 K), is shown in figure 6.12.

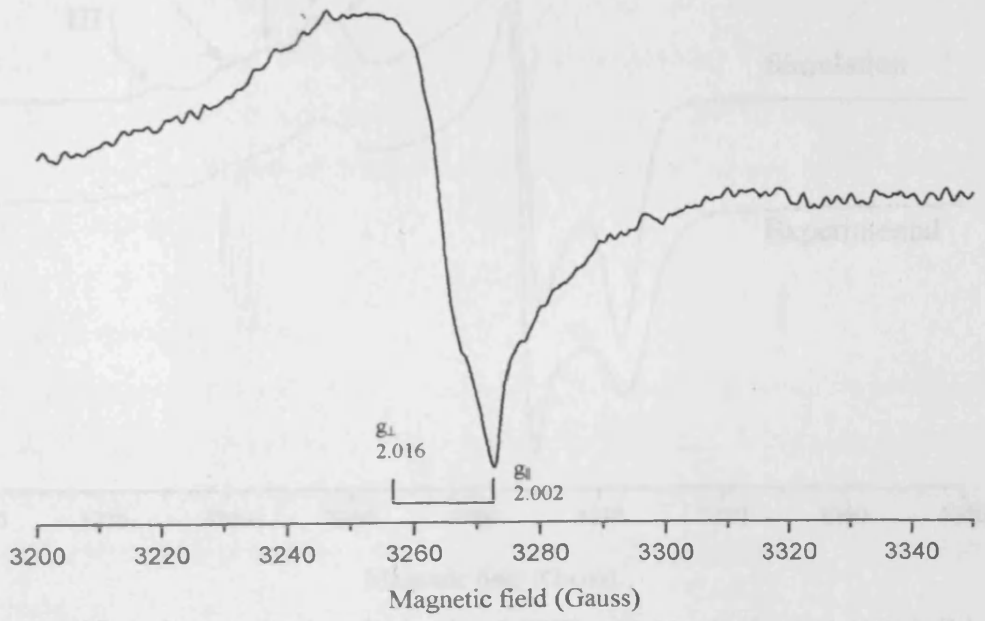

Figure 6.12. X band EPR spectrum (100 K) of fully dehydrated P25 Anatase following UV irradiation under oxygen atmosphere (10 Torr) at 77 K.

As displayed in figure 6.12 following low temperature UV irradiation a new signal, with spin Hamiltonian parameters of $g_{\perp} = 2.016$ and $g_{\parallel} = 2.002$ was produced. The species responsible for this signal was thermally unstable since gently warming the sample to room temperature caused the signal to disappear. Furthermore, the signal decayed in the dark at 100 K, after cessation of the illumination. However, regeneration of the signal could be done by UV irradiation at low temperature. The signal produced after UV irradiation under an oxygen atmosphere can be easily assigned to that of a trapped hole (O^-) stabilised on the surface based on the well known spin Hamiltonian parameters for surface holes (ie., $g_{\perp} = 2.016$ and $g_{\parallel} = 2.002$),. No photogenerated trapped electron centres (Ti^{3+}) were visible under these conditions since the sample was irradiated under an O_2 atmosphere (10 Torr). Therefore, the presence of any photogenerated surface radical of surface Ti^{3+} ion would be invisible due to the excess of O_2. As a result the sample was warmed to 298 K (which destroys the bulk O^- species) and the excess O_2 evacuated at that temperature. The experimental and simulated EPR spectra following oxygen evacuation are displayed in figure 6.13.

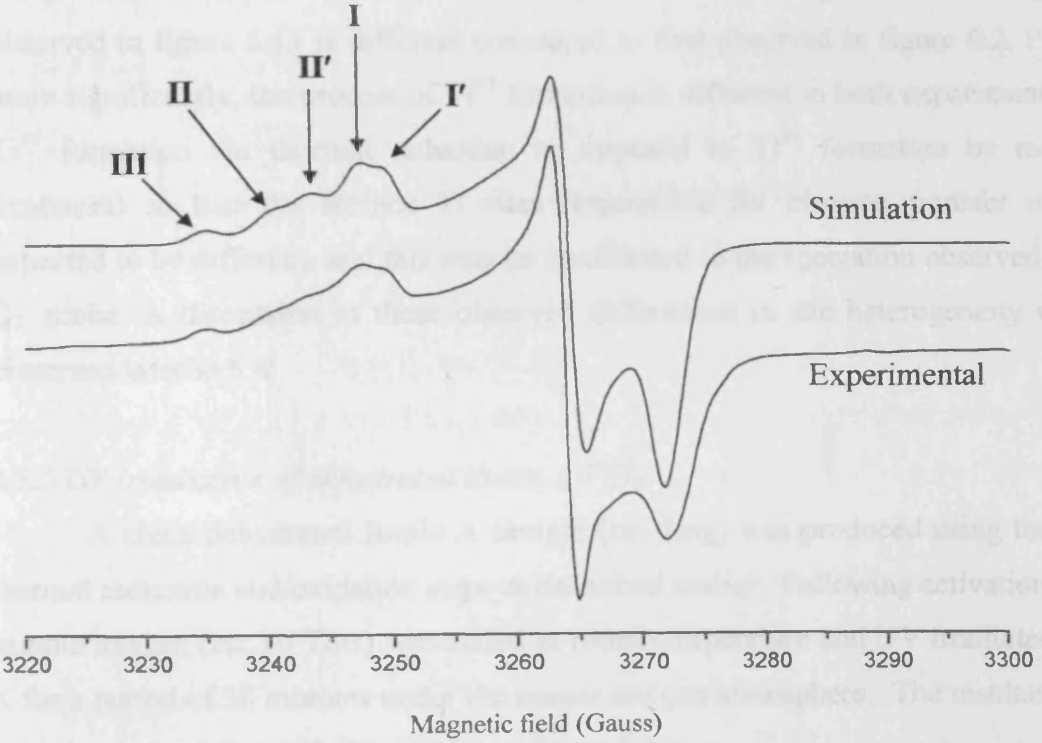

Figure 6.13. Experimental and simulated EPR spectra of photogenerated O_2^- on P25 anatase after UV irradiation under 10 Torr of oxygen at 77 K and subsequent evacuation of the excess oxygen at 298K. The EPR spectrum was recorded at 100 K

From the experimental and computer simulated spectra shown in figure 6.13 an orthorhombic signal with spin Hamiltonian parameters of $g_{xx} = 2.002$, $g_{yy} = 2.008$ and g_{zz}(**I'**) = 2.017, (**I**) = 2.019, (**I'**) = 2.021, (**II**) = 2.023 and (**III**) = 2.026 has been identified. Five different g_{zz} peaks were resolved from the simulation (figure 6.13), indicating the presence of five different radical sites available for stabilisation. This signal has been previously observed and has been identified as the superoxide radical, the g tensors common to O_2^- confirm this identification. The photogenerated superoxide anion was stable on the surface for several days at room temperature.

Comparison of the superoxide stabilised on the thermally reduced surface and activated surface displays differences in the heterogeneity of the sites available for stabilisation of the radical. However, in brief it should be recalled that the thermally reduced surface contains a number of defects created by the oxygen vacancies (i.e., a non-stoichiometric surface) during thermovacuum reduction. By comparison, the clean activated TiO_2 surface (used in the photogeneration experiments) should contain far less defects in this stoichiometric surface. Essentially, while extended morphological defects like steps, terraces, etc., are common to both samples, the clean activated TiO_2 sample should in principle be less defective and certainly different compared to the reduced surface. Therefore, it is not surprising that the heterogeneity observed in figure 6.13 is different compared to that observed in figure 6.2. Perhaps more significantly, the process of Ti^{3+} formation is different in both experiments (i.e., Ti^{3+} formation *via* thermal reduction as opposed to Ti^{3+} formation by radiative treatment) so that the surface Ti sites responsible for electron transfer may be expected to be different, and this may be manifested in the speciation observed by the O_2^- probe. A discussion of these observed differences in site heterogeneity will be presented later in 6.4.

6.3.5 UV irradiation of dehydrated Rutile A TiO_2

A clean dehydrated Rutile A sample (*ca.* 5mg) was produced using the same thermal reduction and oxidation steps as described earlier. Following activation of the sample oxygen (*ca.* 10 Torr) was added at room temperature and UV irradiated at 77 K for a period of 30 minutes under the excess oxygen atmosphere. The resultant EPR spectrum recorded at 100 K is shown in figure 6.14a.

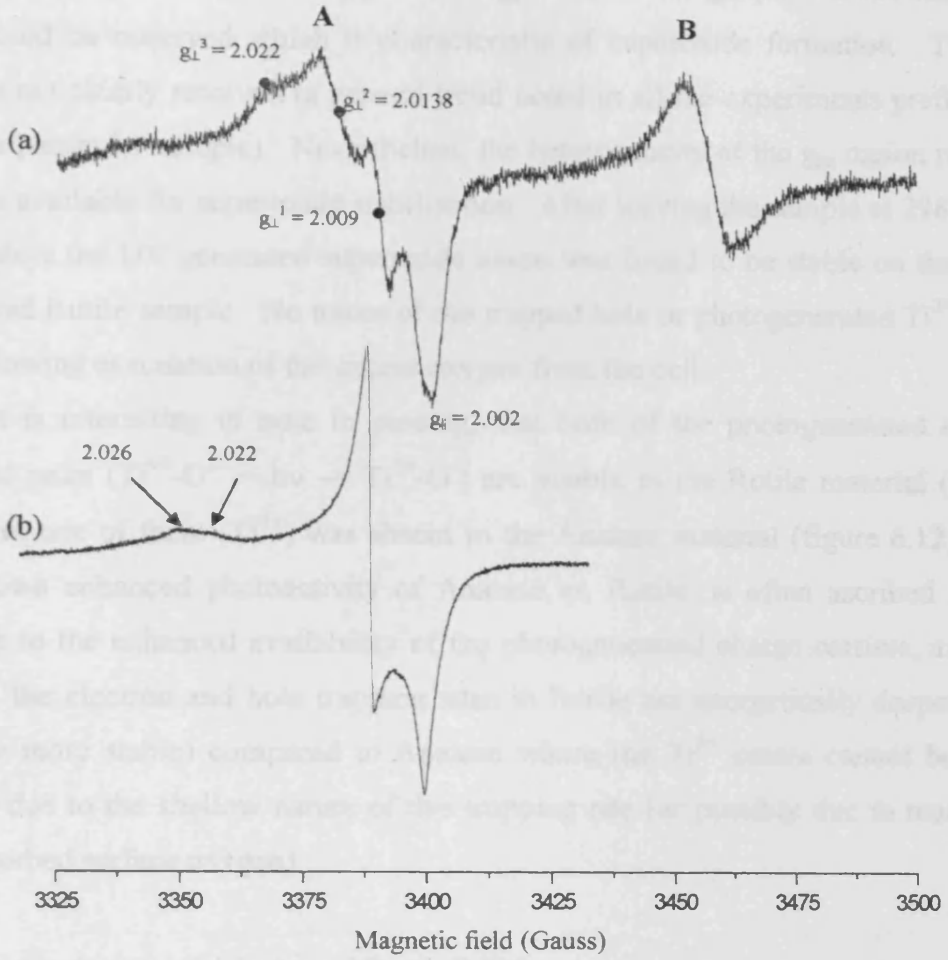

Figure 6.14. X band EPR spectra (100 K) of fully dehydrated Rutile A following (a) UV irradiation under 10 Torr of oxygen at 77 K and (b) after subsequent evacuation of the excess oxygen at 298 K.

As shown in figure 6.14a the low temperature EPR spectrum reveals the presence of two distinct signals labelled **A** and **B**. The former signal **A** with the spin Hamiltonian parameters $g_{\perp}^1 = 2.009$ $g_{\perp}^2 = 2.0138$ $g_{\perp}^3 = 2.022$ and $g_{\parallel} = 2.002$ can be easily assigned to a trapped holes (O^-) stabilised on the sub-surface at low temperature. The latter signal labelled **B** at $g \approx 1.97$ has been previously observed and can be attributed to photogenerated trapped electron centres, Ti^{3+}, as discussed in chapter 5. Warming the sample to 298 K or leaving the sample in the dark caused the trapped hole and Ti^{3+} signals to diminish due to their instability and recombination under these conditions. However, the signals could be regenerated by UV irradiation at low temperature. Following UV irradiation of the activated Rutile A sample the remaining excess oxygen in the cell was evacuated at 298 K. The experimental EPR spectrum following oxygen evacuation is displayed in figure 6.14b. An orthorhombic

signal with the spin Hamiltonian $g_{xx} = 2.002$ $g_{yy} = 2.008$ and g_{zz} (**II**) ≈ 2.022 and (**III**) 2.026 could be observed which is characteristic of superoxide formation. The g_{zz} region is not clearly resolved (a general trend noted in all the experiments preformed with this particular sample). Nevertheless, the heterogeneity of the g_{zz} region reveals two sites available for superoxide stabilisation. After leaving the sample at 298 K for several days the UV generated superoxide anion was found to be stable on the fully dehydrated Rutile sample. No traces of the trapped hole or photogenerated Ti^{3+} were seen following evacuation of the excess oxygen from the cell.

It is interesting to note in passing, that both of the photogenerated charge separated pairs (Ti^{4+}-O^{2-} + hν → Ti^{3+}-O^{-}) are visible in the Rutile material (figure 6.14a) but one of them (Ti^{3+}) was absent in the Anatase material (figure 6.12). The well known enhanced photoactivity of Anatase *vs.* Rutile, is often ascribed in the literature to the enhanced availability of the photogenerated charge carriers, and the fact that the electron and hole trapping sites in Rutile are energetically deeper (and therefore more stable) compared to Anatase where the Ti^{3+} centre cannot be seen possibly due to the shallow nature of this trapping site (or possibly due to reactivity with adsorbed surface oxygen).

6.3.6 UV irradiation of dehydrated Rutile B TiO_2

The third sample investigated in the radiative experiments was Rutile B. The material was firstly activated using the same experimental pre-treatment as before, oxygen (10 Torr) was added to the clean activated sample and the TiO_2 powder was then UV irradiated for 30 minutes at 77 K. The resultant EPR spectrum is shown in figure 6.15a.

As shown in figure 6.15a a signal similar to that seen for both P25 Anatase and Rutile A was observed. This signal has been characterised by the spin Hamiltonian parameters $g_{\perp} = 2.009$ and $g_{\parallel} = 2.002$ and identified as that of a trapped hole. The linewidth of the $g_{\parallel}$ component in 6.16a is unusually large, and the "low field" side of this peak almost creates a derivative-like profile (i.e., this should not occur for a pure parallel component in a powder-type spectrum). One explanation for this could be due to a 'contamination' with a second unresolved $g_{\perp}$ component, as identified in 6.15a, which causes an overall broadening and distortion of the $g_{\parallel}$ peak. However, another explanation is that part of the signal at this g value, close to free

spin, arises from traces of a polarised conduction electron (discussed in detail in the previous chapter) as it is also visible in figure 6.17 (see later).

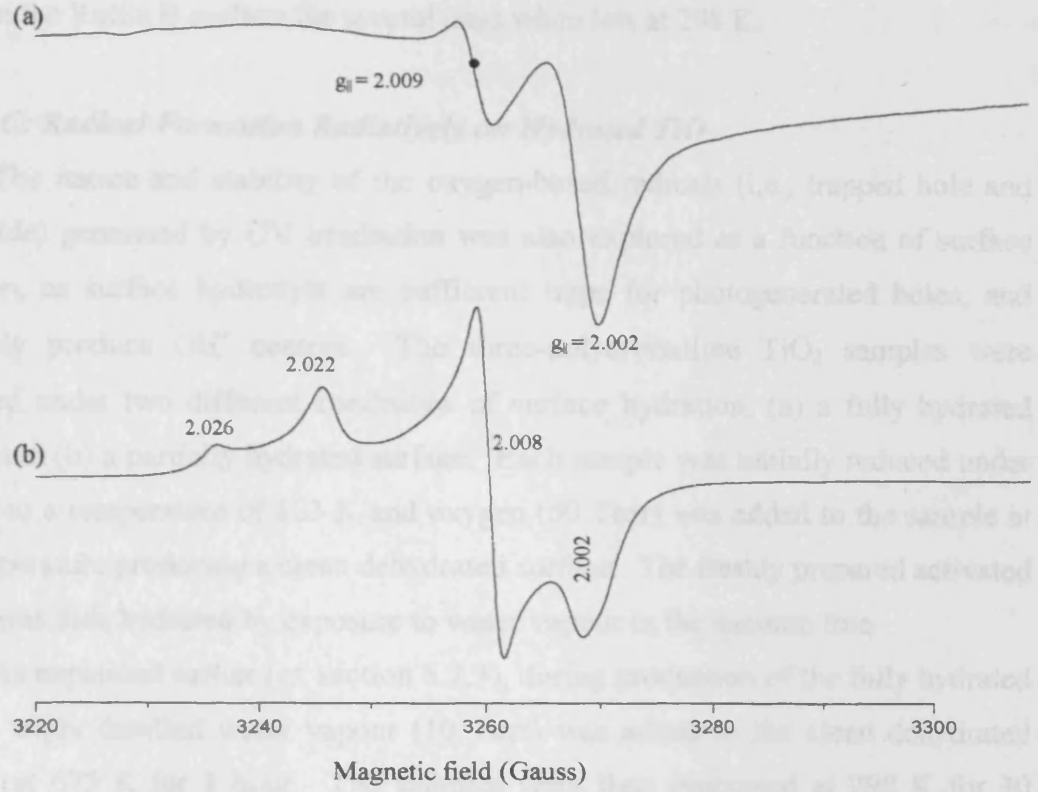

Figure 6.15. X band EPR spectra (100 K) of fully-dehydrated Rutile B following (a) UV irradiation under 10 Torr of oxygen at 77K and (b) subsequent evacuation of excess oxygen at 298 K.

When the sample was warmed to 298 K the trapped hole formed at low temperature became unstable (i.e., the signal disappeared), but it could be regenerated during subsequent low temperature UV irradiation. No traces of trapped electron centres (i.e., Ti^{3+}) were visible during the UV irradiation experiments under the oxygen atmosphere. Unlike the previous Rutile sample studied (section 6.3.5 above), the Rutile B sample is a commercial material containing a large number of transition metal ion impurities.[7] It is well known that such impurities act as preferential electron traps compared to Ti during photoirradiation, as energetically they sit lower in the band gap, this may explain the absence of a Ti^{3+} signal in this particular case. The excess oxygen was then evacuated at 298 K from the cell and the resultant EPR spectrum recorded at 100 K, as shown in figure 6.15b.

Following evacuation an orthorhombic signal with spin Hamiltonian parameters of $g_{xx} = 2.002$, $g_{yy} = 2.008$, $g_{zz} = 2.022$ and 2.026 could be observed. Two g_{zz} peaks were resolved indicating the presence of two different radical sites available for stabilisation of the species. The signal can be easily identified as the superoxide radical, confirmed by the g tensors of the radical. The photogenerated anion was stable on the Rutile B surface for several days when left at 298 K.

Results C: Radical Formation Radiatively on Hydrated TiO_2

The nature and stability of the oxygen-based radicals (i.e., trapped hole and superoxide) generated by UV irradiation was also explored as a function of surface hydration, as surface hydroxyls are sufficient traps for photogenerated holes, and ultimately produce $OH^{\bullet}$ centres. The three-polycrystalline TiO_2 samples were examined under two different conditions of surface hydration, (a) a fully hydrated surface and (b) a partially hydrated surface. Each sample was initially reduced under vacuum to a temperature of 823 K and oxygen (50 Torr) was added to the sample at this temperature producing a clean dehydrated surface. The freshly prepared activated surface was then hydrated by exposure to water vapour in the vacuum line.

As explained earlier (*cf.* section 6.2.3), during production of the fully hydrated surfaces triply distilled water vapour (10 Torr) was added to the clean dehydrated surfaces at 673 K for 1 hour. The samples were then evacuated at 298 K for 30 minutes, sections 6.3.7 to 6.3.9 display the subsequent results observed following UV irradiation of the samples.

Sections 6.3.10 to 6.3.12 are concerned with the effect that partial hydration of the TiO_2 surfaces has on the oxygen based radicals formed during UV irradiation. Here in order to produce the partially hydrated surfaces a mixture of oxygen and water (10:1 ratio, total pressure 10 Torr) was added to the earlier prepared clean dehydrated surfaces at 298 K.

6.3.7 UV irradiation of fully hydrated P25 Anatase TiO_2

When the P25 Anatase surface was fully hydrated using the above method, oxygen (10 Torr) was added to the sample and UV irradiated at 77 K for 30 minutes, analogous to the radiative experiments described above. In this case, no signals were observed in the EPR spectrum (the spectrum, which simply showed a "flat" baseline,

is not shown for brevity). The excess oxygen was then evacuation at 298 K and the EPR spectrum was again recorded at 100 K. Once again, no signals of any kind were observed in the EPR spectrum.

6.3.8 UV irradiation of fully hydrated Rutile A TiO_2

A fully hydrated Rutile A sample was initially prepared using the same method as before. Oxygen (10 Torr) was added to the hydrated surface at 298 K, and UV irradiated for 30 minutes at 77 K. The resultant EPR spectrum recorded at 100 K is shown in figure 6.16a.

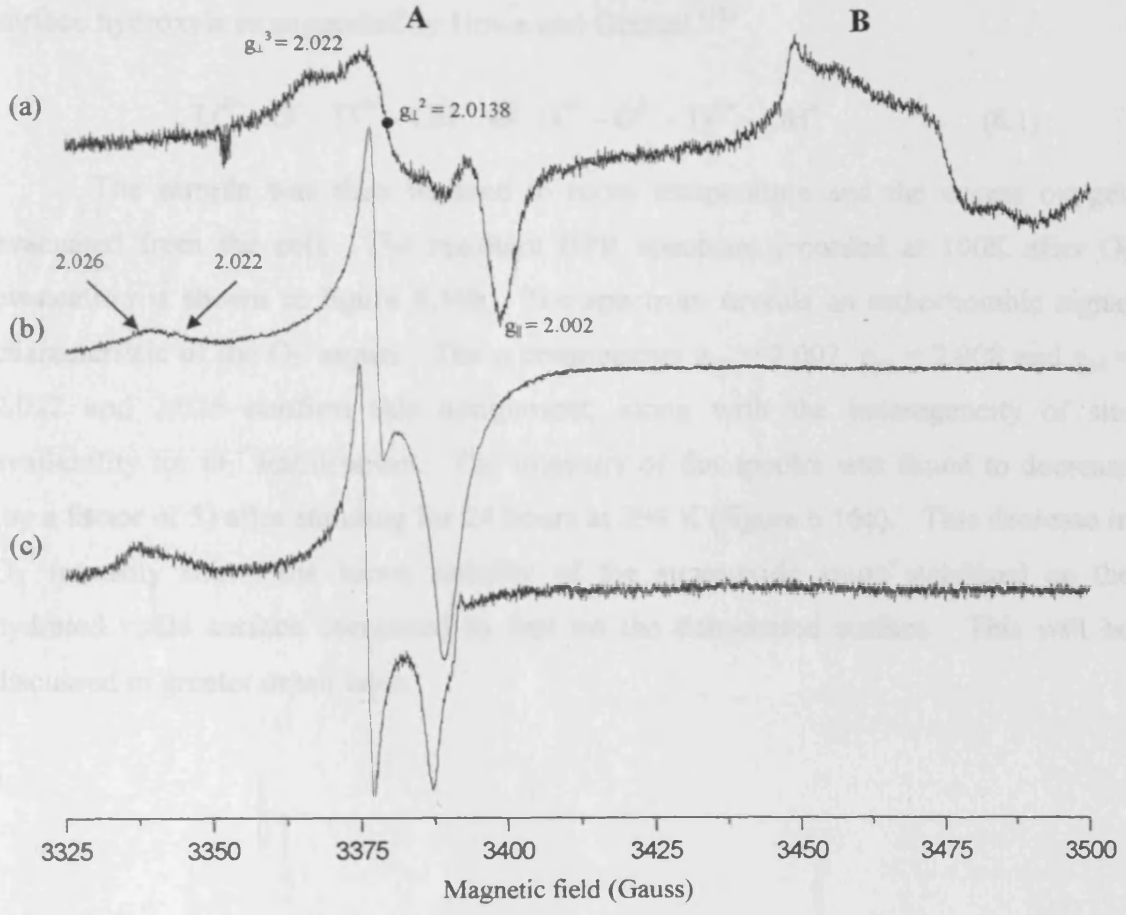

Figure 6.16. X band EPR spectra (100 K) of a fully hydrated Rutile A sample following (a) UV irradiation at 77 K under an oxygen atmosphere, (b) evacuation at 298 K and (c) warming to 298 K for 24 hours followed by re-cooling to 100 K.

As shown in figure 6.16a during UV irradiation of the fully hydrated surface, two signals labelled **A** and **B** have been formed. The former signal labelled **A** with the spin Hamiltonian parameters of $g_\perp^2 = 2.0138$, $g_\perp^3 = 2.022$ and $g_\parallel = 2.002$, can be

easily identified as a trapped hole (O^-). The second signal labelled **B** at the higher field position has been identified as the photogenerated Ti^{3+} centre with the g components $g_\perp = 1.96$ and $g_\parallel = 1.94$, this signal has been previously detailed in chapter 5. Increasing the temperature gently to 298 K caused the two signals to become unstable and diminish. The species were both regenerated following low temperature UV irradiation.

It is also interesting to note that one of the three $g_\perp$ components previously observed in the irradiated Rutile A sample (see figure 6.14a) is now absent in the hydrated equivalent Rutile A powder. This may indicate that one of the two trapped hole centres in Rutile A is a sub-surface species* that is capable of reacting with the surface hydroxyls as suggested by Howe and Gratzel.[12]

$$Ti^{4+} - O^- - Ti^{4+} - OH \rightarrow Ti^{4+} - O^{2-} - Ti^{4+} - OH^{\bullet} \qquad (6.1)$$

The sample was then warmed to room temperature and the excess oxygen evacuated from the cell. The resultant EPR spectrum recorded at 100K after O_2 evacuation is shown in figure 6.16b. The spectrum reveals an orthorhombic signal characteristic of the O_2^- signal. The g components $g_{xx} = 2.002$, $g_{yy} = 2.008$ and $g_{zz} = 2.022$ and 2.026 confirm this assignment, along with the heterogeneity of site availability for O_2^- stabilisation. The intensity of the spectra was found to decrease (by a factor of 5) after standing for 24 hours at 298 K (figure 6.16c). This decrease in O_2^- intensity shows the lower stability of the superoxide anion stabilised on the hydrated rutile surface compared to that on the dehydrated surface. This will be discussed in greater detail later.

---

*; it is unlikely to be a pure surface species as it was present on the fully dehydrated sample containing an excess of adsorbed oxygen. A surface O^- anion may be expected to react with surface oxygen forming the ozonide species. This did not occur in this particular experiment, suggesting that the trapped hole may instead be sub-surface.

6.3.9 UV irradiation of fully hydrated Rutile B TiO_2

The final surface to be examined under full hydration conditions was Rutile B. A fully hydrated surface was initially prepared as before, oxygen (10 Torr) was then added to the sample at 298 K before UV irradiation at 77 K for 30 minutes. The resultant spectrum was recorded at 100 K and is displayed in figure 6.17a.

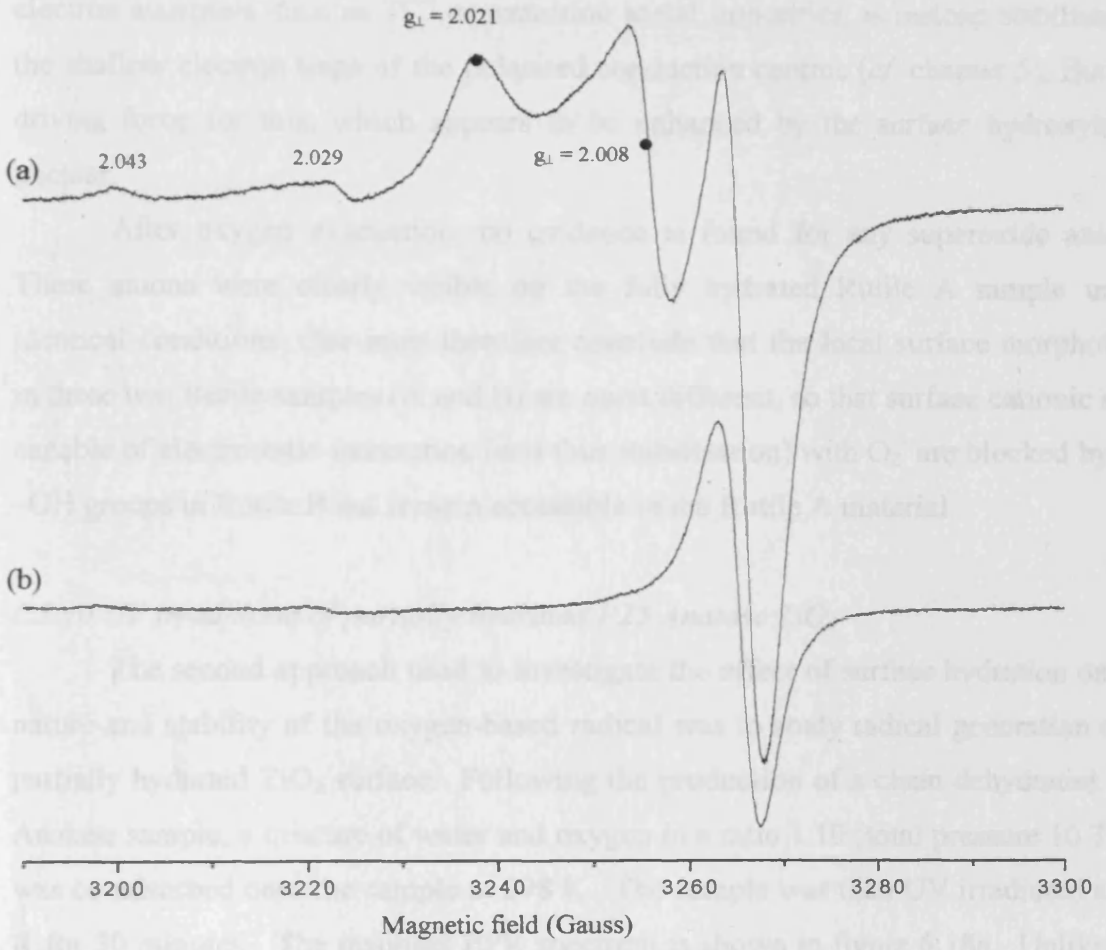

Figure 6.17. X band EPR spectra (100 K) of Rutile B following full hydration of the sample and addition of oxygen (10 Torr) following (a) UV irradiation at 77 K and (b) evacuation at 298 K.

The EPR spectrum in figure 6.17a is rather unusual. It is known from the previous experiments that UV radiation of Rutile under these conditions should produce a visible trapped hole signal (see figure 6.16 for the dehydrated case for example). Indeed the signals at g = 2.008 and g = 2.021 are most likely due to the $g_{\perp}$ components of a trapped hole (O^-) along with those at 2.043 and 2.029.[7] However the region of the $g_{\parallel}$ component is heavily distorted, and this distortion can only be

explained as arising from another species. The most likely candidate is a medium polarised conduction electron, since the signal remained even after annealing and oxygen evacuation at 298 K. It should be recalled that the medium polarised conduction electron is a bulk species, and therefore will not be significantly perturbed by the excess oxygen (hence it is visible in figure 6.17a). However, what is surprising and difficult to explain is the mechanism by which this species is produced. After charge separation, the photogenerated electron, which is usually trapped by deep electron acceptors such as Ti^{4+} or transition metal impurities, is instead stabilised in the shallow electron traps of the polarised conduction centres (*cf.* chapter 5). But the driving force for this, which appears to be enhanced by the surface hydroxyls, is unclear.

After oxygen evacuation, no evidence is found for any superoxide anions. These anions were clearly visible on the fully hydrated Rutile A sample under identical conditions. One must therefore conclude that the local surface morphology in these two Rutile samples (A and B) are quite different, so that surface cationic sites capable of electrostatic interaction (and thus stabilisation) with O_2^- are blocked by the –OH groups in Rutile B but remain accessible in the Rutile A material.

6.3.10 UV irradiation of partially hydrated P25 Anatase TiO_2

The second approach used to investigate the effect of surface hydration on the nature and stability of the oxygen-based radical was to study radical generation on a partially hydrated TiO_2 surface. Following the production of a clean dehydrated P25 Anatase sample, a mixture of water and oxygen in a ratio 1:10 (total pressure 10 Torr) was co-adsorbed onto the sample at 298 K. The sample was then UV irradiated at 77 K for 30 minutes. The resultant EPR spectrum is shown in figure 6.18a. Unlike the previous approach where the surface was completely 'saturated' with –OH groups (and possibly physisorbed water), in this second approach oxygen remains in excess while the 1 Torr pressure of water delivered in the experiment ensures good coverage of the surface.

The low temperature EPR spectrum reveals the presence of four distinct signals labelled **A**, **B**, **B′** and **C** in figure 6.18a. Signal **A** dominates the low temperature spectrum, and this signal is characterised by the g values of $g_\perp = 2.016$ and $g_\parallel = 2.002$. This signal can be easily assigned to a trapped hole (O^-). This signal

was found to be very unstable at 298 K, but could be regenerated following subsequent UV irradiation at 77K. The signals labelled **B** and **B′** are due to the photogenerated Ti^{3+} centres, since the former signal **B** has a g value of $g \approx 1.97$ due to bulk Ti^{3+} at lattice sites while the signal **B′** at $g = 1.99$ is due to interstitial Ti^{3+}.

Finally, signal **C** has a g value of 2.034 has only been mentioned briefly in this study. This new signal was also found to be thermally unstable when warmed to 298 K. This unidentified signal, which is photogenerated on the partially hydrated surface, can be easily assigned to the hydroperoxy radical ($HO_2^{\bullet}$). The g_{zz} component of such hydro peroxy radicals on TiO_2 is always *ca.* 2.034, and is often used as a fingerprint to identify the species.[16,20,22,23] As a result the remaining g values for this species should be present at $g_{yy} = 2.008$ and $g_{xx} = 2.002$, although in this case they are overlapped due to the more abundant O^- signal.

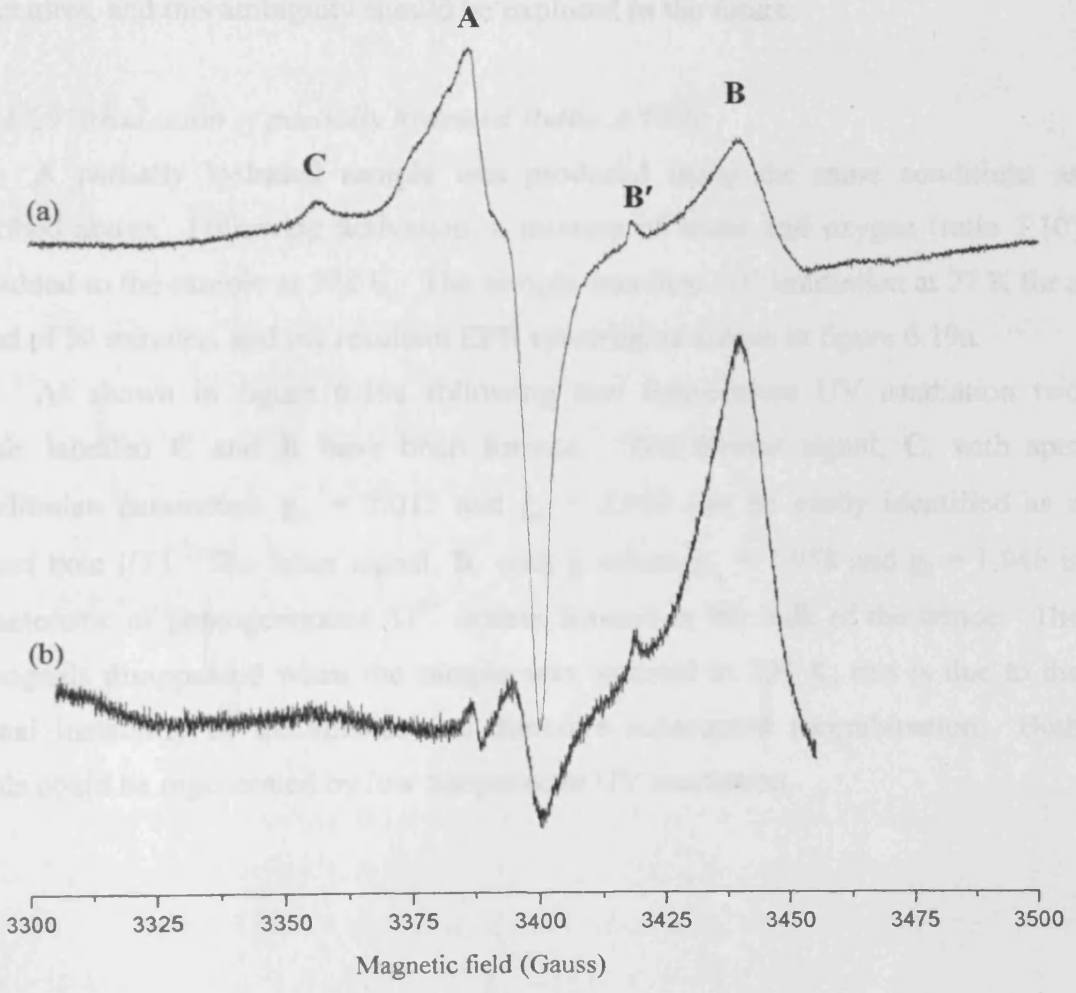

Figure 6.18. X band EPR spectra (100 K) of P25 Anatase after co-adsorption of oxygen/water (10:1 ratio, 10 Torr total pressure) following (a) UV irradiation at 77 K and (b) evacuation at 298 K.

Following the UV irradiation, the excess mixture of water and oxygen was evacuated at 298 K and the resultant EPR spectrum recorded at 100 K is shown in figure 6.18b. Evacuation of the sample at 298 K did not reveal the presence of any superoxide stabilised on the surface, similar to the analogous study on a fully hydrated surface. The photogenerated Ti^{3+} produced prior to evacuation was still present. It should be recalled that on the fully dehydrated and fully hydrated P25 surface, UV irradiation at 77K under an O_2 atmosphere did not lead to any observable Ti^{3+} signal (sections 6.3.4 and 6.3.7 respectively), although trapped holes were detected in the dehydrated sample (figure 6.12). In this current experiment (figure 6.18) only a partial hydration of the surface exists (i.e., 1:10 ratio of H_2O:O_2 with a total; pressure of 10 Torr in the cell), and as a result both trapped holes and trapped electrons are simultaneously visible at 100K. It is not clear why the degree of surface hydration leads to such dramatic differences in the trapping of the photogenerated electrons as Ti^{3+} centres, and this ambiguity should be explored in the future.

6.3.11 UV irradiation of partially hydrated Rutile A TiO_2

A partially hydrated sample was produced using the same conditions as described above. Following activation, a mixture of water and oxygen (ratio 1:10) was added to the sample at 298 K. The sample was then UV irradiation at 77 K for a period of 30 minutes, and the resultant EPR spectrum is shown in figure 6.19a.

As shown in figure 6.19a following low temperature UV irradiation two signals labelled **C** and **B** have been formed. The former signal, **C**, with spin Hamiltonian parameters $g_\perp$ = 2.013 and $g_\parallel$ = 2.002 can be easily identified as a trapped hole (O^-). The latter signal, **B**, with g values $g_\perp$ = 1.958 and $g_\parallel$ = 1.946 is characteristic of photogenerated Ti^{3+} centres formed in the bulk of the lattice. The two signals disappeared when the sample was warmed to 298 K, this is due to the thermal instability of the species and therefore subsequent recombination. Both signals could be regenerated by low temperature UV irradiation.

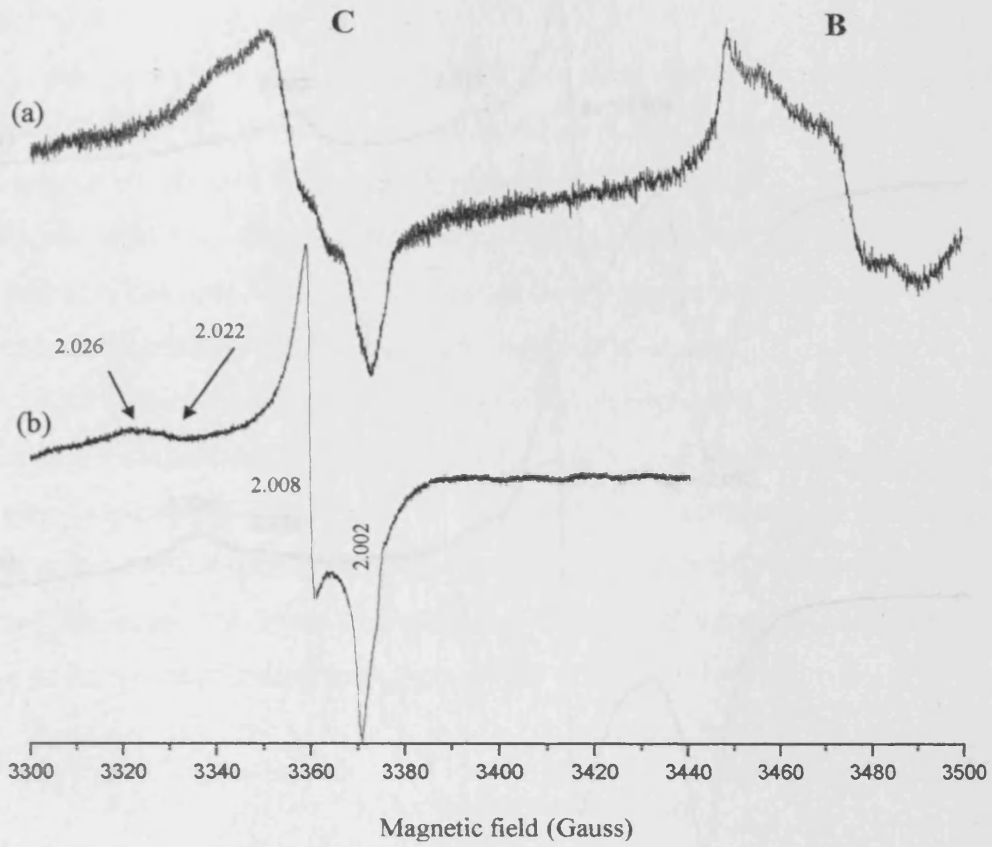

Figure 6.19. X band EPR spectra (100 K) of a partially hydrated Rutile A sample after (a) UV irradiation at 77 K and (b) evacuation at 298 K.

The sample was then warmed to room temperature and the excess mixture evacuated at this temperature. The resultant EPR spectrum recorded at 100 K following evacuation is shown in figure 6.19b. A signal with g values of g_{xx} = 2.002, g_{yy} = 2.008 and g_{zz} (**II**) = 2.022 and (**III**) = 2.026 can be easily identified as the characteristic superoxide anion stabilised on the surface. Although not shown here, the intensity of the superoxide signal decreased over several hours when left at room temperature.

6.3.12. UV irradiation of partially hydrated Rutile B TiO_2

The final TiO_2 sample to be studied under partial hydration conditions was the Rutile B sample. As before following production of the dehydrated sample a mixture of oxygen and water vapour (10: 1 mixing ratio, total pressure 10 Torr) was added at room temperature and the sample UV irradiated at 77 K for 30 minutes. The recorded EPR spectrum is shown in figure 6.20a.

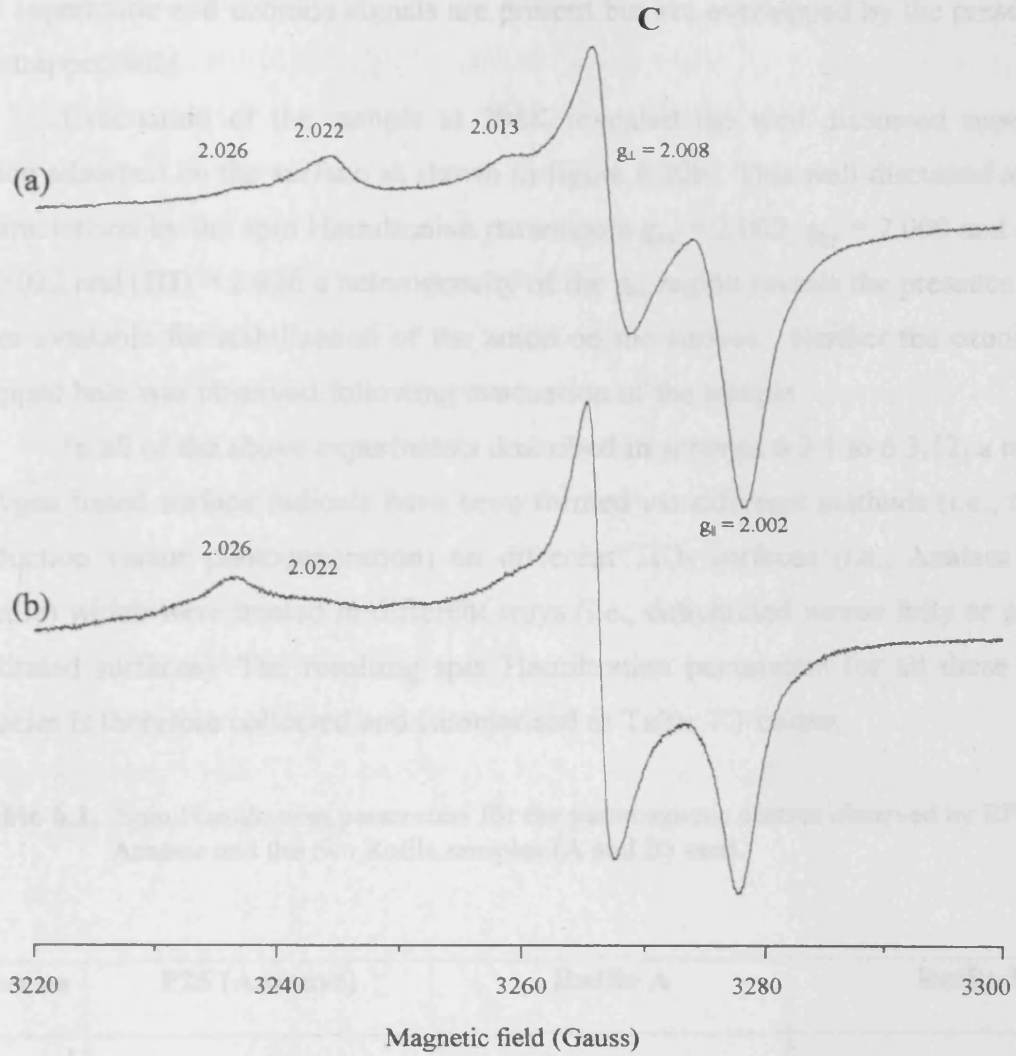

Figure 6.20. EPR spectra of Rutile B after co-adsorption of oxygen /water (10:1 ration, 10 Torr total pressure) following (a) UV irradiation at 77 K and (b) after evacuation at 298 K followed by re-cooling to 100 K.

As displayed in figure 6.20a following UV irradiation a complex EPR spectrum is produced therefore suggesting a number of various radical species are produced. Following close inspection of the spectrum a trapped hole with spin Hamiltonian parameters of $g_\perp = 2.008$ and $g_\parallel = 2.002$ is observed. In addition to this two peaks with g_{zz} values of (**II**) = 2.022 and (**III**) = 2.026 are observed which are due to the stabilisation of the superoxide anion. A final shoulder peak at $g_{zz} = 2.013$, is also observed, this peak is not due to superoxide as the value is too low. Therefore, this final signal is attributed to traces of the ozonide (O_3^-) radical.[9,16,20] It should be noted that the g_{zz} value is crystal field sensitive and is slightly larger than that previously observed for Rutile A (i.e., $g_{zz} = 2.011$). The g_{yy} and g_{xx} regions of both

the superoxide and ozonide signals are present but are overlapped by the presence of the trapped hole.

Evacuation of the sample at 298K revealed the well discussed superoxide anion adsorbed on the surface as shown in figure 6.20b. This well discussed anion is characterised by the spin Hamiltonian parameters $g_{xx} = 2.002$, $g_{yy} = 2.009$ and g_{zz} (**II**) = 2.022 and (**III**) = 2.026 a heterogeneity of the g_{zz} region reveals the presence of two sites available for stabilisation of the anion on the surface. Neither the ozonide nor trapped hole was observed following evacuation of the sample.

In all of the above experiments described in sections 6.3.1 to 6.3.12, a range of oxygen based surface radicals have been formed *via* different methods (i.e., thermal reduction versus photogeneration) on different TiO_2 surfaces (i.e., Anatase *versus* Rutile) which were treated in different ways (i.e., dehydrated *versus* fully or partially hydrated surfaces). The resulting spin Hamiltonian parameters for all these radical species is therefore collected and summarised in Table 7.1 below.

Table 6.1. Spin Hamiltonian parameters for the paramagnetic centres observed by EPR on P25 Anatase and the two Rutile samples (A and B) used.

Species	P25 (Anatase)			Rutile A			Rutile B		
O^-	$g_\perp$ 2.016		$g_\parallel$ 2.002	$g_\perp$ 2.009 2.0138 2.022		$g_\parallel$ 2.002	$g_\perp$ 2.009		$g_\parallel$ 2.002
O_2^-	g_{xx} 2.002	g_{yy} 2.008	g_{zz} 2.019 2.022 2.025	g_{xx} 2.002	g_{yy} 2.008	g_{zz} 2.022 2.026	g_{xx} 2.002	g_{yy} 2.009	g_{zz} 2.022 2.026
O_3^-				g_{xx} 2.002	g_{zz} 2.008	g_{zz} 2.011	g_{xx} 2.002	g_{yy} 2.008	g_{zz} 2.013
$HO_2^\bullet$	g_{xx} 2.002	g_{yy} 2.008	g_{zz} 2.034	g_{xx} 2.003	g_{yy} 2.008	g_{zz} 2.035			

6.3.13 NO as a surface Probe

A probe molecule can be defined as a molecule whose properties in the adsorbed state can be monitored by EPR and provide useful information about the surface.[24] The properties monitored by EPR can concern either from the probe molecule itself or the surface site and the changes of its properties upon adsorption. The superoxide anion is a well-known probe molecule that can distinguish differences in the local adsorption sites (the reasons for this will be discussed shortly in detail in section 6.4.1). However, nitric oxide has also been employed as a surface probe to study the influence of surface crystal fields, mostly recently by Chiesa *et al.*,[25] on an MgO surface. Therefore by comparison with the O_2^- work described earlier, a number of experiments were also carried out using NO. Prior to any NO adsorption on the TiO_2 surfaces, the samples were thermally reduced at 823 K. Oxygen (50 Torr) was added at this temperature and the samples allowed to cool under the excess pressure before evacuating at 298 K, to produce clean dehydrated surfaces. NO (20 Torr) was then admitted to both TiO_2 samples at 298 K. The resultant EPR spectra, recorded at 10 K, are shown in figure 6.21.

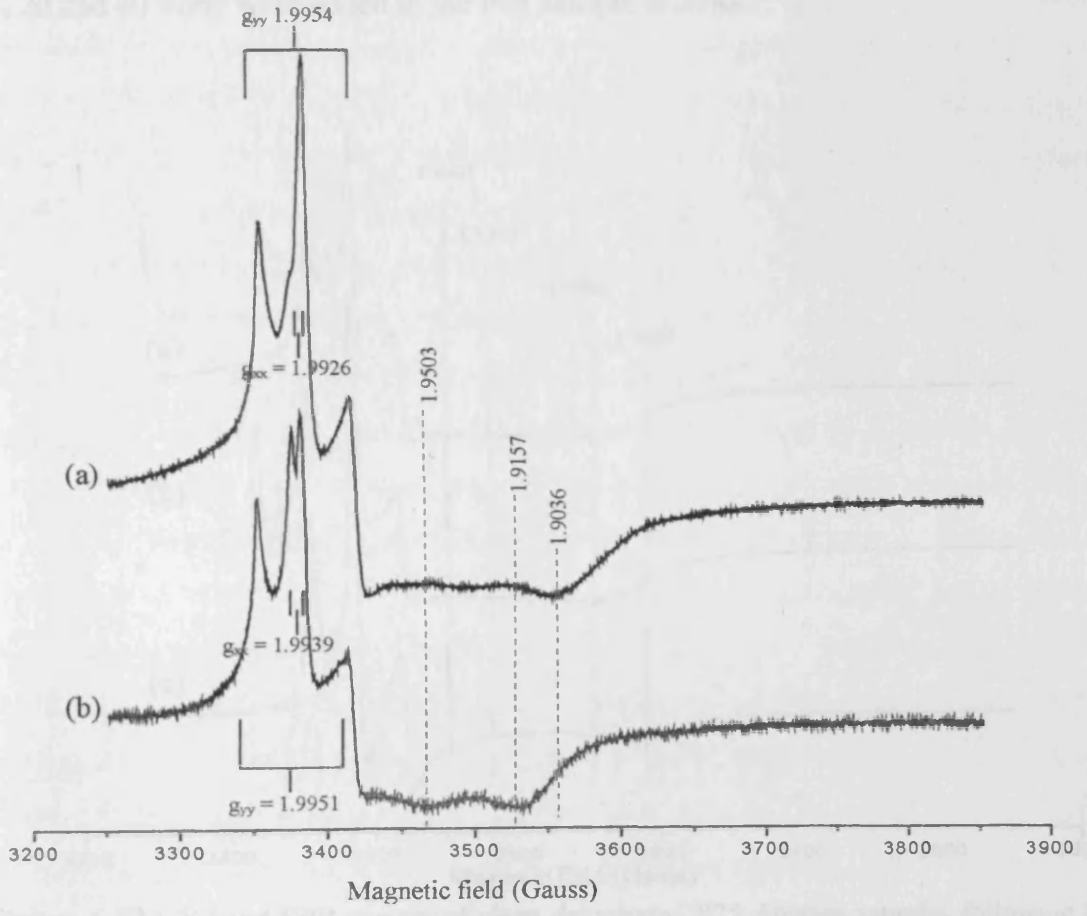

Figure 6.21. EPR spectra (10 K) of NO (20 Torr) on (a) activated P25 Anatase, (b) activated Rutile B.

The EPR spectra shown in figure 6.21 can be easily assigned to the adsorbed NO molecule, with g_{xx} = 1.9926 (A_{xx} = 2.68), g_{yy} = 1.9954 (A_{yy} = 33.4) and a heterogeneity of g_{zz} components at 1.9503, 1.9157 and 1.9036 on P25 (A_{zz} = unresolved), while on Rutile B similar spin Hamiltonian parameters are observed; g_{xx} = 1.9939 (A_{xx} = 2.73), g_{yy} = 1.9951 (A_{yy} = 34.1) and a heterogeneity of g_{zz} components at 1.9503 and 1.9157 (A_{zz} = unresolved). The heterogeneity of the g_{zz} region in both spectra is indicative of NO adsorption at slightly different low coordinated Ti^{4+} where the local electric field removes the degeneracy of the $2\pi^*$ orbitals of the NO molecule. It is clear from this simple experiment that the local coordination environment of the Ti^{4+} cations on the two TiO_2 surfaces (Anatase *vs.* Rutile) is clearly different.

It is possible that the profile of the EPR spectrum is NO pressure dependent. In other words, at low surface coverages (low pressure), the NO molecules will be preferentially adsorbed at the strongest adsorption sites and as the pressure increases, adsorption will occur progressively at the weaker (but potentially more abundant) Ti^{4+} adsorption sites. This result can be seen in figure 6.22, where various amounts of NO (5, 20 and 40 Torr) were added to the P25 sample at 298K.

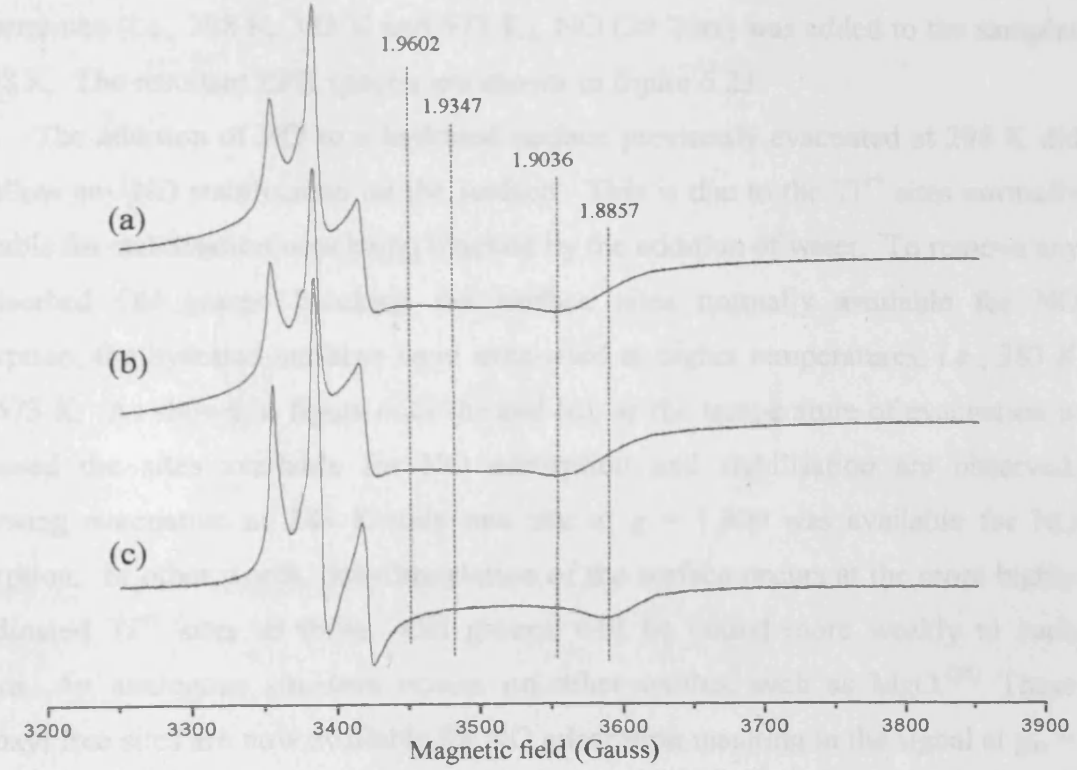

Figure 6.22. X-band EPR spectra of clean dehydrated P25 Anatase samples following (a) NO (5) Torr) addition, (b) NO (20 Torr) addition and (c) NO (40 Torr) addition. All spectra were recorded at 100 K.

At the lowest pressures used, a number of g_{zz} components can be clearly seen at 1.9602, 1.9347 and 1.9036 (the highest g_{zz} representing the site of strongest Ti^{4+}...NO attraction). Therefore, already at 5 Torr a wide distribution of low coordinated Ti^{4+} adsorption sites are populated. However as the pressure is increased to 40 Torr, the overall EPR signal intensity was found to increase by a factor of 3, and now the most dominant g_{zz} component appears at 1.8857, which is presumably the weakest Ti^{4+} adsorption site for NO. Therefore, this experiment confirms that the profile of the spectrum is indeed pressure dependent, and low pressures must be used in order to evidence the heterogeneity of the surface sites.

Using low pressures of NO (i.e., 5 Torr) displays a clear heterogeneity of surface sites available for NO adsorption, i.e., $g_1 = 1.9062$, $g_2 = 1.9347$ and $g_3 = 1.9036$. However, when using higher pressures of NO (20 and 40 Torr), only one site is resolved at $g = 1.8857$. Therefore, using lower pressures resulted in sufficient NO adsorption on the P25 Anatase surface.

In earlier experiments using O_2^-, the pressence of surface –OH groups was found to block the sites responsible for stabilisation of the anion. Therefore, the stability of NO adsorbed on a hydrated TiO_2 surface was examined. Following preparation of a clean dehydrated Rutile B surface as before, water (10 Torr) was added at 298 K for 30 minutes. After evacuation of the water at several different temperatures (i.e., 298 K, 383 K and 573 K), NO (20 Torr) was added to the samples at 298 K. The resultant EPR spectra are shown in figure 6.23.

The addition of NO to a hydrated surface previously evacuated at 298 K did not allow any NO stabilisation on the surface. This is due to the Ti^{4+} sites normally available for stabilisation now being blocked by the addition of water. To remove any physisorbed OH groups blocking the surface sites normally available for NO adsorption, the hydrated surfaces were evacuated at higher temperatures, i.e., 383 K and 573 K. As shown in figure 6.23 (b) and (c), as the temperature of evacuation is increased the sites available for NO adsorption and stabilisation are observed. Following evacuation at 383 K only one site at $g = 1.900$ was available for NO adsorption. In other words, dehydroxylation of the surface occurs at the more highly coordinated Ti^{4+} sites as these –OH groups will be bound more weakly to such cations. An analogous situation occurs on other oxides, such as MgO.[26] These hydroxyl free sites are now available for NO adsorption resulting in the signal at $g_{zz} = 1.900$. At higher evacuation temperatures, the Ti^{4+} cations are progressively

dehydroxylated, so that the spectrum of adsorbed NO on the 573K evacuated sample is very similar to the original spectrum of NO adsorbed on a fully dehydrated surface. In particular the g_{zz} components at 1.9503 and 1.9157, representing binding to stronger Ti^{4+} sites, are now visible. These results compliment the previous O_2^- results and demonstrate how the available adsorption sites for the probe molecules can be easily, and depending on extent of –OH coverage, preferentially blocked for O_2^- or NO adsorption.

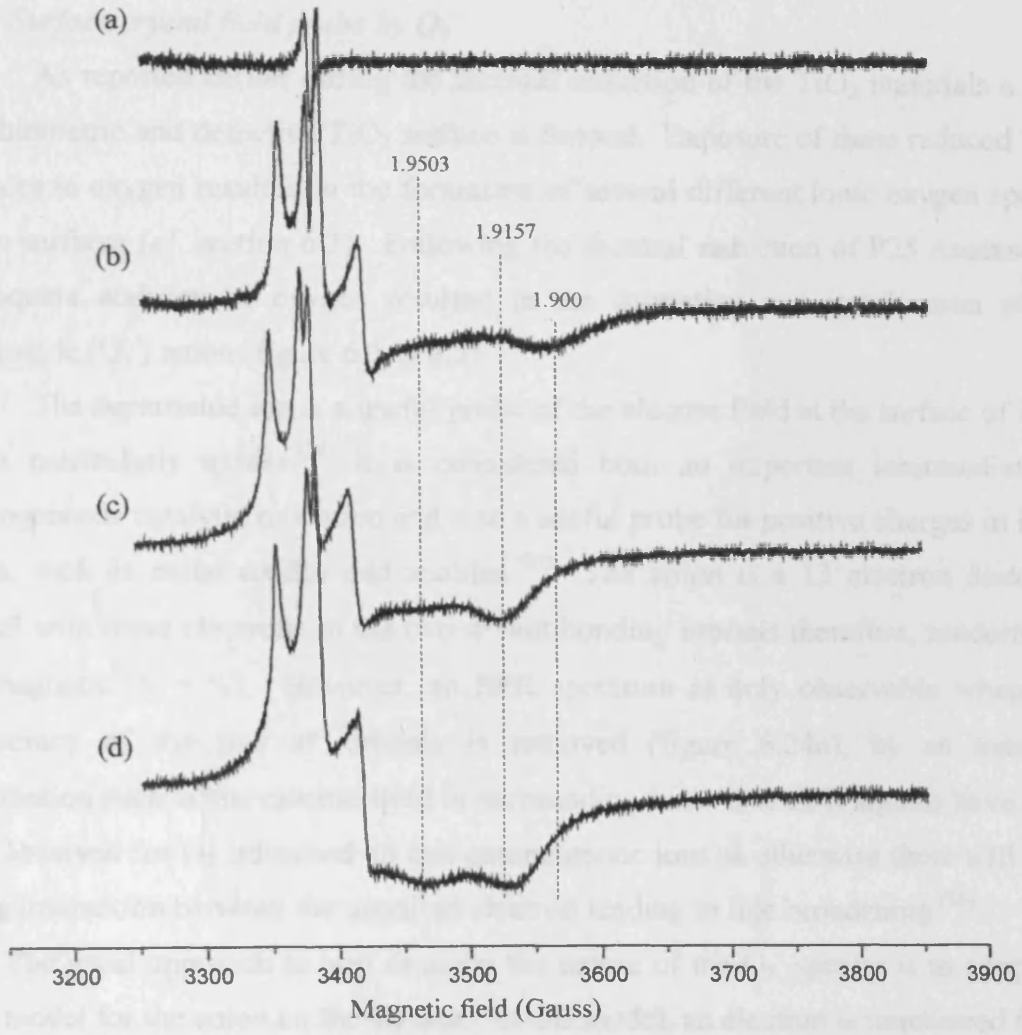

Figure 6.23. EPR spectra (10K) of a hydrated Rutile B sample containing adsorbed NO. The hydrated sample was evacuated at (a) 298 K, (b) 383 K and 573 K to remove excess water or weakly bound –OH groups prior to NO admission. The EPR spectrum of NO adsorbed on a fully dehydrated Rutile B sample is shown in (d), for comparison

6.4 Discussion

Formation of ionic oxygen species at the surface of metal oxides is the subject of active research due to the basic role played by such species in several phenomena at the gas-solid interface, including heterogeneous catalysis,[16,20,27,28] corrosion and contamination of highly pure materials.[29] Among the various species reported in the literature,[15,18] the superoxide O_2^- species is by far the most commonly reported species on oxides, which has been characterised mostly by EPR. A great deal of information about its structure, location stability and surface mobility can therefore be determined.

6.4.1 Surface crystal field probe by O_2^-

As reported earlier during the thermal reduction of the TiO_2 materials a non-stoichiometric and defective TiO_2 surface is formed. Exposure of these reduced TiO_2 surfaces to oxygen resulted in the formation of several different ionic oxygen species at the surfaces (*cf.* section 6.3). Following the thermal reduction of P25 Anatase the subsequent addition of oxygen resulted in the formation and stabilisation of the superoxide (O_2^-) anion (figure 6.1 to 6.5).

The superoxide ion is a useful probe of the electric field at the surface of ionic solids particularly oxides.[24] It is considered both an important intermediate in heterogeneous catalytic oxidation and also a useful probe for positive charges in ionic solids, such as metal oxides and zeolites.[30] The anion is a 13 electron diatomic radical with three electrons in the two π^* antibonding orbitals therefore, rendering it paramagnetic (S = ½). However, an EPR spectrum is only observable when the degeneracy of the two π^* orbitals is removed (figure 6.24a), by an external perturbation such as the electric field or surrounding ions. The EPR signals have only been observed for O_2^- adsorbed on non paramagnetic ions as otherwise there will be a strong interaction between the unpaired electron leading to line broadening.[16]

The usual approach to best describe the nature of the O_2^- species is to adopt an ionic model for the anion on the surface. In this model, an electron is transferred from the surface to the adsorbed oxygen to form O_2^-, and there is an electrostatic interaction between the cation at the adsorption site and the superoxide (eq. 6.2). This process can be written as follows:

$$M^{(n-1)+} + O_2 \longrightarrow M^{n+} \ldots\ldots O_2^- \qquad (6.2)$$

When the O_2^- species is adsorbed at a cationic surface site (M^{n+}), the electrostatic field from the M^{n+} removes the degeneracy of the two π^* oxygen orbitals. As the unpaired electron is confined in a π type orbital the EPR spectrum is intrinsically orthorhombic, where all three axes of the molecule are magnetically inequivalent ($g_{xx} \neq g_{yy} \neq g_{zz}$), where the z direction is specified, as along the internuclear axis, and the x and y direction is perpendicular to the adsorption site as shown in figure 6.24b.

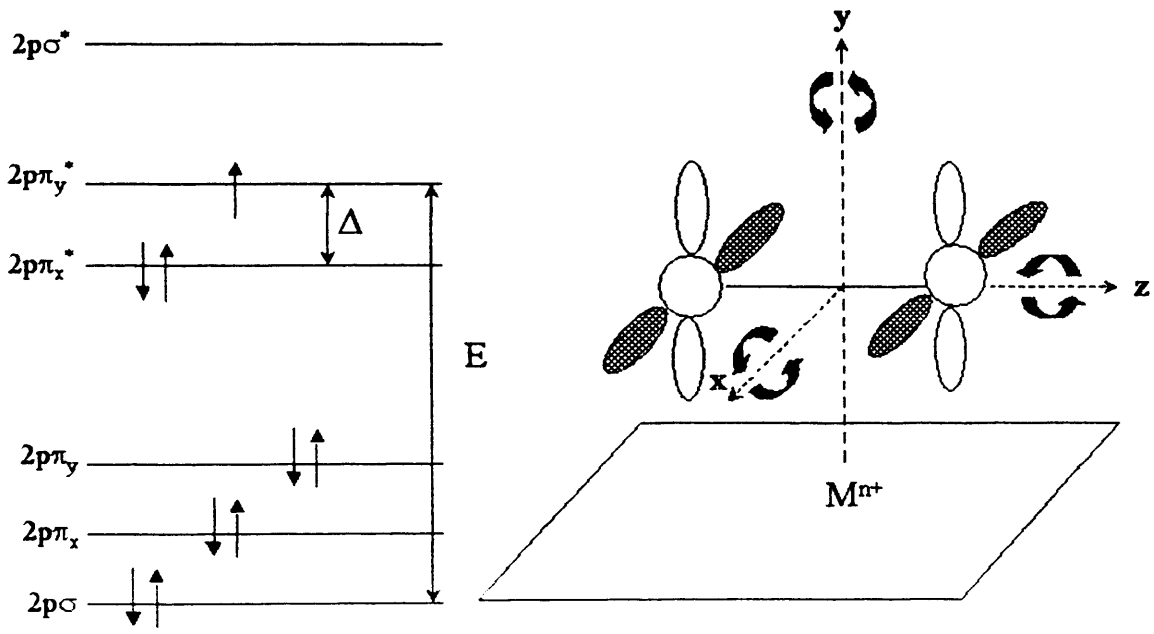

Figure 6.24 (a) Energy level diagram for O_2^- in the ground state. When a crystal field is present the $2p\pi_y^*$ and $2p\pi_x^*$ are not degenerate, (b) Illustration of the adsorption mode of O_2^- on a cationic surface site. Possible local rotation modes of the anion about the axes are shown with the circular arrows,

The expected principal values of the g tensor were first derived by Känzig and Cohen[31] for the case of an ionic superoxide anion in the bulk of alkali halides. The three principle values usually exhibit three distinct g values with the trend $g_{zz} > g_{yy} > g_{xx}$. Ignoring second order terms and assuming $\lambda < \Delta << E$, the g components for a superoxide ion are given by:

$$g_{xx} = g_e \qquad (6.3)$$

$$g_{yy} = g_e + 2\lambda/E \qquad (6.4)$$

$$g_{zz} = g_e + 2\lambda/\Delta \qquad (6.5)$$

Where λ is the spin orbit coupling constant for the oxygen atom, g_e is the free electron g value (2.0023) Δ is the energy splitting between the two antibonding $2p\pi_y^*$ and $2p\pi_x^*$ orbitals and E is the energy difference between the $2p\sigma$ and $2p\pi_y^*$ orbitals as shown in figure 6.24b.

The magnitude of the local crystal field which removes the degeneracy of the two π^* orbitals determines the shift in the g_{zz} component with respect to the free electron g_e value, i.e., the smaller the local electrostatic field felt by the superoxide ion, the smaller the value of Δ and hence the larger the g_{zz} value. The magnitude of the g_{zz} component of the O_2^- ion can therefore be used to determine the nature of the adsorption site. The advantage of this method is much more than the identification of the cation charge.[18] The magnitude of g_{zz} not only distinguishes between sites of different cationic charge (M^{n+}) but also of sites with the same nominal charge, but different coordinate environments, as observed in figures 6.1 and 6.2.

A heterogeneity of g_{zz} components at g_{zz} = (**III**) 2.026, (**II**) = 2.023 and (**I**) = 2.019 reflects the presence of three different radical sites available when only one cationic species (Ti^{4+}) is present. The heterogeneity of sites accessible for O_2^- stabilisation represents the adsorption sites where the effective crystal field is changed as a result of different crystal planes and/or different local coordination. In other words, at least three well-defined sites are available for O_2^- stabilisation; as the radicals are likely to be stabilised at the sites of electron transfer, these sites correspond to different morphological orientations of Ti^{4+}. Decreasing the cation charge increases the value of g_{zz}, the highest g_{zz} value (g_{zz} (**III**)= 2.026) reflects the site of highest co-ordinated Ti^{4+} for O_2^- adsorption i.e., lowest effective cation charge. In comparison to this, the site of the lowest g_{zz} value (g_{zz} (**I**) = 2.019) for O_2^- adsorption is assigned to the lowest co-ordinated site i.e., highest effective cation charge. The difference in site preference of the g_{zz} region is also reflected in the signal intensity, where the lower co-ordinated sites have a higher signal intensity compared to the sites of higher co-ordination (figure 6.2).

Following electron transfer from Ti^{3+} to the O_2, the two resulting charged states are held electrostatically together (Ti^{4+}.... O_2^-). This is an exothermic reaction in the gas phase (-42 kJ/mol) facilitated by the additional Coulombic stabilisation from the lattice. As the g_{zz} component is sensitive to the crystal field environment,

the average g value of 2.022 observed in the figures is consistent with those expected for O_2^- stabilised at a Ti^{4+} site.[16]

The g values obtained during stabilisation of O_2^- on the P25 Anatase surface are compared to those reported in the literature in table 6.2.

Table 6.2. EPR Parameters for O_2^- on various TiO_2 surfaces.

Oxide	g_1 (g_{zz})	g_2 (g_{yy})	g_3 (g_{xx})	Ref
P25 anatase	2.022	2.008	2.003	This study
Rutile TiO_2	2.022	2.011	2.008	7
Rutile TiO_2	2.030	2.008	2.004	32
Rutile TiO_2	2.021	2.010	2.004	33
Anatase TiO_2	2.019	2.009	2.003	34
Anatase TiO_2	2.024	2.009	2.003	35

The g values obtained in this study are very similar to those obtained on the Rutile and Anatase materials in previous studies of thermal reduction and oxygen addition.

6.4.2 TiO_2 surface morphological considerations

The presence of different surface Ti atoms with different environments is important, due to the different reactivities, which may be created at each site. In recent work, research has demonstrated that, titania containing 4-coordinate Ti had an increased selectivity for certain partial oxidation reactions[36] and selective photoreduction of Ag^+ to Ag metal.[37,38] It was suggested that this coordination of Ti may create increased photoreactivity either by altering the rate at which carriers are trapped at the surface or by altering the rate at which photogenerated carriers are transferred across the interfacial barrier. In other words it is possible that the relatively electron rich surface O atoms surrounding the 4-coordinate Ti atoms are more effective hole traps than those surrounding the 5- coordinate Ti sites.[39] In this case, a surface Ti with four O neighbours might bind adsorbed species from the gas or solution phase more readily, and this could promote charge transfer from the crystal to the adsorbate. Whatever, the view of interfacial charge transfer, it is becoming clear

that different surface planes will display different reactivities arising from differences in the degree of Ti coordination.

As previously stated, the superoxide anion is very sensitive to the local crystal fields created by the surface Ti cations, since the g_{zz} region of the anion indirectly reflects the presence of different Ti environments on the surface. However, it is not clear if the three g_{zz} sites (2.019, 2.022 and 2.025) on P25 Anatase for example, represent different degrees of Ti coordination (e.g., 5- or 4- coordinate) or differences in the secondary environment of a single nominally X-coordinate cation (e.g., a series of 4-coordinate Ti atom on different planes, creating slightly different electric fields which split the π^* orbitals of O_2^- producing the distribution of g_{zz} peaks; this has previously been observed on MgO[18]). It is thought that the latter case occurs, but this requires experiments using single crystals of TiO_2 to confirm the assignment. Che and Giamello[28] reported that the known values for the g_{zz} region of the O_2^- anion stabilised at Ti^{4+} sites are between the range of 2.018 to 2.037, ranging from high to low coordinated Ti^{4+} sites. However, as reported here the range of the g_{zz} values are between 2.019 to 2.025 therefore suggesting a single coordinated state.

The range and distribution of the g_{zz} components on the Rutile samples (A and B) was significantly different compared to that on P25 Anatase (i.e., g_{zz} (**I**) = 2.019, g_{zz} (**II**) = 2.022, g_{zz} (**III**) = 2.026 on P25 and g_{zz} (**II**) = 2.022 and g_{zz} (**III**) = 2.026 on the Rutile samples). In addition, while the g_{zz} peaks on P25 Anatase were well defined (suggesting a narrower distribution of adsorption sites) only a broad unresolved distribution of peaks was found on the Rutile samples. It should be recalled, that there is growing evidence in the literature in favour of the idea that the difference in photoactivity between Anatase and Rutile, is not just related to difference in their band-gap (which are very similar) but may also be due to differences in the efficiency of the electron hole pair utilisation at the surface. In other words, how efficiently the electron or hole are transferred across the interface. If the degree if local coordination around a Ti^{4+} cation is different, one may assume that the rate of electron transfer may also be different. It is interesting to note therefore, that on P25 Anatase one superoxide species with a low g_{zz} value (species **I** with 2.019) is present which is absent on the two Rutile surfaces. The generation of reduced surface following thermal reduction is not considered a realistic model for the surface state during photocatalysis, however, as demonstrated an identical distribution of g_{zz}

components can be produced on a P25 Anatase sample following the photoirradiation in the presence of adsorbed O_2 gas, this will be discussed later.

6.4.3 Stability and mobility of O_2^-

To obtain further information on the O_2^- species produced or its environment on the surface, oxygen enriched in ^{17}O was used (see figure 6.4). The hyperfine tensor of the $^{17}O_2^-$ is capable of revealing, both the number of nuclei involved and an indication of the type of bonding with the surface.[40] The $^{17}O_2^-$ results show that the unpaired spin density is similar in both oxygen nuclei and the electron must be regarded as distributed over the entire molecular ion. On TiO_2, the nuclei are so closely equivalent suggesting that the ion is adsorbed with its internuclear axis parallel to the plane of the surface and perpendicular to the axis of symmetry of the adsorption site.[32] The observed hyperfine pattern is identical to that expected for the 'side-on' bonded ionic superoxide species.

For ionic O_2^- radicals, the 'side on' model is normally used to explain the binding mode of the anion on the surface (Figure 6.25). This model is supported by ^{17}O experiments, where the hyperfine coupling arises from the interaction of the unpaired spin with the ^{17}O nucleus equivalency of the two nuclei.[21] For end-on adsorption the inequivalent spin distribution in the radical would be easily observed in the ^{17}O spectrum.

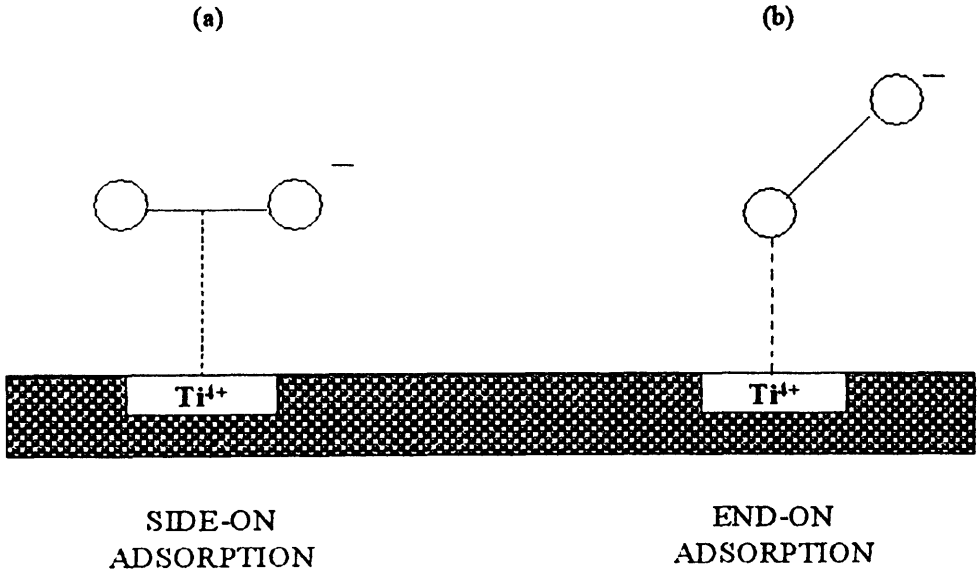

Figure 6.25. Schematic illustration of the two possible orientations for the bonding of the superoxide anion on the surface of a metal oxide, (a) 'side on' mode and (b) 'end on' mode.

The rotational dynamics of the side on model has been studied in depth, particularly for O_2^- on titania systems.[17,41,42] It has been found that at temperatures between 10 and 300 K, the radical will easily rotate about its y axis. Because the electron is confined to one of the two π^* antibonding orbitals, rotation about the z-axis (turning over or twisting about the z-axis) is very unfavourable. Similarly, because the electron is almost completely localized in one of the π^* antibonding orbitals (~ 99.9%) and shared equally between each oxygen atom, then rotation (i.e., end on flipping of the radical) about the x-axis is always unfavourable.

As the temperature is increased, local rotation will occur about the y-axis, resulting in the x and z g-tensors appearing to average, while the y g-tensor remains constant as shown in figure 6.26.

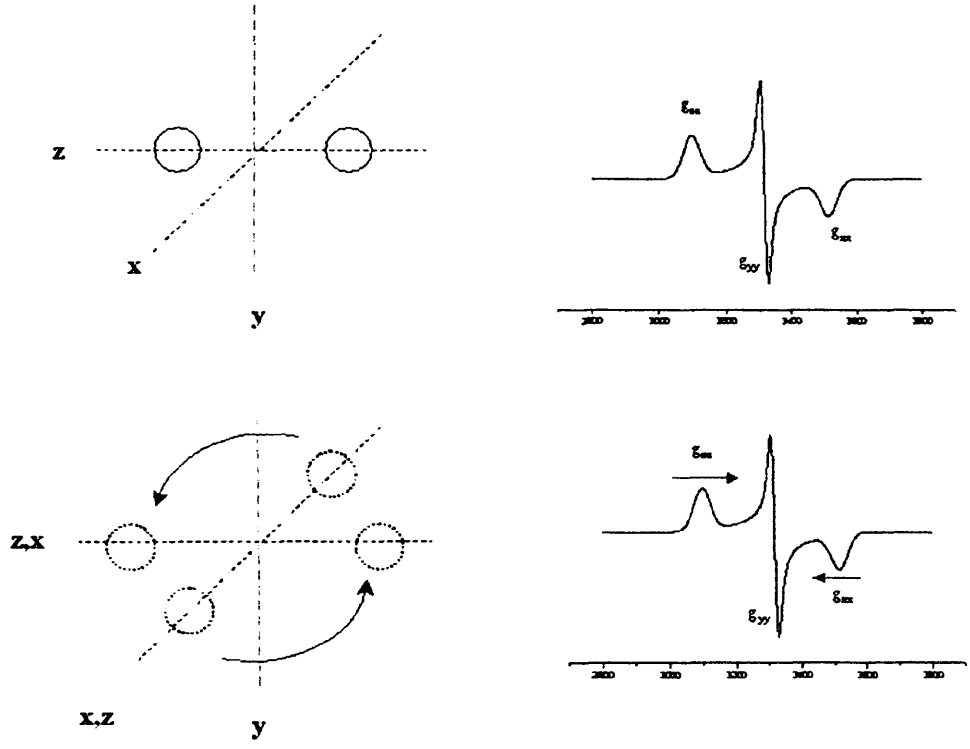

Figure 6.26. Schematic illustration of the rotation of the adsorbed superoxide radical (O_2^-) about its y-axis.

6.4.4 Stability and surface diffusion of O_2^-

As previously mentioned following electron transfer and formation of superoxide, the O_2^- anions are electrostically held together (i.e., Ti^{4+}.... O_2^-). However, as evidenced in figure 6.5, gentle annealing of the sample resulted in the lateral diffusion and redistribution of the anions on the surface as manifested in the number

and intensity of the peaks in the g_{zz} region. Provided the temperature is not too high (and the anions are not destroyed), the radicals can migrate across the surface. Upon cooling the samples to 100 K the anions become stabilised once more at sites often different to those of the initial states. If the temperature is too high, the mobile radicals will interact with each other and the surface with sufficient kinetic energy that causes the radicals to decompose.

As shown in figure 6.5, warming the sample within the lower range of temperatures (i.e., 298 and 313 K) produced a relative distribution of the g_{zz} components with the intensity pattern of **I>II>III**. However, when the sample was annealed to higher temperatures (333 and 353 K) a different distribution of sites was observed with **II>III>I** due to the radicals diffusing across the surface.

The driving force behind the diffusion is the kinetic energy of the O_2^- anions, which overcomes the electrostatic forces between the O_2^- and Ti^{4+} cation. When preformed on other oxide surfaces the anions tend to migrate from low stability sites to those which have a higher stability.[18] In other words although the O_2^- anion is restricted to a specific Ti^{4+} cation where the initial electron transfer occurred, a more favourable electrostatic attraction may be found at other coordinated sites. Usually, the g_{zz} value would be expected to decrease (due to the lower coordinated site creating a stronger electrostatic field). However, this is not the case on P25 whereby the O_2^- anions appear to migrate at elevated temperature from high stability sites (site **I** at 2.019) to lower stability sites (sites **II** = 2.023 and **III** = 2.026).

One tentative explanation for these results is based on the entropy of the surface diffusion process, which dominates over any enthalpy or kinetic considerations. If preferential reduction of specific surface Ti^{4+} sites occurs then; electron transfer will take place from these specific sites producing localised concentrations of O_2^- anions (e.g., at steps, edges). In other words, under these conditions, the resulting O_2^- anions will not be randomly distributed across the TiO_2 surface but instead concentrated on localised areas containing the preferentially reduced Ti^{3+} sites. With the provision of sufficient thermal energy the O_2^- anions will diffuse across the surface, thereby maximising the entropy or randomisation of the radicals, even if this results in a slightly unfavourable enthalpy term resulting from the stabilisation of the anion at less favoured Ti^{4+} coordination sites.

6.4.5 Oxygen adsorption at defect sites on thermally reduced TiO_2

As shown earlier in figure 6.6, superoxide anions are formed on TiO_2 following thermal reduction at different temperatures ranging from 623 K to 873 K. For samples reduced at 623 K only a single adsorption site appears to exist for the O_2^- anion, as characterised by a single g_{zz} component at 2.018. As discussed earlier, the magnitude of this single g_{zz} component at 2.018 should in principle represent a Ti^{4+} site of lowest coordination creating a high electric field gradient (large Δ value). Since the Ti^{3+} centres responsible for electron transfer to O_2 is generated by thermal reduction of the oxide, it suggests that the defectivity created by removal of a surface lattice O^{2-} anion occurs preferentially at the lowest coordinated Ti^{4+} sites on the TiO_2 surface. According to Rusu and Yates,[43] upon loss of neutral molecular oxygen through annealing in vacuum, the two extra electrons are formally shared between two Ti^{3+} neighbours for each O^{2-} ion removed. For example on the TiO_2 (110) surface both bridging and in-plane oxygen exist, but owing to the lower probability of desorption of the in-plane oxygens, the bridging oxygens are most likely to be lost producing the vacancies shown in the models below;

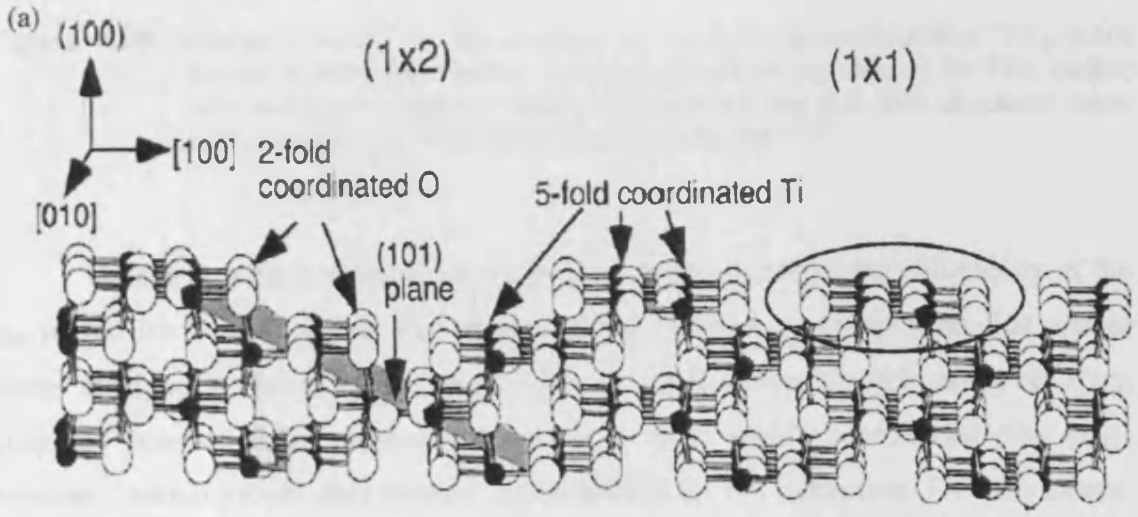

Figure 6.27. Ball-and-stick model of an Anatase TiO_2 surface. Large white balls represent oxygen and small black balls represent titanium atoms.

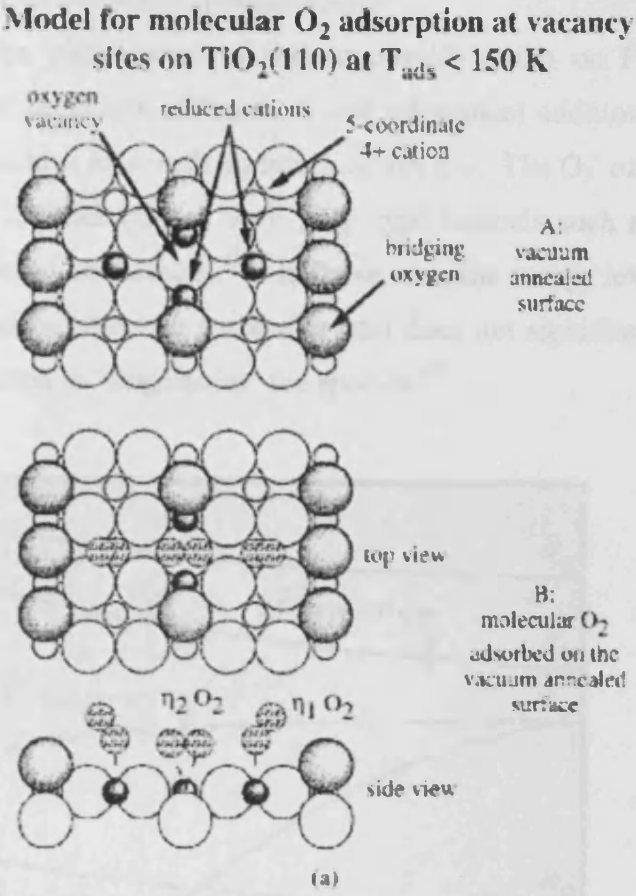

Figure 6.28. Schematic model for the bonding of O_2 both vacuum-annealed TiO_2 (110) surface at low temperatures. Model A shows the top view of the TiO_2 surface with an oxygen vacancy. Model B shows top and side (001 direction) views of O_2 bonding at a vacancy and non-vacancy site.[44,45]

As the reduction temperature is progressively increased, the complexity of the g_{zz} region for the O_2^- anions also increases, but the new g_{zz} components that appear occur at higher g values (2.022 and 2.025). In other words, the defectivity resulting from O^{2-} loss at high temperatures occurs at more highly coordinated sites (e.g., terraces), which presumably require higher energy for O^{2-} extraction. To some extent, this result is not surprising as similar energetic considerations are found on other oxides such as MgO,[46] where the energy required to remove an O^{2-} anion from a step or corner site is lower compared to a flat terrace site. Nevertheless this result is a nice illustration of how EPR can be used to probe the defectivity created by vacuum annealing of a TiO_2 powder.

6.4.6 O^- and O_3^- formation on thermally reduced Rutile

In comparison to the stabilisation of the superoxide anion on P25 Anatase surface, during the thermal reduction of Rutile A and subsequent addition of oxygen, the formation of ozonide is favoured with no traces of any O_2^-. The O_3^- ozonide ion is a 19 electron radical and is isoelectronic with AB_2^- type radicals such as, SO_2^- and NO_3^{2-} that have been observed on surfaces.[16] In these ions, the energy levels are well separated (figure 6.29) and because the surface crystal does not significantly perturb them, the g tensor can be used to 'fingerprint' the species.[47]

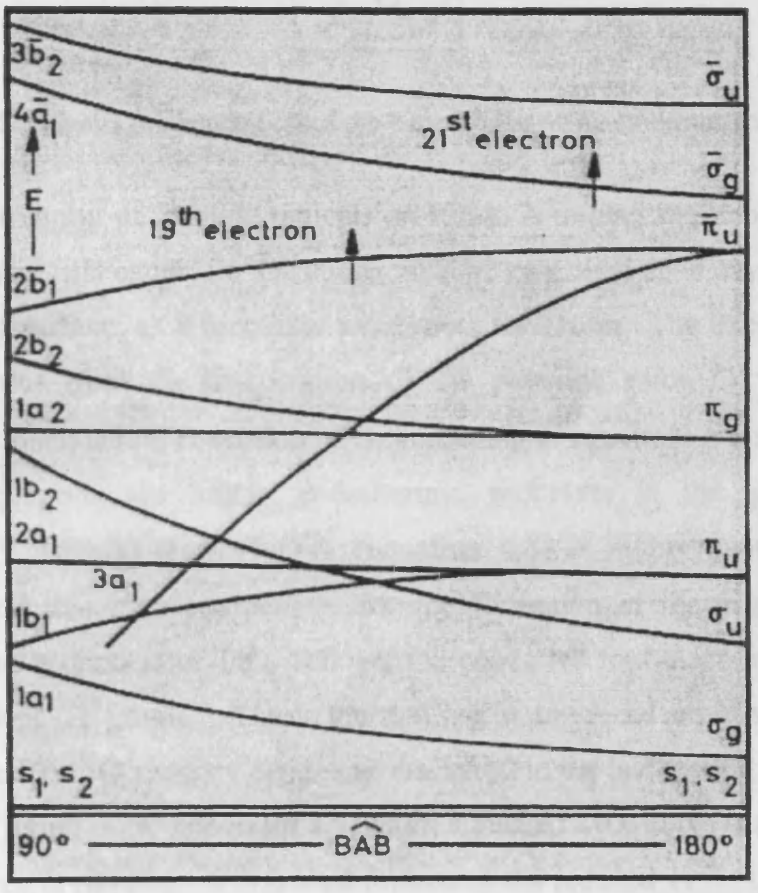

Figure 6.29. Correlation diagram for AB_2 radicals with 19 and 21 electrons.[48]

The O_3^- ion on MgO was first reported by Tench and Lawson[49] with a g tensor in agreement with the theoretical arguments. Based on studies of the thermal stability of the ion using isotopically labelled gases, Wang and Lunsford[50] demonstrated that the three oxygen atoms of the ion are in different environments as shown in figure 6.30 below, where O_a is the original lattice O^- ion. The ozonide ion is clearly distorted so that the 'lattice' oxygen O_a retains most of the negative charge. This

pushes the unpaired spin onto the other two oxygen atoms and mostly onto the outermost atom O_c.

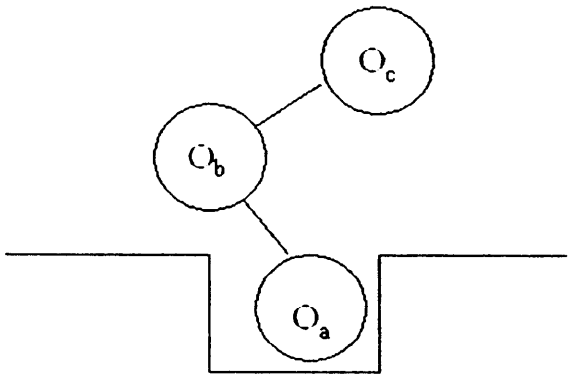

Figure 6.30. Schematic representation of the ozonide ion on an oxide surface.

The formation of ozonide radicals on Rutile A implies that molecular oxygen dissociation must first occur; i.e. O^- anions must be generated upon oxygen adsorption on the reduced surface, as a precursor to ozonide formation. The likely source of O^- anions originates from the dissociation of the peroxide anion O_2^{2-} formed in a simultaneous or sequential reduction of O_2 according to equations 6.6 and 6.7. While these two equations are highly endothermic processes in the gas phase (*ca.* 650kJ/mol),[15,18] dissociation of O_2^{2-} (equation 6.8) is highly exothermic (*ca.* – 435kJ/mol) and this may compensate for the formation of the original peroxide. Thermovacuum reduction of TiO_2 follows the concerted four-electron transfer from $2O^{2-}$ to adjacent Ti^{4+} ions. These thermally generated defective surfaces would contain coupled Ti^{3+}/O vacancy centres as discussed in the last section, and illustrated in the model (figure 6.28) above for a vacuum annealed TiO_2 (110) surface where the bridging oxygen is ensuing. Oxygen adsorption at the reduced Ti^{3+} - II - Ti^{3+} defects could easily occur producing O_2^{2-}. In this non-stoichiometric state there will be a large driving force for O^{2-} formation, so that equations 6.6 to 6.8 could conceivably occur on the Rutile surface. In the presence of excess oxygen the surface O^- anions will react with O_2 to form O_3^- (equation 6.9) as commonly observed on other oxide surfaces.[16,20,22,23]

$$2Ti^{3+} + O_2 \longrightarrow 2Ti^{4+} + O_2^{2-} \qquad (6.6)$$

$$Ti^{3+} + O_2^- \longrightarrow Ti^{4+} + O_2^{2-} \qquad (6.7)$$

$$O_2^{2-} \longrightarrow 2O^- \qquad (6.8)$$

$$O^- + O_2 \longrightarrow O_3^- \qquad (6.9)$$

While it is possible for O^- to form directly *via* alternative pathways as illustrated in equations 6.10 to 6.12 below;

$$O_2 + e^- \longrightarrow O^- + O \qquad (6.10)$$
$$O_2 + 2e^- \longrightarrow 2O^- \qquad (6.11)$$
$$O_2^- + e^- \longrightarrow 2O^- \qquad (6.12)$$

all of these processes are endothermic and are not accompanied by a negative enthalpy process shown in equation 6.8.

The formation of O_3^- ions have also been reported on TiO_2 UV-irradiated under oxygen.[51,52] In this case O^- ions were generated directly by UV irradiation, and O_3^- subsequently by O_2 adsorption. The UV generated O_3^- ion was reported as being unstable at 300 K, similar to that observed in figure 6.8. Einaga *et al.*,[9] also studied the UV irradiation of a Pt/TiO_2 sample, and a paramagnetic species was observed and identified as O_3^-. The O_3^- species were not detected before UV irradiation, confirming that it was photo formed on TiO_2. The radical was also found to be unstable and readily decomposed at room temperature. When the Pt/TiO_2 sample was irradiated with UV light in the absence of O_2, the O_3^- signal was not observed. Thus indicating that O_2 is essential for the O_3^- formation and supports equation 6.9 above.

By comparison to the Rutile A sample, oxygen adsorption on the thermally reduced Rutile B sample resulted in the formation of both O^- and O_2^- (i.e., on P25 O_2^- was exclusively formed, while on Rutile A O_3^- was predominately formed). It should be recalled that while the two samples A and B are both Rutile materials, they were produced by completely different methods (Rutile A *via* a sol-gel synthesis with a SA of 135 m^2g^{-1} while Rutile B is a commercial material used as a whitening pigment prepared *via* a sulphate process with a SA of 97 m^2g^{-1}) and therefore can be expected to have slightly different morphological features.

Without a detailed surface science analysis of this latter material, it is not possible to unambiguously explain how and why oxygen adsorption leads specifically to O^- and O_2^- generation. As discussed above in the mechanism of O_3^- formation, surface sites must be available on the Rutile material, which are capable of splitting the diatomic oxygen molecules to form O^- ions (i.e., the vacancy site on the Rutile (110) surface where neighbouring reduced Ti^{3+} centres could possibly reduce O_2 to O_2^{2-}). Presumably, these bridging sites do not exist on the Anatase surface, so single

isolated Ti^{3+} centres will only lead to a singly reduced O_2 species (i.e., O_2^-). On Rutile B, a mixture of these sites must exist, which can create O^- and O_2^-, although it is surprising that few O_3^- anions are formed suggesting that the O^- anions on this material may exist in inaccessible or recessed sites. Further research is clearly required to understand these unusual results. Nevertheless these results offer a fascinating glimpse into the re-oxidation processes that occur on reduced TiO_2 surface, and the process is not as simple as superoxide formation (which is the standard first step of the reaction for re-oxidation which is widely described in the literature).

6.4.7 Photogeneration of oxygen radicals on dehydrated TiO_2 (Anatase and Rutile)

It is well documented that upon band gap irradiation of TiO_2, photogenerated electrons and holes are produced which are ultimately responsible for the photocatalytic redox reactions. While the mechanistic details remain uncertain, it is clear that the presence of oxygen and water is crucial in controlling the reaction pathways often *via* the intermediacy of Reactive Oxygen Species (ROS).[53-55] As shown in figures 6.12, 6.14a and 6.15a, following UV irradiation under an excess oxygen atmosphere photogenerated trapped holes (O^-) are produced. These active oxygen species appear to have axial symmetry (*cf.* chapter 5) and are characterised by the spin Hamiltonian parameters shown in table 6.1 for each TiO_2 material studied.

Similar resonances have been reported previously in TiO_2 and were assigned to trapped hole states O^-.[12,39,56,57] These active oxygen species are short lived, and decay quickly in the dark or upon warming the sample to room temperature.[8] Results obtained by Howe and Gratzel[12] on hydrated anatase particles in the presence of both light and heavy water concluded that the EPR spectrum of the trapped hole was not due to the $OH^\bullet$ radical and suggested the following structure Ti^{IV}-$O^\bullet$-Ti^{IV}-OH. Results obtained by Micic *et al.*,[39,56] are consistent with the conclusions of Howe and Gratzel, that the hole adduct is a subsurface oxygen anion radical. Work by Micic *et al.*,[39,56] using experiments with ^{17}O doped TiO_2 helped to determine the location of the covalently bound O^-. Analysis showed that O^- is covalently bound to Ti atoms with non-equivalent crystal field splittings from the adjacent atoms. This confirmed suggested that most likely Ti^{IV}-O-Ti^{IV}-$O^\bullet$ radicals are formed.

As displayed in figures 6.12, 6.14 and 6.15 following UV irradiation of the clean dehydrated samples under the excess O_2 atmosphere, and subsequent evacuation at 298 K, the presence of the superoxide anion could be easily observed on all three surfaces. The long-lived photogenerated O_2^- anions were not previously visible under the excess pressure of oxygen (resulting in line broadening). In each case the photogenerated O_2^- was stable for several days on the fully dehydrated surfaces. Deactivation of O_2^- *via* release of an electron into TiO_2 was not observed on the dehydrated surfaces.[58]

Comparison of figures 6.12, 6.14 and 6.15 displays heterogeneity in the g_{zz} region of the superoxide species, which are stabilised on the TiO_2 surfaces following identical preparation methods. The difference in g_{zz} heterogeneity of O_2^- reflects the different surface morphologies (i.e., Anatase *vs.* Rutile), creating slightly different adsorption sites for the anion. Five sites are visible in the P25 Anatase sample (i.e., g_{zz}(**I'**) = 2.017, (**I**) = 2.019, (**II'**) = 2.021, (**II**) = 2.023 and (**III**) = 2.026) while only two adsorption sites exist for both Rutile samples (i.e., g_{zz}(**II**) = 2.022 and (**III**) = 2.026 for the Rutile samples).

6.4.8 Photogeneration of oxygen radicals on hydrated TiO_2 (Anatase and Rutile)

Following the investigation of the photogenerated oxygen radicals on the fully dehydrated TiO_2 surfaces, the analogous experiments were preformed on the fully hydrated surfaces in order to study the effects of surface hydration on the nature of the photogenerated oxygen radicals. When fully hydrated P25 was UV irradiated in the presence of oxygen no evidence was found for any adsorbed O_2^-.

In other words, there was no evidence for any radicals existing with the lifetime of the EPR measurement at low temperatures. By comparison UV irradiation of a partially hydrated P25 anatase sample at 77 K, resulted in the appearance of an intense EPR spectrum. Although the spectrum was dominated by the presence of O^- radicals (with traces of O_2^- and photogenerated Ti^{3+} centres), clear evidence was available for the presence of the hydroperoxy radical ($HO_2^\bullet$). The g_{zz} component of peroxy radicals is always *ca.* 2.034, and is often used as a fingerprint to identify the $HO_2^\bullet$ species.[13,59-61] The radical is likely formed *via* the reaction with surface hydroxyl groups as shown in equation 6.13,

$$O_2^- + H^+ \longrightarrow HO_2^\bullet \qquad (6.13)$$

since exposure of a TiO_2 surface containing pre-adsorbed O_2^- to 5 torr of water vapour resulted in a 5-fold decrease in O_2^- signal intensity, but no new signals arising from $HO_2^\bullet$ were observed (spectrum not shown for breviety).

The most striking difference between the P25 Anatase and Rutile samples however, relates to the stability of the radicals. The intensity of the spectra (figures 6.18, 6.19 and 6.20) was found to decrease (by a factor of 5) only after standing at 300 K for 24 hours. This contrasts significantly with fully hydrated P25 Anatase where no photogenerated oxygen-centred radicals were observed following UV. These results indicate the inherent differences in the lifetimes of the radicals on the P25 Anatase and Rutile surfaces depending on the extent of surface hydration.

In aqueous systems O_2^- radicals readily interact forming the hydroperoxy radicals (according to equation 6.13). Deactivation of the radical can subsequently occur according to the disproportionation reactions;

$$HO_2^\bullet + O_2^- + H^+ \longrightarrow H_2O_2 + O_2, \qquad (6.14)$$

$$HO_2^\bullet + HO_2^\bullet \longrightarrow H_2O_2 + O_2 \qquad (6.15)$$

$$O_2^- + O_2^- + 2H^+ \longrightarrow H_2O_2 + O_2 \qquad (6.16)$$

While it has been reported that O_2^- deactivation on TiO_2 proceeds *via* first-order kinetics, suggesting a reaction with species present in large excess,[58] the presence of the hydroxyl groups on the hydrated surface remove any adsorption sites for O_2^- anions. The O_2^- anions are very stable on dehydrated surfaces, and are often stabilised on the site of initial electron transfer. However, they can be sufficiently mobile on fully and partially hydrated surfaces such that reactions (equations 6.14 – 6.16) may occur. The reason for the different lifetimes observed on Rutile compared to Anatase, is proposed as due to the different morphologies, whereby some surface sites capable of O_2^- stabilisation remain on hydrated Rutile surfaces. This may also explain the difference in $HO_2^\bullet$ abundance on the two surfaces. On P25 Anatase $HO_2^\bullet$ formation occurs easily (signified by the g = 2.034 component), indicating a facile interaction between O_2^- and an adsorbed OH group, while on Rutile the levels of $HO_2^\bullet$ formation is far smaller. This indicates preferential adsorption of the charged anion as O_2^-.

6.4.9 Addition of NO as a surface probe

Similar to the use of oxygen as a surface probe, investigations using the NO molecule as a probe were also completed. The advantage of employing NO is that the molecule can be directly adsorbed on the unperturbed surface.[30] Therefore, low coordinated surface Ti^{4+} sites, responsible for the formation of O_2^- following initial production of the Ti^{3+} cation, can also be probed using NO. The electronic configuration of NO is that of an 11 electron diatomic radical characterised by the presence of a single unpaired electron in the π antibonding orbitals.[25] The interaction between the surface and NO is based on a weak polarisation of the molecule induced by the electric field present at the surface of the ionic solid in correspondence of the adsorption site.[62] This adsorption shows a perturbation on the NO molecular orbitals causing a splitting of the π^* orbitals as shown in figure 6.31 below.

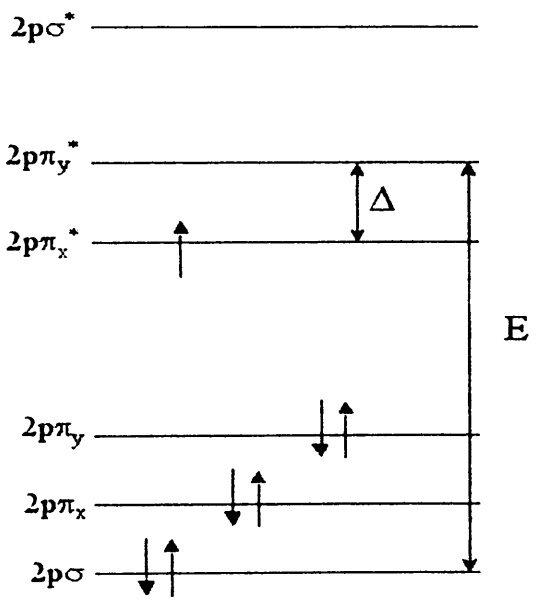

Figure 6.31. The molecular orbital energy diagram for the NO molecule in the surface crystal field (Δ is the energy splitting).

The theoretical principal g values in this case were obtained by Brailsford *et al.*,[63] who adapted the equations originally derived by Känzig,[31] a simplified form of the equations are as follows,

$$g_{zz} = g_e - 2l\sin 2\alpha \qquad (6.17)$$

$$g_{yy} = g_e\cos 2\alpha + (\lambda/E)(1 + \cos 2\alpha + \sin 2\alpha) \qquad (6.18)$$

$$g_{xx} = g_e\cos 2\alpha + (\lambda/E)(\cos 2\alpha - \sin 2\alpha - 1) \qquad (6.19)$$

where, λ is the spin orbit coupling constant , E and Δ are the energy differences shown in figure 6.31while sin2α is defined as λ/Δ and $l = \lambda/\lambda o$.

The equations show that assuming the z direction as the internuclear axis and the y-axis as the perpendicular to the adsorption site then, $g_{yy}>g_{xx}>g_{zz}$ and an important shift from the g_e is expected only for the g_{zz} component. At first order the g_{zz} term reduces to.

$$g_{zz} = g_e - 2\lambda/\Delta \qquad (2.20)$$

As mentioned above, NO adsorption onto an ionic surface causes a weak polarisation of the adsorbed NO molecule resulting in the splitting in the $\pi*$ orbitals. The magnitude of the local crystal field removes the degeneracy of the orbitals thus determining the shift in the g_{zz} component with respect to the free electron g_e value. It should be recalled that during O_2^- stabilisation, the magnitude of the g_{zz} component could be used to determine the nature of the adsorption site however, this did not distinguish between sites of different cationic charge but of sites of different co-ordination environments, the same is true for NO adsorbed on the surface.

A heterogeneity of the sites available for NO adsorption on both P25 Anatase and Rutile B are observed in figure 6.21, where the g_{zz} region of the adsorbed molecule indicates the adsorption occurring at slightly different Ti^{4+} sites. Using the NO probe molecule the local co-ordination environments for the Ti^{4+} sites available in both TiO_2 samples may therefore be indirectly studied, and the differences between the sites available reflecting the differences in TiO_2 materials studied (i.e., Anatase *vs.* Rutile).

The above results (figure 6.22) also indicated that the profile of the EPR spectrum during NO adsorption was pressure dependant. Following adsorption of low pressures of NO (5 Torr) onto the P25 Anatase preferential adsorption of the NO molecule occurred at the lowest co-ordinated Ti^{4+} sites. These lower co-ordination sites (i.e., corners, steps) provide the strongest Ti^{4+}....NO attraction for stabilisation at the lower pressures, with the most strongest attraction occurring at the highest g_{zz} value (1.9602). As the NO pressure is increased adsorption at the higher co-ordinated Ti^{4+} sites now occurs.

Water is extremely important in photocatalytic oxidations, as the OH^- ions trap holes producing $OH^\bullet$ radical ultimately responsible for surface oxidations. Depending on the temperature of evacuation, different groups of OH^- ions are released from the

surface. As shown in figure 6.23, the dehydroxlation of a hydrated Rutile B sample by evacuation at increasing temperatures resulted in the gradual removal of the OH groups from the surface, depending on the local co-ordination environments of the Ti^{4+}. The different Ti^{4+} sites available at increasing temperatures of evacuation were reflected in the adsorption of NO onto the surface. Evacuation at the lower temperatures causes the removal of the OH groups to occur from the highest co-ordinated Ti^{4+} sites. The OH groups are preferentially from these sites due to the weaker interaction with the Ti^{4+} sites, therefore, requiring lower amounts of energy to remove the OH groups. The availability of the higher co-ordinated Ti^{4+} sites is reflected in the low g_{zz} value 1.900 for NO adsorption. As the temperature is increased and more energy is supplied into the system the OH groups at the lower co-ordinated Ti^{4+} sites are removed. The higher g_{zz} value 1.9503 during NO adsorption therefore reflects the availability of the lower co-ordinated Ti^{4+} sites now available following dehydroxlation of the surface.

By varying the experimental conditions, i.e., pressure of the probe molecule added and surface hydration, the cationic sites that are usually available for adsorption can be preferentially altered. Therefore with the aid of NO as the probe molecule the TIO_2 surface may be further investigated and the local co-ordination of the Ti^{4+} sites may be determined as shown above.

6.5. Conclusion

As presented here the nature of the surface paramagnetic oxygen species (i.e., O^-, O_2^-, O_3^- and $HO_2^{\bullet}$) are capable of being altered depending on the pre-treatment conditions and the type of titania surface used. With the aid of the superoxide and NO probes the surface heterogeneity of the Ti^{4+} sites in the TiO_2 samples can be examined. That is the heterogeneity of sites accessible for NO and O_2^- stabilisation reflect the adsorption sites where the crystal field of the molecules and changed as a result of different crystal planes and the local environment of the sites.

As detailed above, both NO and O_2^- molecules are sensitive to local crystal field created by the Ti cations, the g_{zz} region of both adsorbed molecules reflect the different Ti environments n the surface. During the stabilisation of the O_2^- cation on the TiO_2 surfaces the lowest g_{zz} value (**I** = 2.019) represent sites of lowest co-ordinated Ti^{4+} cations where the strongest attraction between Ti^{4+} ... O_2^- is

experienced. Following adsorption of NO onto the TiO_2 surfaces the highest g_{zz} value observed corresponds to the lowest co-ordinated Ti^{4+} sites, again where the strongest interaction occurs.

As demonstrated in this chapter, the nature of the surface paramagnetic oxygen species can change depending on the pre-treatment conditions and nature of the surface studied. During the thermal reduction of the TiO_2 samples a non-stoichiometric defective surface is produced. Addition of oxygen to the reduced surfaces resulted in the production of various oxygen radicals i.e., O^-, O_2^- and O_3^-.

Following thermal reduction of the P25 Anatase sample the addition of oxygen resulted in the formation and stabilisation of O_2^- on the surface. A heterogeneity of sites available for stabilisation of the anion are observed reflecting the sites of different morphological orientations of the Ti^{4+} centres. During the gradual thermal reduction of the P25 sample and subsequent addition of oxygen the initial removal of lattice oxygen from the surface is reflected in the increased complexity of the superoxide on the surface. That is at lower temperatures of reduction the lattice oxygen was removed more favourably from sites of lower co-ordination where the interaction is weaker.

A redistribution of the O_2^- on the TiO_2 surface was favoured during gentle annealing of the sample to temperatures of 353 K. The radicals were observed to migrate across the surface from the original sites of stabilisation **I>II>III** to **II>III>I**. The driving force behind the redistribution is attributed to the entropy of the surface diffusion overcoming the kinetic and enthalpy considerations thus resulting in the stabilisation at high co-ordinated Ti^{4+} sites.

During the thermal reduction of both Rutile A and B samples addition of oxygen to the samples resulted in a variety of oxygen species formed on the surfaces. Following the thermal reduction of Rutile A and addition of oxygen the preferential formation of O_3^- on the surface occurs, along with traces of $HO_2^{\bullet}$ due to the presence of surface hydroxyl groups on the TiO_2 surface following thermal reduction. The presence of O_3^- demonstrates the strong preference for oxygen dissociation following addition to the surface, which leads to the O^- formation. By comparison, oxygen adsorption on the thermally reduced Rutile B sample resulted in the formation of both O^- and O_2.

As demonstrated, during the thermal reduction and subsequent addition of oxygen to the TiO_2 samples an appreciable difference in the nature, stability and lifetimes of the oxygen species formed have been observed. These differences in formation of oxygen species on the non-stiochiometric surfaces reflect the dependence on surface morphology used (i.e., anatase *vs.* rutile).

The thermal reduction of the TiO_2 surfaces are not ideal representations of the TiO_2 surface used in photocatalysis therefore, in comparison a variety of oxygen radicals can be generated over dehydrated and hydrated TiO_2 surfaces.

Irradiation of the dehydrated TiO_2 sample under an oxygen atmosphere resulted in the formation of the thermally unstable trapped hole (O^-). Removal of the oxygen from the samples revealed the characteristic signal of the O_2^- anion stabilised on each dehydrated TiO_2 surface. However, a difference in the g_{zz} region of the O_2^- formed on the dehydrated surface reflects the different surface morphologies (i.e., Anatase *vs.* Rutile), creating slightly different adsorption sites for the anion. Five sites are visible in the P25 Anatase sample (i.e., g_{zz}(**I'**) = 2.017, (**I**) = 2.019, (**II'**) = 2.021, (**II**) = 2.023 and (**III**) = 2.026) while only two adsorption sites exist for both Rutile samples (i.e., g_{zz}(**II**) = 2.022 and (**III**) = 2.026 for the Rutile samples).

In comparison (i.e., dehydrated *vs.* hydrated), UV irradiation of hydrated forms of the TiO_2 surfaces a number of oxygen species were generated, O^- O_2^- and $HO_2^{\bullet}$. However, addition of various amounts of water (i.e., partially and fully hydrated) was found to block the sites responsible for stabilisation of the different anions. No radicals were stabilised on the fully hydrated P25 Anatase surface however, a trapped hole and $HO_2^{\bullet}$ were generated on the partially hydrated form of the surface but with no traces of the superoxide stabilised on the surface following evacuation.

During the analogous hydrated experiments preformed on the Rutile samples a range of oxygen species were once again generated. In addition to the formation of O^- and $HO_2^{\bullet}$ following UV irradiation, the subsequent evacuation of the two hydrated forms of the Rutile samples revealed the presence of photogenerated O_2^- anions (with the exception of the fully hydrated Rutile B sample). The stability of the superoxide formed on the hydrated surfaces was found to be far less stable than that formed on the dehydrated surfaces, decaying 5 fold over 24 hours at 300K. These differences in formation and stability of the photogenerated radicals on the TiO_2 surfaces not only

reflect the differences in the TiO_2 samples studied but the effects of surface hydration (i.e., partially *vs.* fully hydrated).

The effect of surface hydration on the TiO_2 samples was also examined during the addition of NO to the surface. It was observed that the addition of water to the TiO_2 surfaces did not allow any adsorption of the NO molecule due to the Ti^{4+} sites normally available for stabilisation now being blocked by the water. However, the thermal evacuation of the sample followed by NO addition resulted in the adsorption of the molecule at the higher co-ordinated Ti^{4+} sites. This was due to selective removal of the OH groups at the lower temperatures of evacuation. It was observed that by increasing the temperature the NO molecule was then adsorbed at the lower co-ordinated sites. In both cases it was demonstrated how the sites usually available for adsorption of the O_2^- or NO can be preferentially blocked.

The results presented here have shown the inherent differences in radical formation and stability on the TiO_2 surfaces not only depends on the Anatase *vs* Rutile surface, but also the pre-treatment conditions used, i.e., thermal *vs.* UV irradiation and dehydration *vs.* hydrated effect.

6.6 References

1. J. M. Coronado, A. J. Maira, J. C. Conesa, K. L. Yeung, V. Augugliaro, J. Soria, *Langmuir*, **17**, 5368, (2001).
2. A. J. Maira, K. L. Yeung, J. Soria, J. M. Coronado, C. Belver, C. Y. Lee, V. Augugliaro, *Appl. Catal. B*, **29**, 327, (2001).
3. D. R. Park, B. J. Ahn, H. S. Park, H. Yamashita, M. Anpo, *Kor. J. Chem. Eng.*, **18**, 930 (2001).
4. D. R. Park, J. Zhang, K. Ikeue, H. Yamashita, M. Anpo, *J. Catal.*, **185**, 114, (1999).
5. P. Claus, A. Bruckner, C. Mohr, H. Hofmeister, *J. Am. Chem. Soc.*, **122**, 11430, (2000).
6. M. Okumura, J. M. Coroando, J. Soria, M. Haruta, J. C. Conesa, *J. Catal.*, **203**, 168, (2001).
7. C. A. Jenkins, D. M. Murphy, *J. Phys. Chem. B*, **103**, 1019, (1999).
8. A. L. Attwood, J. Edwards, C. C. Rowlands, D. M. Murphy, *J. Phys. Chem. B*, **107**, 1779, (2003).
9. H. Einaga, A. Ogata, S. Futamura, T. Ibusuki, *Chem. Phys. Lett.*, **338**, 303, (2001).
10. H. Liu, A. I. Kozlov, A. P. Kozlova, T. Shido, K. Asakura, Y. Iwasawa, *J. Catal.*, **185**, 252, (1999).
11. R. F. Howe, M. Gratzel, *J. Phys. Chem.*, **89**, 4495, (1985).
12. R. F. Howe, M. Gratzel, *J. Phys. Chem.*, **91**, 3906, (1987).
13. A. R. Gonzalez-Elipe, M. Che, *J. Chim. Phys.*, **79**, 355, (1982).
14. M. Anpo, T. Shima, Y. Kubokawa, *Chem. Lett.*, 1799, (1985).
15. T. A. Egerton, E. Harris, E. J. Lawson, B. Mile, C. C. Rowlands, *Phys. Chem. Chem. Phys.*, **2**, 3275, (2000).
16. M. Che, A. J. Tench, *Adv. Catal.*, **32**,1, (1983).
17. M. Shiotani, G. Moro J. H. Freed, *J. Chem. Phys.*, **74**, 2616, (1981).
18. E. Giamello, D. Murphy, E. Garrone, A. Zecchina, *Spec. Acta.*, **49**, 1323, (1993).
19. D. M. Murphy, E. W. Griffiths, C. C. Rowlands, F. E. Hancock, E.Giamello, *Chem. Commun.*, 2177, (1997).
20. M. Che, A.J. Tench, *Adv. Catal.*, **31**, 77, (1982).
21. M. Chiesa, E. Giamello, M. C. Paganini, Z. Sojka, D. M. Murphy, *J. Phys. Chem.*, **116**, 4266, (2002).

22. E. Giamello, D. Murphy, *Top. Mol. Org. Eng.*, **13**, 147, (1995).
23. D. M. Murphy, E. Giamello, in *Electron Paramagnetic Resonance*, B. C. Gilbert, M. J. Davies, D. M. Murphy,(Eds), **13**, 183. Royal Society of Chemistry, Cambridge, (2002).
24. M. Che E. Giamello, in *'Spectroscopic Characterisation of Heterogeneous Catalysis', Part B, Stu. Surf Sci. Catal., (Ed. J. L. G. Fierro), Elsvier Science Publishers, Amsterdam,* **57** B265, (1987).
25. C. Di Valentin, G. Pacchioni, M. Chiesa, E. Giamello, S. Abbet, U. Heiz, *J. Phys. Chem. B*, **106**, 1637, (2002).
26. D. M. Murphy, R. D. Farley, I. J. Purnell, C. C. Rowlands, A. R. Yacob, M. C. Paganini, E. Giamello, *J. Phys. Chem. B*, **103**, 1944, (1999).
27. J. Haber, A. Bielanski, *Oxygen in Catalysis*. Marcel Dekker, New York (1991),
28. M. Che, E. Giamello, A. J. Tench, *Colloids and Surfaces*, **13**, 231, (1985).
29. D. L. Grimscom, P. Hart, J. M. Jewell, J. T. Kohli, J. E. Shelby, J. *Non-Cryst. Solids*, **103**, 300, (1988).
30 M. Anpo, M. Che, B. Fubini, E. Garrone, E. Giamello, M. C. Paganini, *Topics in Catalysis*, **8,** 189, (1999).
31. W. Kanzig, M. H. Cohen, *Phys. Rev. Lett.*, **3**, 509, (1959).
32. C. Naccache, P. Meriaudeau, M. Che, A. J. Tench, *Trans. Faraday Soc.*, **67**, 506, (1971).
33. R. D. Iyengar, M. Codell, *Advan. Colloid Interface Sci.*, **3**, 365, (1972).
34. M. Setaka, S. Fukazawa, Y. Kirino, T. Kwan, *Chem. Pharm. Bull.*, **16**, 1240, (1968).
35. M. Dufaux, M. Che, C. Naccache, *C. R. Acad. Sci.*, **268**, 2255, (1969).
36. H. Idriss, K. Pierce, M. A. Barteau, *J. Am. Chem. Soc.*, **113**, 715, (1991).
37. J. B. Lowekamp, G. S. Rohrer, P. A. Morris, J. D. Bolt, W. E. Farneth, *J. Phys. Chem. B*, **102**, 7323, (1998).
38. P. A. Morris Hotsenpiller, J. D. Bolt, W. E. Farneth, J. B. Lowekamp, G. S. Rohrer, *J. Phys. Chem. B*, **102**, 3216, (1998).
39. O. L. Micic, Y. Zhang, K. R. Cromack, A. D. Thirfunac, M. C. Thurnauer, *J. Phys. Chem.*, **97**, 7277, (1993).
40. M. Che, A. J. Tench *Chem. Phys. Letts.*, **18**, 199, (1973).
41. K. Tatsumi, M. Shiotani J. H. Freed, *J. Phys. Chem.*, **87**, 3425, (1983).
42. R. F. Howe W. C. Timmer, *J. Chem. Phys.*, **85**, 6129, (1986)

43. C. N. Rusu, J. T. Yates Jr., *Langmuir*, **13**, 4311, (1997).
44. U. Diebold, *Surf. Sci. Reports*, 48, 53, (2003).
45. M. A. Henderson, W. S. Epling, C. L. Perkins, C. H. F. Peden, U. Diebold, *J. Phys. Chem. B*, **103**, 5328, (1999).
46. M. C. Paganini, M. Chiesa, E. Giamello, S. Coluccia, G. Martra, D. M. Murphy, G. Pacchioni, *Surf. Sci.*, **421**, 246, (1999).
47. M Che, *Magnetic Resonance in Colloid and Interface Science* (J. P. Fraissard H. A. Resing, (Eds.)) 79 Reidel, Dordrecht, (1980).
48. P. W. Atkins, M. C. R. Symons, *The structure of Inorganic radicals*, 121Elsvier, Amsterdam, (1967).
49. A. J. Tench, T. Lawson, *Chem. Phys. Lett.*, **7**, 459, (1970).
50. N. B. Wang, J. H. Lunsford, *J. Phys. Chem.*, **56**, 2664, (1972.).
51. P. Meriaudeau, J. C. Vedrine, *J. Chem. Soc. Faraday Trans. II*, **72**, 472, (1976).
52. A. R. Gonzalez-Elipe, G. Munuera, J. Soria, *J. Chem. Soc. Faraday Trans. I*, **75**, 748, (1979).
53. T. Tatsuma, S. Tachibana, A. Fujishima, *J. Phys. Chem. B*, **105**, 6987, (2001).
54. R. Nakamura, S. Sato, *J. Phys. Chem. B*, **106**, 5893, (2002).
55. S. H. Szczepankiewicz, A. J. Colussi, M. R. Hoffmann, *J. Phys. Chem. B*, **104**, 9842 (2000).
56. O. I Micic, Y. Zhang, K. R. Cromack, A. D. Trifunac, M. C. Thurnaur, *J. Phys. Chem.*, **97**, 13284, (1993).
57. D. Zwingwl, *Solid State Commun.*, **20**, 397, (1976).
58. K. Ihibashi, Y. Nosaka, K. Hashimoto, A. Fujishima, *J. Phys. Chem. B*, **102**, 2117, (1998).
59. A. L. Attwood, J. Edwards, C. C. Rowlands, D. M. Murphy, J. *Phys. Chem. B*, **107**, 1779, (2003).
60. M. D. Sevilla, D. Becker, M. Yao, *J. Chem. Soc., Faraday Trans.*, **86**, 3279, (1990).
61. D. C. McCain, W. E. Palke, *J. Magn. Reson.*, **20**,52, (1975).
62. P. Martino, M. Chiesa, M. C. Paganini, E. Giamello, *Surf. Sci.*, **527**, 80, (2003).
63. J. R. Brailsford, J. R. Morton, L. E. Vannotti, *J. Phys. Chem.*, **50**, 1051, (1969).

Chapter 7
Transient Radical Formation on Photo-irradiated TiO_2 Powders

7.1 Introduction

Photocatalytic reactions over semiconductor powders have potential applications in the degradation of a wide range of both gaseous and aqueous pollutants.[1-3] The widespread use of volatile organic compounds (VOCs) in both domestic and industrial activity has caused significant environmental problems, such as degrading air quality, contaminating groundwater, global warming and stratospheric ozone depletion.[4] Approximately 50% of the priority pollutants on the US Environmental Protection Agency (EPA) list are composed of VOCs.[5]

In recent years the photocatalytic degradation of these organic compounds over semiconductors into non-toxic compounds, such as CO_2 and H_2O, have been the subject of many studies.[6] One of the most active and efficient semiconductors is TiO_2. The use of titanium dioxide for the remediation of VOCs has several advantages over traditional heterogeneous catalysts. TiO_2 has the ability to operate at ambient temperature and pressures, the reaction products are usually CO_2 and H_2O, it exhibits high corrosion resistance and it also displays efficient photocatalytic conversion rates when in contact with both liquid and gas phases. Despite the growing interests in the applications of TiO_2 for photocatalytic oxidation of gas phase organic compounds, more research is required in order to gain a complete understanding of the photocatalytic mechanisms involved.

To explore the reaction mechanism of VOC decomposition in heterogeneous photocatalysis, identification of the reaction intermediates by spectroscopic methods is required under reaction conditions. Considering the role of surface orientation in the photochemical reactivity of TiO_2 (as demonstrated on both thin films[7] and polycrystalline materials[8]), it is also necessary to characterise these intermediates directly at the surface, before desorption and subsequent reactivity in the gas phase.

Electron Paramagnetic Resonance (EPR) is a powerful technique for exploring the photochemical reactions that occur on the polycrystalline powders under in-situ conditions. The method has been widely used in the past for the characterisation of surface radical species over TiO_2.[9,10] As previously reported in chapters 5 and 6 many paramagnetic species have been identified (i.e., O^-, O_2^-, O_3^-, $HO_2^\bullet$ and Ti^{3+}) but the direct role and participation of some of the radicals in the photocatalytic reactions

remains unclear. While the spin Hamiltonian parameters of these individual oxygen species are sufficiently distinct that unambiguous assignments can be made. In some cases they can be similar to each other, so that in many photocatalytic experiments overlapping signals may appear due to the simultaneous presence of multiple oxygen centred radicals. Therefore the spin Hamiltonian parameters should not be the only factor considered in the assignment of surface paramagnetic centre. Information about the stability, mobility characteristics, simulated profile, etc., of the radical should also be taken into account.

Ketones, aldehydes and alcohols have been regarded as the central class of VOCs responsible for air quality since these compounds comprise the most widely used organic solvents.[11-14] In the present work the intermediates involved in the oxidation of these organic materials have been studied. During this investigation direct evidence is provided for the formation of a thermally unstable surface alkyl peroxy radical ($ROO^{\bullet}$) formed during the low temperature UV irradiation of co-adsorbed acetone/O_2 over TiO_2. The use of ^{17}O labelled O_2 confirms the assignment of the radical. This is the first reported identification of such an intermediate in the photocatalytic reaction of acetone with O_2 over TiO_2.

Jenkins and Murphy[15] investigated the co-adsorption of aldehydes and oxygen on a thoroughly dehydrated TiO_2 (Rutile) surface under conditions of continuous UV irradiation. Using EPR spectroscopy a surface peroxyacyl radical ($RCO_3^{\bullet}$) was identified on the rutile surface. Therefore, for comparison the ability to form and stabilise these peroxyacyl radicals on a dehydrated anatase surface has also been examined in this study. In order to aid in the unambiguous identification of the peroxyacyl radical, a series of experiments were also preformed using labelled ^{17}O. Finally, evidence will be provided in this chapter for the formation of an oxidative intermediate formed during the low temperature UV irradiation of co-adsorbed alcohols and oxygen on a P25 anatase sample.

7.2 Experimental

A detailed description of the experimental methods used in handling of the TiO_2 powders, manipulation of the samples on the vacuum line and operation of the EPR spectrometer was thoroughly described in chapter 4. In this section, only the

specific experimental conditions used in the preparation and study of the organic and oxygen over TiO_2 will be outlined.

7.2.1 Preparation of clean polycrystalline TiO_2

Throughout the work described in this chapter the titanium dioxide samples studied were, P25 Anatase (*Degussa*) with a surface area *ca.* 49 m^2g^{-1} and a rutile sample hereafter labelled Rutile A with a surface area of *ca.* 135 m^2g^{-1}. This latter material was synthesised by hydrolysis of an aqueous solution of $TiCl_4$.[16] The polycrystalline TiO_2 samples (*ca.* 5 mg) were initially evacuated to a residual pressure of 10^{-4} Torr at 298 K in an EPR quartz cell. The samples were then heated to 393K under vacuum overnight in order to remove any physisorbed water from the surface.

The polycrystalline TiO_2 samples were subsequently slowly heated (over a 5 hour period) to a temperature of 823 K, and held at this temperature for approximately 1 hour. Oxygen (50 Torr) was added to the sample at 823 K and the samples cooled to room temperature under the excess oxygen atmosphere. This produced a clean dehydrated surface free from contaminants or surface hydroxyls. Exposure of a thermally reduced TiO_2 surface to O_2 at 298K leads to the formation of paramagnetic surface oxygen radicals (i.e., O^-, O_2^- or O_3^- as evidenced in previous chapters). However, exposure of TiO_2 to O_2 at high temperatures (823K) leads to the formation of diamagnetic surface O^{2-} lattice anions, as the surface is effectively re-oxidized at this high temperature. At no time during this treatment were the samples exposed to air, thus ensuring that the surface remained clean.

Throughout this work the vast amount of experiments were carried out on dehydrated clean surfaces, as described above. However, a small number of investigations were also carried out on partially hydrated surface in these few experiments the partially hydrated samples were prepared as follows. Prior to the co-adsorption of organic:O_2 mixtures, the vapours from triply distilled water (10 Torr) was added to the sample under vacuum at 298 K for a 1 hour period before evacuation for a further 30 minutes at 298K. In this way most of the weakly bound physisorbed water is removed but the surface remains heavily hydrated.

7.2.2 Addition of organic:oxygen mixtures

Following the preparation of the clean dehydrated samples, the TiO_2 material was then exposed to the probe gases (total pressure of 10 Torr) at 298 K from a

vacuum manifold. The organics were all purified by repeated freeze-pump-thaw cycles before use, to remove any oxygen. The organic to oxygen ratio was 10:1 in all these co-adsorption experiments.

After exposure of the TiO_2 samples to the organic:O_2 mixture, the EPR sample cells were then placed into the EPR spectrometer at low temperature (i.e., 100K, 77K, or 10K depending on the experiment) and UV irradiated in-situ for 30 minutes at this temperature. A 1000 W *Oriel Instruments* UV lamp, incorporating a Hg/Xe arc lamp (250 nm to 2500 nm), was used for all irradiations in the presence of a water filter. The UV output below 280 nm accounts for only 4 – 5% of the total lamp output.

The high purity O_2 gas was supplied by *BOC Ltd.* The organics (acetone, deuterated acetone, ethanol and benzaldehyde) were of analytic grade and were supplied by *Aldrich Chemicals Ltd.* ^{17}O-labelled dioxygen gas (63% enrichment) was supplied by *Icon Services Inc.* (New Jersey) and used without further purification.

7.2.3 Measurement of EPR spectra

The EPR spectra were recorded on a Bruker ESP 300E series spectrometer incorporating an EPR 4102 ST rectangular cavity. All spectra were recorded at X-band frequencies, 100 kHz field modulation and 5 mW microwave power. The g values were obtained using a Bruker ER035M NMR gaussmeter calibrated using the perylene radical cation in concentrated H_2SO_4 (g = 2.002569). EPR computer simulations were performed using the SIM14S program (QCPE 265).

7.3 Results

7.3.1 Co-adsorbed Acetone:Oxygen

A sample of clean fully dehydrated P25 was irradiated at 77 K in the presence of co-adsorbed acetone:O_2 (10:1 ratio; total pressure = 10 Torr). The resulting EPR spectrum recorded at 10K is shown in figure 7.1 along with the associated computer simulation. The features at g = 1.989 and g ≈ 1.972 can be easily assigned to Ti^{3+} cations at substitutional and normal lattice sites, respectively (*cf.* chapter 5). The latter broad signal at g ≈ 1.972 is actually a composite signal, with an asymmetric g tensor ($g_\perp$ = 1.972 and $g_\parallel$ = 1.960: $\Delta H \approx 21$ G) arising from the presence of primarily bulk Ti^{3+} centres, as reported previously in chapter 5 and in the literature.[9,10,15,17,18]

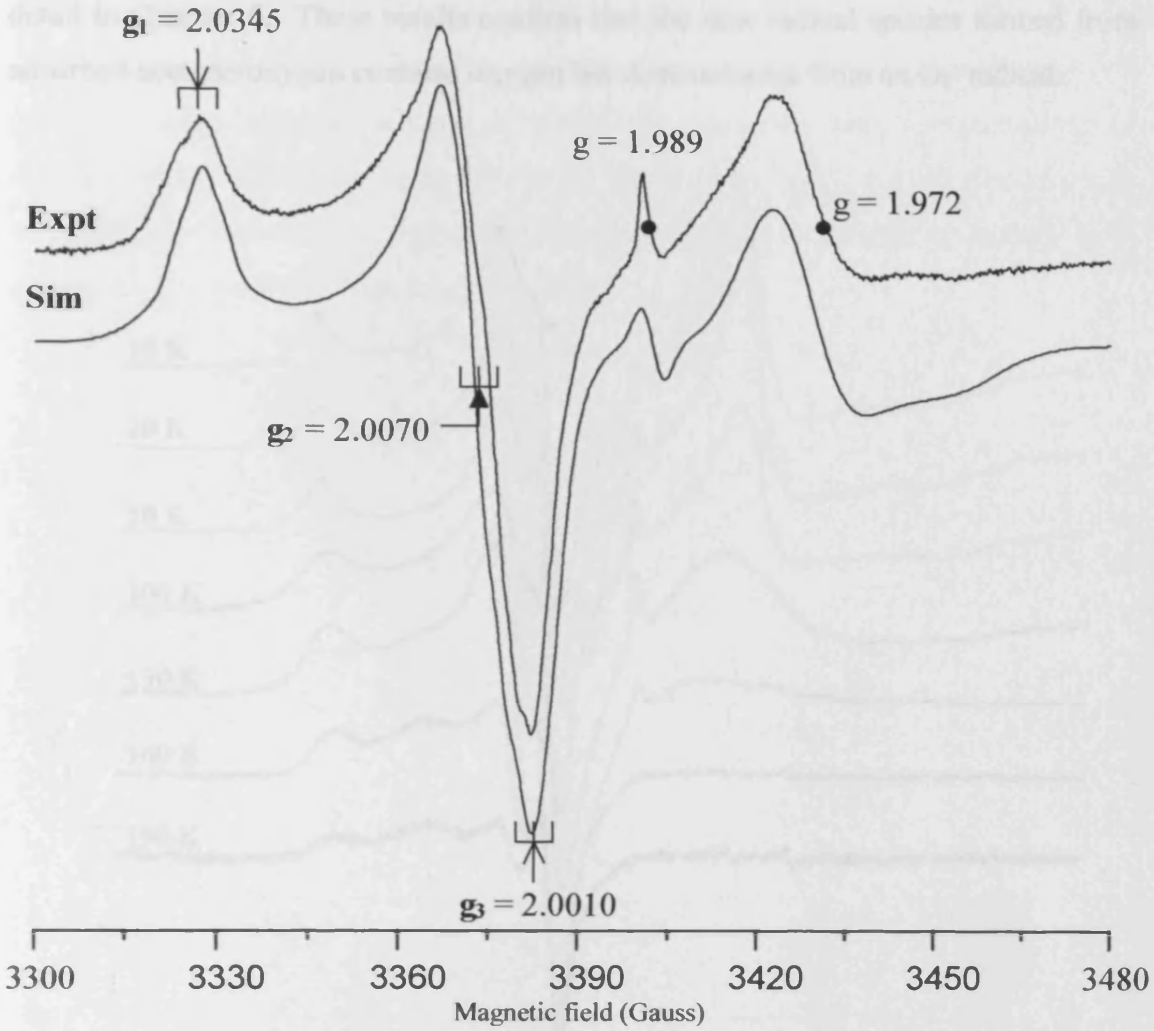

Figure 7.1. Experimental and simulated EPR spectrum of dehydrated P25 after UV irradiation for 30 minutes at 77 K in the presence of the co-adsorbed acetone:O_2 (10 Torr total pressure in a 10:1 ratio). The EPR spectrum was recorded at 10 K.

A second new low field orthorhombic signal with the spin Hamiltonian parameters of $g_1 = 2.0345$, $g_2 = 2.0070$ and $g_3 = 2.0010$ is also visible in the spectrum. Raising the temperature to 298 K and subsequent re-cooling to 10 K caused the signal to disappear, indicating the thermal instability of the species as shown in figure 7.2. The signal could however, be regenerated by subsequent UV illumination at low temperature. The observation of the new signal only occurs in an acetone rich environment when co-adsorbed with oxygen. The new signal was not produced during irradiation of the sample containing only acetone. Similarly irradiation of the sample under an oxygen only atmosphere (or in an oxygen rich mixture) produced the

trapped hole (O^-) followed by the superoxide spectrum, as previously discussed in detail in Chapter 6. These results confirm that the new radical species formed from adsorbed acetone/oxygen contains oxygen but does not arise from an O_2^- radical.

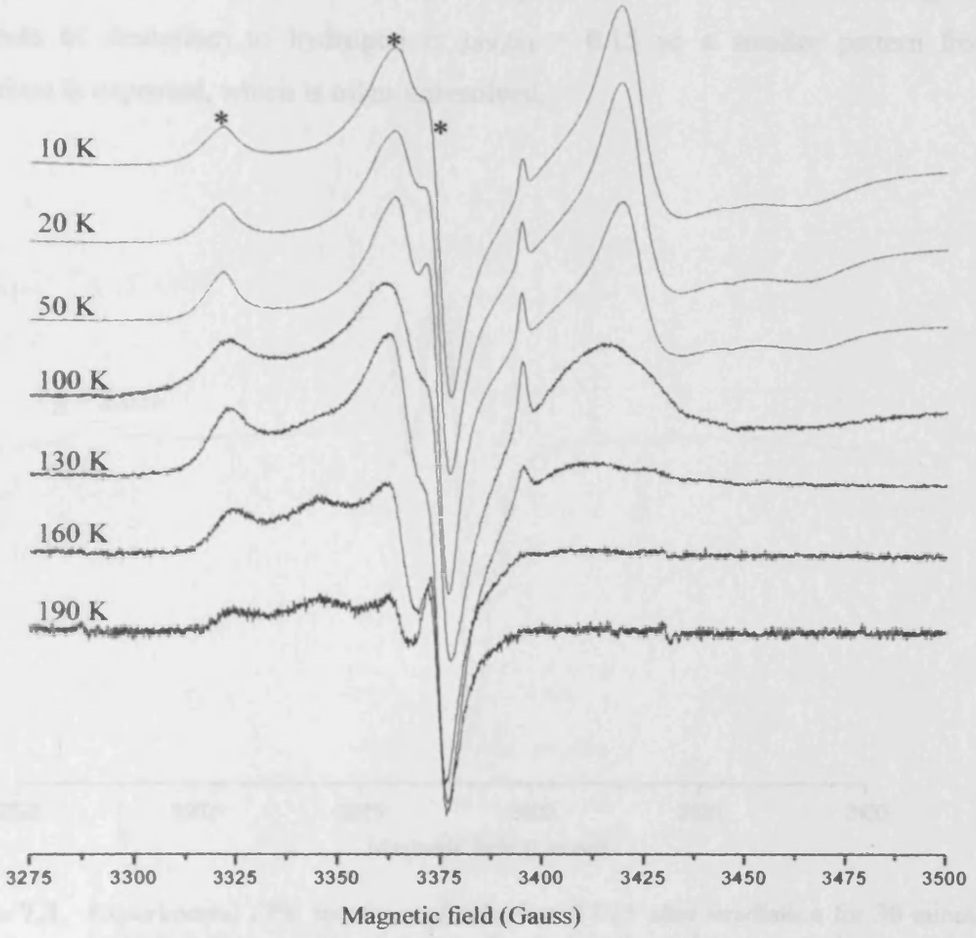

Figure 7.2. Variable temperature EPR spectra of UV irradiated P25 containing co-adsorbed acetone:O_2. The new radical species responsible for the peaks labelled * decays at T > 190 K.

The presence of a small superhyperfine structure superimposed on each of the three g values can just be resolved in figure 7.1. The computer simulation of the EPR spectrum also assists in the identification of the superimposed superhyperfine structure. The most satisfactory simulation of the EPR spectrum was found using two equivalent I = ½ nuclei ($^{H}A_1$ = 3.4 G, $^{H}A_2$ = 1.0 G, $^{H}A_3$ = 2.9 G and a_{iso} = 2.43 G). Using three equivalent I = ½ nuclei produced an unsatisfactory fit. This strongly

suggests the presence of a $-CH_2-$ fragment weakly interacting with the unpaired electron spin in this fully dehydrated material.

Further confirmation for the presence of the superhyperfine structure was also produced using deuterated acetone (CD_3COCD_3), where a pronounced narrowing of the line width was observed as shown in figure 7.3. The ratio of the magnetic moments of deuterium to hydrogen is $\mu_D/\mu_H = 0.15$ so a smaller pattern from deuterium is expected, which is often unresolved.

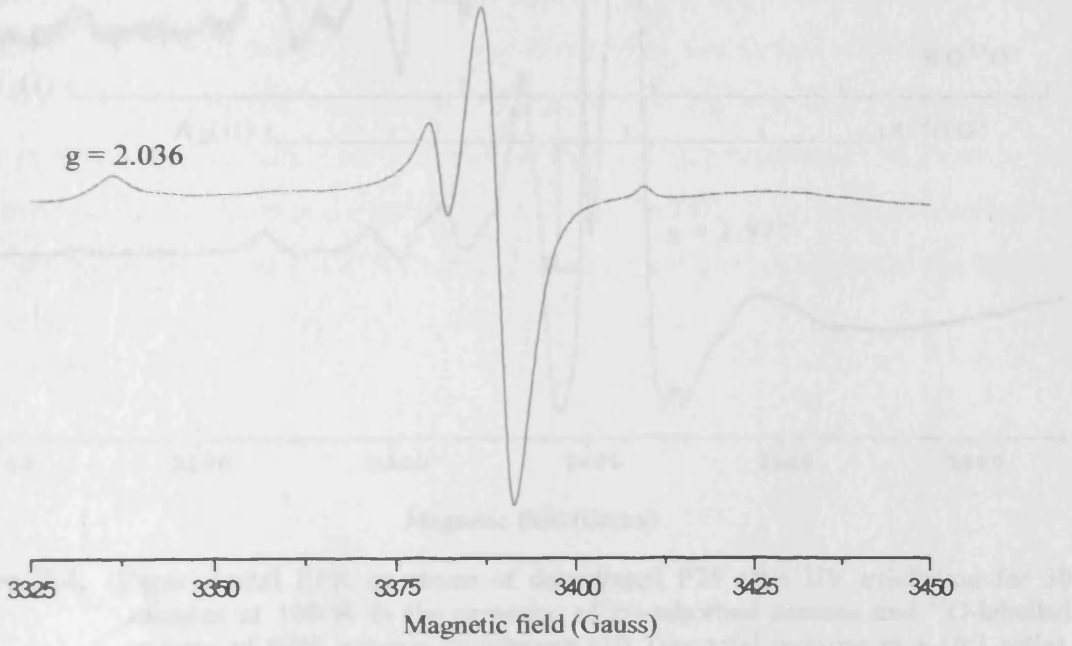

Figure 7.3. Experimental EPR spectrum of dehydrated P25 after irradiation for 30 minutes at 77 K in the presence of the co-adsorbed deuterated acetone and oxygen (total pressure 10 Torr, 10:1 ratio). The EPR spectrum was recorded at 10 K.

In order to obtain further details of the nature and subsequent identification of the new orthorhombic signal, experiments were carried out using ^{17}O labelled O_2. As detailed earlier, the TiO_2 sample was activated in the usual manner, and a mixture of CH_3COCH_3:$^{17}O_2$ in a 10:1 ratio (total pressure 10 Torr) was then co-adsorbed onto the TiO_2 surface before UV irradiation at 100K. The resulting spectrum is shown in figure 7.4.

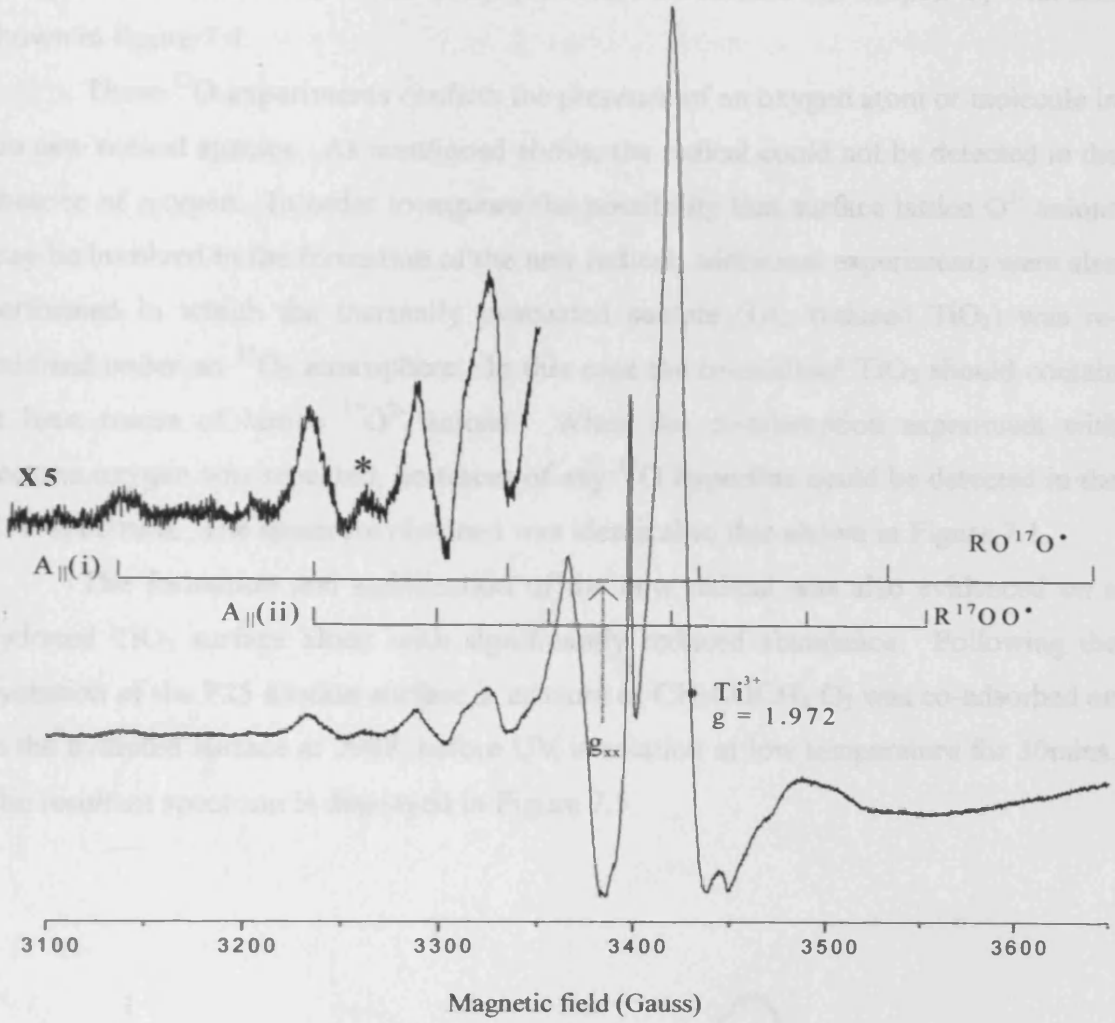

Figure 7.4. Experimental EPR spectrum of dehydrated P25 after UV irradiation for 30 minutes at 100 K in the presence of co-adsorbed acetone and ^{17}O-labelled oxygen of 63% isotopic enrichment (10 Torr total pressure in a 10:1 ratio). The EPR spectrum was recorded at 10K. The peak marked * is due to one transition from traces of $^{17}O_2^-$

Calculation of the relative abundance of the isotopmers ($^{16}O_2$, $^{17}O^{16}O$ and $^{17}O_2$) present in the gas mixture can be easily done similar to that described by Cheisa *et.al.*[19] Therefore, with a 63% enrichment level, the six line hyperfine pattern from the I = 5/2 nucleus of $^{17}O^{16}O^-$ is expected to dominate the EPR spectrum, with smaller contributions from $^{16}O_2^-$ and $^{17}O_2^-$. As a consequence, the intensity of the EPR spectrum is now distributed primarily over six lines causing the spectrum to appear less intense compared to that of the Ti^{3+} signal as illustrated in figure 7.4.

It should be noted that the peak marked as * in figure 7.4 can be assigned to one transition from the $^{17}O_2^-$ anion. This was confirmed by measuring and comparing

the spectrum of the $^{17}O_2^-$ anion directly on the P25 surface (*cf.* chapter 6) with that shown in figure 7.4.

These ^{17}O experiments confirm the presence of an oxygen atom or molecule in the new radical species. As mentioned above, the radical could not be detected in the absence of oxygen. In order to explore the possibility that surface lattice O^{2-} anions may be involved in the formation of the new radical, additional experiments were also performed in which the thermally evacuated sample (i.e., reduced TiO_2) was re-oxidised under an $^{17}O_2$ atmosphere. In this case the re-oxidised TiO_2 should contain at least traces of lattice $^{17}O^{2-}$ anions. When the co-adsorption experiment with acetone:oxygen was repeated, no traces of any ^{17}O hyperfine could be detected in the EPR spectrum. The spectrum obtained was identical to that shown in Figure 7.1.

The formation and stabilisation of the new radical was also evidenced on a hydrated TiO_2 surface albeit with significantly reduced abundance. Following the hydration of the P25 anatase surface, a mixture of CH_3COCH_3:O_2 was co-adsorbed on to the hydrated surface at 298K before UV irradiation at low temperature for 30mins. The resultant spectrum is displayed in Figure 7.5.

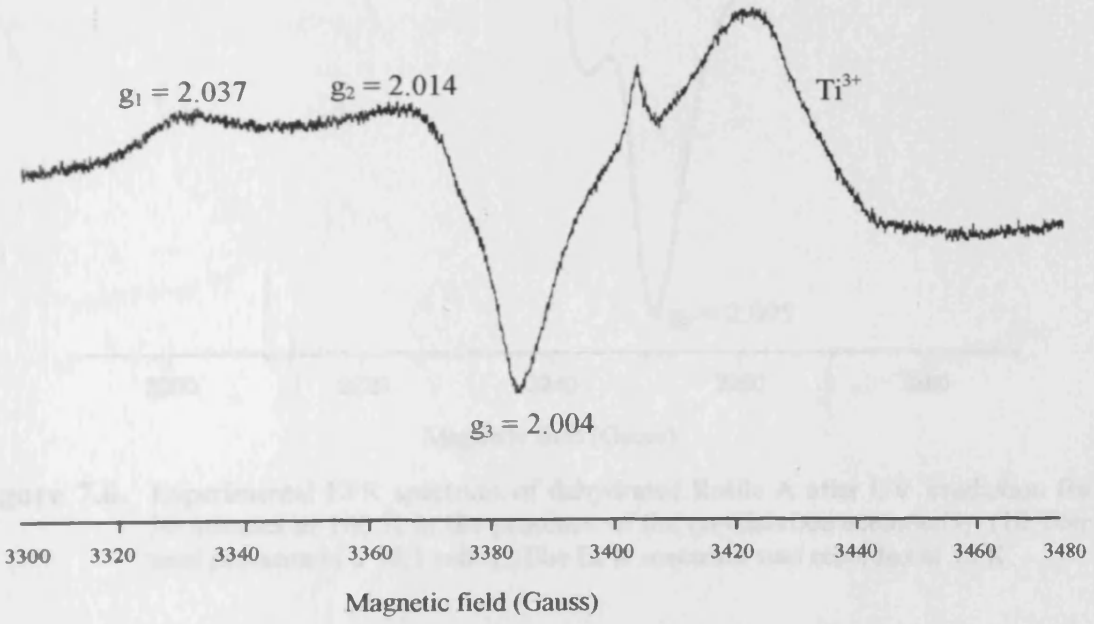

Figure 7.5. Experimental EPR spectrum of hydrated P25 Anatase following UV irradiation for 30 minutes at 77 K, in the presence of acetone and oxygen (10:1 ratio, 10 Torr total pressure). The EPR spectrum was recorded at 100 K.

Although the reported EPR spectrum (in figure 7.5) displays the new signal, the resultant spectrum appears lower in intensity compared to the fully dehydrated sample for reasons discussed later. The features at g = 1.993 and g ≈ 1.976 are easily assigned to Ti^{3+} cations as discussed previously.

Along with generation of the new reported radical on both the dehydrated and hydrated forms of P25 anatase, the new radical was also generated on the rutile form of TiO_2 (i.e., rutile A). The TiO_2 sample was firstly activated using the same technique adopted for the P25 anatase samples. Following this pre-treatment a mixture of acetone and oxygen, (10:1 ratio, total pressure 10 Torr) was co-adsorbed onto the surface. The sample was then irradiated at low temperature and the resultant EPR spectrum shown is in figure 7.6.

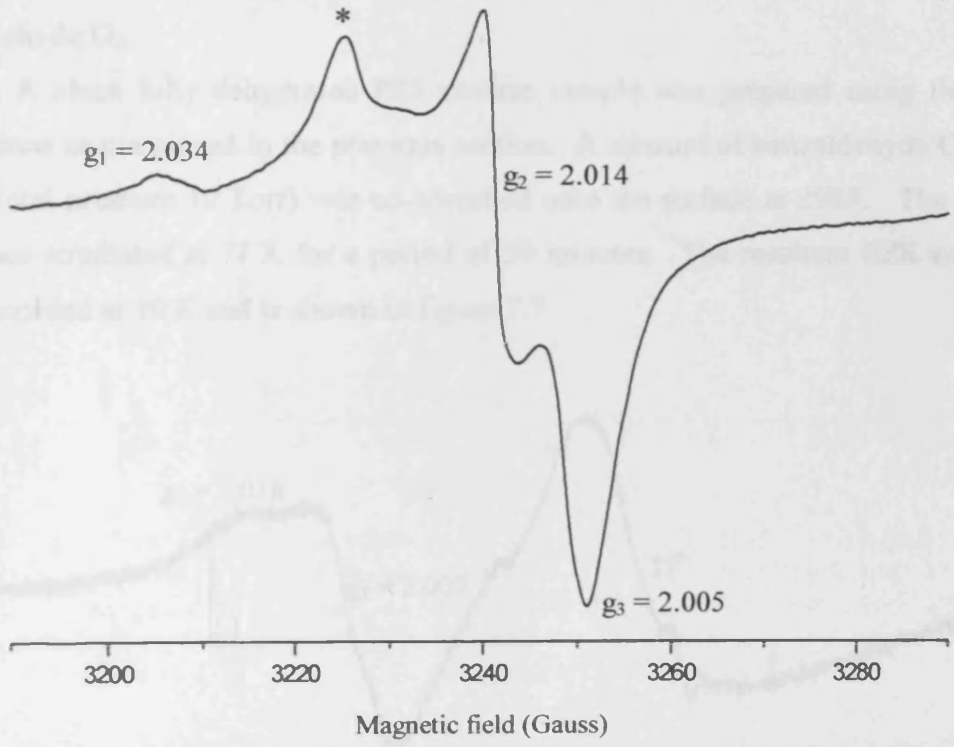

Figure 7.6. Experimental EPR spectrum of dehydrated Rutile A after UV irradiation for 30 minutes at 100 K in the presence of the co-adsorbed acetone:O_2 (10 Torr total pressure in a 10:1 ratio). The EPR spectrum was recorded at 10 K.

As seen in figure 7.6, following UV irradiation of the sample at low temperature a signal with spin the Hamiltonian parameters $g_1 = 2.034$, $g_2 = 2.011$, $g_3 = 2.005$ is observed. This signal is analogous to that produced under the same

conditions on the anatase material. The EPR signal generated on the Rutile A was of a lower intensity than that generated on the anatase surface. A second signal at g = 2.022 can also be identified, and this signal has been attributed to the well-reported g_{zz} component of O_2^- on the rutile surface (*cf.* chapter 6). The lack of this O_2^- signal in figure 7.1 probably relates to the difference in surface morphologies of the two samples (anatase *vs.* rutile) and therefore stabilisation of the radicals on the surface under the specific conditions adopted in this experimental study.

7.3.2 Co-adsorbed Benzaldehyde:Oxygen

As already mentioned, the co-adsorption of aldehydes was previously investigated by Jenkins and Murphy.[15] The reported work described the formation and identification of the peroxyacyl radical $RCO_3^{\bullet}$ over a dehydrated rutile surface (i.e., the rutile B sample adapted in previous chapters 5 and 6). Therefore, P25 anatase was used for the analogous experiments in the study of co-adsorption bezaldehyde:O_2.

A clean fully dehydrated P25 anatase sample was prepared using the same conditions as mentioned in the previous section. A mixture of benzaldehyde:O_2 (10:1 ratio; total pressure 10 Torr) was co-adsorbed onto the surface at 298K. The sample was then irradiated at 77 K for a period of 30 minutes. The resultant EPR spectrum was recorded at 10 K and is shown in figure 7.7.

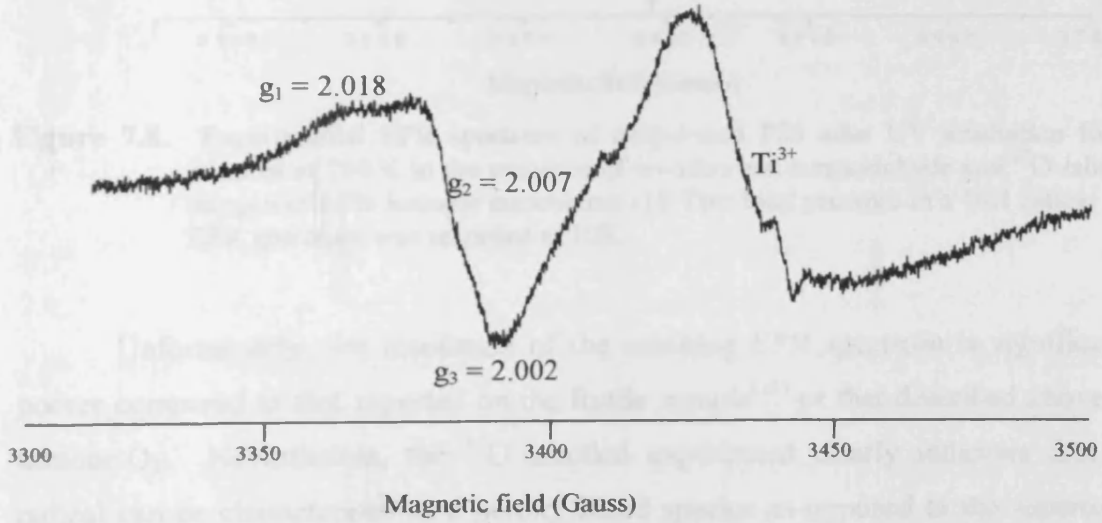

Figure 7.7. Experimental EPR spectrum of dehydrated P25 anatase after UV irradiation at 100 K in the presence of co-adsorbed benzaldehyde:O_2 (10:1, 10 Torr total pressure). The EPR spectrum was recorded at 10 K.

Similar to previous work,[15] an orthorhombic signal could just be resolved on the anatase sample with the spin Hamiltonian parameters of $g_1 = 2.018$, $g_2 = 2.007$ and $g_3 = 2.002$, suggesting that the peroxyacyl intermediate could be formed on the P25 sample. In order to obtain additional information on the nature of the radical formed with co-adsorbed benzaldehyde:O_2 experiments were performed using ^{17}O. The TiO_2 sample was pre-treated as detailed earlier, and a mixture of benzaldehyde:$^{17}O_2$ (10:1 ratio, total pressure 10 Torr) was then co-adsorbed onto the TiO_2 surface before UV irradiation at 77 K. The EPR spectrum was recorded at 10 K and is shown in figure 7.8.

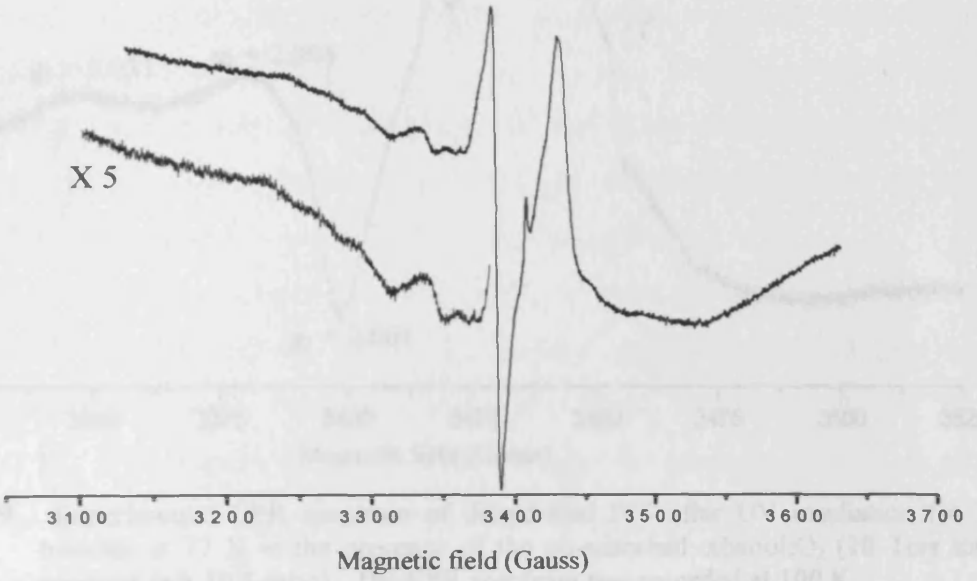

Figure 7.8. Experimental EPR spectrum of dehydrated P25 after UV irradiation for 30 minutes at 100 K in the presence of co-adsorbed benzaldehyde and ^{17}O-labelled oxygen of 63% isotopic enrichment (10 Torr total pressure in a 10:1 ratio). The EPR spectrum was recorded at 10K.

Unfortunately, the resolution of the resulting EPR spectrum is significantly poorer compared to that reported on the Rutile sample[15] or that described above for acetone:O_2. Nevertheless, the ^{17}O labelled experiment clearly indicates that the radical can be characterised as a peroxy based species as opposed to the superoxide type species. A more detailed discussion of this peroxy-based radical will be presented later.

7.3.3 Co-adsorption of Alcohols:Oxygen

Following the preparation of a clean dehydrated anatase P25 sample a mixture of alcohol (either methanol, ethanol or propan-2-ol) and oxygen (10:1 ratio, total pressure 10 Torr) was co-adsorbed onto the surface at 298 K. The sample was then irradiated for *ca.* 30 minutes at 77 K. The resulting spectrum for co-adsorbed ethanol and O_2 recorded at 100K is shown in figure 7.9 below.

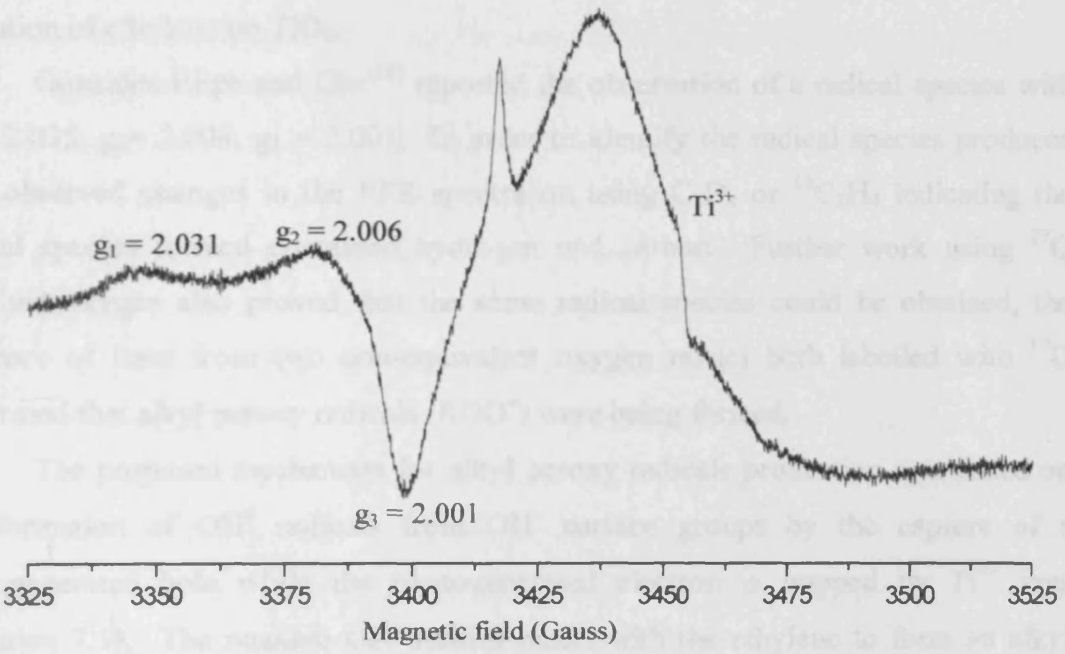

Figure 7.9. Experimental EPR spectrum of dehydrated P25 after UV irradiation for 30 minutes at 77 K in the presence of the co-adsorbed ethanol:O_2 (10 Torr total pressure in a 10:1 ratio). The EPR spectrum was recorded at 100 K.

As seen in the figure 7.9, following UV irradiation of co-adsorbed ethanol:O_2 over TiO_2, a clear orthorhombic signal with spin Hamiltonian parameters of g_1 = 2.031 g_2 = 2.006 g_3 = 2.001 can be observed. A second feature at g = 1.99 and g ≈ 1.96 can also be identified and this has been assigned to the presence photogenerated Ti^{3+} cations. The same set of signals was also observed for both methanol and propan-2-ol (spectra not shown for brevity) but with less intensity and resolution. Warming the sample to 298 K caused the signal to disappear; thus suggesting that a transient radical species is formed as an intermediate. The signal produced was not particularly intense; this is probably related to the instability of the intermediate at increased temperatures. The broadness of the signal produced means that any

isotopically labelled $^{17}O_2$ work would not be possible, as the hyperfine splitting arising from the $^{17}O_2$ gas would not be seen.

7.4 Discussion

The study of transient radical formation is very important when determining the mechanism of photo-oxidation of organics over a metal oxide surface. However, very few people have studied the formation of transient radicals and even fewer have characterised the species formed. One such group Gonzalez-Elipe and Che[20] have studied and characterised a transient radical on the TiO_2 surface during the photo-oxidation of ethylene on TiO_2.

Gonzalez-Elipe and Che[20] reported the observation of a radical species with $g_1 = 2.035$, $g_2 = 2.008$, $g_3 = 2.001$. In order to identify the radical species produced they observed changes in the EPR spectra on using C_2D_4 or $^{13}C_2H_4$ indicating the radical species formed contained hydrogen and carbon. Further work using ^{17}O enriched oxygen also proved that the same radical species could be obtained, the presence of lines from two non-equivalent oxygen nuclei both labelled with ^{17}O confirmed that alkyl peroxy radicals ($ROO^{\bullet}$) were being formed.

The proposed mechanism for alkyl peroxy radicals production was based on the formation of $OH^{\bullet}$ radicals from OH^- surface groups by the capture of a photogenerated hole while the photogenerated electron is trapped by Ti^{4+} ions (equation 7.1). The reactive $OH^{\bullet}$ radical reacts with the ethylene to form an alkyl radical (equation 7.2), which in turn reacts with oxygen to form the observed alkyl peroxy radical (equation 7.3).

$$OH^- + h^+ - e^- \longrightarrow OH^{\bullet} + e^- \quad (7.1)$$

$$OH^{\bullet} + C_2H_4 \longrightarrow HO\text{-}CH_2\text{-}CH_2^{\bullet} \quad (7.2)$$

$$HO\text{-}CH_2\text{-}CH_2^{\bullet} + O_2 \longrightarrow HO\text{-}CH_2\text{-}CH_2\text{-}OO^{\bullet} \quad (7.3)$$

The successful EPR characterisation of several neutral surface peroxyacyl species (general formula $RCO_3^{\bullet}$) on a TiO_2 surface has been recently demonstrated at Cardiff. With the exception of these, no identification of any radical transient species have not been identified following the photo-oxidation of ketones, aldehydes and alcohols on TiO_2 surfaces. Therefore, the following discussion will be concerned with the characterisation of a series of peroxy radicals following the co-adsorption and UV irradiation of acetone, benzaldehyde and ethanol on TiO_2 surfaces.

7.4.1 Nature of the radical species formed with co-adsorbed Acetone:O_2

During the low temperature UV irradiation of co-adsorbed acetone:O_2 mixture over a dehydrated P25 anatase sample, a new signal was generated which has been previously unreported in the literature. In order to fully identify this new species, several different radicals were considered as potential candidates and several mechanistic pathways can be discussed.

A number of oxygen centred radicals can be formed on the TiO_2 surface, including O^-, O_2^-, O_3^-, $OH^\bullet$, $HO_2^\bullet$ and $ROO^\bullet$ radicals. The g values for the O^-, O_2^- and O_3^- radicals are well known (as shown in Table 7.1) and can be immediately eliminated as possible candidates for the characterisation of the new radical species shown in figures 7.1 to 7.4. The O_2^- and O_3^- radicals are very stable at room temperature, and persist for several days on the dehydrated TiO_2 surface. Although O^- is unstable in the TiO_2 lattice, and is irreversibly lost upon warming the sample to 298K, the predicted g values of O^- do not coincide with those observed in the co-adsorption experiments. In particular, the largest g values observed for O^- in P25 is $g_\perp$ = 2.026. As previously reported[15] it is only possible for this g value to become larger than 2.026 if significant levels of cationic impurities are present in the bulk of the material, causing an increase in the splitting of the π orbitals of the O^- radical (which in turn influence the g values). In the present case, the largest g value observed in the co-adsorption experiment was 2.034, thus ruling out the possibility of O^- as an explanation, since no cationic impurities are found in P25.

While the organic:oxygen ratio may be different in the adsorbed state as compared to the gaseous state, perhaps due to differences in the adsorption characteristics of the two gases on TiO_2, nevertheless, it is clear that the organic remains in excess on the surface due to the absence of any O_2^- signal. In other words, in an oxygen rich environment, superoxide formation would occur rapidly. The O^-, O_2^- and O_3^- radicals have no intrinsic superhyperfine interaction with a proton. It is possible for a superhyperfine interaction to produce a small coupling in the spectrum (e.g.,$OH_{surf}\cdots O_2^-$ as described by Giamello *et al.*,[21,22] on MgO) but as previously stated, the observed ^{17}O hyperfine pattern (see figure 7.4) is not typical of $^{17}O^-$, $^{17}O_2^-$, or $^{17}O_3^-$.[23]

Table 7.1. Spin Hamiltonian parameters for a selection of oxygen-centred radicals formed on the TiO_2 surface.

Species	g_1	g_2	g_3	$^{17O}A_{\|\|}$(i)a	$^{17O}A_{\|\|}$(ii)a	Comment	Ref
O^-	2.026	2.026	2.002				9, 23
O_2^-	2.025	2.008	2.0016				9, 23
O_3^-	2.17	2.011	2.001				23, 24
$HO_2^\bullet$	2.034	2.008	2.002			Hydrated surface	23
$RCO_3^\bullet$	2.017	2.008	2.003			Coadsorbed aldehyde/O_2	15
$ROO^\bullet$	2.034	2.010	2.001	95	35	Coadsorbed ethylene/O_2	20
$ROO^\bullet$	2.0345	2.0070	2.0010	94.5	55.2	Coadsorbed acetone/O_2	This work

For comparison purposes, the EPR spectrum of ^{17}O-labelled O_2^- was also generated (*cf.* chapter 6) producing the well-discussed six and eleven line hyperfine patterns of $(^{17}O^{16}O)^-$ and $(^{17}O^{17}O)^-$ respectively. Close analysis of the spectrum obtained from the co-adsorption of acetone:^{17}O (see figure 7.4) shows the presence of two sextets with $^{17O}A_{\|}$(i) = 94.5G and $^{17O}A_{\|}$(ii) = 55.2G which are both centred on the g_3 (or g_{xx}) component at 2.0010. The parameters obtained here are different from those obtained in $^{17}O_2^-$ spectrum and so are clearly not related to $^{17}O_2^-$.

The $HO_2^\bullet$ radical was also generated on a fully hydrated TiO_2 surface (*cf.* chapter 6) for comparison, the large characteristic coupling from the single proton can be clearly resolved (figure 7.5). While $HO_2^\bullet$ is also thermally unstable, the g values are distinctly different from the new radical intermediate (see Table 7.1) and so can be discounted as being responsible for the signal in figures 7.1 to 7.4. Another possible candidate is the $OH^\bullet$ radical. This radical is an extremely short-lived and very reactive intermediate which cannot be directly observed by EPR on the TiO_2 surface, even at low temperatures (10 K). However, it can be indirectly observed by spin trapping experiments or through analysis of the secondary radicals formed by the reactions of $OH^\bullet$.[25] Nevertheless, the spin Hamiltonian parameters of bulk[26] $OH^\bullet$ and OH in irradiated ice[27,28] are well known and are different to those obtained in this work.

The final applicant in the assignment of the new signal is that of a surface peroxy radical ($ROO^\bullet$). An extensive study of the carbon based peroxyl radicals by Sevilla *et al.*,[29] reported that the g values for these species vary only slightly from g_1

= 2.035, g_2 = 2.008 and g_3 = 2.003; the greatest deviation was found for the crystal field sensitive g_1 component. The stability of the radical is highly sensitive to the terminal oxygen spin density, according to McCain and Palke[30], and the average g values of the ROO$^\bullet$ radicals depends on the electronic structure of the R group. In other words, as the nature of the R group varies, the stability will change slightly in addition to the observed g values. In this case, the average g value for the new radical generated here is 2.014, which is in the range typical of alkylperoxy radicals. The spin density in the peroxy radical is localized primarily in the p_z orbital of the two oxygens. The terminal oxygen hyperfine coupling ($RO^{17}O^\bullet$) is usually labelled $A_{\|}$(i), while the inner oxygen hyperfine coupling ($R^{17}OO^\bullet$) is labelled $A_{\|}$(ii). By examination of figure 7.4 the hyperfine couplings were ascertained as $A_{\|}$(i) = 94.5G and $A_{\|}$(ii) = 55.2G. Anisotropic hyperfine couplings from spin densities in such p_z orbitals should follow approximate axial symmetry with $A_{\|} = (a+2B)\rho\pi$ and $A_{\perp} = (a-B)\rho\pi$, where ρ is the spin density in the p_z orbital. An accurate value for $A_{\perp}$ could not be obtained because of the strong overlapping signal from Ti^{3+}, though the value is expected to be very small. A good estimate of the spin density distribution in the p_z orbitals can then be obtained from the relation $\rho^{\pi}(i) = |A_{\|}(i)|/154G$, $154G = |a+2B|$ using the $A_{\|}$ value only.[31] The terminal spin density value can therefore be estimated at 0.61 from this relation, which is expected for a peroxy radical. Stable surface methylperoxy and propylperoxy species have also been observed by EPR at 10 K on MgO[32] and Bi_2O_3[33] respectively, and terminal oxygen spin densities have been measured in the range ρ^{π} = 0.70 – 0.61. As most of the unpaired spin density is associated with the terminal peroxy oxygen, this accounts for the usual absence of any strong hyperfine interaction with the protons of the R group, although in this case small couplings were in fact observed.

As the sum of the two $A_{\|}$ couplings for carbon-based peroxy radicals is nearly constant, this suggests that little spin density is delocalised into the R group of ROO$^\bullet$.[31] The presence of a small almost isotropic hyperfine coupling (a_{iso} – 2.43G) with two equivalent protons (i.e., two I = ½ nuclei) has been revealed using computer simulations as shown in figure 7.1. The proton coupling is smaller than that observed for HO$^\bullet$ ($A_1 = A_3 \cong 0G$, a_2 = 57G, a_{iso} = 19G[26]) and $HO_2^\bullet$ (A_1 = 12G, A_2 = 12G, A_3 = 14G a_{iso} = 12G)[34] where the proton is directly attached to the oxygen atoms, rather than through a C-O bond. The hyperfine pattern and simulation of the EPR spectrum

was found to fit best using two equivalent I = ½ nuclei as shown in figure 7.1 thus suggesting that R is an alkyl species (also confirmed by the average g value of 2.014[20]). The possibility of a –CH- or $-CH_3-$ fragment attached to the $-OO^{\bullet}$ is eliminated due to unsatisfactory fits when using either one or three equivalent I = ½ nuclei. In other words, the X band EPR spectral evidence supports the assignment of the new radical species as an alkylperoxy species ($R-CH_2OO^{\bullet}$).

7.4.2 Mechanistic considerations of peroxy radical formation with acetone

A series of possible mechanisms into the likely formation steps of the radical have been considered. In the case of acetone adsorption, electron transfer from the surface to the adsorbed organic molecule can occur which results in the population of the lowest unoccupied π_{CO}* molecular orbital forming an acetone ketyl radical:[30]

$$(CH_3)_2CO + e^- \longrightarrow (CH_3)_2CO^{\bullet-} \qquad (7.4)$$

This is unlikely to occur as the ketyl radical is expected to be a more powerful reductant than a surface trapped electron ($(CH_3)_2CO/(CH_3)_2C^{\bullet}OH$ = - 1.81 *vs* NHE).[36] The resulting acyl ($CH_2CO^{\bullet}$) and methyl radical ($^{\bullet}CH_3$), occurring from ketyl fragmentation could react with oxygen to form peroxy radicals ($CH_3CO-OO^{\bullet}$ and $CH_3-OO^{\bullet}$). However, the features in figures 7.1 to 7.4 are not consistent with this assignment.

It is also possible, that during the course of UV irradiation electron transfer can also occur to surface trapped holes O^- centers, or Ti^{3+} producing an adsorbed cation radical. This quickly deprotonates by H^+ transfer to the surface oxide, producing propanone. Both steps are summarised in equation 7.5.

$$CH_3COCH_3 + O^- \longrightarrow CH_3COCH_2^{\bullet} + OH^- \qquad (7.5)$$

A reaction similar to this is capable of occurring between acetone and the hydroxyl radicals.[37] The propanone radical can then react with oxygen forming the peroxy radical as shown in equation 7.6.

$$CH_3COCH_2^{\bullet} + O_2 \longrightarrow CH_3COCH_2OO^{\bullet} \qquad (7.6)$$

Since the rate of hole transfer is thought to be much faster than the rate of electron transfer across the interface (100ns *vs* several milliseconds, respectively), $CH_3COCH_2^{\bullet}$ radicals may be formed on the surface. The addition of molecular oxygen to these radicals would also produce a peroxy radical (CH_3COCH_2-$OO^{\bullet}$) and because the CO group is not directly attached to the O-O group, g_1 values (g_1 = 2.035), which are typical of peroxy radicals, may still be seen. It should be noted that, the EPR spectrum obtained using $^{16}O_2$ indicated the presence of only two weakly interacting protons, as expected for an R-CH_2-$OO^{\bullet}$ fragment as in CH_3COCH_2-$OO^{\bullet}$. Thus, the mechanistic considerations strongly support the EPR evidence in identifying the radical intermediate as CH_3CO-$CH_2OO^{\bullet}$.

7.4.3 Nature of the radical species formed with co-adsorbed Benzaldehyde:O_2

In a previous study,[15] co-adsorption of a range of aldehydes (including formaldehyde, acetaldehyde and bezaldehyde) with oxygen on illuminated TiO_2 surfaces were reported. Several neutral surface peroxyacyl species (general formula $RCO_3^{\bullet}$) were adopted, which are well known oxidative intermediates in the initiated gas phase oxidation of aldehydes.[38] The generated $RCO_3^{\bullet}$ radicals are also reported to participate in the formation of the respiratory irritant peroxyacyl nitrate, which is capable of accumulating to dangerously high levels in photochemical smogs.[39] Indoor sources of volatile aldehydes include cigarette smoke and slow release from furnishing materials.[40]

The free radical mechanism of aldehyde oxidation is well known.[38] It is initiated by H atom abstraction *via* reaction with a valence band hole in TiO_2-mediated photocatalysis

$$RCHO + h^{+} \longrightarrow RCO^{\bullet} \qquad (7.7)$$

$$RCO^{\bullet} + O_2 \longrightarrow RCO_3^{\bullet} \qquad (7.8)$$

$$RCO_3^{\bullet} \longrightarrow RCO_3H + RCO^{\bullet} \qquad (7.9)$$

$$RCO_3H + RCHO \longrightarrow 2CH_2(CO)OH \qquad (7.10)$$

The above equations, (7.7 – 7.10), represent an idealized reaction scheme in which several possible side reactions of the $RCO_3^{\bullet}$ radical are omitted for clarity, e.g., dimerization to form an unstable tetraoxide intermediate.[36] Following the initial $H^{\bullet}$ abstraction step to form an acyl-type radical, the oxidation proceeds *via* the chain reaction sequence. The peroxyacyl reactive intermediates are only formed under co-

adsorption conditions since predosing the reduced surface with aldehyde followed by O_2, or vice versa, will not produce the $RCO_3^{\bullet}$ species.

The reported g values were $g_1 = 2.017$, $g_2 = 2.008$ and $g_3 = 2.003$. Owing to the close proximity of the electrophilic carbonyl group in these radicals, the spin density on the oxygen atom is less than that usually observed for other peroxy radicals, thus explaining the low g_1 value. In this previous work, the intermediate was only identified over a dehydrated rutile material (rutile B). Furthermore, no experiments were carried out using $^{17}O_2$ to unambiguously identify the nature of the radical (proposed as $RCO_3^{\bullet}$). Therefore, P25 anatase was used for the co-adsorption of benzaldehyde with both $^{16}O_2$ and $^{17}O_2$.

In comparison to the previous work by Jenkins and Murphy, an orthorhombic signal with g values $g_1 = 2.018$, $g_2 = 2.007$, $g_3 = 2.002$, can indeed be identified on the anatase sample following UV irradiation (see figure 7.7 and 7.8), suggesting that the peroxyacyl intermediate can also be formed on P25. Unfortunately, the resolution of the spectrum is significantly poorer compared to that seen on the rutile sample. Nevertheless, the $^{17}O_2$ labelled experiment (see figure 7.8) clearly indicates that the radical can be characterised as a peroxy based species as opposed to a superoxide type species (*cf.* chapter 6).

The hyperfine pattern observed in figure 7.8 is unusual however, since it appears that the largest hyperfine tensor is based on the g_{yy} component (as shown in figure 7.10a.) as opposed to the g_{xx} component typical of an alkyl-peroxy radicals formed during the UV irradiation of acetone:O_2 (figure 7.10b).

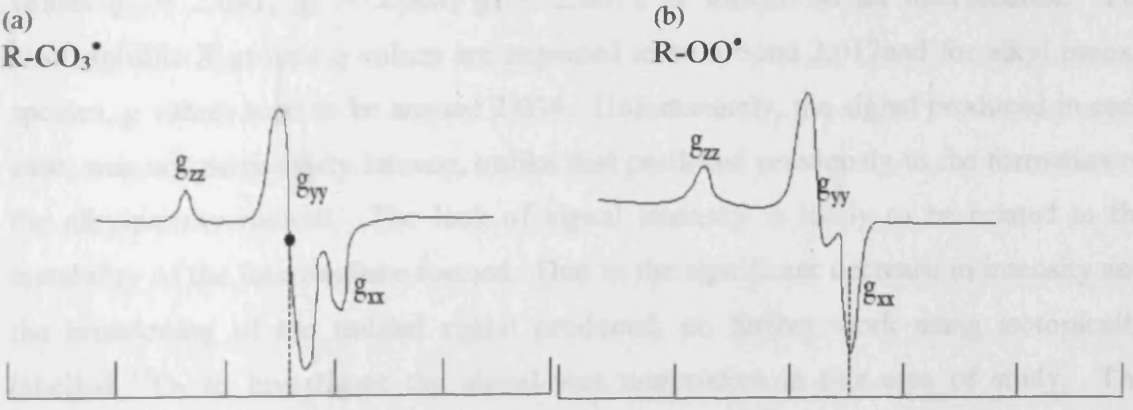

Figure 7.10. Schematic diagram of the hyperfine pattern for (a) centred on the g_{yy} component and (b) centred on the g_{xx} component

This observed difference in the electronic structure of the –OO- fragment may provide more direct evidence for the $RCO_3^{\bullet}$ assignment. Further investigation and analysis of the superhyperfine coupling with other co-adsorbed aldehydes is needed in order to fully understand this observation and confirm if the –OO- fragment is attached to an acyl species ($RO^{\bullet}$) as opposed to an alkyl species ($R^{\bullet}$).

Finally as previously mentioned, the resolution of the $RCO_3^{\bullet}$ spectra observed on anatase (P25) in this work, are significantly less than those previously observed on rutile (ex 'Tioveil'). This difference between the spectra may be due to differences in surface morphologies, stability/reactivity of the intermediates or due to differences in impurity levels. In other words, trace levels of dopants may have an influence on the nature of the surface radical.

7.4.4 Nature of the radical species formed with co-adsorbed alcohols and oxygen

During the low temperature UV irradiation of the co-adsorbed alcohol and oxygen on the dehydrated anatase surface, an orthorhombic signal is produced as shown in figure 7.9. The same signal was produced when mixtures of methanol and oxygen or propan-2-ol and oxygen were co-adsorbed onto the dehydrated P25 anatase surfaces. The resultant EPR spectra in each case were of a much lower intensity and so not shown here for brevity. As discussed previously, this newly generated signal disappears following gentle annealing to 298 K, suggesting that the produced signal must be due to a surface intermediate. The disappearance of the signal upon warming the sample suggests that a radical species, probably of a peroxy type (based on the g values $g_1 = 2.031$, $g_2 = 2.008$, $g_3 = 2.001$), is formed as an intermediate. For electrophillic R groups g values are expected to be around 2.017and for alkyl peroxy species, g values tend to be around 2.034. Unfortunately, the signal produced in each case, was not particularly intense, unlike that produced previously in the formation of the alkylperoxy radical. The lack of signal intensity is likely to be related to the instability of the intermediate formed. Due to the significant decrease in intensity and the broadening of the radical signal produced, no further work using isotopically labelled $^{17}O_2$ to investigate the signal was undertaken in this area of study. The observation of any hyperfine splitting arising from the $^{17}O_2$ gas would be impossible due to the increase in the signal broadness.

However, based on the magnitude of the g_{zz} component, the radical can be assigned to a peroxy ($ROO^{\bullet}$) radical. The exact electronic structure of the $ROO^{\bullet}$ group cannot be ascertained however due to unsuccessful ^{17}O experiments.

7.5 Conclusion

As reported here during irradiation of co-adsorbed acetone:O_2 mixture, the resultant EPR spectra have provided direct evidence for the formation of a thermally unstable surface alkylperoxy radical ($ROO^{\bullet}$). The use of ^{17}O-labelled dioxygen, assisted in the confirmation of the radical intermediate as a peroxy-based radical ($ROO^{\bullet}$). Simulations of the well resolved EPR spectrum obtained with $^{16}O_2$ indicated the presence of a $-CH_2-$ fragment in the R group. On this basis the alkylperoxy radical was conformed as $CH_3COCH_2OO^{\bullet}$, generated by hole transfer to adsorbed acetone, and this represents the first identification of such an intermediate with acetone/O_2. Under the adopted conditions of co-adsorbed acetone:O_2 no ionic molecular oxygen radicals (i.e., O_2^-, O_3^-) are formed. This was confirmed by comparing the $^{17}O_2$ EPR spectrum for both the generated alkylperoxy radical and that of superoxide. The alkylperoxy radical was capable of being generated and stabilised on both the anatase and rutile surfaces, although with a higher intensity on the anatase dehydrated surface. The reason for the difference in radical abundance on each surface is not clear, and it may suggest a morphological dependence on the surface reactivity and / or stability of the radicals.

A previous study by Jenkins and Murphy[15] reported the formation of several neutral surface peroxyacyl species ($RCO_3^{\bullet}$) on the rutile surface. Results here have also shown that this radical can also be formed on an anatase surface. Confirmation of the peroxy nature of the radical has been confirmed through the ^{17}O experiments. Further analysis of the superhyperfine coupling will enable identification that the $-OO-$ fragment is attached to an acyl species ($RCO^{\bullet}$) as opposed to an alkyl species ($R^{\bullet}$). Irradiation of co-adsorbed alcohols:O_2 over the anatase surface generated a surface radical intermediate. The generated radical was easily assigned to that of a peroxy ($ROO^{\bullet}$) radical based on the g_{zz} component magnitude. However, the exact electronic structure of the $ROO^{\bullet}$ group could not be determined due to unsuccessful ^{17}O experiments.

Finally it should be noted that, the utility of the co-adsorption method, as opposed to pre-adsorption, is demonstrated to be a key experimental feature in obtaining a successful model reaction system for photocatalytic oxidation processes, since the nature of the radical formed depends entirely on how the surface is pre-treated with reactants. These results also show that transient radical species can indeed be observed by EPR over TiO_2 surface, and the experiments demonstrate the necessity to characterise the material under in-situ conditions in order to obtain a more realistic view ion the nature of the radicals involved – the photo-oxidative process.

7.6. References

1. M. A. Fox, M. T. Dulay, *Chem. Rev.*, **93**, 341, (1993).
2. A. L. Linsebigler, G. Q. Lu, J. T. Yates, *Chem. Rev.*, **95**, 735, (1995).
3. M. R. Hofmann, S. T. Martin, W. Choi, D. W. Bahnemann, *Chem. Rev.*, **95**, 69, (1995).
4. W. Xu, D. Raftery, *J. Phys. Chem. B*, **105**, 4343, (2001).
5. R. M. Alberici, W. F. Jardim, *Appl. Catal. Environ.*, **14**, 55, (1997).
6. W. Xu, D. Raftery, *J. Catal*, **204**, 110, (2001)
7. P.A. Morris Hotsenpiller, J. D. Bolt, W.E. Farneth, J. B. Lowekamp, G. S. Roher, *J. Phys. Chem. B*, **102**, 3216, (1998).
8. J. B. Lowekamp, G. S. Roher, P. A. Morris Hotsenpiller, J. D. Bolt, W. E. Farneth, *J. Phys. Chem. B*, **102**, 7323, (1998).
9. (a) R. F. Howe, M. Gratzel, *J. Phys. Chem.*, **89**, 4495, (1985). (b) R. F. Howe, M. Gratzel, *J. Phys. Chem.*, **91**, 3906, (1987).
10. (a) O. I. Micic, Y. Zhang, K. R. Cromack, A. D. Trifunac, M.C.Thurnauer, *J. Phys. Chem.*, **97**, 7277, (1993). (b) O. I. Micic, Y. Zhang, K. R. Cromack, A. D. Trifunac, M.C.Thurnauer, *J. Phys. Chem.*, **97**, 13284, (1993).
11. J. Peral, D. Ollis, *J. Catal.*, **136**, 554, (1992).
12. A. V. Vorontsov, G. B. Barannik, O. I., Snegurenko, E. N. Savinov, V. N. Parmon, *Kinet. Catal.*, **38**, 84, (1997).
13. L. Stevens, J. A. Lanning, L. G. Anderson, W. A. Jacoby, N. Chornet, *J. Air Waste Manag. Assoc.*, **48**, 979, (1999).
14. S. Hager, R. Bauer, *Chemosphere*, **38**, 1549(1999).
15. C. A. Jenkins D. M. Murphy, *J. Phys. Chem. B*, **103**, 1019, (1993).
16. T. A. Egerton, E. Harris, E. J. Lawson, B. Mile, C. C. Rowlands, *Phys. Chem. Chem. Phys.*, **2**, 3275, (2000).
17. M. Anpo, T. Shima, Y. Kubokawa, *Chem. Lett.*, 1799, (1985).
18. J. M. Coronado, A. J. Maira, J. C. Conesa, K. L. Yeung, V. Augugliaro, J. Soria, *Langmuir*. **17**, 5368, (2001).
19. M. Chiesa, E. Giamello, M.C. Paganini, Z. Sojka, D. M. Murphy, *J. Phys. Chem.*, **116**, 4266, (2002).
20. A. R. Gonzalez-elipe, M. Che, *J. Chim. Phys.*, **79**, 355, (1982).

21. E. Giamello, P. Ugliengo, E. Garrone, *J. Chem. Soc. Faraday Trans., I*, **85**, 1373, (1989).
22. E. Giamello, P. Ugliengo, E. Garrone, *J. Chem. Soc. Faraday Trans., I*, **85**, 3987, (1989).
23. A. L. Attwood, D. M. Murphy, J. L. Edwards, T. A. Egerton, R. W. Harrison, *Res. Chem. Intermed.*, **29**, 449, (2003).
24. (a) M Che, A. J. Tench., *J. Adv. Catal.*, **31**, 77, (1982). (b) M Che, A. J. Tench., *J. Adv. Catal.*, **32**, 1, (1983).
25. C. A. Jenkins, D. M. Murphy, C. C. Rowlands, T. A. Egerton. *J. Chem. Soc., Perkin Trans., 2,* 2479, (1997).
26. E. Giamello, L. Calosso, B. Fubini, F. Geobaldo, *J. Phys. Chem.*, **97**, 5735, (1993).
27. J. A. Brivati, M. C. R. Symons, D. J. A. Tinling, H. W. Wardale, D. O. Williams, *Trans. Faraday Soc.*, **63**, 2112, (1967).
28. J. A. Brivati, M. C. R. Symons, D. J. A. Tinling, D. A. Williams, *J. Chem. Soc. A*, 719, (1969).
29. M. D. Sevilla, D. Becker, M. Yao, *J. Chem. Soc., Faraday Trans.*, **97**, 5735, (1990).
30. D. C. McCain., W. E. Palke, *J. Magn. Reson.*, **20**, 52, (1975).
31. M. D. Sevilla., D. Becker., M. Yao., *J. Chem. Soc., Faraday Trans.*, **86**, 3279, (1990).
32. T. Ito, Y. X. Wang, C. H. Lin, J. H. Lunsford, *J. Am. Chem. Soc.*, **107**, 5062, (1985).
33. D. J. Driscoll, K. D. Campbell, J. H. Lunsford, *Adv. Catal.*, **35**, 139 (1987).
34. R. C. Catton, M. C. R. Symons, *Inorg. Phys. Theor.*, 1393, (1969).
35. C. C. Lai, G. R. Freeman, *J. Phys. Chem.*, **94**, 302, (1990).
36. P. Wardman, *J. Phys. Chem. Ref. Data*, 18, 1637, (1989).
37. W. B. DeMore, S. P. Sander, D. M. Golden, R. F. Hampson, M. J. Kurylo., C. J. Howard, A. R. Ravishankara,. C. E. Akolb, M. J. Molina, *J. P. L. Publ.*, **1**, 891, (1997).
38. N. A. Clinton, R. A. Kenley, T. G. Taylor. *J. Am. Chem. Soc.*, **97**, 3746, (1975).
39. E. Gosser, I. Baunok, S. Afri, *J. Sci.* **88**, 375 (1992).

40. G. Leonardos, D. Kendall, N. Barnard, *J. Air Pollut. Control Assoc.*, **19**, 91, (1969).
41. Y. Ohko, D. A. Tryk, K. Hashimoto, A. Fujishima, *J. Phys. Chem. B.* **102**, 2699, (1998).

Chapter 8

An EPR investigation into the Photodynamics of bulk and surface Ti^{3+} excitation in TiO_2 under UV illumination

8.1 Introduction

The final section of this thesis is concerned with the photodynamics of various paramagnetic centres in the thermally reduced and photo-irradiated titania samples. The response of the thermally produced Ti^{3+} signal and medium polarised conduction electron to UV light may be investigated using in-situ EPR spectroscopy. UV irradiation of TiO_2 causes excitation of the electrons to low lying states within the conduction band or just within the conduction band. When the Ti^{3+} signal is irradiated with UV light, the EPR signal intensity decreases due to the formation of the transient $Ti^{\delta 4+}$ state, as the electrons are photoexcited to other sites. Providing the irradiation does not affect the spectrometer sensitivity (i.e., causing excessive photoconductivity), it is possible to measure these changes in the concentrations of the paramagnetic defects involved, both during and after irradiation.[1] The kinetics and photodynamics of this process can also be followed by EPR at different temperatures. In this way, determination of relative reaction rates and their variation with temperature may be studied. Estimates of the activation energies associated with particular trapping centres may then be obtained from analysis of the EPR decay curves.

The photo-response of the thermally generated electron traps have been investigated at several temperatures in both the Anatase and Rutile samples. This has been carried out in order to differentiate between any differences in the mechanism of excitation of the electrons from sample to sample which could be caused by the difference in surface morphology. In addition to this the photo-response of surface *versus* bulk Ti^{3+} cations will be investigated in each sample in order to ascertain if the mechanism of photo-excitation in the surface defects is different to that of the bulk defects. In addition to this a second type of photoresponse process (Thermoluminesence) will be discussed whereby the addition of excess energy to the system is required in order to return the signal to its original intensity following UV irradiation.

8.2 Experimental

A detailed account of the experimental methods used in the handling of the powders, manipulation of the samples on the vacuum line and operation of spectrometers and UV lamp were thoroughly described in chapter 4. In this section, only the specific experimental conditions used in the preparation and study of paramagnetic centres in TiO_2 will be summarised.

8.2.1 Preparation of the polycrystalline TiO_2 samples

Throughout the work described in this chapter the titanium dioxide, P25 Anatase (*Degussa*) with a surface area of *ca.* 49 m^2g^{-1} was used, along with a Rutile sample hereafter labelled Rutile A with a surface area of *ca.* 135 m^2g^{-1}. This material was synthesised by hydrolysis of an aqueous solution of $TiCl_4$.[3] A second rutile sample, hereafter labelled Rutile B with a surface area of *ca.* 97 m^2g^{-1} was supplied by Huntsman Tioxide. Each TiO_2 sample was initially evacuated to a residual pressure of 10^{-4} Torr at 298K in an EPR quartz cell. The samples were then heated to 393K under vacuum overnight in order to remove any physisorbed water from the surface and then slowly heated under vacuum to a final temperature of 823 K (over a 5 hour period). They were held at this temperature for approximately 1 hour. Following the thermal reduction under vacuum, bulk and surface Ti^{3+} states (predominately surface) were formed in addition to the medium polarised conduction electrons as discussed in chapter 5. The photo-response of the Ti^{3+} and the medium polarised electrons, were then studied at selected temperatures.

This sample was then subsequently oxidised under oxygen, so that the surface Ti^{3+} centres are exclusively destroyed while the signal due to the bulk centres remains. In this way the photoresponse of the bulk centres can be studied without interference from the surface centres. Note, that while O_2 addition to the thermally reduced TiO_2 powder will produce O_2^- anions after preferential reaction with surface Ti^{3+} centres, subsequent annealing at 250 K destroys the O_2^- signal but does not affect the bulk Ti^{3+} signal. No new Ti^{3+} centres are generated during this treatment. Therefore, a 'clean' EPR spectrum of the bulk Ti^{3+} can be studied.

8.2.2 Measuring the photoresponse

Prior to any UV irradiation of the sample *in situ*, accurate field positions of the Ti^{3+} centres (for both surface and bulk forms) and medium polarised electrons were required. In order to obtain these values accurately, an EPR spectrum was recorded at the required temperature and the field position obtained. Figure 8.1 shows a reduced TiO_2 sample (P25 Anatase) and the field positions of the $Ti^{3+}_{(surf)}$ and medium polarised conduction electron for each.

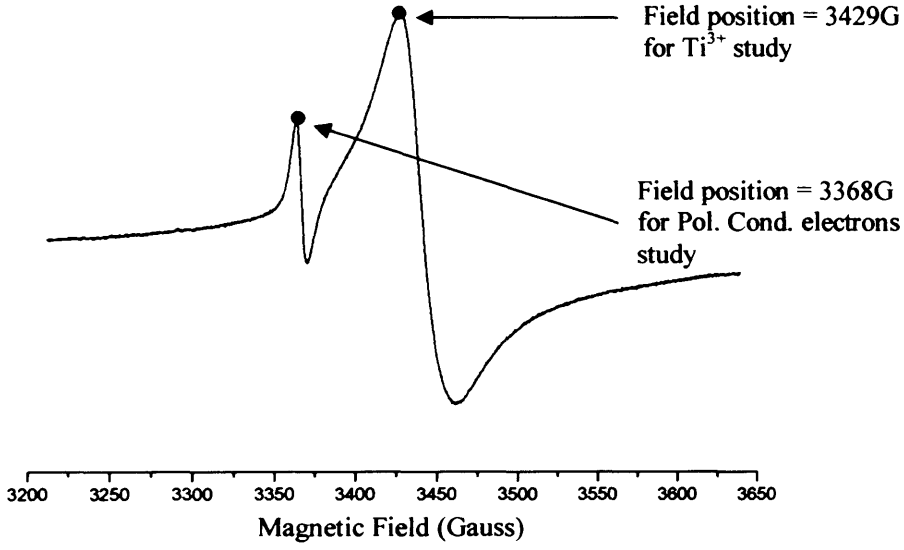

Figure 8.1. EPR spectrum of thermally reduced P25 with field positions of both Ti^{3+} and medium polarised conduction electrons

The magnetic field sweep was then set to zero and the centre field set to coincide with the maximum of the peak to be examined. The photo-response of the peak could then be followed. In order to obtain an accurate baseline for the signal under study, the initial response of the peak under dark conditions was first recorded. This process was carried out for all signals and temperatures, which were studied. After obtaining a background signal the peak in question was then periodically irradiated for a set time. An example of the typical photo-response experienced is shown in figure 8.2. All signals were irradiated to a point of saturation at which no further change of signal intensity was observed.

A 1000 W *Oriel Instruments* UV lamp, incorporating a Hg/Xe arc lamp (250 nm to 2500 nm), was used for all irradiations in the presence of a water filter. The UV output below 280 nm accounts for only 4 – 5% of the total lamp output.

Irradiation of samples at low temperature were preformed *in situ* in the EPR cavity *via* an optical transmission window.[2]

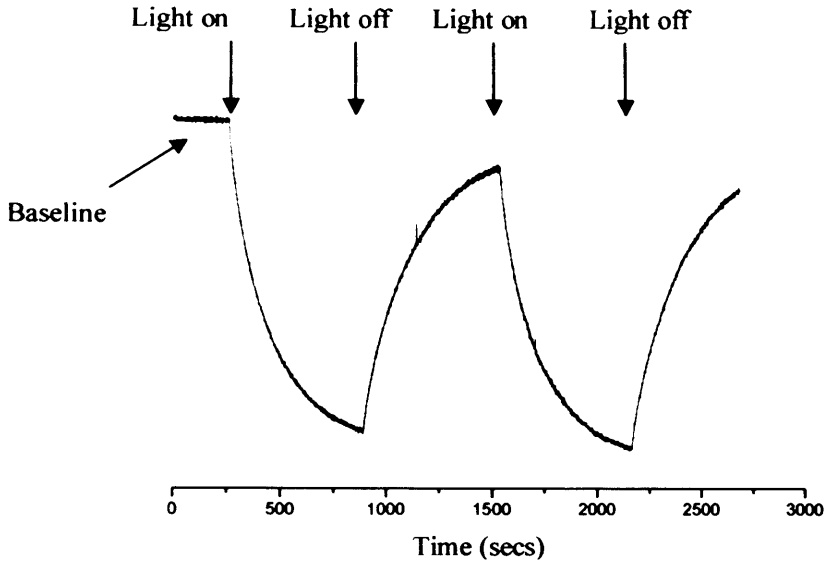

Figure8.2. Example of photo-response decay curve obtained during UV irradiation of a Ti^{3+} signal.

8.2.3 Measurement of EPR spectra

The EPR spectra were recorded on a Bruker ESP 300E series spectrometer incorporating an EPR 4102 ST rectangular cavity. Variable temperature studies were conducted using a Bruker B-VT2000 temperature controller. All spectra were recorded at X-band frequencies, 100 kHz field modulation and 10 mW microwave power. In addition, the sharp resonance at g = 2.0030 was previously measured accurately using an NMR gaussmeter calibrated to the perylene radical cation in concentrated H_2SO_4, and this was therefore used as an internal marker for the g values.

8.3 Results

8.3.1 Photodynamic study of thermally reduced P25 Anatase

The polycrystalline P25 Anatase sample (*ca.* 5mg) was slowly heated under vacuum to a final temperature of 823 K and held at this temperature for 1 hour generating a blue coloured powder indicative of Ti^{3+} production (chapter 5, section 5.3.1). Prior to any photoresponse study, the EPR spectrum was recorded at the necessary temperature in order to obtain an accurate field positions (at the operating frequency of the spectrometer) of the two resonances at $g \approx 1.97$ and g = 2.0030 (i.e., surface Ti^{3+} and medium polarised conduction electron). The photoresponse of the two thermally generated signals were initially studied at 120 K. The signals were

examined following a 10-minute periodic interval of UV irradiation. The resultant responses are shown below in figure 8.3.

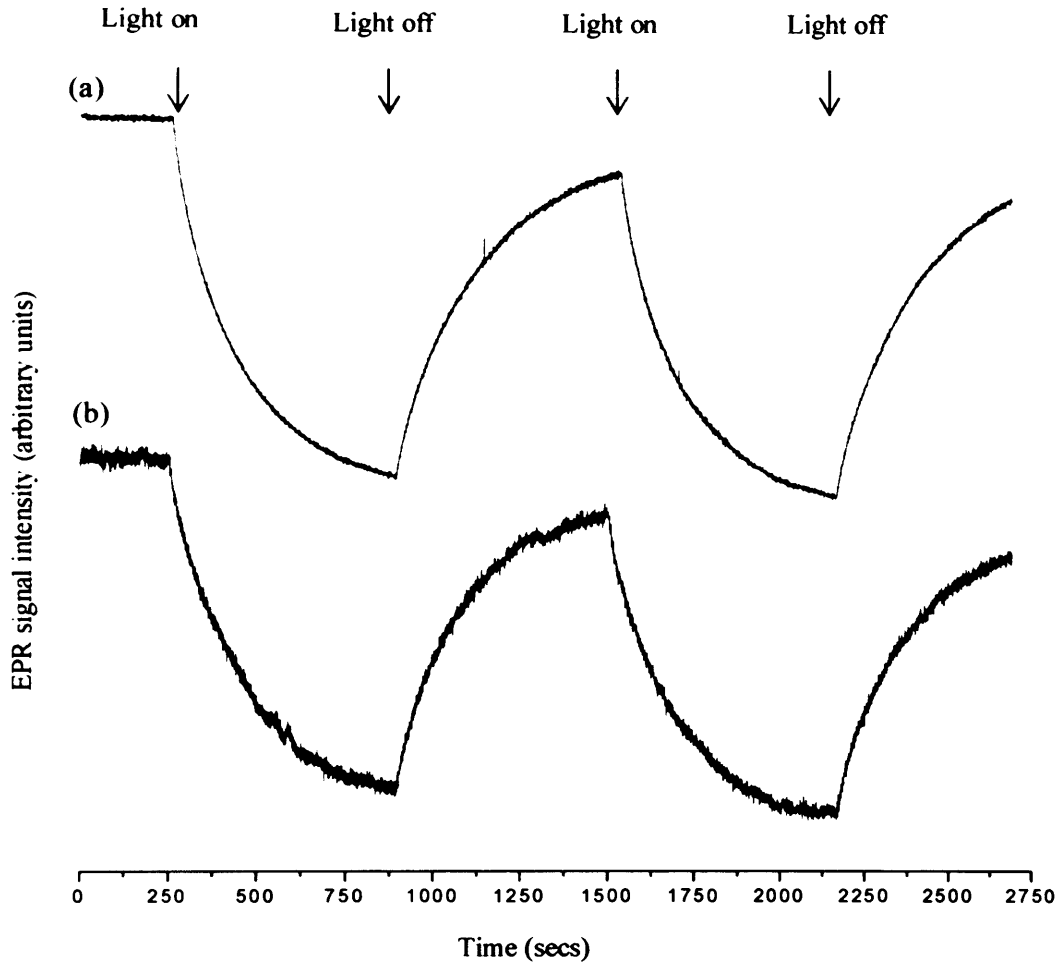

Figure 8.3. EPR study of the photo-response of (a) Ti^{3+}, (b) medium polarised conduction electron and following periodic UV irradiation at 120 K. Field positions = 3429 G and 3368 G respectively.

As shown in figure 8.3a, when the signal at $g \approx 1.97$ due to surface Ti^{3+} was illuminated at 120 K, the intensity decreased immediately, indicating a decrease in the population of the centres responsible for the absorption of light, i.e., the Ti^{3+} centres. Cessation of the illumination resulted in the remediation of the signal to its former intensity, demonstrating the reversibility of the process. The photo-response of the signal at $g = 2.0030$ (i.e., medium polarised conduction electron) was also observed to undergo a similar behaviour (figure 8.3b). Upon UV irradiation of the peak, the signal intensity decreased, whilst switching the light off caused the signal intensity to increase again indicating a reversible process. The profile of the photo-response curve in both cases is very similar. It should be noted that all signals examined in the

photo-response studies were UV irradiated to a point of saturation in each case (EPR spectra have been removed for brevity).

In order to obtain additional information on the behaviour of the signals under UV irradiation, further studies were completed at different temperatures. The photo-response curves of the surface Ti^{3+} signal at increasing temperatures are shown in figure 8.4.

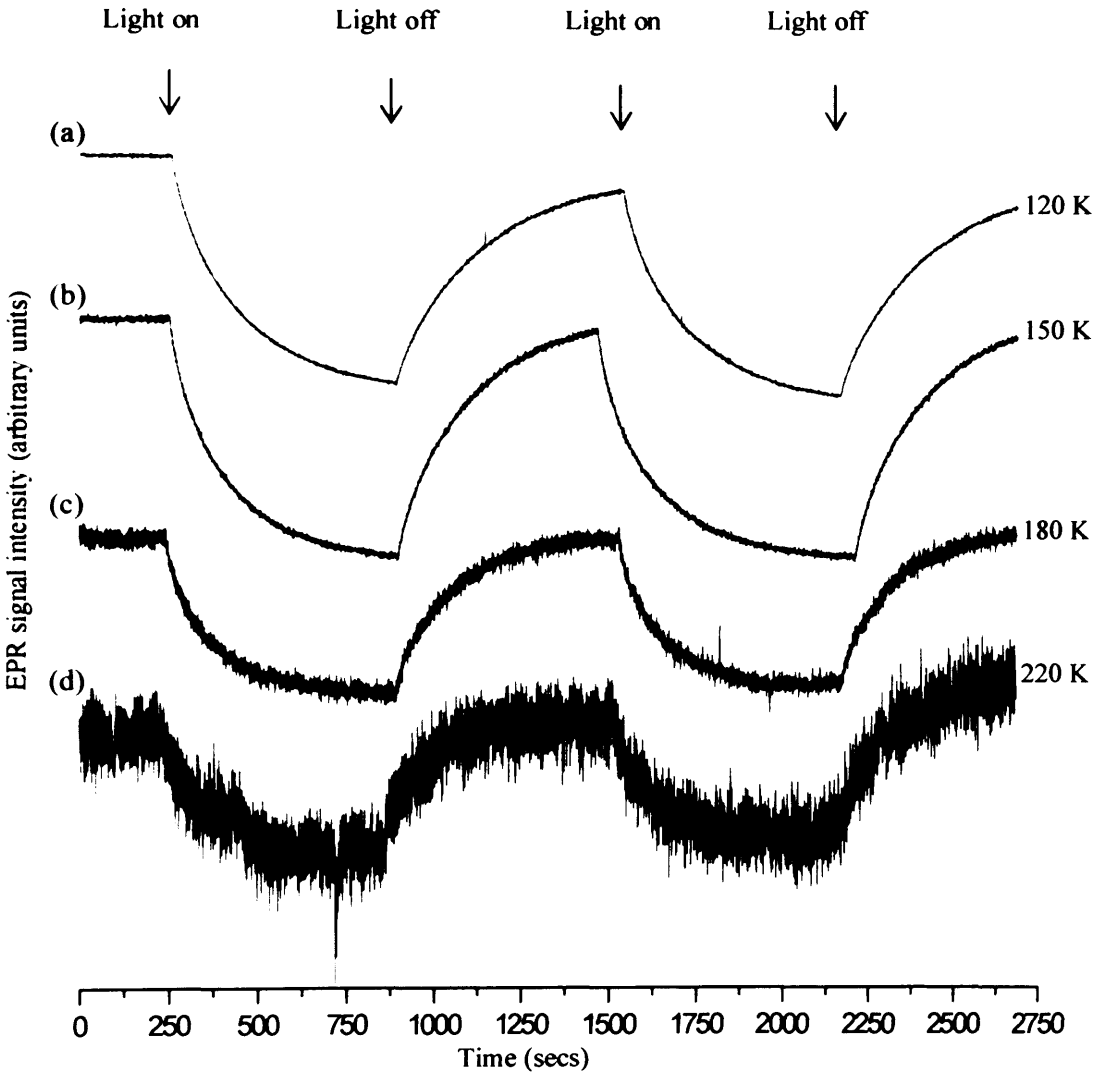

Figure 8.4. Variable temperature photo-response study of the $Ti^{3+}_{(surf)}$ centres on thermally reduced P25. The photodynamic experiments were recorded at (a) 120 K, (b) 150 K, (c) 180 K and (d) 220 K (Field position of peak = 3429 G).

As the temperature of illumination was increased, the decay curve for the Ti^{3+} centres appears to have a similar profile. However, most importantly the point at which the Ti^{3+} signal was saturated (i.e., no further decay in the signal) was reached more quickly. Along with this a decrease in EPR signal resolution was also noted. A

more detailed discussion about the effect of temperature increase will be presented later. The corresponding photo-response of the medium polarised conduction electrons in the P25 anatase sample was also investigated at increasing temperatures; the results are presented in figure 8.5 below.

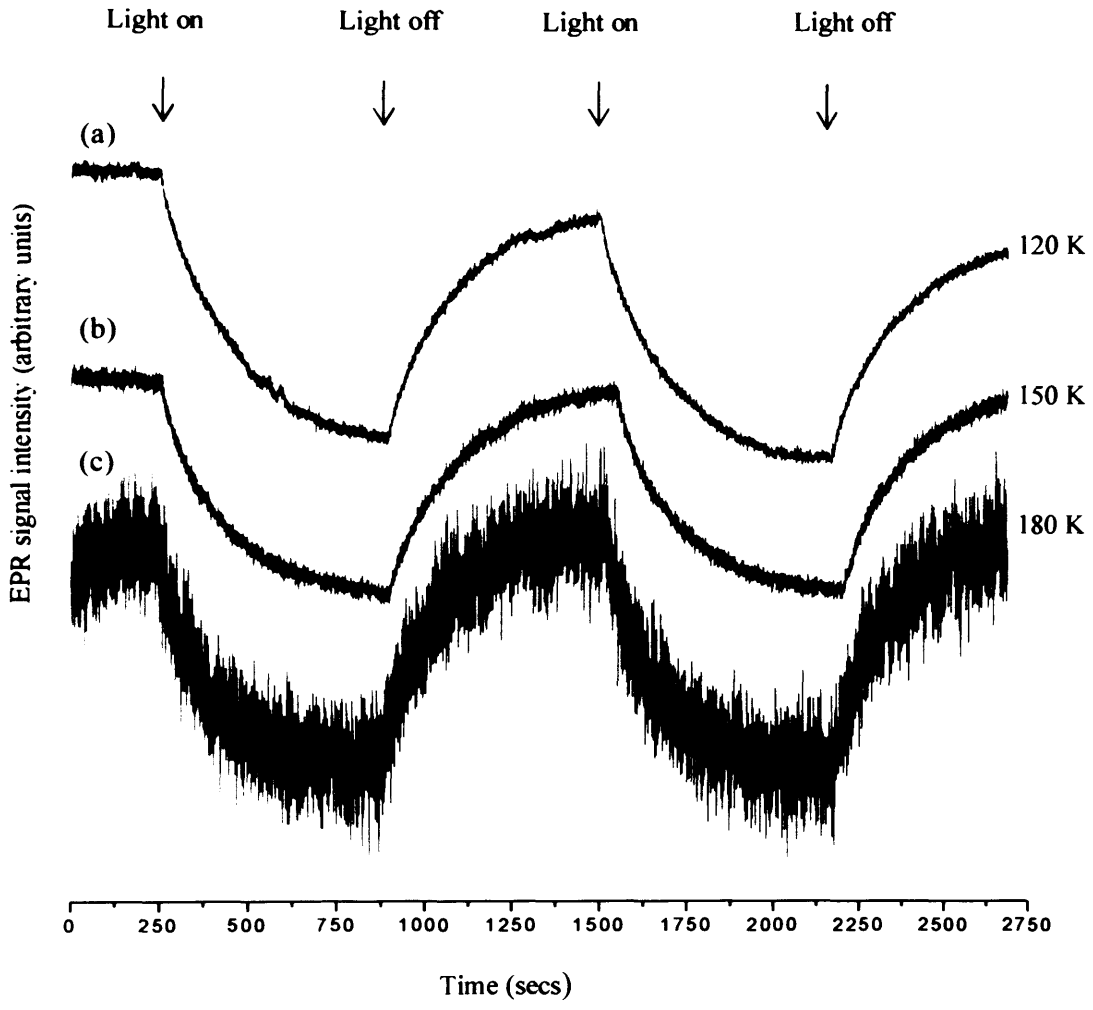

Figure 8.5. Variable temperature photo-response study of the localised conduction electron signal in P25 following UV irradiation for 10-minute periods. The photodynamic experiments were recorded at (a) 120 K, (b) 150 K and (c) 180 K (Field position = 3368G).

As before, the saturation point for the signal was reached more easily at increasing temperature. It should be noted that the EPR signal of the reduced sample (in dark conditions) decreases at increased temperatures due to naturally spin lattice relaxation effects. Therefore, the highest possible temperature permitted to study the localised conduction electrons was ~ 180 K; at 220 K for e.g., the signal and therefore photo-response was so weak it could not be shown.

As described in the experimental section (8.2.1), the surface Ti^{3+} centres could be easily destroyed by addition of oxygen, leaving the signal due to residual and unreacted bulk Ti^{3+} centres. In this way the photodynamics of the bulk Ti^{3+} centres could be studied independently from the surface Ti^{3+} centres. The results are shown in figure 8.6. It should be recalled (figure 5.11, chapter 5) that the reduction temperature of 823 K at least 90% of the Ti^{3+} centres visible by EPR are surface states. In the preceding section (8.3.1) the minimum 10% contribution of bulk Ti^{3+} centres to the photo-response study was disregarded.

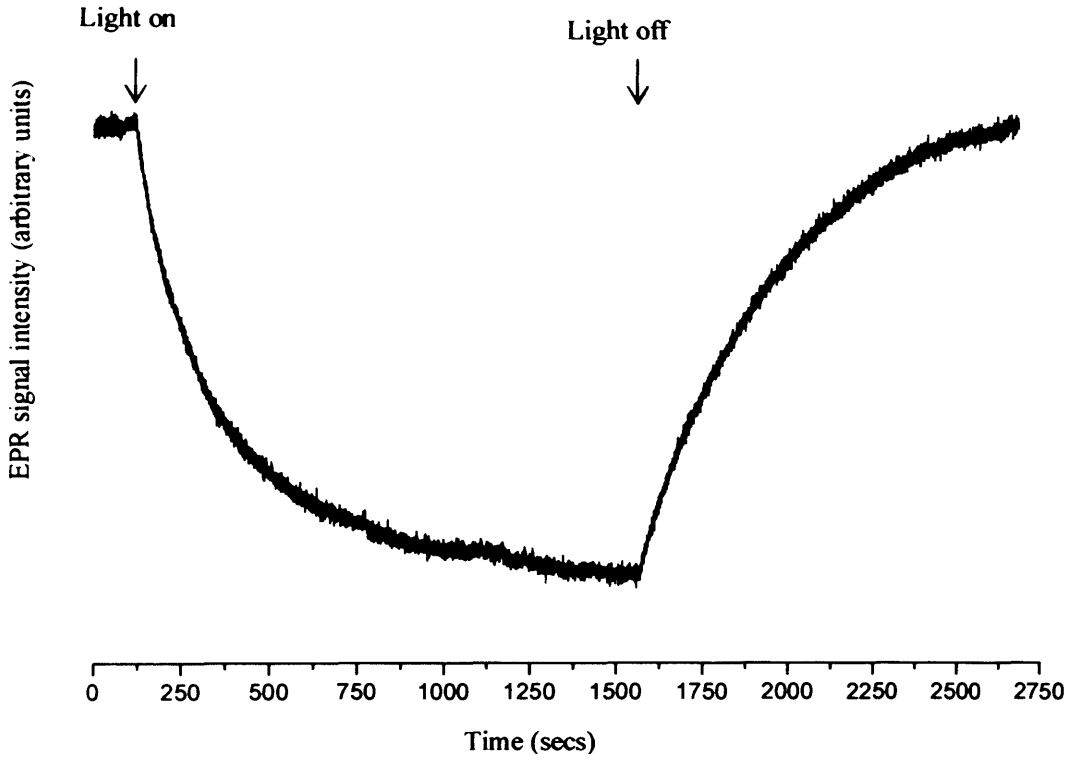

Figure 8.6. EPR study of the photo-response of $Ti^{3+}_{(bulk)}$ signal in P25 and following periodic UV irradiation at 120 K. Field position = 3444 G

As shown in figure 8.6 illumination of the bulk Ti^{3+} was illumianetd at 120 K, the signal intensity immediately decreased. Termination of the illumination resulted in the restoration of the signal to its original intensity. Further, photo-response studies of the bulk Ti^{3+} signal at inceasing temperatures resulted in the same profile curves. The photo-response curves of the bulk Ti^{3+} at increasing temperatures are shown in figure 8.7.

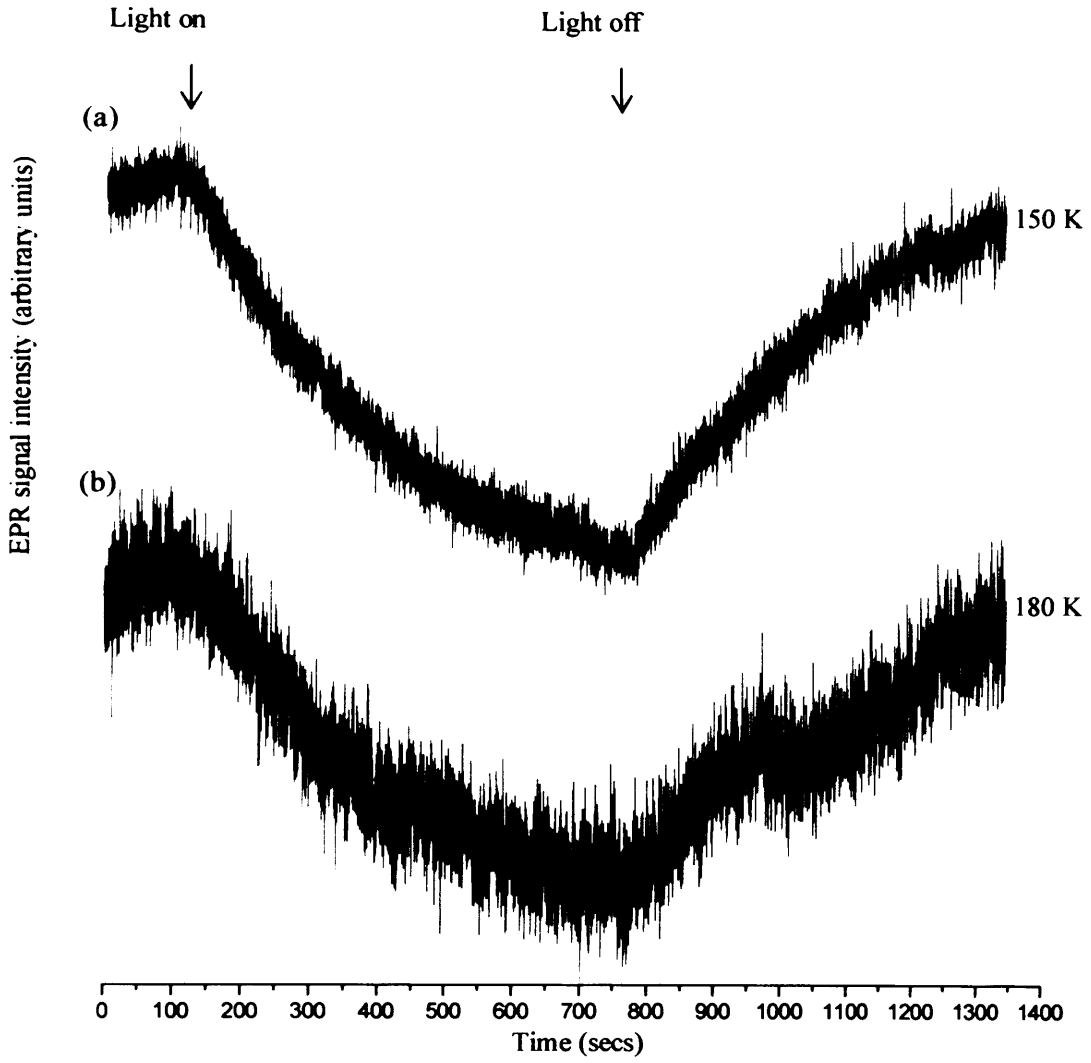

Figure 8.7. Variable temperature photo-response study of the bulk Ti^{3+} in P25 Anatase following UV irradiation for 10 minute periods. The photodynamic experiments were recorded at (a) 150 K and (b) 180 K (field position = 3444 G).

As the temperature of UV irradiation was increased, the decay curve for the bulk Ti^{3+} centres have similar profiles. Upon increasing the temperature it must be noted that the point at which saturation of the signal occurs was achieved more rapidly

8.3.2 Photodynamics study of thermally reduced Rutile A

A similar photodynamics study was carried out for the surface Ti^{3+} centres and medium polarised conduction electrons in the Rutile A sample. The variable temperature photo-response curves for the surface Ti^{3+} centres are shown in figure 8.8 below. Above 150 K, the intensity of the native Ti^{3+} signal began to diminish

dramatically so that the corresponding signal – to – noise ratio in the photo-response curves also increased (figure 8.8c and d).

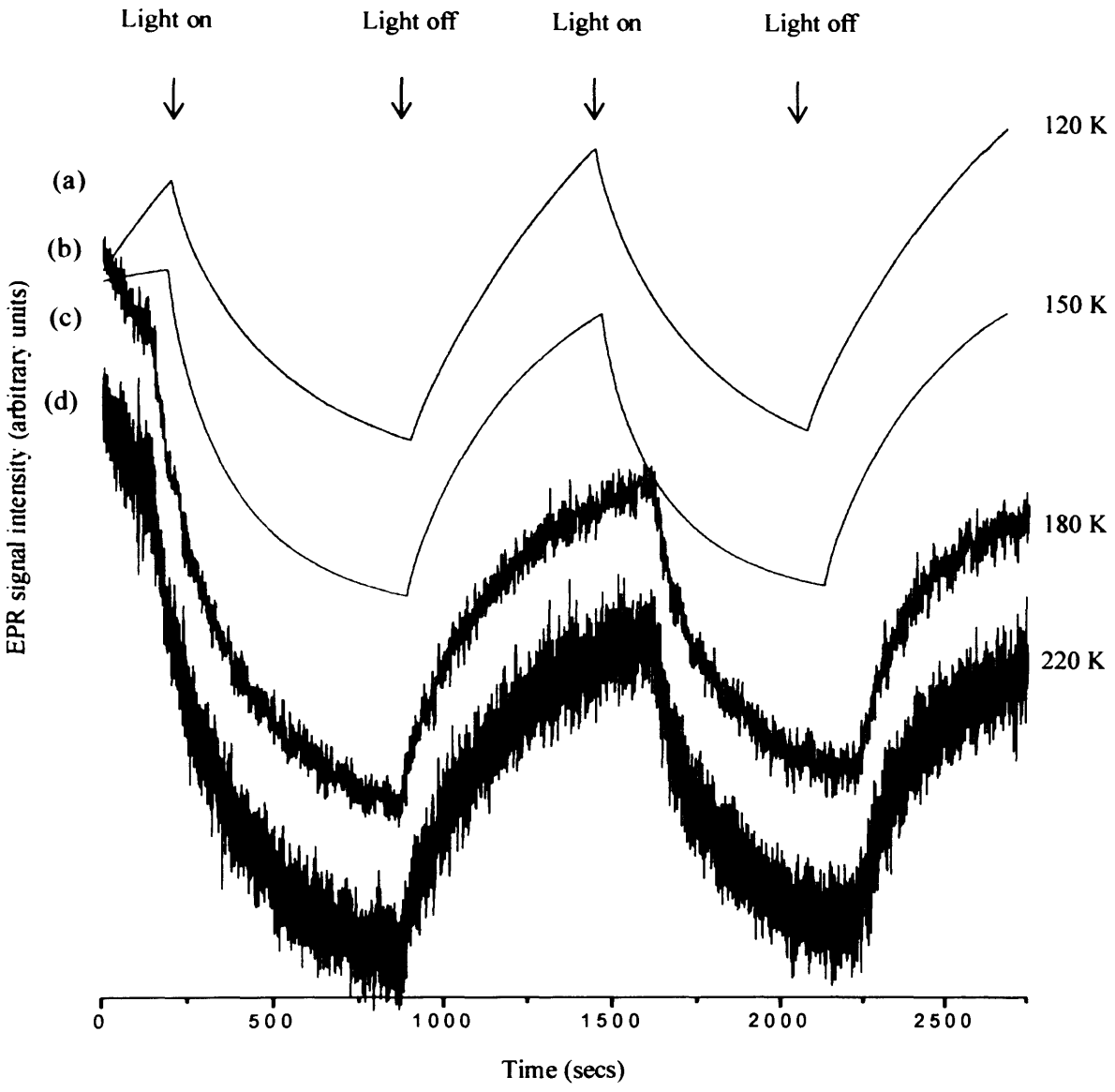

Figure 8.8. Variable temperature photoresponse study of the Ti^{3+} centres in Rutile A following UV irradiation. The photodynamic experiments were recorded at (a) 120 K, (b) 150 K, (c) 180 K and (d) 220 K (Field position = 3325 G).

The signal intensity of the $Ti^{3+}_{(bulk)}$ species decreased at all temperatures studied, as expected. In addition, an actual increase in the time required to achieve the point of saturation of the Ti^{3+} signal was noted when the temperature was increased (figure 8.8d). As a general comparison, the time required to achieve the point of saturation was found to be longer than that required at the same temperature for P25 anatase. An example of the saturation limit for Ti^{3+} in Rutile A is shown in

figure 8.9, where the saturation point is achieved at a much slower rate when compared with both the Ti^{3+} surface and bulk centres in P25 Anatase. A more detailed analysis of the differences in rate of saturation for each sample at the various temperatures will be presented later.

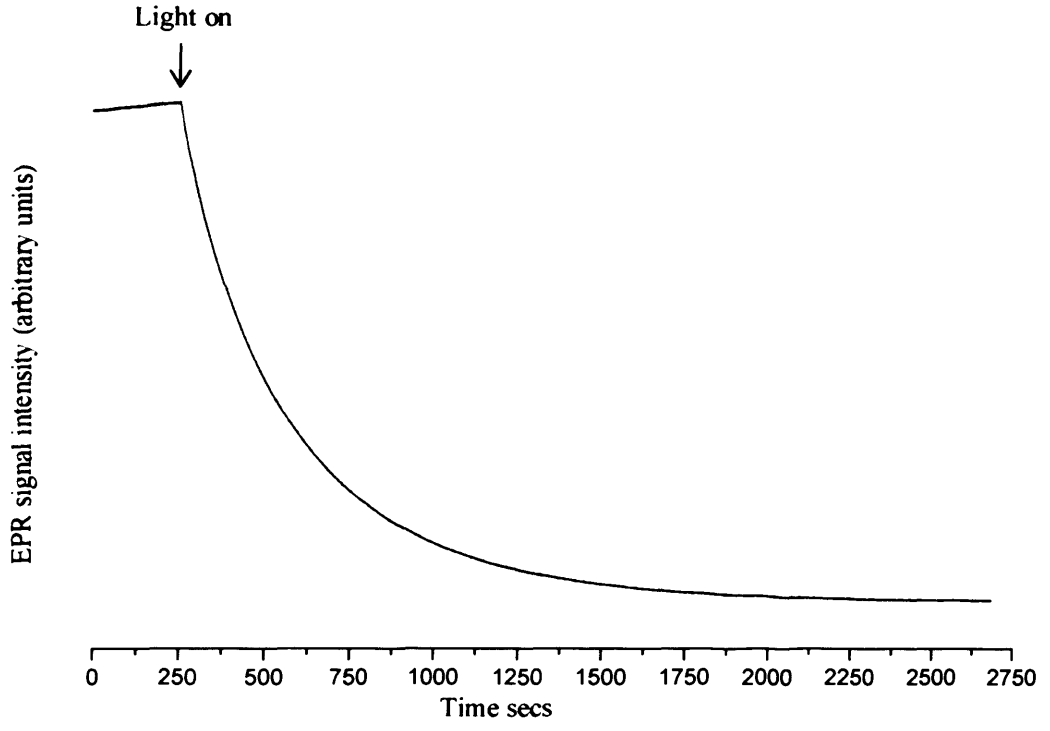

Figure 8.9. Photoresponse of Ti^{3+} saturation in Rutile A irradiated and recorded at 120 K.

The corresponding photo-response of the medium polarised conduction electron species, formed during thermal reduction of the Rutile A sample, was also studied. At increasing temperatures the resultant photo-response curves are shown in figure 8.10.

Similar to the observation in P25 Anatase, increasing the temperature resulted in the saturation point being reached more quickly, contrasting that observed for the $Ti^{3+}_{(surf)}$ present in Rutile A. The highest temperature of study for the localised conduction electron was found to be ~ 180 K, this was due to the signal decreasing at increased temperatures therefore, causing the photo-response of the signal to become progressively weaker.

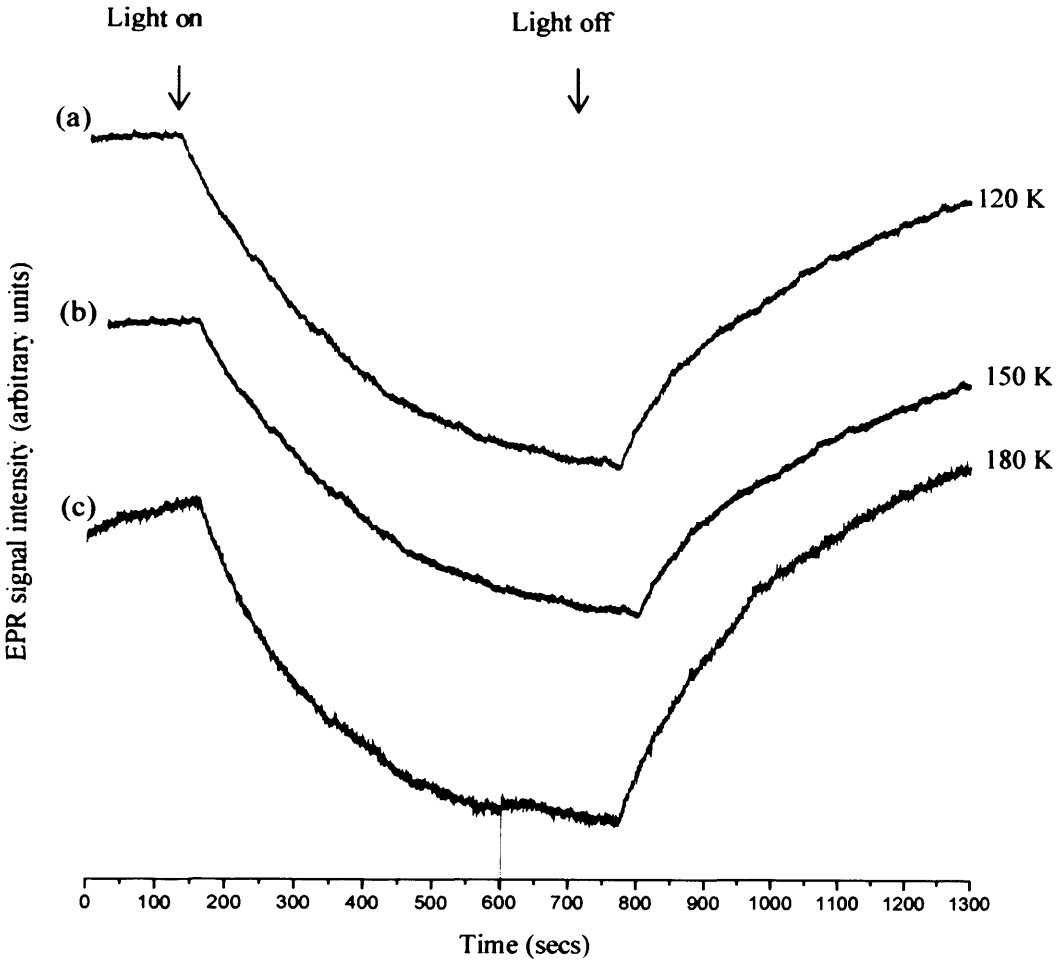

Figure 8.10. Variable temperature photo-response study of the localised conduction electron in Rutile A following UV irradiation. The photodynamic experiments were recorded at (a) 120 K, (b) 150 K and (c) 180K (Field Position = 3325 G).

It should be noted that no photo-response study of the bulk Ti^{3+} signal present in Rutile A studies was carried due to the addition of oxygen at 298 K to the reduced sample resulted in the removal of all bulk Ti^{3+} centres.

8.3.3 *Photodynamic study of thermally reduced Rutile B*

The final sample studied in the photodynamic experiments was the Rutile B sample. Both surface and bulk Ti^{3+} centres were investigated. The polycrystalline sample was firstly reduced at 823 K and held at this temperature for 1 hour. The sample produced contained predominately surface Ti^{3+} cations along with a second resonance attributed to the medium polarised conduction electron. Prior to any photo-response study of either signal the EPR signal was recorded at the required temperature to achieve accurate field positions of both resonances, this process was

followed at each new temperature studied. Figure 8.11 shows the photo-response of the surface Ti^{3+} species at increasing temperatures under UV illumination.

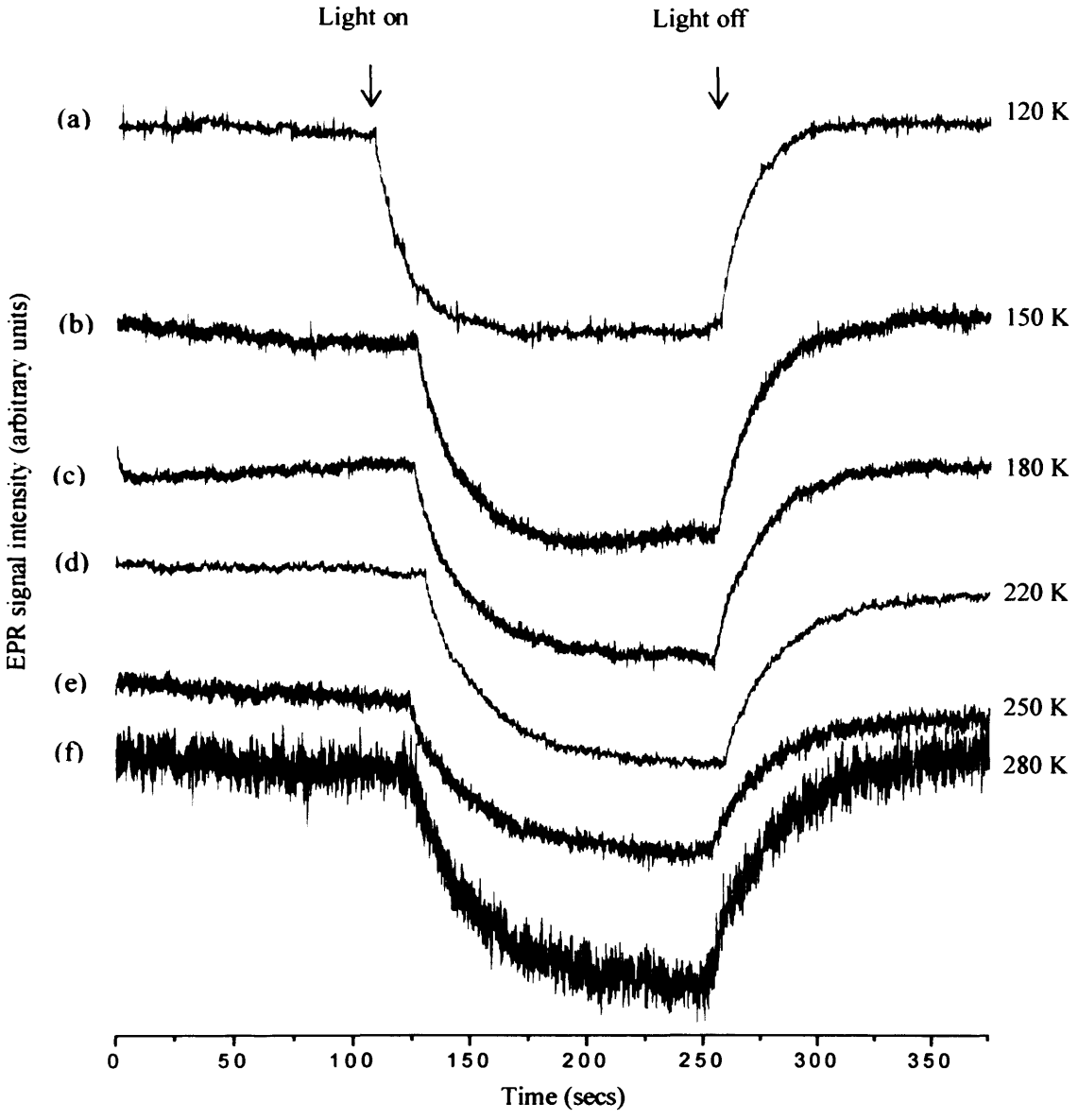

Figure 8.11. Variable temperature photo-response study of the $Ti^{3+}_{(surf)}$ centres in thermally reduced Rutile B. The photodynamic experiments were recorded at (a) 120 K, (b) 150 K, (c) 180 K, (d) 220 K, (e) 250 K and (f) 280K (Field position = 3317 G).

As shown in figure 8.11, at all temperatures investigated the $Ti^{3+}_{(surf)}$ signal intensity decreased instantly when illuminated. When the UV irradiation was removed the signal intensity returned to its original state. Similar to the observation in Rutile A, the time required for the Ti^{3+} centre to reach saturation (i.e., no further charge in the photo-response curves) was found to increase at increasing temperatures. It must be recalled, that the reverse trend was found in P25 Anatase.

The photo-response curves for the bulk Ti^{3+} centres in vacuum reduced Rutile A are shown in figure 8.12.

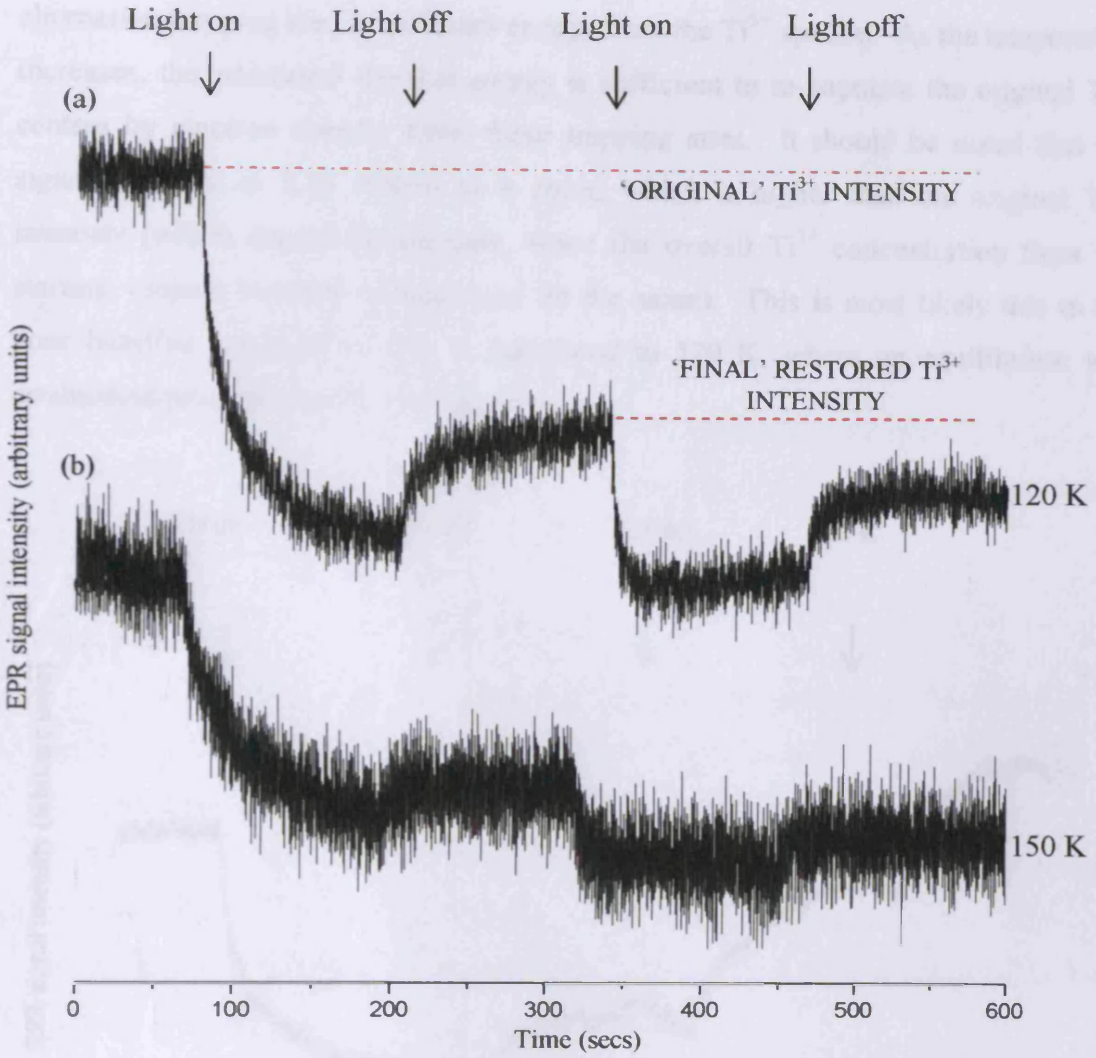

Figure 8.12. Variable temperature photo-response study of the $Ti^{3+}_{(bulk)}$ centres in thermally reduced Rutile B. The photodynamic experiments were recorded at (a) 120 K and (b) 150 K (Field position = 3332 G).

Following UV irradiation at 120 and 150 K, the bulk Ti^{3+} intensity decreases immediately, eventually to a point of saturation as expected. However, under dark conditions, the photo-response curve did not return to its original intensity as previously observed. This unusual behaviour was observed upon subsequent irradiation of the signal at both temperatures studied. This photo-response study of $Ti^{3+}_{(bulk)}$ centres was examined on several occasions and in each case the resultant EPR spectra recorded where identical to that in figure 8.12.

The signal was however restored to its original intensity by annealing the sample at increasing temperatures (figure 8.13). This simple experiment demonstrates that possibly the photo-excited electron (from the Ti^{3+} centre) is stabilised at an alternative-trapping site, of different energy from the Ti^{3+} species. As the temperature increases, the additional thermal energy is sufficient to re-populate the original Ti^{3+} centres by electron transfer from these trapping sites. It should be noted that the signal intensity in 8.13 returns to a point, which is higher than the original Ti^{3+} intensity (which cannot be the case, since the overall Ti^{3+} concentration from the starting vacuum reduced sample must be the same). This is most likely due to the poor baseline achieved at 180 K compared to 120 K, where an equilibrium was established prior to any UV irradiation.

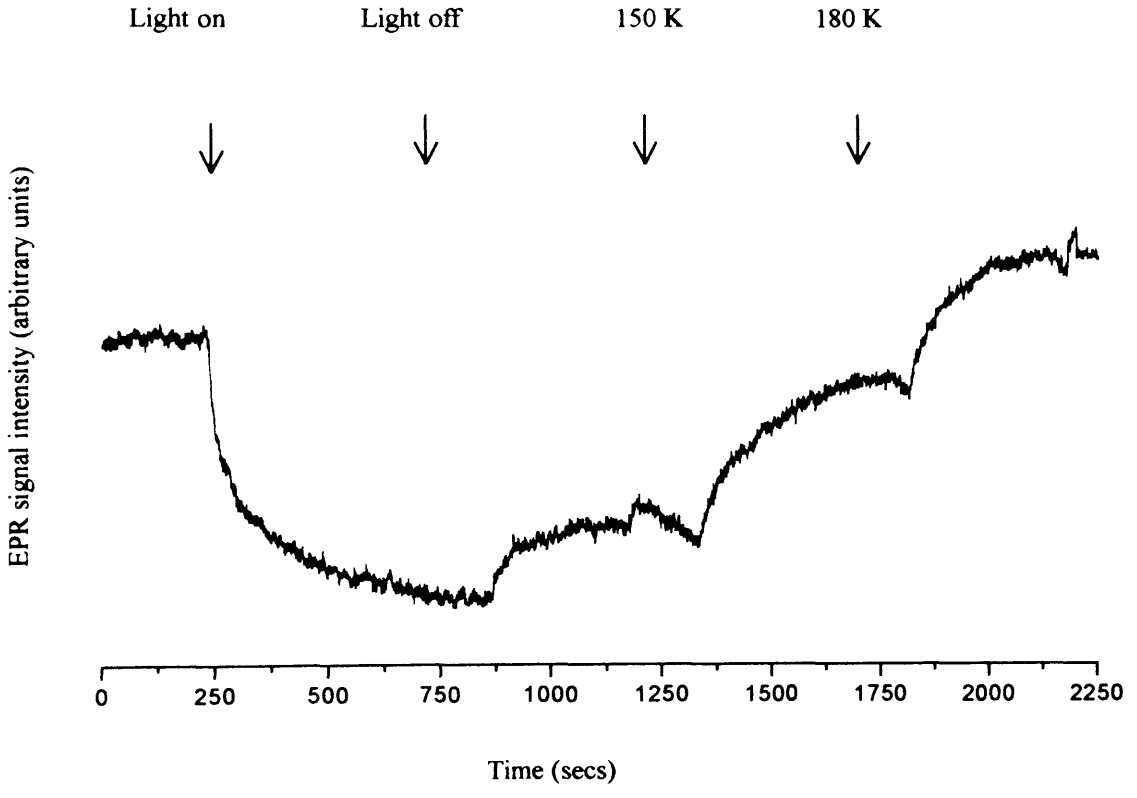

Figure 8.13. Photo-response of bulk Ti^{3+} in Rutile B sample, following UV irradiation at 120K then warming to 150 and 180 K whilst under dark conditions

8.3.4. Determination of reaction rates

In order to measure reaction rates, the concentration of reactants and products at given times after the reaction is initiated must be known[3]. Therefore the rate of

reaction is defined in terms of the rate change of the concentration of a designated species.

$$\text{Rate of reaction} = k\,[A][B] \qquad (8.1)$$

The coefficient k, is characteristic to the reaction being studied and is called the rate constant which is independent of the concentrations and temperature dependant. An experimentally determined equation of this kind is called the rate law; and it provides a basis for the classification of reactions according to their kinetics. The reactions belonging to the same class will have similar kinetic behaviour – their rates will vary with composition in a similar way.

The classification of reactions is based on the 'order'. The order of a reaction with respect to each species is the power to which the concentration of the species is raised in the rate law. The overall order of a reaction is the sum of the orders of all the components.

Integrated rate laws

An integrated rate law is an expression that gives the concentration of a species as a function of the time. The use of integrated rate laws provide two pieces of information i) predict the concentration of a species at any time following the start of the reaction, ii) find the rate constant and order of reaction. Almost all-experimental work in chemical kinetics deals with integrated rate laws; their great advantage being that they are expressed in terms of the experimental observable of concentration and time.

First and second order rate laws and half lives

For a first order reaction the integrated rate law is defined as,

$$\ln([A]_o/[A]) = kt \qquad (8.2)$$

Where t is time (seconds), k the rate constant, $[A]_o$ the initial concentration of A at time t = 0 and [A] is the concentration at a given time. Equation 8.2 above is also equivalent to

$$\ln [A] = \ln[A]_o - kt \qquad (8.3) \text{ or}$$
$$[A] = [A]_o e^{-kt} \qquad (8.4)$$

A common feature of all first order reactions is that the concentration of the reactant decays exponentially with time. If $\ln([A]/[A]_o)$ is plotted against t, then a first-order reaction will produce a straight line, the slope of the graph is equal to the k, the rate constant.

For a second order reaction the integrated rate law is defined as;

$$1/[A] = 1/[A]_o + kt \qquad (8.5)$$

For a second-order reaction, a plot of 1/[A] against t should produce a straight line, the slope of which is equal to the rate constant k. In a second order reaction the concentration of A decreases with time but not as rapidly as first order reactions.

A useful indication of the rate of a first order chemical reaction is the half-life $t_{½}$, of a reactant. That is the time it takes for the concentration of the species to fall to half its initial value and it can be calculated by,

$$t_{½} = \ln 2/k \qquad (8.6)$$

where, $t_{½}$ is the half life, k the rate constant for the reaction. For a second order chemical reaction the half life $t_{½}$ may be calculated by,

$$t_{½} = 1/k[A]_o \qquad (8.7)$$

where $[A]_o$ the initial concentration at t = 0. For a first order reaction, the half-life of a reactant is independent of its initial concentration. In contrast the half-life for a second order reaction does depend on the initial concentration of the reactant.

The Arrhenius equation

The rates of most reactions increase as the temperature is raised. It has been noted that a graph of ln k against 1/T (where T is the (absolute) temperature), should produce a straight line with a slope characteristic of the reaction.

$$\ln k = \ln A - Ea/(RT) \qquad (8.8)$$

This equation is known as the Arrhenius equation where, A is the pre-expontential factor (which has the same units as k), Ea the activation energy and R the gas constant (8.3145 $JK^{-1}mol^{-1}$). The Arrhenius equation is often written as,

$$K = Ae^{-Ea/RT} \qquad (8.9)$$

From the gradient of the slope the activation energy of the reaction may be calculated. A reaction with zero activation energy has a rate that is largely independent of temperature.

8.3.5 Kinetics of surface and bulk Ti^{3+} photo excitation in P25Anatase

As shown in figure 8.4 following UV irradiation of the $Ti^{3+}_{(surf)}$ for a period of 10 minutes the rate of decay alters quite significantly, following an increase in temperature. As the temperature of illumination is increased the point at which the Ti^{3+} signal was saturated was reached more quickly. In order to determine the rate at which the $Ti^{3+}_{(surf)}$ signal decays at 120 K the signal was plotted according to first and second order rate laws. A plot of $\ln([A]/[A]_o)$ against time (sec) for a first order reaction, whilst a plot of $1/[A]$ against time (sec) for a second order reaction, the resultant graphs are shown in figure 8.14, errors have been omitted for clarity.

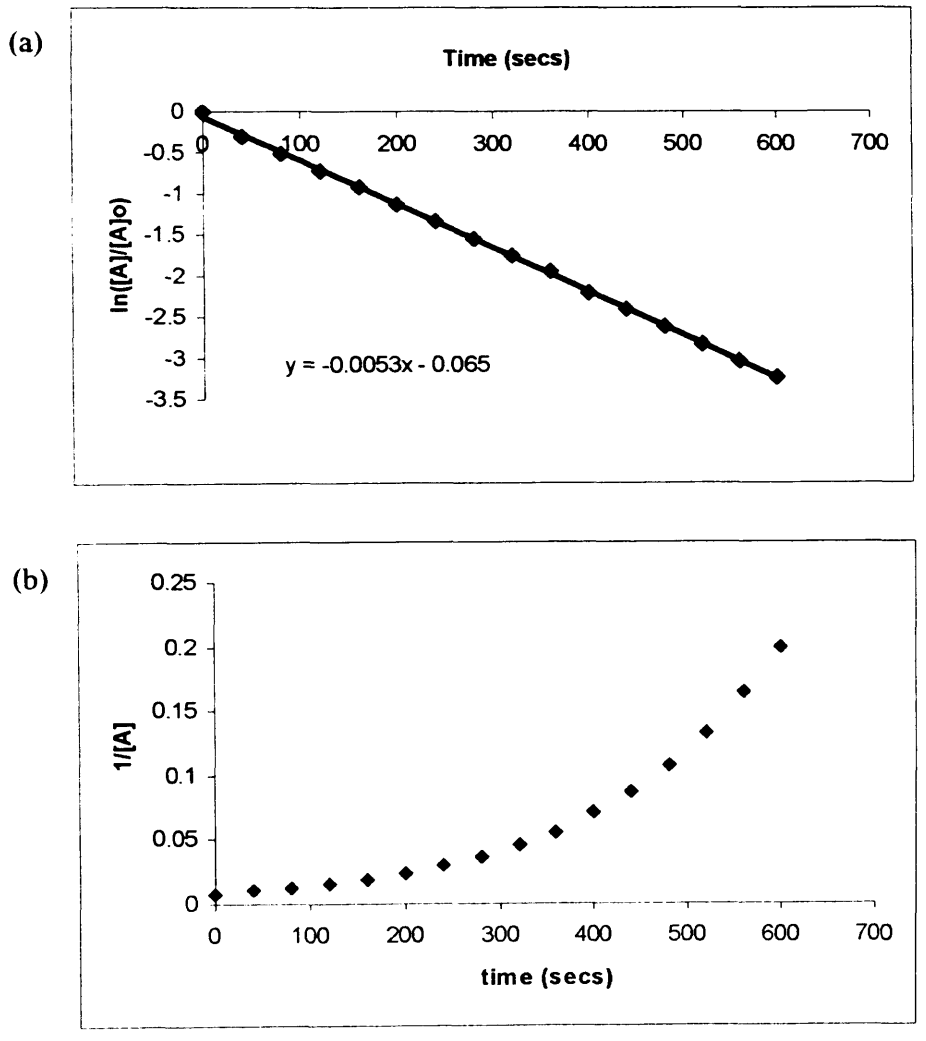

Figure 8.14. (a) First order and (b) second order kinetics. Decay curves for the photo-response of Ti^{3+} in P25 Anatase at 120 K.

As evidenced in figure 8.14a, a straight-line graph is obtained when the photo-response curve is plotted based on first order kinetics. This indicates that the photo-response process follows a first order rate of decay at 120 K. When the photo-response curve was plotted according second order kinetics a non-linear line was produced, therefore, confirming the reaction does not undergo a second order decay. As shown in figure 8.15a-c the decay of the $Ti^{3+}_{(surf)}$ signals at increasing temperatures have also been plotted using first order kinetics. According to equation 8.10 below, the slope of the graphs obtained (figures 8.14a and 8.15) determines the rate constants for each temperature studied. The values obtained are given in table 8.1.

$$\ln([A]o/[A])/t = k \qquad (8.10)$$

Table 8.1. Calculated rate constants, k, and half-lives for the $Ti^{3+}_{(surf)}$ signal at increasing temperatures.

Temperature / K	Rate constant k / (s^{-1})	Half- life / (s)
120	0.00533 ± 0.001	130.1±0.3
150	0.00606 ± 0.002	114.4±0.4
180	0.00676 ± 0.004	102.5±0.6
220	0.00759 ± 0.008	91.3±1.1

The half-life for each temperature may also be calculated using equation 8.6 above. The calculated half-lives are shown in table 8.1 above. As seen in table 8.1, there is a noticeable decrease in the half-life of the signals as the temperature of study is increased. This is also due to a decrease in the time required for the peak to reach saturation at the higher temperature of study. These results coincide as expected with those calculated for the rate constant at corresponding temperatures of study.

To determine the activation energy for the photo-response of the $Ti^{3+}_{(surf)}$ centre, a plot of ln k against 1/T (where T is the absolute temperature) has been made. The resultant graph is shown in figure 8.16 giving an activation energy of Ea = 0.77 ± 0.03kJmol^{-1}

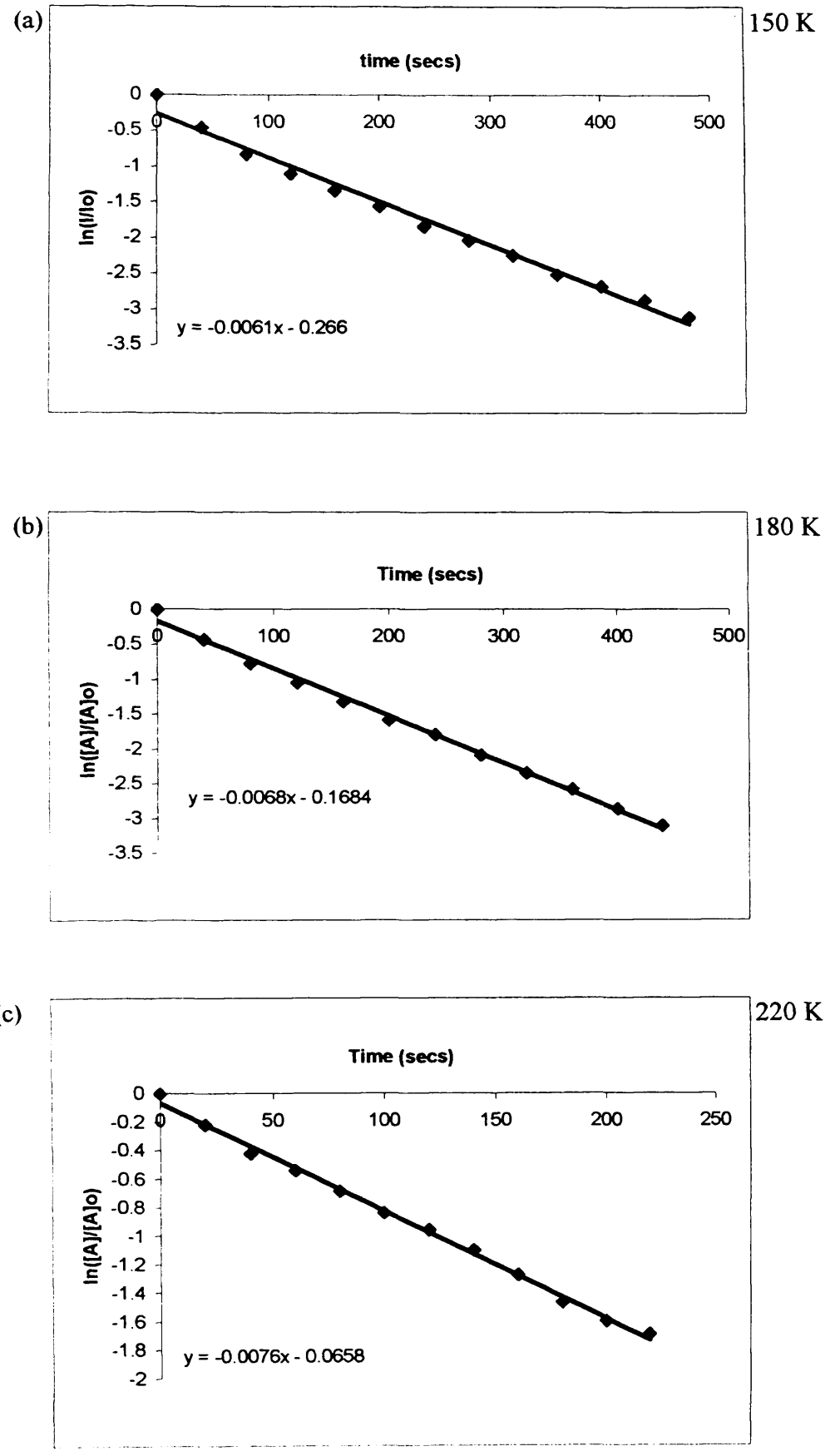

Figure 8.15. Photo-response of $Ti^{3+}_{(surf)}$ in P25 Anatase obeying first order kinetics studied at (a) 150 K, (b) 180 K and (c) 220 K.

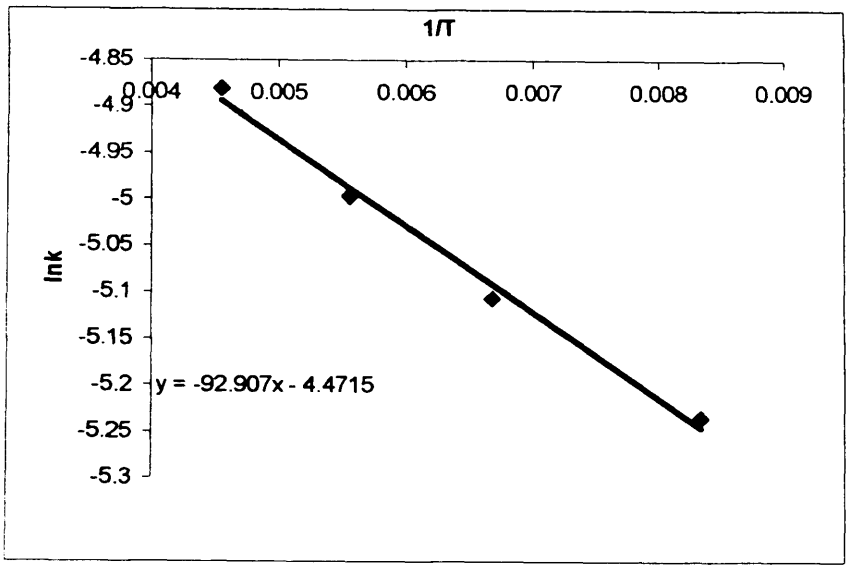

Figure 8.16. An Arrhenius plot of ln k against 1/T for $Ti^{3+}_{(surf)}$ in P25 Anatase.

The kinetics for photo-initiated excitation of the bulk Ti^{3+} centres in P25 were also examined. As described above, the decay curves for the bulk signals at different temperatures were plotted according to a first and second order rate law. However the data was found to fit the first order rate law (similar to the surface centres); the resulting first order plots are shown in figure 8.17a-c. The rate constants determined from each graph are tabulated in table 8.2. Once again, the rate constant (and half life) was found to increase at the higher temperatures, although the absolute values for k and t½ are different for the bulk centres compared to the surface Ti^{3+} centres. The activation energy of the photo excitation of the bulk Ti^{3+} centres was also calculated and the results are given in figure 8.18 with a value of $1.31 \pm 0.09 kJmol^{-1}$.

Table 8.2. Calculated rate constants, k, and half-lives for the $Ti^{3+}_{(bulk)}$ signal in P25 Anatase at increasing temperatures.

Temperature K	Rate constant k (s^{-1})	Half life (s)
120	0.00320 ± 0.003	216.6 ± 2.1
150	0.00409 ± 0.007	169.4 ± 2.8
180	0.00496 ± 0.011	139.7 ± 3.2

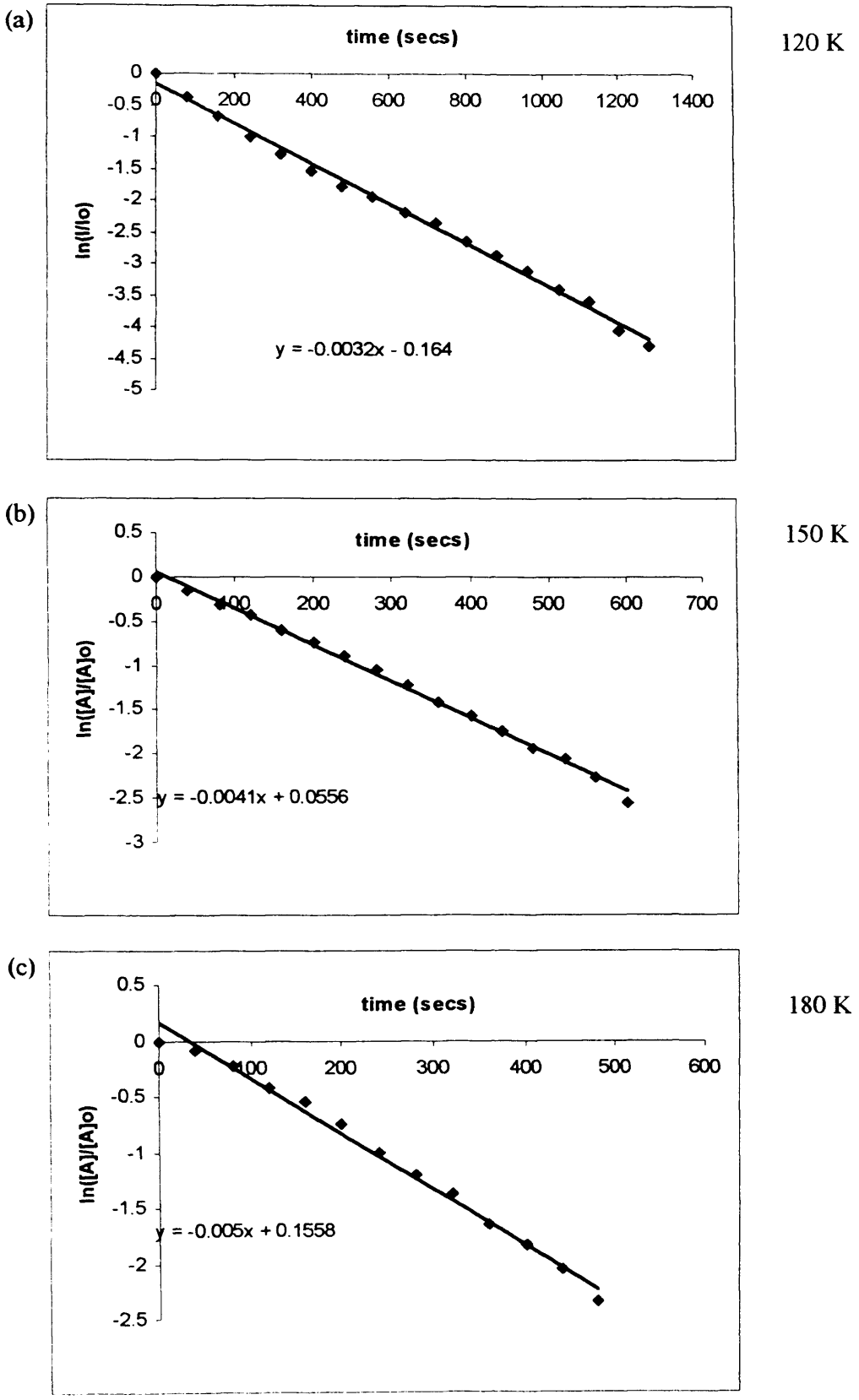

Figure 8.17. Photo-response of $Ti^{3+}_{(bulk)}$ in P25 Anatase obeying first order kinetics studied at (a) 120 K, (b) 150 K and (c) 180 K.

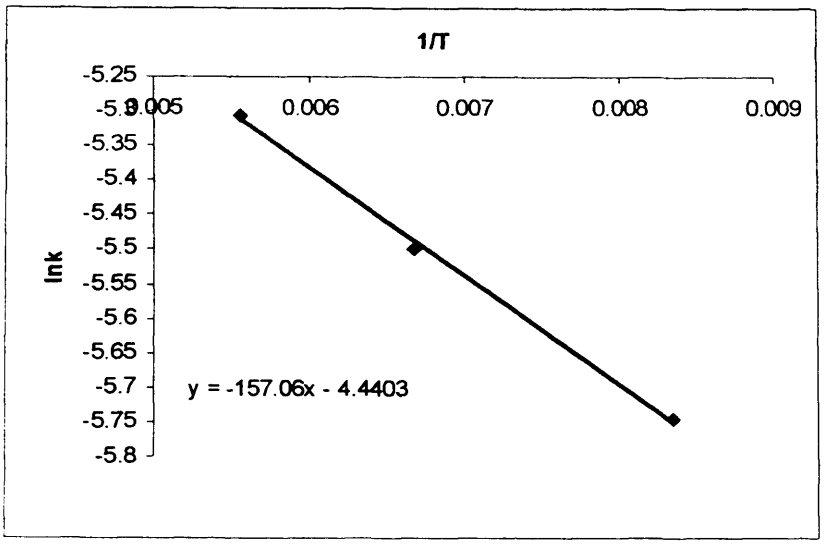

Figure 8.18. An Arrhenius plot of ln k against 1/T for $Ti^{3+}_{(bulk)}$ in P25 Anatase.

As shown above both Ti^{3+} signals (surface and bulk) undergo a loss in signal intensity following UV irradiation at various temperatures. The decay in signal intensities were both found to follow first order kinetics. A comparison of the rate constants, obtained for each form of Ti^{3+} reveals that the signal undergoes a much more rapid decay at the surface than in the bulk form of the Ti^{3+} centre. The calculated half-lives for each Ti^{3+} form also confirms this as the half life for the Ti^{3+} to decay occurs at a much quicker rate than in the bulk of the sample. The activation energy required for each signal at increasing temperatures shows that a higher amount of energy is required for the photo-response of $Ti^{3+}_{(bulk)}$ (i.e., $1.31 \pm 0.03 kJmol^{-1}$) centres to undergo any alteration in signal intensity, whereas the $Ti^{3+}_{(surf)}$ requires a lot less energy almost half (i.e., 0.77 ± 0.09 $kJmol^{-1}$). The differences in the rate of decay for the two signals reflect the differences in the bulk and surface Ti^{3+} centres. That is a lesser amount of time is required as the surface Ti^{3+} centres are in excess i.e., during thermal reduction 80% of the generated Ti^{3+} centres are surface forms, therefore lowering the activation energy required for the reaction.

8.3.6 Kinetics of medium polarised conduction electrons photo excitation in P25

Studies by Serwicka *et al.*,[4] were concerned with the photo-response of both the Ti^{3+} centres and medium polarised conduction electron. Therefore, in order to complete the study of P25 Anatase the rate of decay of the medium polarised

conduction electron was calculated at increasing temperatures along with the half-life and activation energy of the process.

As observed here and by Serwicka *et al.*,[4] when the signal at g = 2.003 was irradiated at low temperatures the signal intensity decayed. In order to determine the rate of decay for the signal at 120 K first and second order graphs were plotted as in the above cases. The decay curve was found to fit the first order rate law (similar to surface and bulk Ti^{3+} centres in P25). The resultant first order plots for all temperatures examined are shown in figure 8.19.

The gradient of each first order plot is equal to the rate constant at the corresponding temperature of study. The rate constant at each temperature studied is shown in table 8.3. Similar to the Ti^{3+} centres (surface and bulk) in P25 the rate constants were found to increase upon temperature increase.

The half-life for each temperature may also be calculated using equation 8.6 the results are shown in table 8.3. A noticeable decrease in the half-life of the signals occurs as the temperature of study is increased. This is also due to a decrease in the time required for the peak to reach saturation at the higher temperatures of study. These results coincide with those calculated for the rate constant where an increase at corresponding temperatures of study is observed.

To determine the activation energy for the photo-response of the $Ti^{3+}_{(surf)}$ centre, a plot of ln k against 1/T (where T is the absolute temperature) has been made. The resultant graph is shown in figure 8.20 giving an activation energy of Ea = 0.20516 ± 0.09kJmol^{-1}.

Table 8.3. Calculated rate constants, k, and half-lives for the medium polarised conduction electrons signal in P25 Anatase at increasing temperatures.

Temperature / K	Rate constants k / (s^{-1})	Half life / (s)
120	0.0074 ± 0.002	93.6 ± 0.3
150	0.00777 ± 0.004	89.2 ± 0.5
180	0.00792 ± 0.009	87.5 ± 1

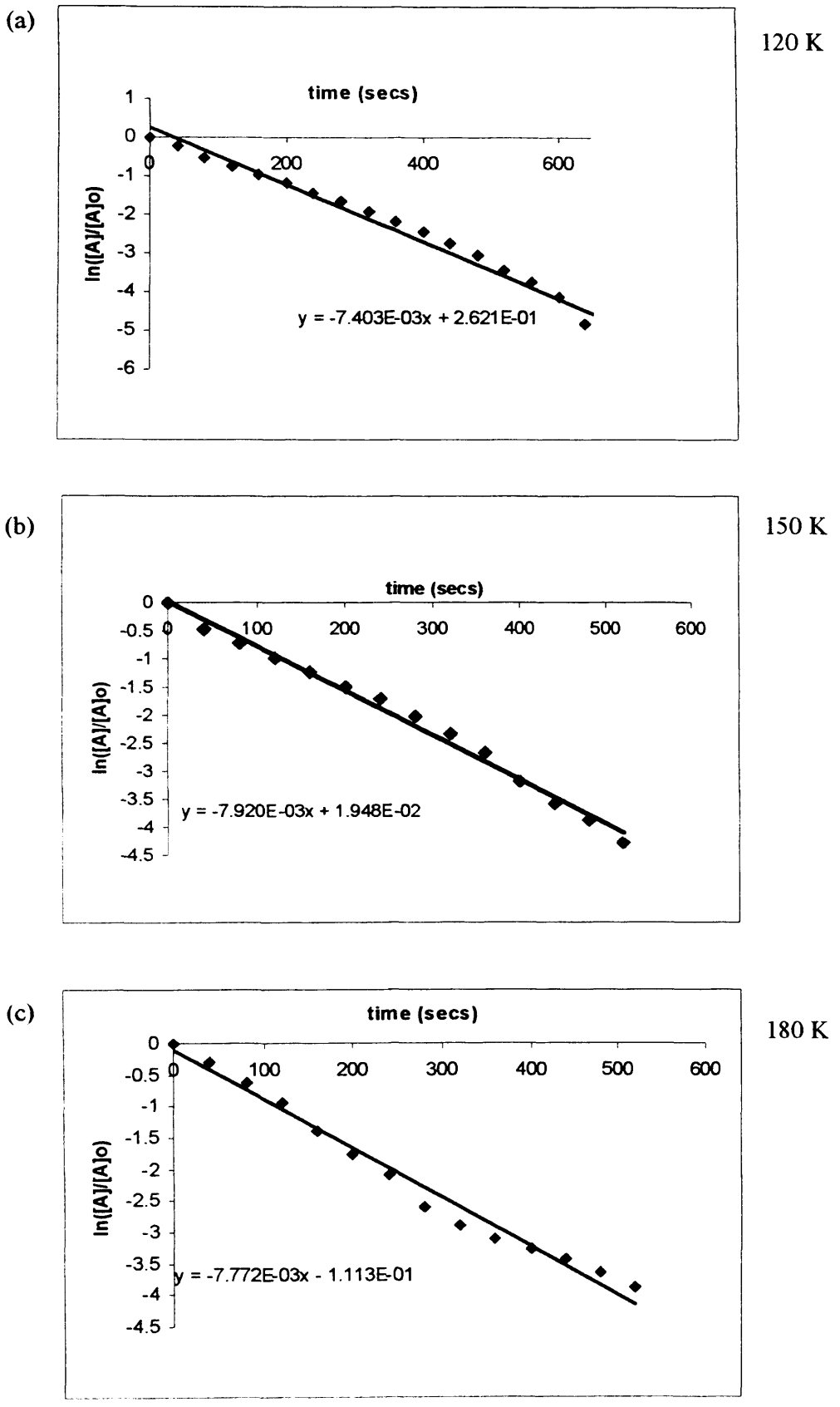

Figure 8.19. Photo-response of medium polarised conduction electron in P25 Anatase obeying first order kinetics studied at (a) 120 K, (b) 150 K and (c) 180 K.

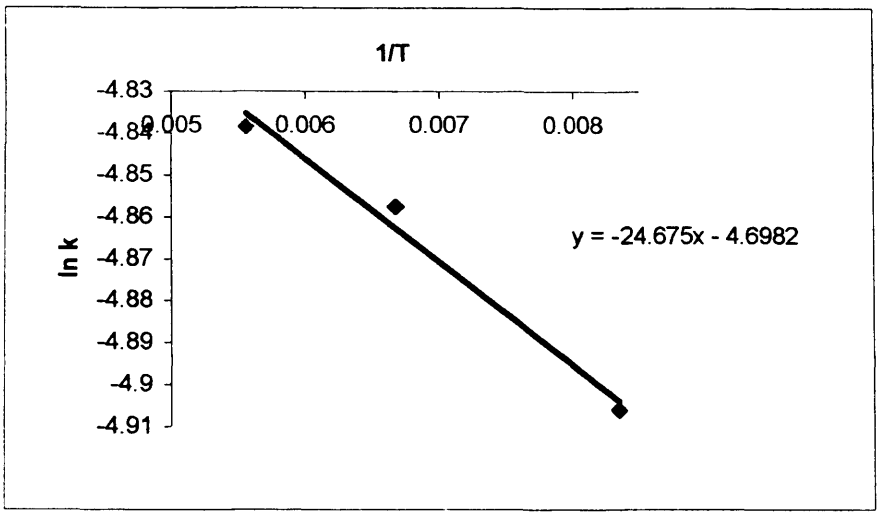

Figure 8.20. An Arrenhius plot of ln k against 1/T for the medium polarised conduction electrons in P25 Anatase.

8.3.7 Kinetics of Ti^{3+} photo excitation in Rutile A

The second TiO_2 sample examined was Rutile A. As outlined above the TiO_2 samples were thermally reduced and the photo-response of the thermally generated Ti^{3+} signal at various temperatures were examined. As shown in figures 8.8 and 8.9 following UV irradiation of the $Ti^{3+}_{(surf)}$ for a period of 10 minutes the rate at which the signal decayed altered, following an increase in temperature. As the temperature of illumination is increased the point at which the Ti^{3+} signal was saturated was reached more slowly than at lower temperatures. In order to determine the rate at which the $Ti^{3+}_{(surf)}$ signal decays at 120 K the signal was plotted according to first and second order rate laws. Similar to the P25 Anatase sample the photo-response curve of the Ti^{3+} signal at 120 K in Rutile A was found to fit the first order rate law as shown in figure 8.21. The corresponding first order plots at increasing temperatures are shown in figure 8.22.

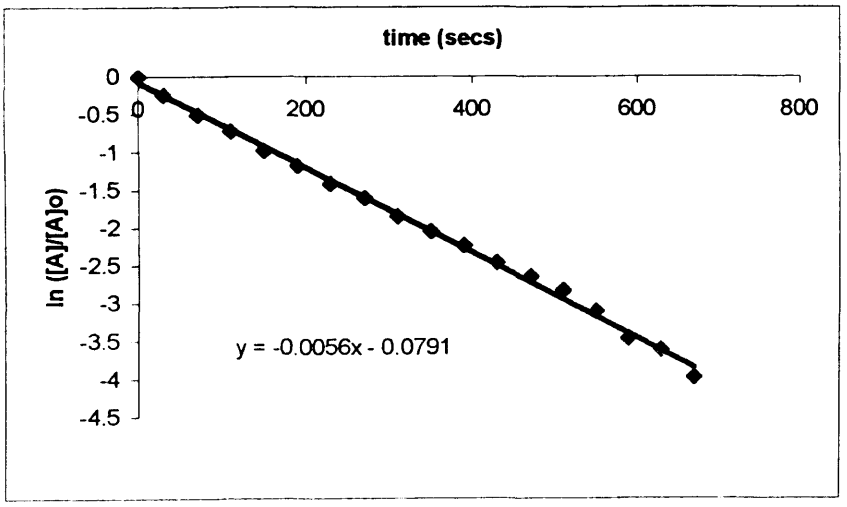

Figure 8.21. First order decay curve for the photoresponse of Ti^{3+} in Rutile A at 120 K

(a)

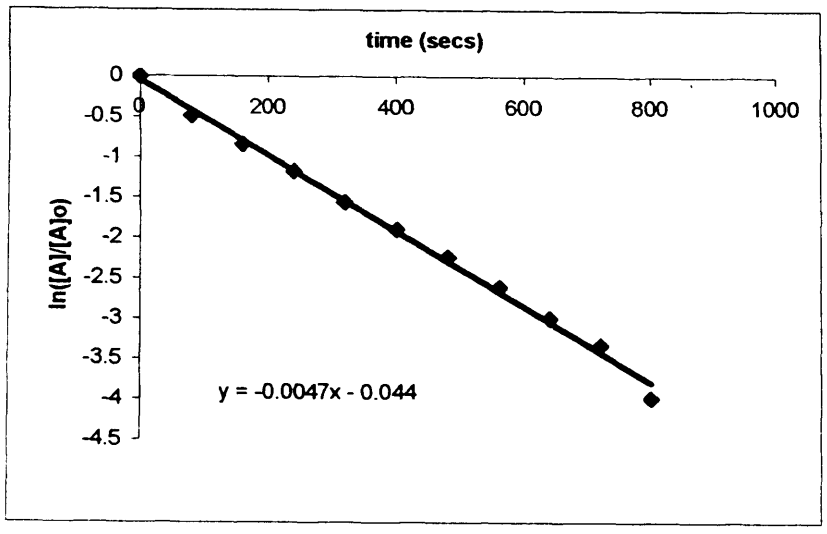

150 K

(b)

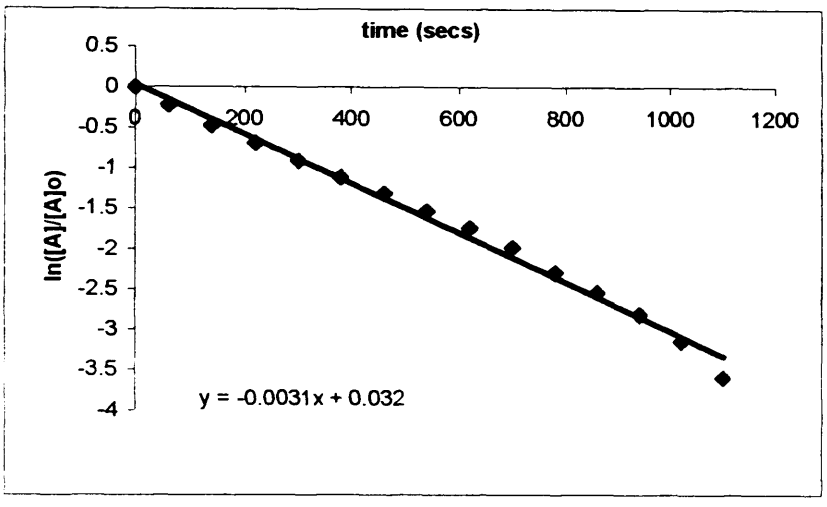

180 K

Figure 8.22. Photo-response of Ti^{3+} in Rutile A obeying first order kinetics studied at (a) 150 K and (b) 180 K.

The gradient of each first order plot is equal to the rate constant at the corresponding temperature of study. The rate constants determined from each graph at the increased temperature of study are tabulated in table 8.4.

Table 8.4. Calculated rate constants, k, and half-lives for the Ti^{3+} in Rutile A at increasing temperatures.

Temperature / K	Rate constants / (s^{-1})	Half life / (s)
120	0.00533 ± 0.001	130.0 ± 1.3
150	0.00468 ± 0.0025	148 0 ± 2.8
180	0.00306 ± 0.004	223.6 ± 4.6

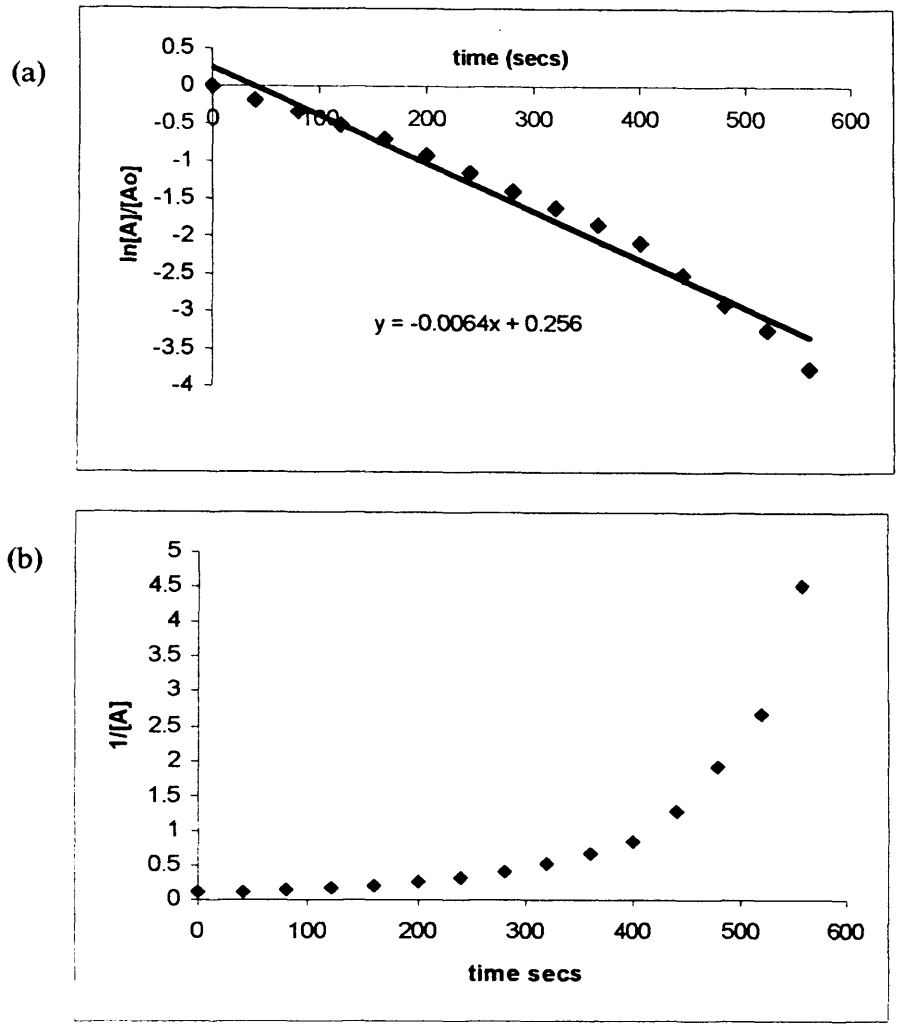

Figure 8.23. (a) First order and (b) second order kinetics. Decay curves for the photo-response of medium polarised conduction electrons in Rutile A at 120 K.

The data was found to fit the first order rate law, the resulting first order plots are shown in figure 8.24. The rate constants were found to increase as the temperature was increased as the calculated half life decreased (shown in table 8.5). The activation energy of photo excitation was calculated and the results given in figure 8.25 with a value of Ea = 0.015 ± 0.002 kJmol^{-1}.

Table 8.5. Calculated rate constants, k, and half-lives for the medium polarised conduction electron in Rutile A at increasing temperatures.

Temperature / (K)	Rate constant / (s^{-1})	Half life / (s)
120	0.00643 ± 0.0001	107.8 ± 1.6
150	0.00718 ± 0.0002	96.3 ± 2.4
180	0.00912 ± 0.0004	76.2 ± 3.4

(a)

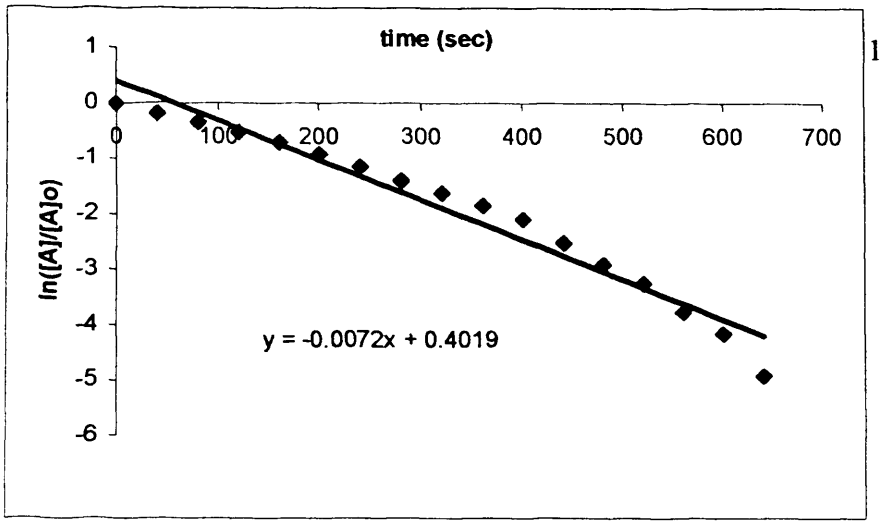

150 K

(b)

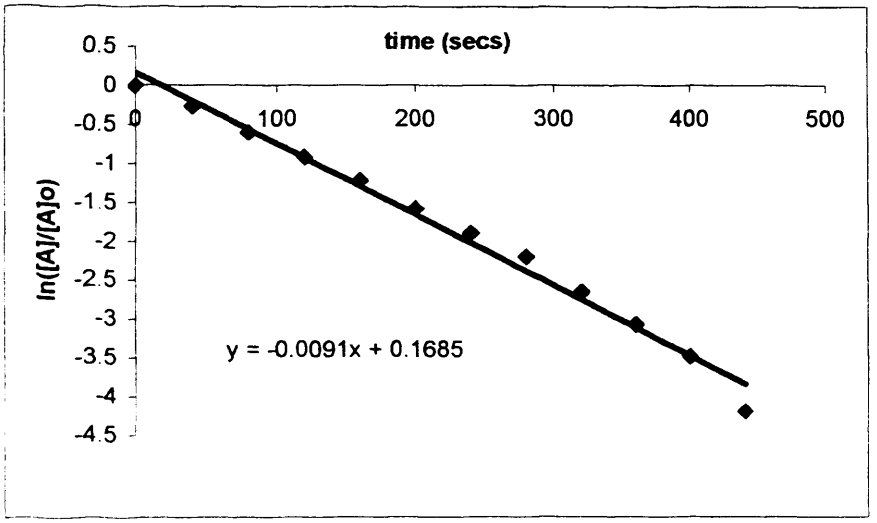

180 K

Figure 8.24. Photo-response of medium polarised conduction electron in Rutile A obeying first order kinetics studied at (a) 150 K and (b) 180 K.

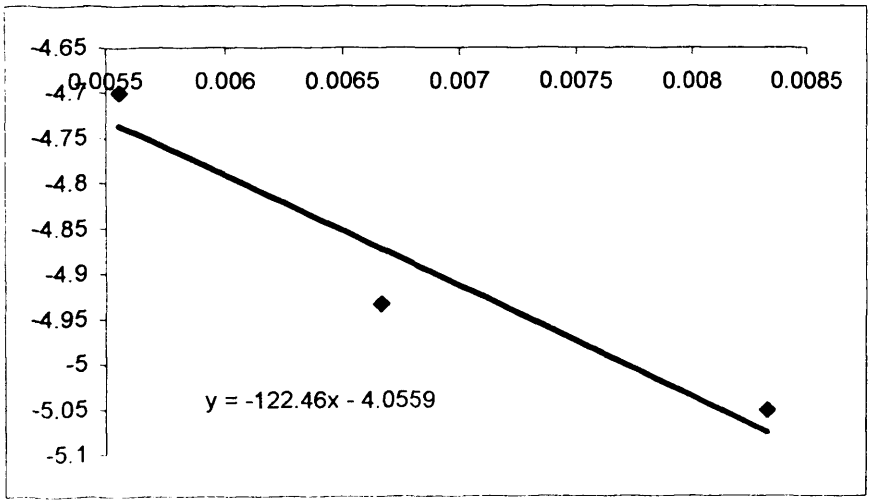

Figure 8.25. An Arrenhius plot of ln k against 1/T for the medium polarised conduction electrons in Rutile A.

8.3.9 *Kinetics of $Ti^{3+}_{(surf)}$ photo excitation in Rutile B*

The kinetics for the photo-initiated excitation of the surface Ti^{3+} centres in Rutile A were also calculated. The decay curves for the surface signals at 120 K were plotted according to first and second order rate laws. Graphs of the ln([A]/[A]o) against time and 1/[A] against time were plotted first and second order reactions respectively. The resultant graphs are shown in figure 8.26.

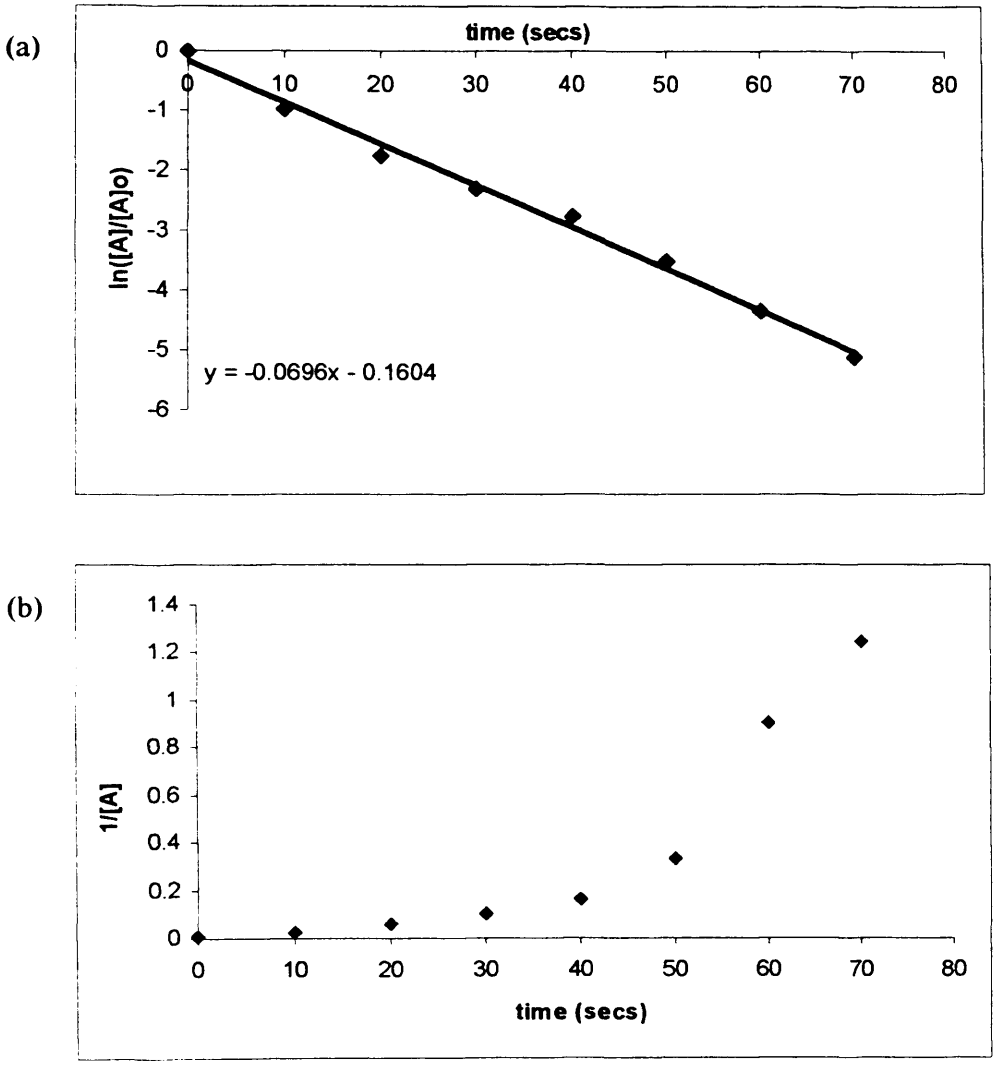

Figure 8.26. (a) First order kinetics and (b) second order kinetics decay curves for the photo-response of $Ti^{3+}_{(surf)}$ in Rutile A at 120 K.

The data was found to fit the first order rate law. A selection (for brevity) of the resulting first order plots (150, 220 and 280 K) are shown in figure 8.27. However, table 8.6 shows the rate constants determined from all temperatures studied.

Similar to the Ti^{3+} signals in Rutile A, the rate constants were also shown to decrease at the higher temperatures studied. Examination of figure 8.11, showed that upon increasing the temperature an increase in the time required for the signal to

reach its saturation limit, this was reflected in the rate constants. The calculated half-lives are also shown in table 8.6. There is a noticeable increase in the half-live of the signals as the temperature was increased as expected. This is due to an increase in the time required for the Ti^{3+} signal to reach saturation (i.e., no further decay in the signal). These results coincide with the rate constants at corresponding temperatures.

It should also be noted however; that the overall time required in reaching saturation of all $Ti^{3+}_{(surf)}$ signals in Rutile B was significantly lower than that required for Rutile A.

Table 8.6. Calculated rate constants, k, and half-lives for the $Ti^{3+}_{(surf)}$ in Rutile B at increasing temperatures.

Temperature / K	Rate constant / (s^{-1})	Half – life / (s)
120	0.0696 ± 0.001	10 ± 0.1
150	0.0509 ± 0.002	13.6 ± 0.6
180	0.0463 ± 0.0025	15 ± 0.8
220	0.0401 ± 0.003	17.2 ± 1.5
250	0.0273 ± 0.004	25.4 ± 3.3
280	0.024 ± 0.006	28.9 ± 5.2

Identical to the Rutile A sample no activation energy, Ea, for the photo excitation of Ti^{3+} centres in Rutile B was unable to be calculated due to the decrease the rate constants as the temperature is increased.

The corresponding kinetics of the photo initiated excitation of the bulk Ti^{3+} centres in Rutile B were not calculated due to the unusual behaviour experienced following removal of the UV illumination (i.e., the signal was not restored to its original value). This unusual behaviour previously not seen in the other TiO_2 samples is thought to occur due to the impurity of the Rutile B sample. The presence of impurities provides more traps in the material allowing preferred stabilisation of the photo excited electrons and therefore, do not allow the original intensity of the signal to be achieved in the dark. The use of thermal treatment restores the signal to its original intensity. A detailed mechanism of the process occurring will be presented later.

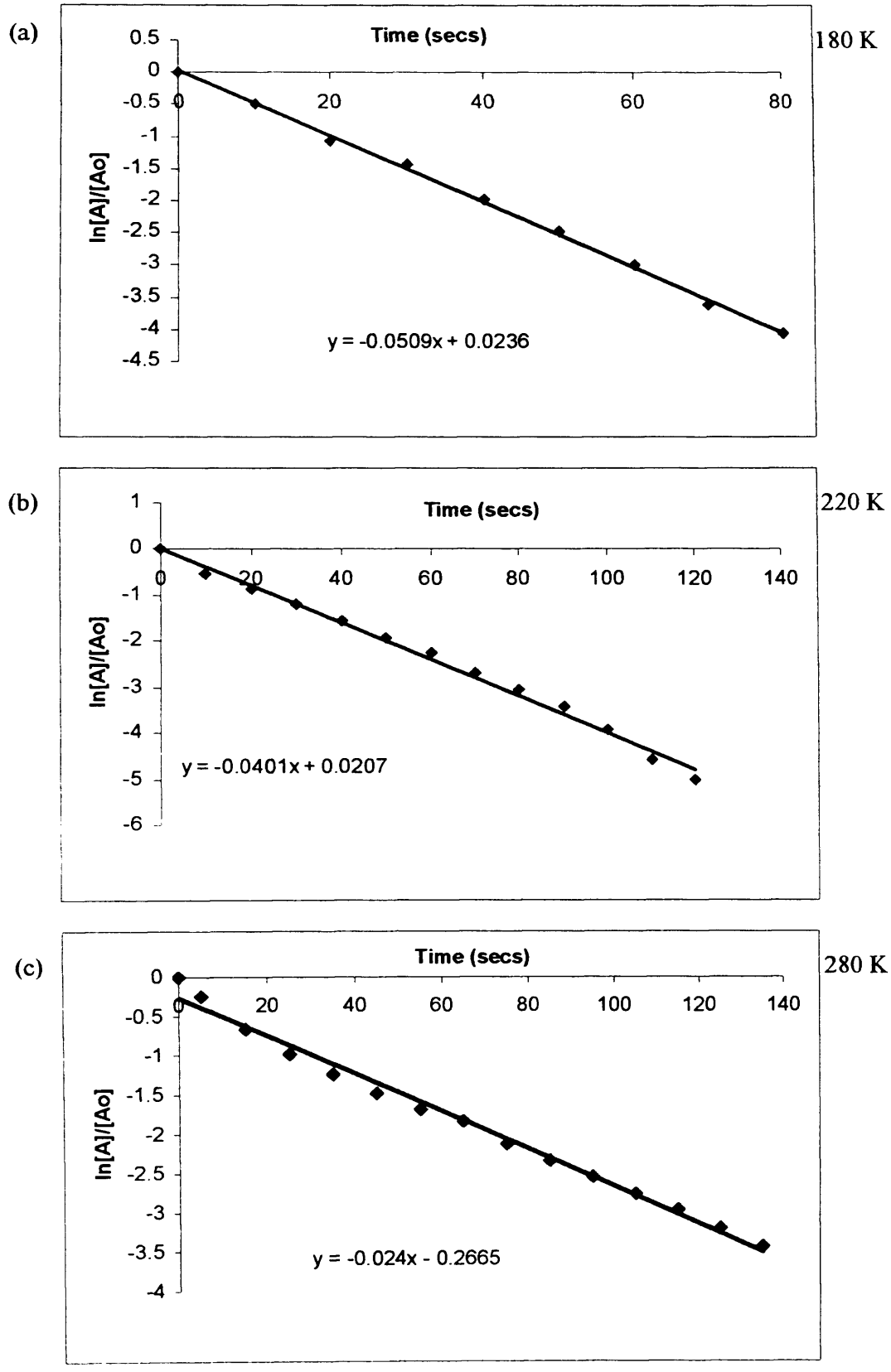

Figure 8.27. Photo-response of $Ti^{3+}_{(surf)}$ in Rutile A obeying first order kinetics studied at (a) 180 K, (b) 220 K and (c) 280 K.

8.4 Discussion

As presented in the above data, the photo-response of the signals due to Ti^{3+} (both surface and bulk) and the medium polarised conduction electron signals undergo an exponential decay in intensity when UV irradiated. The rate at which these signals decay is different for each sample and different at various temperatures.

Serwicka *et al.*,[4] also studied the photo-response behaviour of both Ti^{3+} and medium polarised conduction electrons in a Rutile sample. They reported that when the signal at g = 2.003 (medium polarised conduction electron) was UV irradiated at 120 K the signal intensity decreased, which they suggested was due a decrease in concentration of the centres responsible for the absorption of UV. Removal of the illumination allowed the signal to be restored to its original intensity. It was also noted that the photo-response signal due to Ti^{3+} centres undergoes the same photo-response when UV irradiated.

The decrease in Ti^{3+} signals occurs by absorption of light, this causes electrons to be excited to the low-lying states just below the conduction band. An increase in the transient formation of $Ti^{\delta 4+}$, occurs as the electrons are excited to the states and therefore reduces the intensity of the Ti^{3+} signal. In another study the photo-response of the Ti^{3+} signal was observed to undergo the same loss in signal intensity following UV irradiation.[7] This observed variation in signal intensity, during the reported photo-response study, was compared to the photoconductance of the corresponding signal by Scalafini and Herrmann.[8] The photo-response of the Ti^{3+} signal was noted to behave inversely proportional to the photoconductance response[8] i.e., interrupting the irradiation causes the Ti^{3+} centres concentration to increase, as witnessed here.

8.4.1 Photodynamics of Ti^{3+} in anatase versus rutile

As detailed above, following illumination of the thermally generated Ti^{3+} signals present in TiO_2 a decrease in signal intensity occurs, as the electrons are photo-excited to other transient states. Cessation of the illumination caused the Ti^{3+} signal intensity to return to its original value (with the exception of the rutile B sample; discussed later). The rate of signal decay was found to be temperature dependent but also surprisingly sample dependant. In other words the photodynamic behaviour of the surface Ti^{3+} centres was not only different on anatase *versus* rutile,

but it also showed an inverse behaviour in the two different materials. Nevertheless, in all of the photo-response studies presented here, the rate of signal decay followed first order rate behaviour.

The first order rate dependency of the photo-response process is essentially as expected, as the rate will be dependent on the concentration of Ti^{3+} centres present. However, the observed difference in the rates of Ti^{3+} excitation in anatase *versus* rutile is more difficult to explain, a tentative proposal for the differences is related to the different level of defects and impurities in both materials.

It should be recalled that, during the photo-response of the Ti^{3+} centres a decrease in signal intensity is observed due to a decrease in the population of the centres responsible for light adsorption (i.e., the Ti^{3+} centres). Upon UV illumination the electrons present in the Ti^{3+} states, of all TiO_2 samples, are only excited to low lying states positioned just below the conduction band, resulting in the decay of signal the Ti^{3+}intensity in favour of the $Ti^{\delta 4+}$ species formed. Upon removal of the UV illumination the Ti^{3+} centres are reformed as the electrons return to their original Ti^{3+} "ground state". However, during the photo-response study of the P25 Anatase sample the rate of signal decay of the Ti^{3+} signal (both surface and bulk) was observed to *increase* upon increasing the temperature. One possible suggestion for this increase in signal decay is, the presence of other trapping sites with energies close to those of the Ti^{3+} centres, creating a competition for electron trapping at higher temperatures. In other words, at low temperatures, the formation of the Ti^{3+} centre is favoured after the photoexcitation process, even though the closely spaced levels of the neighbouring defects are available. As the temperature increases the rate of trapping at both Ti^{3+} states and the defect states increases, so that a competition occurs at the higher temperatures. The electron is therefore temporally trapped at another defect / impurity site. At lower temperatures the electron escapes from this trap state to reform the Ti^{3+} centre, while at higher temperatures there is a competition between the reformation of the Ti^{3+} centres and the trapping at another more stable site. The competition between the two sites results in an overall decrease in Ti^{3+} reformation at higher temperatures thus causing an increase in the observed rate constants for the anatase samples. It should be noted, that the P25 sample studied here is not a pure form of anatase. On the contary, it contains approximately 80% anatase, while the remaining 20% contains microdomains of rutile.[9] It is known that mixed phases of

TiO_2 are more photoactive than either single (anatase or rutile) phases, so the unusal photoresponse behaviour for P25 may be due to these mixed phases, as opposed to an inherent pecularity of anatase.

As mentioned above, the photo-response dynamics of the Ti^{3+} centres in Rutile A and $Ti^{3+}_{(surf)}$ centres in Rutile B followed the opposite trend in rate constant (ie., the rate constant decreases at increasing temperature for rutile, while it increases at increasing temperatures for anatase P25). In other words it takes longer for the Ti^{3+} signal to decay in the rutile material at higher temperatures. A possible hypothesis for this trend is based on the ground that an electron is photo-excited from a surface Ti^{3+} centre. The electron is temporally trapped at a series of low lying states just below the conduction band and the rate of escape from this trap state back to reform the Ti^{3+} centres increases with increasing temperature. In other words, at the higher temperatures, it is thought, that the electrons are returning to the Ti^{3+} states more quickly, re-populating the Ti^{3+} levels, and therefore it becomes more difficult (i.e., it takes longer) to saturate the Ti^{3+} signal. At low temperatures, the photoexcited electrons, remain in the virtual states for longer, and therefore the Ti^{3+} states are not re-populated. This is a possible explanation as to why the rate of Ti^{3+} decay is faster at the lower temperatures.

The trends observed for the surface Ti^{3+} states in rutile B follow the same trends as discussed above for the rutile A sample. However, for the bulk Ti^{3+} states in rutile B the signals did not return to their original intensity even after the UV illumination was ceased. As in all other cases the $Ti^{3+}_{(bulk)}$ signals are illuminated causing photo excitation of the electrons to various trapping states (i.e., low lying trapping states, defects/impurities) in the TiO_2 sample. Removal of the UV illumination allows some electrons to escape from the traps to reform the Ti^{3+} centre. However, during this study a large amount of the electrons are trapped at defect/impurity sites, these electrons have restricted movement and so cannot return to their original position due to the fluctuation of electrons at one temperature. Therefore, only a small amount of the Ti^{3+} centres are reformed as they have enough energy to escape the trapping sites. It was however, shown in figure 8.13 that increasing the temperature slowly after UV irradiation caused the signal intensity to increase to the respective saturation points at each temperature. By increasing the temperature slowly electrons, which are trapped at the impurity/defect sites are provided with extra energy to overcome the trapping effects experienced at these sites. The trapped electrons are then able to escape these

impurity/defect traps and return to their original Ti^{3+} site thus regenerating the signal intensity.

The process by which the original $Ti^{3+}_{(bulk)}$ signal intensity is achieved is known as thermoluminescence.[10] Luminescence describes the process of emission of optical radiation from a material. Luminescence embraces many similar but specific effects, each of which can be described by the addition of a prefix to the term luminescence, thermoluminescence is an example of this. Thermoluminescence is a particular form of luminescence related not to the means of excitation but to the time scale over which emission takes place. In this case the emission is the return of the trapped electrons to the conduction band and eventually to the original Ti^{3+} site. As mentioned throughout this section when the signal in question is UV irradiated a transfer of energy to the electron occurs and their displacement to a higher energy state namely the conduction band is reflected in the loss of signal intensity. The presence of an electron trap (supplied by the impurities in the sample) causes the return of the electrons to the original state to be delayed when under dark conditions at a constant temperature. The low-lying traps are representative of shallow electron traps and electrons returning from these sites require energy. The electrons are forbidden to return to their original position directly from their trapped state. By increasing the temperature, the probability of the electron returning to its original state is increased and therefore accelerates the rate of increase in signal intensity; this process is known as thermoluminescence and occurs readily in the photo-response of $Ti^{3+}_{(bulk)}$ centres in the Rutile B sample.

However, in support of the discussion above further evidence is required to thoroughly understand the fundamental processes occurring during UV irradiation of these defect sites in the TiO_2 material studied. To obtain a more accurate perceptive of the actual processes which are occurring during UV irradiation work on single crystals is essential in this area of study.

8.5 Conclusion

During the study of the photo-response of the thermally generated paramagnetic centres on TiO_2, a common decrease in signal intensity was observed with only a slight variation in the trends depending on the sample. The decrease in EPR signal intensity for the Ti^{3+} states was due to the trapped electrons being excited to low-lying states present just below the conduction band edge. Altering the

temperature of study for each signal caused a change in the signal intensities along with a difference in the time required to achieve 'saturation' of the respective signals. As shown in the above discussion, the photo-response signals were found to decay according to first order kinetics.

During the photo-response study of P25 Anatase, an increase in the rate of Ti^{3+} signal decay was observed at increasing temperatures. Similar photo-response decay profiles were observed for the Rutile A and B samples. However, a noticeable decrease in the rate of Ti^{3+} signal decay was observed at increasing temperatures for both Rutile A and Rutile B samples studied. In all cases, the Ti^{3+} signal intensities returned to their original value in dark conditions (i.e., after cessation of the UV illumination) indicating a reversible reaction. However, during the study of $Ti^{3+}_{(bulk)}$ in the Rutile B sample, this was not the case and excess energy (in the form of heat) was required to return all the photo-excited electrons to the original Ti^{3+} state due to the thermoluminescence of the process. Due to the large number of impurities present in this particular sample of rutile, additional low-lying states (i.e., transition metal impurities) below the conduction band edge are available for stabilising the photo-excited electron. By supplying excess energy into the system, these electrons may then return to their original positions in the TiO_2 sample and in so doing, the Ti^{3+} signal intensity returns to its initial value.

As demonstrated by these results, the photo-response of the thermally generated surface and bulk Ti^{3+} centres in the TiO_2 samples may be successfully examined using the EPR technique. The change in signal intensity can be followed and the rate at which the signal decays, along with the half-lives and activation energies, may then be easily calculated. This analysis has shown that the photodynamics of the different TiO_2 samples varies from sample to sample. To obtain further information on the photo-response of each signal examined in the TiO_2 materials further work examining the exact energy required by the use of cut off filters as detailed previously by Serwicka *et al.*[4] In addition to this, examination of the photo-response experienced by defect and impurity free forms of the Anatase and Rutile materials should also be studied to provide additional information of the photo-response experienced by the Ti^{3+} centres in the TiO_2 samples.

8.6 References

1. S. W. Hodgskiss PhD Thesis, University of Durham, (1981).
2. Dipl. Ing. Martin Sterrer *Photoinduced Surface Phenomena on Highly Dispersed MgO*, Institut fur Materialchemie, (2003).
3. Peter Atkins & Julio de Paula, '*Physical Chemistry*,' Seventh Edition, Oxford, 2002.
4. E. Serwicka, M. W. |Schlierkamp, R. N. Schindler, *Z. Naturforsch*, **36a**, 226, (1981).
5. S. Sazonova, T. P. Khokhlova, G. M. Sushentseva, N. P. Keier, *Kinet. Katiliz*, **3**, 655, (1962).
6. A. K. Ghosh, R. B. Lauer, R. R. Addis, *Phys. Rev.* **8**, 4832, (1973)).
7. C.A. Jenkins, PhD Thesis, University of Wales, Cardiff, (1998).
8. A. Sclafani, J. M Herrmann, *J. Phys. Chem.*, **100**, 13655, (1996).
9. D. C. Hurum, A. G. Agrios, K. A. Gray, T. Rajh, M. C. Thurnauer, *J. Phys. Chem. B*, **107**, 45545, (2003).
10. Thermoluminescence Dosimetry, *Medical Physics Handbooks, 5*, A. F. McKinlay, (1981).

Chapter 9
Conclusions

This thesis has employed the technique of EPR spectroscopy to study the various methods of generation and subsequent behaviour of the paramagnetic states in different TiO_2 materials with a range of different probe molecules or organic substrates of specific interest. Owing to its sensitivity, non-invasive properties and the specificity of the spin Hamiltonian parameters, the results presented in this Thesis have demonstrated the unique role of the EPR technique for the study of heterogeneous photocatalytic and photo-dynamics processes.

Based on the EPR experiment, the nature, stability and lifetimes of the radicals stabilised on the TiO_2 surface have been shown to depend on a number of distinct factors including type of TiO_2 sample (i.e., Anatase *vs.* Rutile), pre-treatment conditions (i.e., hydrated *vs* dehydrated surfaces) and even the manner in which the adsorbates are exposed to the sample (i.e., co-adsorption *vs* sequential adsorption). Furthermore, the photo-dynamics of the paramagnetic species were also found to be dependant on various parameters, including temperature, dopant level, location of the paramagnetic species (i.e., surface *vs* bulk) and even the type of TiO_2 sample employed.

It has been demonstrated that the surface properties of a polycrystalline oxide will suffer different degrees of perturbation and change depending on the physical and/or chemical pre-treatment conditions. In turn the defectivity and extent of the surface planes will vary thus changing the reactivity of the samples, and ultimately the rate of generation and subsequent lifetimes of the trapped charge carriers. For example, as demonstrated in chapter 5, trapped charge carriers can be generated in a number of different ways, either by thermal reduction under vacuum or under a hydrogen atmosphere or alternatively by radiative treatment. Following thermal reduction of the TiO_2 samples, two distinct species were identified, namely medium polarised conduction electrons and Ti^{3+} centres. The Ti^{3+} states were found to be thermally stable at the TiO_2 surface for several hours at room temperature whilst no evidence was found for the formation of trapped hole states under these preparative conditions. However, following UV irradiation of the TiO_2 samples under an oxygen atmosphere, photo-generated sub-surface trapped holes were observed. In the case of

Rutile A, the simultaneous formation and stabilisation of trapped holes and Ti^{3+} centres were observed, while no traces of the signal due to the medium polarised conduction electrons were observed during UV irradiation of the samples.

The reactivity of the thermally generated surface and bulk centres were examined by the judicious choice of probe molecules, particularly dioxygen and the resultant superoxide anion. A number of different oxygen centred species were identified depending on the nature of the non-stoichiometric TiO_2 surface following addition of oxygen. For example, during oxygen addition to the reduced P25 Anatase surface, the well-known superoxide anion was formed. However, oxygen addition to the Rutile A sample resulted in the predominant formation of the ozonide species whilst the analogous experiment on the Rutile B sample led to a complex mixture of both O^- and O_2^- anions. In other words, the rutile surface displays a strong propensity towards dioxygen bond cleavage, presumably through formation and subsequent decomposition of the doubly charged peroxy anion (O_2^{2-}). These unusual results are difficult to explain based purely on thermodynamic or even kinetic considerations, and must instead be intimately linked to the nature of the different adsorption sites on the anatase *vs* the surface, and the electron transfer step itself.

The superoxide anion has once again been shown to be an excellent surface probe, which provides abundant and meaningful information on the local environment where it is stabilised. An excellent example of the type of information provided on the nature of the local environment around the Ti^{4+} centre is demonstrated through the observed heterogeneity of adsorption sites resulting from the thermal evacuation of the sample at increasing temperatures. At lower reduction temperatures the removal of lattice oxygen, O^{2-}, from the surface was favoured at the low co-ordinated Ti^{4+} sites generating Ti^{3+} cations. Following oxygen addition, superoxide anions with particularly high g_{zz} components, which are typical of low coordinated cations, were observed and this suggests that the early Ti^{3+} formation (at low temperatures) occurs at low coordinated sites. Increasing the temperature of thermal reduction resulted in the removal of lattice oxygen at the higher co-ordinated Ti^{4+} sites. This was reflected in the increase heterogeneity of sites available for superoxide formation, particularly those with progressively lower g_{zz} values. This simple experiment has therefore revealed, for the first time, perhaps the obvious conclusion, that the surface oxygen anion defects on TiO_2 are formed preferentially at the lowest coordination sites, while

higher coordination Ti^{4+}-O_2^- sites are only deoxygenated (producing oxygen vacancies and reduced Ti^{3+} centres) at substantially higher temperatures.

While thermal treatment of the TiO_2 samples leads to paramagnetic states on a non-stoichiomeric surface, photo-irradiation of the sample at low temperatures will also result in the formation of trapped charge carrier states. For example, low temperature UV irradiation of the clean dehydrated TiO_2 samples under an oxygen atmosphere led to the formation of thermally unstable trapped holes on all samples (P25 Anatase, Rutile A and Rutile B). However, the formation of the Ti^{3+} centres were only visible on the Rutile A sample. Removal of the excess oxygen revealed the photo-generated superoxide anion on all TiO_2 samples examined; this was not previously seen under the excess oxygen atmosphere due to line broadening. The heterogeneity of the g_{zz} components for the resulting anions was different on the different surfaces, revealing a difference in the speciation of the radicals on these surfaces. At least five sites were observed for O_2^- stabilisation on the P25 Anatase sample while only two poorly resolved sites were available on both Rutile samples. In all cases, the superoxide anions formed were found to be stable for several days at room temperatures. The differences in the heterogeneity of sites available for photo-generated O_2^- during UV irradiation of the TiO_2 samples highlights the differences in the Anatase and Rutile samples used along with the pre-treatment conditions.

The effect of UV irradiation and subsequent generation of trapped charges along with transient intermediates have also been examined in a series of experiments in which excess O_2 was co-adsorbed with an organic molecule. This has been examined in the relation to reaction mechanisms of VOC decomposition in heterogeneous photocatalysis over TiO_2 surfaces. The reaction intermediates involved during the oxidation of organic materials have been successfully identified. During the co-adsorption of acetone and oxygen over the TiO_2 surface, direct evidence was provided for the formation of a thermally unstable surface alkyl peroxy radical ($ROO^{\bullet}$) formed during the low temperature UV irradiation. The use of ^{17}O labelled O_2 has aided in the confirmation of this radical. On this basis the alkylperoxy radical was conformed as $CH_3COCH_2OO^{\bullet}$, generated by hole transfer to adsorbed acetone, and this represents the first identification of such an intermediate with acetone/O_2.

The transient intermediates formed during the UV irradiation of co-adsorbed aldehydes/O_2 and alcohols/O_2 were also studied in a complimentary series of

experiments to the acetone/O_2 mixtures. The results have demonstrated that during the UV irradiation of co-adsorbed aldehdye/O_2 mixtures, acyl peroxy radicals were formed on the Anatase surface, as previously observed on the Rutile B sample. In addition, the formation of a transient peroxy radical ($ROO^{\bullet}$) was also observed during the UV irradiation of a co-adsorbed mixture of alcohols/O_2 on the anatase surface.

The utility of the co-adsorption method, as opposed to pre-adsorption, is demonstrated to be a key experimental feature in obtaining a successful model reaction system for photocatalytic oxidation processes, since the nature of the radical formed depends entirely on how the surface is pre-treated with reactants. In other words, if oxygen is preadsorbed on the surface and reacts to form the relatively stable superoxide anion, the subsequent reactions with the organic substrates may yield different reaction products, compared to the species formed *via* reaction of the peroxy radicals identified exclusively in the co-adsorption experiments. These results also show that transient radical species can indeed be observed by EPR over TiO_2 surface, and the experiments demonstrate the necessity to characterise the material under *in-situ* conditions in order to obtain a more realistic view ion the nature of the radicals involved – the photo-oxidative process.

In "real" photocatalytic processes, the TiO_2 surface will frequently be exposed to moisture, and therefore a study of the hydrated surface is perhaps a more realistic model for study of surface processes. Therefore, the nature and stability of the oxygen-based radicals (i.e., trapped hole and superoxide) generated by UV irradiation were also examined as a function of surface hydration. It was observed that by increasing the amount of surface hydration on the P25 Anatase sample, no oxygen centred radicals could be detected by EPR. This does not necessarily mean that the radicals are NOT formed; on the contrary, it is quite conceivable that the lifetimes of the paramagnetic species are too short to detect by EPR as no surface sites are available for stabilisation. By decreasing the amount of surface hydration and subsequent UV irradiation, a selection of species including O^-, $HO_2^{\bullet}$ and Ti^{3+} were identified. In comparison to this, following UV irradiation of the hydrated Rutile samples a number of species were stabilised on the surfaces under various amounts of hydration; these included O^-, traces of $HO_2^{\bullet}$, and Ti^{3+} centres. Evacuation of the samples following low temperature UV irradiation in most cases revealed the stabilisation of the superoxide anion. The Rutile A sample was capable of stabilising

the O_2^- anion on both forms of the hydrated surface (i.e., partial and full hydration). The sites available for O_2^- formation were observed to be identical to those during photo-generation of the anion on the dehydrated Rutile A surface, however, the intensity of the superoxide signal decreased over several hours when left at room temperature unlike that on the dehydrated forms where the O_2^- was stable for several days. During UV irradiation of the hydrated forms of the Rutile B sample the superoxide anion was only photo-generated and stabilised on the partially hydrated form of the sample, no traces were observed on the fully hydrated form of the surface. The stability and intensity of the alkyl peroxy radical ($CH_3COCH_2OO^{\bullet}$) was also noted to decrease upon UV irradiation of the co-adsorbed acetone/O_2 over a hydrated P25 Anatase surface.

The addition of water to the TiO_2 surfaces not only demonstrates the blocking of sites available for photo generated O_2^-, but also a decrease in signal intensity and stability of the oxygen centred radicals. Complementing these results were those obtained during the addition of NO to the hydrated TiO_2 surfaces. Similar to the stabilisation of the O_2^- anion on the different hydrated forms of TiO_2 surfaces the sites available for NO adsorption were observed to be preferentially blocked preventing any NO adsorption. Dehydroxylation of the TiO_2 surfaces at increased temperatures resulted in the sequential removal of the OH groups from high co-ordinated sites initially to those of lower co-ordination sites, therefore with the aid of NO the identification of the local co-ordination environment of the sites available at increased temperatures were identified.

As demonstrated here, complete knowledge of the TiO_2 sample is necessary (i.e., Anatase *vs.* Rutile, Thermal *vs.* UV irradiated and hydrated *vs.* dehydrated) in order to fully understand the reactions that can occur both at the TiO_2 surface and bulk. In addition to this, the differences in the photo-dynamics experienced by the TiO_2 samples are also related to the various forms of TiO_2 samples examined. For example, UV irradiation of the bulk or surface Ti^{3+} centres resulted in the significant decrease in EPR signal intensity, which was restored after cessation of the illumination. The decrease in intensity was due to the photo excitation of the electrons to low lying states positioned just below the conduction band thus generating transient $Ti^{4\delta+}$ states. The decay curves for the photo-dynamic responses were observed to follow first order kinetics. However, the rate at which these signals decayed varied

significantly from sample to sample and at different temperatures. In the case of P25, the rate of EPR signal decay for both surface and bulk Ti^{3+} centres was found to increase at increasing temperatures. However on all of the rutile samples, the opposite trends were observed. These observed differences in the rate of signal decay are thought to be due to the differences in the surface morphologies i.e., Anatase *vs.* Rutiile. The presence of surface defects in each sample are likely to act as additional traps, thus, altering the photodynamic rates. The most significant alteration in photo-response due to the presence of defects/impurities was observed in the photo-response study of bulk Ti^{3+} centres in Rutile B. The addition of these impurities act as additional traps for the photo excited electrons. However, the electrons trapped at these sites are incapable of reforming the Ti^{3+} after removal of the UV illumination due to insufficient energy in escaping these traps. To overcome this problem the temperature of the sample was gently increased providing enough energy to allow the electrons to return to their original positions (i.e., thermoluminescence).

Overall, the results presented in this Thesis have illustrated the many differences in the surface chemistry and photodynamics of Anatase and Rutile TiO_2, which can be clearly related back to differences in surface morphologies.